Investigation of the low temperatures phase equilibria involving molecular solids : application to LNG production

Salem Hoceini

PSL UNIVERSITÉ PARIS

THÈSE DE DOCTORAT
DE L'UNIVERSITÉ PSL

Préparée à MINES ParisTech

Investigation des équilibres de phases à basses températures incluant des solides moléculaires : application à la production du GNL

Investigation of the low temperatures phase equilibria involving molecular solids: application to LNG production

Soutenue par

Salem HOCEINI

Le 10 décembre 2021

Ecole doctorale n° 621

Ingénierie des systèmes, matériaux, mécanique, énergétique

Spécialité

Energétique et génie des procédés

Composition du jury :

Jean-Noël JAUBERT Professeur Université de la lorraine	*Président*
Laura Annamaria PELLEGRINI Professeur Politecnico di Milano	*Rapporteur*
Martin TRUSLER Professeur Imperial College London	*Rapporteur*
Marcelo ZABALOY Professeur Universidad Nacional del Sur (UNS)	*Examinateur*
Jean-Luc DARIDON Professeur Université de Pau et Pays de l'Adour	*Examinateur*
Paolo STRINGARI Chargé de recherche Ecole des Mines ParisTech	*Directeur de thèse*
Marco CAMPESTRINI Ingénieur de recherche Ecole des Mines ParisTech	*Examinateur*

MINES ParisTech | PSL

Acknowledgments

I would like to express my gratitude to all the jury members. Many thanks to Pr. Laura Annamaria Pellegrini and Pr. J.P. Martin Trusler for accepting to read and evaluate my work. Many thanks also to Pr. Jean-noel Jaubert, Pr. S. Marcelo Zabaloy, and Pr. Jean-Luc Darridon for agreeing to be examiners of my work.

I would like to acknowledge Dr. Kai Fischer from Shell, Dr. Oliver Koch from Linde, Mr. Hicham Guedacha, and Dr. Laurent Benoit from Engie for supporting the JIP "evaluation of the crystallization risk in LNG production" and for all the discussion, we shared during the different meetings.

I would like also to express my gratitude to my directeur de thèse Dr. Paolo Stringari and my maître de these Dr. Marco Campestrini. Thank you for encouraging me and for all the constructive discussions that we shared during these last three years. Many thanks for allowing me to grow as a researcher.

I would like to thank all the staff of the Center of Thermodynamics of Processes. Thank you to Pr. Christophe Coquelet for your welcome in this laboratory and your advice on my research project as well as on my career. Many thanks to Dr. Elise El Ahmar, Dr. Celine Houriez, Pr. Alain Gaunand, and Pr. Arnaud Delebarre for your advice and guidance. I wish to thank Alain Valtz, Eric Boonaert, Snaide Ahamada, Pascal Theveneau, Hervé Legendre, and David Marques for all your technical advice that was precious and helpful for my experimental work. Many thanks to Marie-Claude Watroba and Jocelyne Galy for helping me with the different administrative tasks.

Thanks to Dyhia, Esther, Martin, Remy, Mattieu, Charlie, Salah-Eddine, Thibault, Julien, Serena, Nicolo, Gabrielly, Driss, and Nicola. I appreciated the discussions we shared during these last three years. I wish you much success in your personal and professional projects.

Many thanks to the most important person in my life, my wife, who has always been there to support me and help me through the most difficult and stressful periods. Many thanks to all my family for encouraging and helping me in my research project and my career.

Table of contents

Table of contents

List of tables

List of figures

List of figures

List of figures

List of figures

List of figures

Abstract

and

Résumé

Abstract

This work aims at investigating the low-temperature (from ambient temperature down to 100 K) phase equilibria including molecular solids by means of original measurements and the development of accurate models.

Thanks to the deep bibliographic research that has been carried out in this work for collecting the available solid-fluid equilibrium data, several binary systems of scientific and industrial interest have been selected and experimental campaigns have been carried out for investigating their thermodynamic behavior at low temperatures. Three apparatuses and two experimental procedures have been used for this experimental investigation. The static-analytic method has been used for measuring the solubility limits of several components (benzene, ethylbenzene, p-xylene, m-xylene, o-xylene, and tetrahydrothiophene) in methane as a solvent; the effect of the presence of ethane and nitrogen on the solubility of benzene and p-xylene in methane has been also studied. In addition, the thermodynamic behavior of the methane+neopentane system has been deeply investigated using both the static-analytic and the synthetic-indirect methods; indeed, the solid-liquid, the solid-liquid-vapor, and the low-temperature liquid-vapor equilibria have been measured over a large range of temperature (from 344 K down to 100 K).

To overcome some of the limitations and drawbacks of our existing static-analytic apparatuses, a new apparatus using an original sampling system has been designed and built. The apparatus has been validated by carrying out experimental measurements of the solid-liquid and solid-liquid-vapor equilibria of ethane+benzene system and the data showed a good agreement compared to the available literature values.

Concurrently to the experimental investigation, a modeling work has been carried out for improving the representation of the low-temperature solid-fluid equilibria. The used modeling approach is based on the coupling of the so-called classical approach for the solid phase fugacity and the Peng Robinson cubic equation of state with classical mixing rules for the calculation of the fluid phase properties. The main outcomes of the modeling investigation are *i)* the tendency of the binary interaction parameter, k_{ij}, to reach a constant value at low temperatures and *ii)* the continuity of the k_{ij} between the solid-fluid equilibrium and the fluid-fluid equilibrium. Based on these observations, constant k_{ij} values have been regressed on the fluid-

fluid equilibrium data of selected binary mixtures at temperatures close to the triple point temperature of the solid formers and used for predicting the solid-fluid equilibrium of these mixtures; and very satisfactory results have been obtained.

The results of these experimental and modeling investigations have allowed acquiring new knowledge about the global phase diagrams and the solid-fluid equilibria of several mixtures. In addition, This study is of high interest for the natural gas liquefaction process, since it provides accurate information about the solubility limits of the studied components and allows optimizing the purification process upstream the liquefaction.

Résumé en français

Cette thèse vise à étudier les équilibres de phases entre des solides moléculaires et des phases fluides à basse température (de la température ambiante à environ 100 K) grâce à des mesures originales et le développement de modèles.

Grâce à une recherche bibliographique approfondie menée dans le contexte de ce travail pour collecter les données d'équilibre solide-fluide, plusieurs systèmes binaires d'intérêt scientifique et industriel ont été sélectionnés et des campagnes expérimentales ont été menées pour étudier leur comportement thermodynamique à basse température. Trois appareillages et deux protocoles expérimentaux ont été utilisés pour cette étude. La méthode statique-analytique a été utilisée pour mesurer les limites de solubilité de plusieurs composants (benzène, éthylbenzène, p-xylène, m-xylène, o-xylène et tétrahydrothiophène) dans le méthane. L'effet de la présence d'éthane et d'azote sur la solubilité du benzène et du p-xylène dans le méthane a également été étudié. De plus, le comportement thermodynamique du système méthane+néopentane a été étudié au moyen de méthodes statique-analytique et synthétique-indirecte. Les équilibres solide-liquide, solide-liquide-vapeur et liquide-vapeur à basses températures ont été mesurés sur une large gamme de températures (de 344 K jusqu'à 100 K).

Résumé / Abstract

Un nouvel appareillage utilisant un système d'échantillonnage original a été conçu et construit pour surmonter certaines des limitations et des inconvénients de nos appareillages existants. L'appareillage a été validé grâce à des mesures expérimentales d'équilibre solide-liquide et solide-liquide-vapeur du système éthane+benzène.

Parallèlement à l'investigation expérimentale, un travail de modélisation a été mené pour améliorer la modélisation des équilibres des phases solide-fluide. L'approche de modélisation utilisée est basée sur le couplage de l'approche dite classique pour le calcul de la fugacité des phases solides et de l'équation d'état cubique avec des règles de mélange classiques pour le calcul des propriétés des phases fluides. Les principaux résultats du travail de modélisation sont *i)* la tendance du paramètre d'interaction binaire, k_{ij}, à atteindre une valeur constante à basse température et *ii)* la continuité du k_{ij} entre les équilibres solide-fluide et fluide-fluide. En se basant sur ces observations, une valeur constante de k_{ij} a été obtenue par régression du modèle sur les données d'équilibre fluide-fluide de certains mélanges binaires à des températures proches de la température du point triple du composé le plus lourd. Ce k_{ij} a été utilisée pour prédire l'équilibre solide-fluide et des résultats très satisfaisants ont été obtenus.

Les résultats de ce travail ont permis d'acquérir des nouvelles connaissances sur les diagrammes de phases globaux et les équilibres solide-fluide de plusieurs mélanges. Ces informations sont d'interêt particulier pour procédé de liquéfaction du gaz naturel et permettent de fournir des informations précises sur les limites de solubilité des composants étudiés et ainsi permettre l'optimisation du procédé de purification en amont de la liquéfaction.

Introduction

One of the most important axes of the energy transition in the short and medium-term is the use of Natural Gas (NG) for replacing other fossil fuels whose use entails larger emissions of carbon dioxide and air pollutants. This resulted in an important increase in the natural gas demand (+ 44% in the last two decades, International Energy Agency Outlook for natural gas 2017); this rapid growth is supported by the development of the Liquefied Natural Gas (LNG) industry.

The liquefaction process requires the cooling of the NG down to about 110 K at atmospheric pressure. During the liquefaction process, some components of NG can solidify and cause functioning issues and then more frequent maintenance operations. Because of the lack of knowledge of the phase behavior (and then the solubility limits) of these components, LNG companies adopt strict specifications during the purification processes to ensure a minimum content of potential solid formers to minimize the risk of crystallization. This can lead to an oversizing of the purification units and then excessive energy consumption.

This work aims at investigating and studying the low temperatures (from ambient temperature down to 100 K) phase equilibria including molecular solids for molecules composing natural gas (mainly light hydrocarbons, aromatics, nitrogen, carbon dioxide, and sulfur components), by means of original measurements and the development of models allowing the accurate representation and prediction of the low-temperature phase equilibria.

The results of this investigation have allowed acquiring new knowledge about the global phase diagrams and the solid-fluid equilibrium of several mixtures. This information is of high interest for the optimization of the natural gas liquefaction process and allows adopting optimal purification limits upstream the liquefaction, thus increasing the safety and the profitability of the LNG plants.

In particular, this thesis is part of a Joint Industry Project led by the Center of Thermodynamics of Processes (CTP) and funded by Shell, Engie, and Linde, which aims to evaluate the crystallization risk in LNG production.

This manuscript is organized as follows:

Chapter 1 gives a brief description of the main units involved in typical natural gas purification and processing plant; in addition, the liquefaction of the natural gas using the cascade refrigeration cycles and the C3-MR (propane-mixed refrigerant) are described.

Chapter 2 presents the state of the art of low-temperature phase equilibria data available in the scientific literature. It presents the bibliographic research of the Solid-Fluid Equilibria (SFE) of the mixtures of interest for the natural gas liquefaction. A description of the different experimental methods allowing the measurements of the SFE is given in this chapter, together with the description of the common approaches

used for the modeling of the SFE (phase equilibrium including molecular solid phases) in the context of the natural gas liquefaction.

In Chapter 3, a detailed description of the apparatuses and the experimental procedures (the static-analytic and the dynamic-synthetic methods) used to carry out original measurements of solid-fluid, solid-fluid-fluid, and fluid-fluid equilibria of mixtures of interest for the LNG production is presented. In this section, a list of all the studied systems is given; in addition, the methane+neopentane system is presented as a case study for the deep analysis and description of the thermodynamic behavior of binary mixtures at low temperatures.

Concurrently to the experimental investigation, a modeling work has been carried out during these last three years for improving the modeling of the solid-fluid equilibria. The modeling approach used in this work is based on the coupling of the so-called classical approach for the solid phase fugacity calculation and the cubic equation of state for the calculation of the fluid phase properties.

In Chapter 4, the main outcomes of the modeling investigation are presented and discussed. A new fast and robust method based on pseudo-experimental activity coefficients calculated from SFE data for the regression of binary interaction parameter (k_{ij}) has been developed as a valid alternative to common algorithms. The regressed k_{ij} in the low-temperature region for a certain number of binary systems has shown two very interesting features: *i)* the tendency of the k_{ij} to reach a constant value at low temperatures and *ii)* the continuity of the k_{ij} across the triple point of the heavy component or solid former (this temperature representing usually the transition from FFE to SFE). Based on these observations, a constant k_{ij} regressed on the fluid-fluid equilibria data at temperatures close to the triple point temperature of the solid former has been used for predicting the SFE of a certain number of binary mixtures. In addition, the complete modeling of the phase equilibrium behavior of the methane+neopentane system is presented; the modeling results are compared to the data obtained in this thesis and presented in chapter 3.

To overcome some of the limitations and drawbacks of our existing static-analytic apparatuses, a new apparatus has been designed and built. The originality of this new apparatus consists of a new sampling system. The new equilibrium cell is equipped with 4 small cells, which allow trapping constant volume of the fluid phase at equilibrium with a solid phase. After having emptied the equilibrium cell, the trapped samples are totally vaporized at ambient temperature and analyzed thanks to a Valco valve (6-port 2-positions), which allows realizing several gas-chromatographic analyses for each sample. The apparatus has been validated by carrying out experimental measurements of the ethane+benzene system. The selection of this system was motivated by several elements: *i)* the inconsistency of the literature SLE data, *ii)* the recent publications that report the presence of a co-crystal at temperatures much higher than the triple point of ethane (this observation challenges the representation of the global phase diagram of this system and makes

its investigation very exciting), and *iii)* the interest of this system for the LNG production process but also for planetary science, in particular for understanding the formation of evaporites in Titan, the largest moon of Saturn. Chapter 5 is dedicated to the description of this new apparatus and the presentation of the experimental results concerning the ethane+benzene system.

Chapter 1:

Introduction to gas processing and LNG production

Résumé du chapitre 1 Français

Le gaz naturel brut est un mélange de plusieurs composants, il contient principalement du méthane et une quantité significative d'autres gaz tels que l'éthane, le propane, l'azote, le dioxyde de carbone et le sulfure d'hydrogène. De plus, il contient aussi des quantités plus faibles de composants plus lourds (n-alcanes, cyclo-alcanes, iso-alcanes, aromatiques, composés soufrés, eau, etc). Le gaz naturel se forme suite à la transformation de la matière organique dans le sous-sol, cette transformation se produit à des conditions de pression et de température spécifiques. Selon l'origine du gaz naturel, sa composition peut changer considérablement.

L'utilisation du gaz naturel à la place des autres énergies fossiles (pétrole et charbon) permet de réduire les émissions de gaz à effet de serre et les particules fines tout en assurant tout en répondant à la demande énergétique mondiale (les réserves de gaz naturel sont suffisantes pour satisfaire l'offre pendant plusieurs années). Grâce à ses faibles émissions de CO_2 et les polluants de l'air, l'utilisation du gaz naturel a connu un grand essor ces dernières années (+ 44% depuis 20 ans). Cet essor est soutenu par le développement du Gaz Naturel Liquéfié (GNL).

Avant commercialisation, le gaz naturel brut subit un processus de purification et de traitement pour éliminer ou réduire la quantité de certains composants qui sont dangereux pour le bon fonctionnement de la chaîne du gaz naturel, nocifs pour les consommateurs, ou sans bénéfices énergétiques. En fonction des exigences de l'utilisateur final et du mode de transport, la purification et le traitement du gaz naturel visent à répondre à trois spécifications principales :

- Les spécifications liées au transport par gazoduc : définissent les caractéristiques du gaz naturel injecté dans les gazoducs et visent à assurer un gaz propre et sûr pour les consommateurs.
- Les spécifications d'interchangeabilité : expriment la compatibilité des caractéristiques de combustion d'un gaz avec celles d'un autre gaz. Deux gaz sont interchangeables lorsque l'un peut être remplacé par l'autre sans perturber le bon fonctionnement du brûleur.
- Les spécifications liées à la production gaz naturel liquéfié : sont plus sévères que les spécifications liées au transport par gazoduc et visent à éviter le risque de solidification lors de la liquéfaction.

Les principales unités impliquées dans une usine typique de purification et de traitement du gaz nature sont décrites dans ce chapitre.

Afin de surmonter certaines limitations du transport du gaz naturel par gazoduc (longue distance, barrières géographiques et géopolitiques, diversification du marché), le transport du gaz naturel sous forme liquide en utilisant des bateaux s'est imposé comme une alternative. La liquéfaction du gaz naturel nécessite son

refroidissement à environ 110 K à pression atmosphérique. Pour liquéfier le gaz naturel il existe deux principaux procédés de liquéfaction du gaz naturel, à savoir, les cycles de réfrigération en cascade et le C3-MR. Ces deux procèdes sont décrit à la fin de ce chapitre.

1 Introduction to gas processing and LNG production

Natural Gas (NG) was discovered in China 2400 years ago. At that time, it was used to vaporize brine and collect salt crystals. During the 17th and 18th centuries, small local projects for home and public lighting were undertaken in Great Britain and the United States. It was not until the end of the Second World War to witness an industrial use of natural gas, thanks to technological and engineering advances which allowed the construction of reliable and safe facilities [1].

The NG forms as a result of the transformation of organic matter in the underground, occurring at specific pressure-temperature conditions. Depending on the natural gas resources (the origin of the NG reservoir), the composition of the raw natural gas can change considerably. Raw NG is a multi-component mixture that contains mainly methane and a significant amount of other gases such as ethane, propane, nitrogen, carbon dioxide, and hydrogen sulfide (sour gas). In addition, lower amounts of some heaviest components (n-alkanes, cycloalkanes, iso-alkanes, aromatics, sulfur compounds, water, etc) are present in raw natural gas.

1.1 Role of natural gas in the energy transition

For containing the rise in the global temperature and reducing global warming, it is necessary to reduce greenhouse gases emissions and promote all the actions aiming at reaching energy efficiency. This requires a deep change in our daily habits and the use of less polluting energy sources.

At the same time, the great challenge is to meet the energy demand (constantly increasing) while ensuring the energy transition. One of the main solutions allowing meeting this challenge is the use of natural gas as a bridge between the use of the other fossil fuels (oil and coal) and renewable energy sources (solar, wind, biogas, etc). On one hand, the NG reserves are enough for ensuring access to energy for everybody (216 tcm (trillion cubic meter) of proven reserve of natural gas, and the global annual demand is 3.6 tcm [2]); on the other hand, NG is significantly less polluting compared to other fossil fuels. When burnt, NG emits around 40% less Carbone Dioxide (CO_2) than coal and 20% less than oil. The advantage of the natural gas over the other fossil fuels is reinforced by its almost zero emission of air pollutants (fine particles, sulfur dioxide, and nitrogen oxide [2]); these pollutants (or the resulting components of the reactions involving these substances) are responsible for the main harmful effects of poor air quality. Fig1.1 shows the share of the different energy sources in the total energy-related emissions of selected air pollutants and CO_2.

Since 2010, replacing coal with natural gas has saved more than 500 mega-tones of CO_2; this is equivalent to 200 million additional electric vehicles running on zero-carbon electricity on the road during the same period [3]. The rise of the use of shale gas has pushed the coal-to-gas switching in the United States and it allowed saving almost a fifth of CO_2 emissions since 2010. The improvement of the air quality is the main driving reason for the coal-to-gas switching in China; concurrently, this allowed saving CO_2 emissions [3]. Fig1.2 shows the quantity of the CO_2 saved in certain regions between 2010 and 2018 thanks to the coal-to-gas switching.

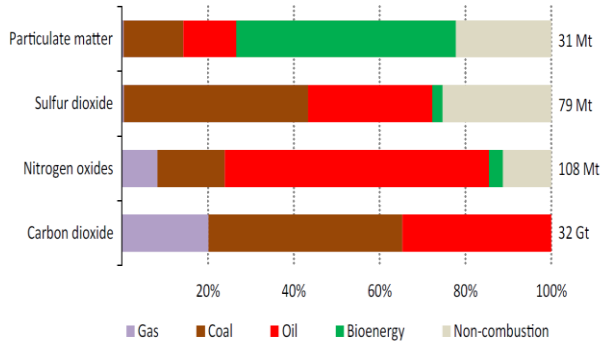

Figure 1.1: share of the different energy sources in the total energy-related emissions of selected air pollutants and CO_2 (Gt = Giga-tone, Mt=Mega-tone) [2]

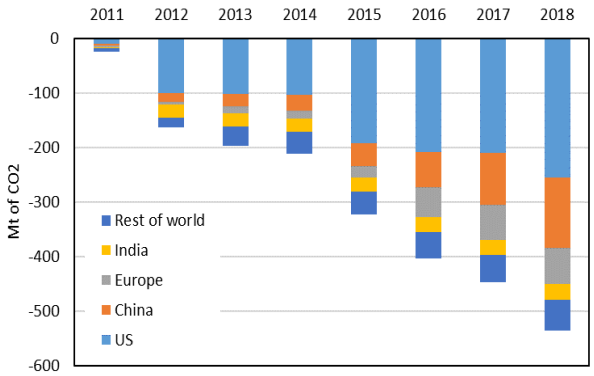

Figure 1.2: CO_2 savings from coal-to-gas switching in selected regions between 2010 and 2018 [3]

1.2 Natural gas purification and processing

The raw natural gas undergoes a purification process to remove or reduce the amount of the components that are dangerous for the proper functioning of the natural gas chain, or harmful for the consumers, and those having no energy benefits. In addition, some components (like light hydrocarbons and nitrogen) are recovered and upgraded separately. Depending on the NG specifications suitable for the requirements of the final user and the mode of transportation, the NG purification and processing aim at meeting three main specifications:

i) The pipelines specifications: define the characteristics of the natural gas injected into the pipelines and aim at ensuring clean and safe gas for the consumers.

ii) The interchangeability specifications: express the compatibility of the combustion characteristics of one gas with those of another gas. Two gases are interchangeable when one can be replaced by the other without disturbing the operation of the burner.

iii) The Liquefied Natural Gas (LNG) specifications: are more severe than the pipeline specifications and aim at avoiding the risk of freeze-out in the Main Cryogenic Heat Exchanger (MCHE) by reducing the amount of the potential solid formers (impurities).

In this manuscript, all components having a triple point temperature higher than the temperature of the LNG (approximately 110 K) are considered as natural gas impurities and thus potential solid formers in the LNG production. Fig1.3 shows the triple point temperature of the main natural gas components and a comparison to the LNG temperature.

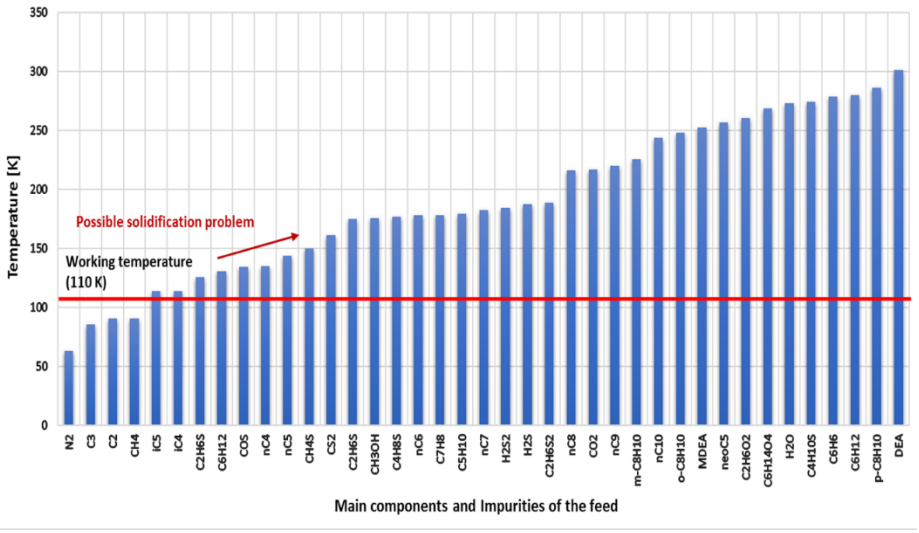

Figure 1.3: triple point temperature of the main natural gas components

A brief description of the main units involved in the natural gas purification and processing (acid gas removal, gas dehydration, mercury removal, natural gas liquid removal, and nitrogen rejection) are presented in this section. The information given in the following are a typical description of the different units and can change depending on several factors.

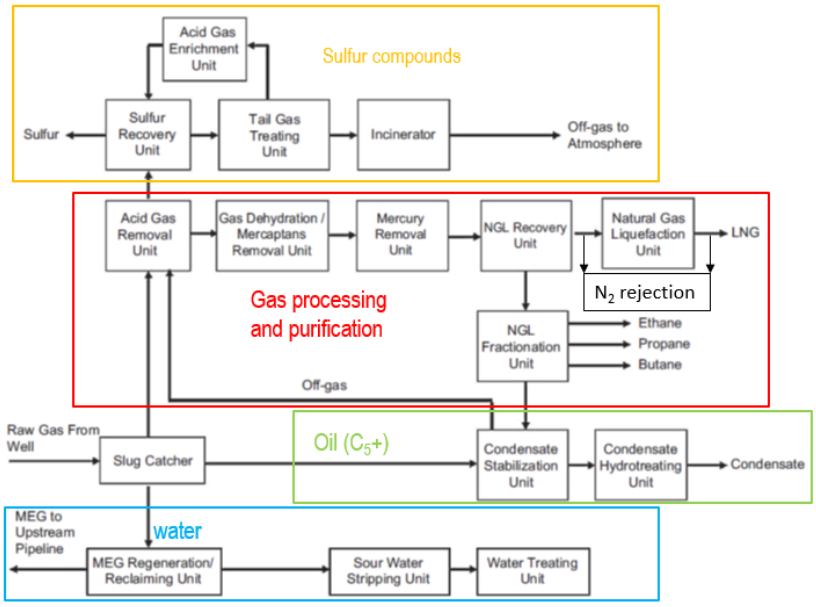

Figure 1.4: main units involved in an LNG plant [4]

1.2.1 Acid gas removal

Acid gases (carbon dioxide, and hydrogen sulfide) are present in significant proportion in the natural gas coming from the production wells (40% of the proven reserves are sour and/or with high CO_2 content [2]). Hydrogen sulfide (H_2S) is very toxic and harmful for several systems in the body and it is very corrosive for natural gas facilities. CO_2 does not present any particular health risk, but it is removed from natural gas in order to rise its energy density (natural gas upgrading) and also to avoid the crystallization risk in the case of LNG production and the corrosion of the natural gas chain facilities.

The main techniques used for removing the carbon dioxide and hydrogen sulfide are:

i) Amines scrubbing technology that uses a reversible chemical reaction, which allows converting the carbon dioxide and the hydrogen sulfide to water-soluble salts
ii) Chemical adsorption with carbonates
iii) Physical absorption
iv) Membranes for CO_2 removal
v) Cryogenic capture of CO_2

Because of its toxicity and its high crystallization risk in LNG production, the purification limit of H_2S is lower than 6 ppmv (parts per million in standard volume) in case of pipeline transportation and less than 3.3 ppm in case of LNG production. However, the purification limit of CO_2 varies from 2% to 4% (molar) in the case of pipeline transportation and is lower than 50 ppmv in case of the LNG production [1].

1.2.2 Gas dehydration.

Because of the contact between the raw natural gas and water in the underground reservoir and the contact with the amines solution (aqueous solution) used for the acid gas removal, the natural gas is completely saturated with water. Water is eliminated for avoiding the risk of hydrate formation, which can cause pipe blockage.

Gas dehydration is achieved using two main techniques:

i) Absorption: a liquid having a high affinity with water is used for drying the natural gas; Glycols are the most used absorbents.
ii) Adsorption: a solid sorbent is used for trapping the molecules of water on its surface.

The specification of the water content depends on the transport mode: minimum water content of 150 ppmv has to be guaranteed for the pipeline; whereas, the concentration of water in the feed gas before the liquefaction must be lower than 0.1 ppmv in case LNG production [1].

1.2.3 Mercury removal

Besides the environmental pollution and health concerns, the embrittlement of the aluminum constituting the natural gas facilities is one of the main problems that can be caused by mercury. Given the danger of the presence of mercury in NG, its purification limit is very low and the final concentration must not exceed $0.01 \mu g/Nm^3$ [1]. Two main techniques are used for removing mercury from natural gas:

i) The non-regenerative mercury removal process entails the reaction of mercury with sulfur to form a stable compound on the sorbent surface.

ii) The regenerative mercury removal process uses silver on a molecular sieve to chemisorb elemental mercury. The mercury-saturated bed is then regenerated by hot regeneration gas (typically heated at 290 °C).

1.2.4 Natural gas liquids recovery

Natural Gas Liquids (NGLs) are all the hydrocarbons present in raw natural gas excepting methane. Depending on their concentrations, they can condensate in the cold points of the pipelines or even freeze out during the LNG production (except ethane and propane). Furthermore, the energy requirements for NG liquefaction are higher if NGLs are not removed from the feed because they have a heat capacity, C_p, higher than methane. On the other hand, the NGLs can be collected and sold separately, thus increasing the profitability of the natural gas processing plant.

Taking into account that a variety of NGLs recovery processes are described in the literature and used in the NG plants, the choice of the process depends on several factors such as the composition of the raw NG, the pressure of the feed gas, the quantity of the feed gas to be processed, the gas heating content targets, the possibility of economical valorization of LPG or ethane, etc. The main processes are:

i) Lean oil for NGLs removal: the raw natural gas is circulated in an absorber column on counter-flow through a solvent, a lean oil with a molecular weight of 100-150 g/mol. In contact with the feed gas, the lean oil is enriched with the heavy compounds since these have a higher affinity with the lean oil than with the gas. The resulting "rich oil" is regenerated and sent back to the absorber column. Although lean oil absorption is one of the oldest processes, it does not allow an optimal recovery of the NGLs. A schematic description of a basic lean oil process is presented in Fig1.5.

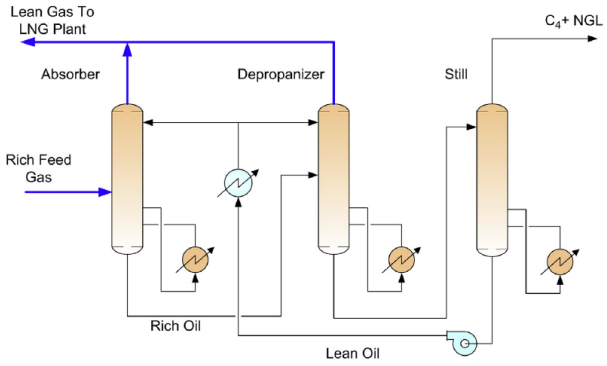

Figure 1.5: lean oil process for the NGLs recovery [4]

ii) The Joule-Thomson (JT) process: in the case of high-pressure raw natural gas, the NGLs can be recovered using a JT valve. Once the feed gas is dried, it is passed through a gas-gas heat exchanger where it is cooled thanks to the cold gas and the liquid coming from the low-temperature separator. The cold gas exiting the exchanger undergoes an expansion in the JT valve and is transferred to the low-temperature separator where the liquid phase rich in NGLs is recovered. In a second time, ethane can be recovered in the deethanizer column and then mixed with the gas feeding the LNG plant. The schematic description of the JT process is presented in Fig1.6.

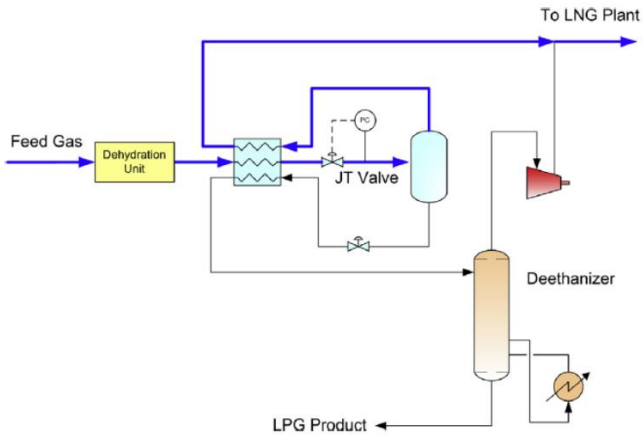

Figure 1.6: Joule-Thomson process for the NGLs recovery [4]

iii) Refrigeration process: when the pressure of the feed gas exiting the dehydration unit is not enough for using the JT process, an external refrigeration process is used for the NGLs recovery. Depending on the expected composition of the natural gas after the NGLs recovery, different refrigeration processes can be used (the highest is the purification limits; the complex is the refrigeration process). For low purification limits, the use of a simple refrigeration cycle with propane as working fluid is enough; however, a turbo-expander coupled with an absorber can be included in the propane refrigeration

process for achieving 70-80% of propane recovery; the turbo-expander allows reaching lower temperature than the JT expansion. The gas exiting the expander is transferred to an absorber where the NGLs and methane are separated; ethane-rich fluid is then separated from the heaviest hydrocarbons in the deethanizer. The propane refrigeration and the turbo-expander processes are presented in Figs1.7-8. A refluxed absorber and a refluxed deethanizer can be used for high recovery of the propane (over 99%).

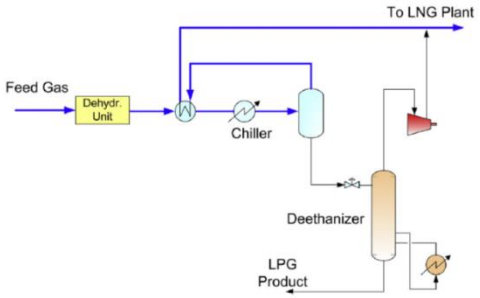

Figure 1.7: propane refrigeration process for the NGLs recovery [4]

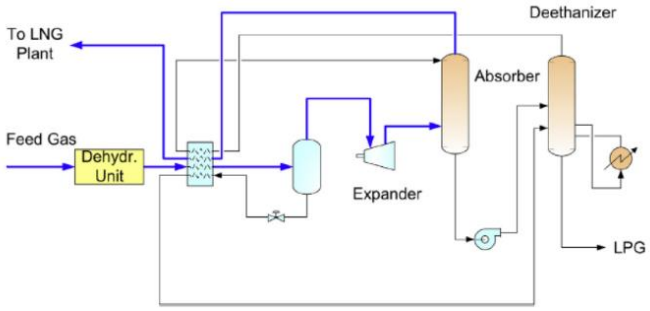

Figure 1.8: turbo-expander process for the NGLs recovery [4]

1.2.5 Nitrogen removal

The presence of nitrogen in the natural gas reduces its heating value and increases the energy required for the liquefaction; in addition, it favors the stratification and can lead to rollover problems. Depending on the concentration of the nitrogen in the raw natural gas and the target concentration after the purification, nitrogen can be removed upstream or downstream of the liquefaction.

The downstream nitrogen removal is suitable when the concentration of nitrogen is less than 5% (the quantity of nitrogen does not increase excessively the energy needed for the liquefaction). The LNG leaving the MCHE is expanded using a hydraulic turbine for flashing-off the nitrogen content; the flashed liquid (nitrogen lean LNG) is pumped for storage and the flashed vapor (nitrogen-rich gas) is returned to the fuel gas system.

The upstream nitrogen removal is recommended when the concentration of the nitrogen is higher than 5%; thus, decreasing the energy necessary for the NG liquefaction. Three basic methods can be used for the upstream removal of nitrogen from natural gas: *i)* the cryogenic distillation, *ii)* the adsorption, and *iii)* the membrane separation.

The membrane separation and the pressure swing adsorption using molecular sieves are economically feasible only for low-volume of natural gas; whereas, cryogenic distillation is the most viable technique since it provides a high nitrogen rejection for high-volume of natural gas. A single column process can be

used for the treatment of feed gases with nitrogen content lower than 20%, while a dual column with a recycling compressor is needed for higher concentrations [1].

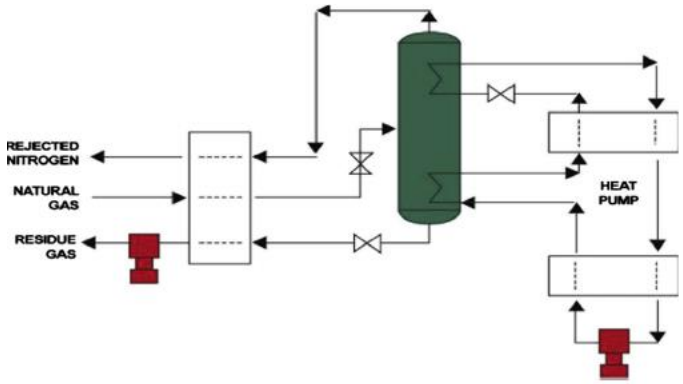

Figure 1.9: single column Cryogenic Distillation for nitrogen removal [5]

1.3 LNG production

Traditionally, natural gas is transported through pipelines in the gaseous state. This means of transport presents some limitations such as the long-distance between the producer and the customer, crossing geographical barriers (oceans, mountains, etc) or unstable regions, and market diversification constraints. A valid alternative allowing overcoming these disadvantages is the transport of the NG in the liquid form using an LNG ship. The liquefaction of the natural gas allows increasing its density by more than 600 times; consequently, a given volume of liquefied natural gas has a heating value 600 times higher than that of the natural gas at room temperature and atmospheric pressure. The liquefaction process involves the cooling of the natural gas down to about 110 K (the target LNG temperature depends on several factors such as the NG composition, the storage condition, etc).

1.3.1 Basic refrigeration cycle

The refrigeration cycle is composed mainly of an evaporator (heat exchanger), a compressor, a condenser, and a throttle valve (expansion valve).

The vapor refrigerant undergoes compression in the compressor (path 1-2 in Fig1.11); the superheated vapor is introduced into the condenser and converted to liquid (2-3). The resulting liquid undergoes an expansion in the throttle valve (3-4), and its temperature reaches a minimum value. The cold fluid (liquid+vapor) is converted to all vapor in the evaporator (4-1) where heat exchange occurs with the circulating natural gas.

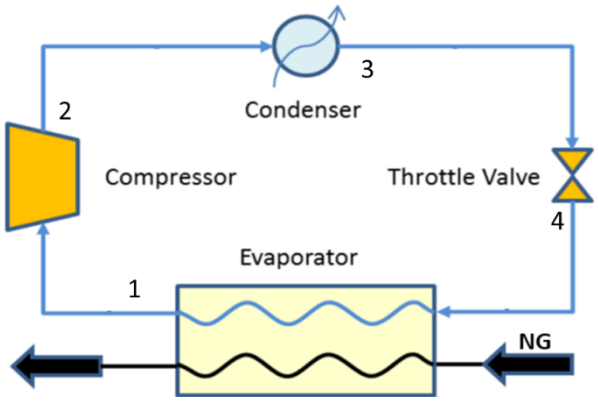

Figure 1.10: basic refrigeration cycle [6]

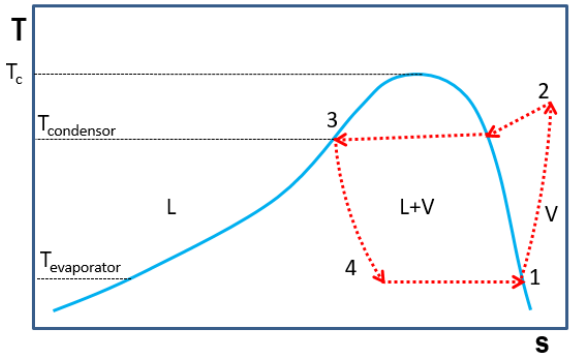

Figure 1.11: temperature-entropy diagram of the refrigerant in a basic refrigeration cycle

1.3.2 Cascade refrigeration cycle

The liquefaction of the natural gas cannot be reached using a simple refrigeration cycle because of the high-temperature difference between the feed gas (about 298 K) and the LNG (about 110 K). In such a case, the use of a cascade refrigeration cycle (Fig1.12) is mandatory. This configuration uses several nested cycles with a common heat exchanger between cycles; the evaporator of the former cycle is the condenser of the following cycle. In addition, it is necessary to use several refrigerants with different thermodynamic properties for allowing the cooling of the natural gas down to 110 K.

During the liquefaction, it is preferred to have a refrigerant cooling curve similar to the NG cooling curve for reducing energy consumption. For this purpose, it is possible to use several consecutive refrigeration cycles operating at different pressure for each used refrigerant; this allows obtaining a discrete refrigerant temperature profile as shown in Fig1.13.

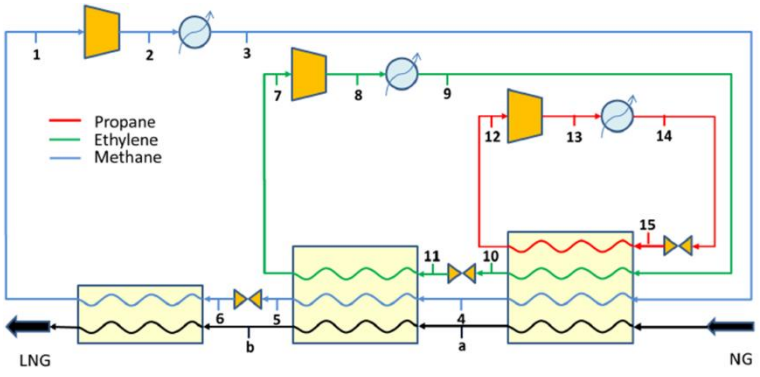

Figure 1.12: cascade refrigeration cycle [6]

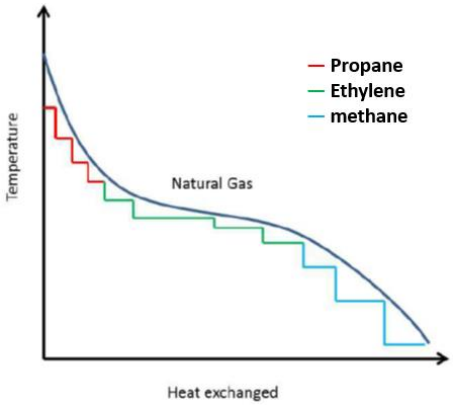

Figure 1.13: temperature-heat exchanged diagram of a typical cascade refrigeration cycle

1.3.3 C3-MR refrigeration cycle

The C3-MR (propane-mixed refrigerant) refrigeration cycle consists of a pre-cooling of the natural gas and the mixed refrigerant using the propane down to around 240 K and then the use of a mixed refrigerant for achieving the liquefaction of the natural gas.

According to the process diagram given in Fig1.14, the liquefaction process of the NG using the C3-MR can be described as follows.

- Both the feed gas and the mixed refrigerant are pre-cooled using a propane cascade refrigeration cycle.
- Because the temperature achieved with this first refrigeration is not enough to completely liquefy the mixed refrigerant (the MR is at vapor-liquid equilibrium), the liquid and vapor fractions of the MR are separated in the Separation Column (SC).
- The liquid MR is then introduced and subcooled in the bottom part (position 1 according to Fig1.14) of the Coil-Wound Heat Exchanger (CWHE) and then expanded (position 2) and released to the lower part of the CWHE for producing cold. This allows condensing the vapor MR introduced into the lower part of the CWHE.
- The resulting subcooled liquid is expanded in the upper part of the CWHE (position 3) and used for cooling and liquefying the natural gas (the further up in the CWHE, the colder it is).

Seeing that the MR is not a pure component, its liquefaction at given pressure occurs over a temperature range and not at a specific temperature, this allows having a cooling curve very similar to the one of the natural gas, and thus reducing the energy required for the liquefaction.

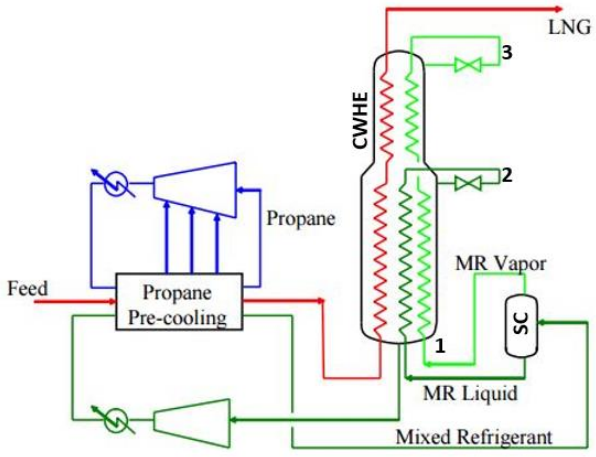

Figure 1.14: C3-MR refrigeration cycle [7]

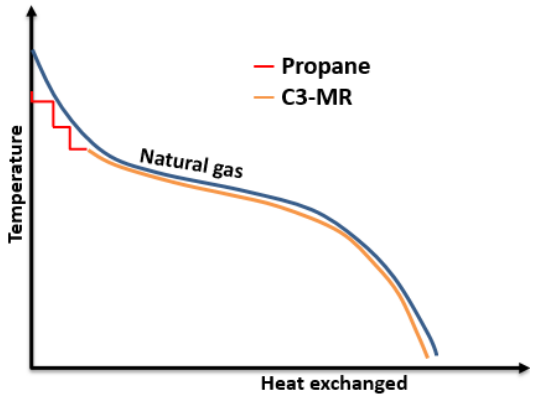

Figure 1.15: temperature-heat exchanged diagram of a typical C3-MR refrigeration cycle

References

[1] A. J. Kidnay et W. R. Parrish, fundamentals of natural gas processing, 2006.

[2] World Energy Outlook, 2017.

[3] F. Birol, The Role of Gas in Today's Energy Transitions. IEA, 2019.

[4] S. Mokhatab, J. Mak, J. V. Valappil, et D. A. Wood, Handbook of liquefied natural gas, 1st. edition. Amsterdam: Elsevier, GPP, 2014.

[5] D. Elliot, J. C. Kuo, et P. Nasir, Plant processing of natural gas, 2. ed. Austin, Tex: University of Texas at Austin, 2008.

[6] A. Trigilio, A. Bouza, et S. Di, Modelling and Simulation of Natural Gas Liquefaction Process, in Advances in Natural Gas Technology, H. Al-Megren, Éd. InTech, 2012.

[7] M. De Falco, LNG R&D for the Liquefaction and Regasification Processes, University UCBM, Italy.

Chapter 2:

State of the art: measurement and modeling of the SFE

Résumé du Chapitre 2 en Français

La matière peut se trouver sous différents états : solide, liquide ou vapeur. L'état solide est la forme la plus compacte, et celle ayant la plus faible énergie cinétique. En fonction des forces exercées par les molécules, plusieurs types de solides peuvent être définis : les solides ioniques, les solides covalents, les solides métalliques et les solides moléculaires. Ces derniers se forment grâce aux laissons hydrogène et les forces van der Waals. Ces forces sont tellement petites que les solides moléculaires se forment généralement à très basses températures, comparés aux autres types de solides. Les équilibres de phases étudiées dans cette thèse concernent les solides moléculaires en équilibre avec les phases fluides (liquides et vapeurs).

Les équilibres de phases incluant les solides moléculaires sont d'intérêt majeur pour plusieurs applications industrielles comme la séparation cryogénique de l'aire, la liquéfaction du gaz naturel, biogaz et l'hydrogène, et aussi pour le captage et le stockage cryogénique du CO_2, mais aussi pour certaines applications scientifiques telles que l'investigation et la contribution à la compréhension de certains phénomènes en planétologie.

Le chapitre 2 contient les résultats de la recherche bibliographique qui a été mené pour collecter toutes les données d'équilibres de phase en présence de phase solide pour les systèmes d'intérêt pour le gaz naturel. La recherche bibliographique a montré que la majorité des systèmes investigués dans ce travail ne présentent pas suffisamment données qui permettent de comprendre leurs comportements thermodynamiques.

Les méthodes expérimentales qui permettent d'étudier les équilibres solide-fluide peuvent être regroupées dans deux principales familles, à savoir : les méthodes analytiques et les méthodes synthétiques.

Les méthodes synthétiques nécessitent la connaissance de la composition exacte du système à étudier. Le principe des méthodes synthétiques consiste à varier une propriété du système (principalement la température) et voir son effet sur les autres propriétés (en général la formation de la phase solide engendre une variation notable des propriétés du système). Parmi les méthodes synthétiques on peut citer : *i)* la méthode visuelle qui est très utilisé dans la littérature et permet de détecter visuellement les conditions de solidification ; *ii)* la méthode indirecte qui consiste à refroidir le fluide et enregistrer en continue la variation de sa pression (P) et sa température (T), la formation de la phase solide engendre un changement de la pente de la fonction $P=f(T)$; *iii)* la calorimétrie qui permet à la fois de détecter la formation des phases solides et la mesure de certaines propriétés calorimétriques.

Les méthodes analytiques ne nécessitent pas la connaissance exacte de la composition globale du mélange à étudier (contrairement aux méthodes synthétiques) ; néanmoins, la concentration du composé le plus lourd doit être suffisante pour se solidifier à la température d'étude (il doit être en excès). Les méthodes

analytiques (appelées aussi méthodes isothermes) nécessitent deux étapes principales : la première est le refroidissement du système jusqu'à la température d'étude, et la seconde est l'analyse de la composition de la phase fluide en équilibre avec la phase solide pour déterminer sa composition. La spectroscopie ou la chromatographie en phase gazeuse sont les techniques les plus utilisées pour l'analyse de la composition de la phase fluide. Parmi les méthodes analytiques on peut citer la méthode statique-analytique et la méthode dynamique.

Plusieurs méthodes sont utilisées dans la littérature pour modéliser les équilibres solide-fluide, le choix de la méthode dépend principalement des systèmes à étudier et des conditions de pression et de température. Dans le contexte de l'évaluation des risques de solidification lors de la production du gaz naturel liquéfié, deux principales méthodes ont été utilisé dans la littérature : d'une part, il y a les corrélations développées par *J. P. Kohn and K. D. Luks** et qui ont été adopté par les membres du GPA (Gas Prossessor Association) comme équations de références pour de longues années. D'une autre part, il y a la méthode basée sur le couplage de deux modèles distincts, un pour la phase solide et l'autre pour les phases fluides. Cette approche se repose sur l'utilisation de l'approche classique qui permet de calculer la fugacité de du composé en phase solide pure à partir sa fugacité dans la phase liquide sous-refroidie en utilisant un facteur correctif.

La dernière section de ce chapitre est consacrée à la description des principaux diagrammes de phases globaux rencontrés lors de l'étude de systèmes binaires impliquant des composants de gaz naturel. *J. P. Kohn and K. D. Luks** ont proposé quatre différents types de diagrammes de phase en présence de phases solides (A, B, C, et D), ces diagrammes sont représentatifs de la plupart des systèmes qui constituent le gaz naturel.

* *J. P. Kohn and K. D. Luks, Solubility of hydrocarbons in cryogenic LNG and NGL mixtures, GPA R- 22 76, 1976.*

2 State of the art: measurement and modeling of the SFE

The solid phase is the most compact form of matter; molecules in the solid phase have the lowest kinetic energy compared to the molecules in the other states (liquid and vapor). Depending on the forces exerted by the atoms or the molecules constituting the solid phase, different types of solids can be defined.

Ionic solids are formed by cations (positively charged ions) and anions (negatively charged ions); the atoms are kept together thanks to the electrostatic bonds. Ionic crystals are characterized by high binding energy.

Covalent solids are crystals whose constituents are linked by covalent bonds; the binding energy comes from the sharing of the valence electrons between each pair of atoms.

Metallic solids are constituted by atoms that are linked by metallic bonds; the binding energy of metals comes mainly from the kinetic energy of their valence electrons.

Molecular solids are formed by molecules exerting hydrogen bonds or van der Waals forces (Keesom, Debye, and London dispersion forces). Because of the weakness of these forces compared to those involved in the other types of solids, molecular solids form at temperatures much lower than the other type of solids (many molecular solids form at temperatures lower than the room temperature).

The purpose of this thesis is the investigation of the phase equilibria involving molecular solids.

2.1 Applications of the solid-fluid phase equilibria

Phase equilibria involving fluid phases (vapor and liquid) and molecular solids are less studied with respect to Fluid-Fluid Equilibria (FFE) (as Vapor-Liquid Equilibrium (VLE), for instance), this is particularly true for systems constituted by small molecules, for which the solid phases form at low-temperatures (lower than the room temperature).

The phase equilibria involving fluid phases and molecular solids occurring at cryogenic temperatures are of high interest for several industrial processes such as the liquefaction of the energy carriers (natural gas, biogas, and hydrogen), the cryogenic carbon capture and storage, the cryogenic air separation; but also for scientific fields as planetary science.

2.1.1 Liquefaction of the energy carriers

Meeting the increasing world's energy demand while reducing the human impact on global warming is a global challenge. One of the main solutions to this issue in the short and medium-term is the use of natural gas instead of the other fossil fuels (natural gas is abundant and emits much fewer pollutants compared to other fossil fuels) and concurrently developing sustainable energies like biogas/biomethane and hydrogen.

Considering that these energy sources (natural gas, hydrogen, and biogas) are in a gaseous state at the ambient temperature and pressure, their energy density is low compared to liquid fossil fuels. In addition, their transport as gases by means of pipelines is a real issue, especially when the transport network has to cover huge distances between the production site and the consumption site or crosses unstable regions, or can be even damaged (hydrogen embrittlement). A valid alternative to overcome the low energy density in the gaseous state and some drawbacks related to the transport and storage of these energy carriers as gases is their liquefaction; for instance, the energy densities of methane and hydrogen in the liquid state are respectively about 600 and 900 times higher than the ones in the gaseous state.

The liquefaction process of these gases involves their cooling down to cryogenic temperatures (around 110 K for methane and 20 K for hydrogen). Since the gas feeding the liquefaction plant is usually multicomponent mixtures, the components having a triple point temperature higher than the liquefaction temperature may solidify and cause serious issues during the liquefaction process. For avoiding the solid phase formation, it is mandatory to know the solubility limits (and related Solid-Fluid Equilibria (SFE)) of the potential solid formers in the feed gas in order to adopt adequate purification limits upstream the liquefaction train. Acquiring such knowledge requires performing low-temperature measurements and developing accurate models.

2.1.2 Cryogenic carbon capture and storage

Carbon Capture and Storage (CCS) is a process aiming at capturing the carbon dioxide emitted by industrial plants and storing it usually in geological reservoirs. It is a worldwide-recognized method allowing the mitigation of the global warming caused mainly by the use of fossil fuels. Carbon dioxide (CO_2) can be captured using different technologies, such as adsorption, absorption, membrane separation, and cryogenic separation.

The cryogenic capture of CO_2 is mainly used in the purification process of natural gas and biogas. This technology uses the difference between the sublimation and the condensation properties of the main raw gas component (methane) and that of CO_2, and allows obtaining an almost complete separation [1]. Several processes have been proposed in the literature for the cryogenic capture of the CO_2, for instance, the cryogenic packed bed [2], the external cooling loop cryogenic carbon capture [3], the anti-sublimation process [4], the cryogenic distillation [5], the controlled freezing zone [6], the CryoCell® process [7], the Stirling cooler system [8].

The design and the optimization of such processes require the knowledge of the low-temperature phase equilibria involving CO_2, especially the methane+carbon dioxide system. Therefore, this system remains

one of the most investigated mixtures in the literature, even if the effect of other components (nitrogen, light hydrocarbons, hydrogen sulfide) on the solubility of CO_2 in methane is gaining attention.

2.1.3 Cryogenic air separation

Although air is mainly composed of nitrogen, oxygen, and argon, it contains traces of several components (xenon, helium, krypton, carbon dioxide, water, light hydrocarbons, air pollutants, etc). The cryogenic separation of the main air components is based on their different boiling temperatures and relative volatilities, which result in a series of vapor-liquid equilibria occurring within the different stages of the distillation columns. The operating conditions of such a process are conditioned by the saturation properties of nitrogen, oxygen, and argon; the knowledge of the phase diagram involving these components is crucial for the design of such a process.

The impurities present in the feed air can solidify during the separation process; this may lead to several operating issues. As a consequence, the knowledge of the solubility limits of the different solid formers in the main air components is mandatory in order to properly design the purification units treating the air feeding the distillation columns.

2.1.4 Planetary science

Planetary science is a very fascinating research area; large synergy between several disciplines is required in order to understand complex planetary phenomena. Besides Earth, Titan, the largest Saturn's moon, is the only space body where liquid surfaces (seas, lakes, etc) have been found. Titan has a relatively dense atmosphere with a pressure of around 0.15 MPa and a surface temperature between 94 and 97 K [9]. Titan's surface and atmosphere are composed mainly of nitrogen, methane, ethane, and other heaviest hydrocarbons, carbon dioxide, and water [9]. The study of the low-temperature fluid-fluid and solid-fluid equilibria involving these components is of high interest for the understanding of the Titan's surface-atmosphere interactions and mass exchange. In addition, the study of the phase equilibria of selected systems contributes to the determination of the composition of the liquid surface and the evaluation of the presence of evaporites originating from the solidification of the heaviest components.

2.2 Commonly used methods for the measurement of the SFE

Molecular solids are known to form at low temperatures, thus performing experimental measurements dealing with phase equilibria involving this kind of crystals is a challenge. The complexity of setting up experimental apparatuses allowing the measurement of the SFE involving molecular solids results in a small amount of literature works that report SFE data compared to the FFE.

The measurement of the solubility limits of solid formers in liquid or vapor solvents can be carried out using different methods that can be classified into two main families: the synthetic methods (visual, indirect, calorimetric, etc) and the analytic methods (static analytic, dynamic, etc). Some attempts of reviewing these experimental procedures are presented in the literature (see for instance [10] [11] [12]).

2.2.1 The synthetic methods

Measuring the solid-fluid equilibria using a synthetic method requires the knowledge of the global composition of the system to be investigated. The principle of the synthetic techniques is based on the variation of one property of the system (mostly the temperature) and analyzing its effect on the other properties.

The mixture to be studied using a synthetic method can be prepared directly inside the Equilibrium Cell (EC) or in an auxiliary cell connected to the EC. Depending on the components involved in the mixture to be studied, the pressure, and the temperature, two principal methods are used in the literature for the preparation of the mixture. The first technique is based on the weighing of the different species involved in the mixture while the second is based on the Pressure-Volume-Temperature (PVT) measurement before and after the loading of each component in EC. The weighing method is very accurate but difficult to set up especially if the preparation of the mixture is done directly inside the cell; in addition if the weight of the auxiliary cell is relatively high compared to the weight of the species involved in the mixture increases the uncertainties on the calculated composition. The PVT method requires a precise knowledge of the physical properties of each component, the temperature uniformity throughout the loading circuit, and the accurate knowledge of the volume charged into the EC (avoiding the dead volumes in the loading circuit).

2.2.1.1 Visual method

The synthetic visual method is one of the most used procedures for the investigation of the solid-fluid equilibria. This method requires two principal conditions: the first is that the equilibrium cell must be transparent (or contains a visual window) for allowing the visual detection of the solid formation (solid-fluid transition) and the second is the exact knowledge of the composition of the studied mixture.

Once the EC is filled with a mixture of known composition, the temperature of the system within the equilibrium cell is lowered until the solid phase appears (solidification temperature); the temperature is then increased until all the solid disappears (melting temperature); the phase change is detected by visual observation. Once these two temperatures have been found, the system is heated or cooled using increasingly slower temperature rates until the two temperatures converge to the same temperature, which corresponds to the solid-fluid equilibrium temperature. The equilibrium pressure is determined at this temperature by

means of a pressure-reading device, and then additional solvent can be added for carrying out new experimental measurements at lower temperatures. This method suffers from the eventual presence of two fluid phases when crystals form, like at Solid-Liquid-Vapor Equilibrium (SLVE) or Solid-Liquid-Liquid Equilibrium (SLLE). In such case, the global composition of the mixture loaded into the EC cannot be considered as the solubility limit of the solid former in the solvent at the equilibrium temperature; the only possibility is to apply a material balance and thermodynamic modeling for evaluating the compositions of the two fluid phases, provided that the volume of each phase in the EC is known.

The research group of Kohn and Luks performed a large number of studies using the visual method [13], [14], [15], [16], and [17]. These works are one of the most important contributions to the investigation of the low-temperature phase equilibria involving solid phases. In addition, solid-fluid equilibria of systems of interest for the LNG have been investigated using the visual technique in [18], [19], [20], and [21].

This method is very suitable for the study of the thermodynamic behavior of unknown systems that may present liquid immiscibility before solidification. In addition, cell transparency allows determining the crystallization morphology when coupled with a suitable device.

One of the most challenges of this technique is the proper determination of the solid-fluid transition temperature by the visual detection of the first small crystals of solid forming within the EC. To overcome this difficulty, some authors propose to induce the solid to form on a selected and restricted area represented by a "cold spot", namely a spot slightly colder than the entire equilibrium cell [11] [20]. Despite these efforts aiming to improve this technique and rise the efficiency of the visual detection of the solid, the visual method cannot be used for investigating systems characterized by very low-solubility limits (Siahvashi et al. [21] report that the minimum detectable amount of solid when using their apparatus ranges from 2 mg down to 0.2 mg).

2.2.1.2 Indirect method

This experimental method consists of charging the equilibrium cell with the mixture to be studied (the global composition is known) at a temperature-pressure condition slightly higher than the crystallization condition. The system is slowly cooled at isochoric condition and the temperature (T) and the pressure (P) are recorded and plotted in a $P = f(T)$ diagram. The solid phase appearance induces a change in the slop of the P-T diagram. Some works are reported in the literature for the investigation of the SLVE of methane+carbon dioxide binary mixture using this technique [22], [23].

The knowledge of the qualitative thermodynamic behavior of the investigated system is mandatory for the interpretation of the experimental results (for instance to distinguish the formation of a second liquid phase

from the formation of a solid phase). Moreover, in some cases, the solid formation does not induce any significant change in the P-T slop (for instance in case of very low solubility); thus completely prevents the detection of the phase change within the EC.

The equilibrium cells used with this method are commonly made of stainless steel or other metal alloys enabling to work at high pressures; however, it does not allow observing the phase transition occurring within the equilibrium cell. This method is the same as that used for the high-pressure bubble point measurement.

In the context of this PhD thesis, the synthetic-indirect method has been used for the investigation of the SLVE of methane+neopentane, methane+ethane+neopentane, and methane+nitrogen+neopentane systems.

2.2.1.3 Calorimetric method

Among several calorimetric methods reported in the literature for the measurement of the solid-fluid phase equilibria, the most relevant and widely used are the Differential Scanning Calorimetry (DSC) and the Differential Thermal Analysis (DTA).

The principle of the DSC method is the cooling down or heating up of a mixture of known composition inside a calorimeter, then, the heat flow is plotted as a function of the temperature of the system; when the phase transition occurs, a peak in such a curve is observed. This technique offers the possibility of determining some physical properties of the system under study, like the heat capacity or the enthalpy concurrently with the investigation of the phase transition.

Examples of the application of the DSC for the evaluation of the SFE are the works of McConville et al. that focused on the study of the global temperature-composition diagram of the benzene+acetonitrile system in the context of the investigation of Titan's surface composition [24], and of Wang et al. who investigated the cryogenic eutectic behavior of the trifluoromethane+difluoromethane binary system [25].

2.2.2 The analytic methods

Unlike the synthetic methods, the exact knowledge of the global composition of the mixture is not a primary information when using the analytic methods, nevertheless, the amount of the solid former should be enough to form the solid phase at the target temperature and pressure.

The analytic methods (known also as isothermal methods) require two main steps: the first one is the cooling of the system down to the target temperature, and the second one consists of the composition analysis of the fluid phase in equilibrium with the solid phase to determine its composition. Spectroscopic or gas chromatographic are the most used techniques for the analysis of the composition of the fluid phase.

2.2.2.1 Static-analytic method

The static-analytic method is widely used in the literature and has shown its efficiency for both the study of fluid-fluid equilibria and for the low solubility solid-fluid equilibria. This experimental procedure requires the feeding of the equilibrium cell with the different species involved in the studied mixture and then the cooling of the system down to the target temperature. At this temperature, the pressure of the system can be adjusted if needed by adding some solvent. The system is maintained at this P-T condition until the thermodynamic equilibrium is reached.

Depending on how the composition of the fluid phase is analyzed, we can define two main techniques: the Gas Chromatographic (GC) analysis and the spectroscopy analysis.

- ***The GC analysis*** needs the use of a sampling device that allows withdrawing fluid samples from the EC, which are then transferred to the GC in order to determine their composition.

  Several works dealing with the solubility measurement using this technique are reported in the literature. Kohn and Luks have used GC analysis for the investigation of the SFE of systems of interest for the Liquefied Natural Gas (LNG) and the Natural Gas Liquids (NGL); they have reported that this technique is suitable for systems presenting low solubilities (5% down to some ppm) [16].

  Our laboratory (CTP) has large expertise in the investigation of the solubility of solid formers in cryogenic solvents using the static-analytic method with the GC analysis. The first work was carried out by Baba Ahmed and coworkers who developed an apparatus for investigating systems of interest for cryogenic air separation [26]. This work kicked off an interesting series of experimental works aiming at determining the fluid-fluid and the solid-fluid equilibria in the context of the cryogenic air distillation and the natural gas liquefaction [27] [28] [29] [30] [31] [32] [33] [34].

  Additional information concerning the static-analytic method are given in chapter 3 where the original measurements obtained in this work are presented.
- ***The spectroscopic analysis*** allows an in-situ analysis of the composition of the fluid phase (no sampling device is required). Raman, ultraviolet, or infrared spectroscopy can be used to measure the fluid composition. A spectrum passes through the fluid phase and its analysis provides the proportion of the species present in this phase (the calibration of the spectrum response for each component involved in the mixture is performed earlier). This technique is unusual for the study of the solid-fluid equilibria of the systems of interest for the LNG but it is significantly used in other research areas. As an example, we can cite the work of Diez-y-Riega and coworkers who have measured the solubility of solid benzene in liquid methane and ethane in the context of the

investigation and the comprehension of the composition of Titan's surface and atmosphere [35]. Nevertheless, these data are of high interest also for the evaluation of the risk of the crystallization of benzene in LNG production.

2.2.2.2 Dynamic method (circulating method)

The dynamic method consists of a continuous circulation (or recirculation) of the solvent through an equilibrium cell where a certain amount of the solid former has been previously crystallized. The equilibrium cell is kept at constant temperature and the experimental pressure is the one of the circulating fluid. The permanent contact between the circulating fluid and the solid phase allows matter exchange between the solid solute and the solvent until reaching the saturation limit. The fluid phase escaping the cell (recirculated) is continuously analyzed. Once the saturation of the solvent is reached, its composition tends to a constant value, which corresponds to the solubility limit of the solid former in the used solvent.

Kuebler and McKinley investigated the solubility of some hydrocarbons (n-butane and n-pentane in [36], n-hexane, n-heptane, benzene, and toluene in [37] and tert-butylthiol in [38]) in liquid methane using the circulating method coupled with a GC analysis. Baughman et al. used this technique for investigating the solubility limits of solid neopentane in vapor methane, argon, nitrogen, and helium [39].

2.3 Available literature data on the SFE

One of the main axes of this research project is the development of a complete database of phase equilibria involving solid phases for systems of interest for LNG production. For this purpose, a deep bibliographic research has been carried out in order to collect the available solid-liquid, solid-vapor, and solid-liquid-vapor equilibrium data. The experimental works dealing with such measurements are scarce because of the complexity of carrying out such measurements that generally occur at cryogenic temperatures (severe conditions compared to the fluid-fluid equilibrium). Nevertheless, some systems have been well-studied thanks to their relatively high scientific and industrial interest, and the fundamental need of mastering their thermodynamic behavior.

Tab2.1 shows all the couples of components investigated in this work: green cells show the systems for which data exist in the literature while the white ones show those for which no data are available in the literature.

Table 2.1: summary of the systems investigated in the present bibliographic research

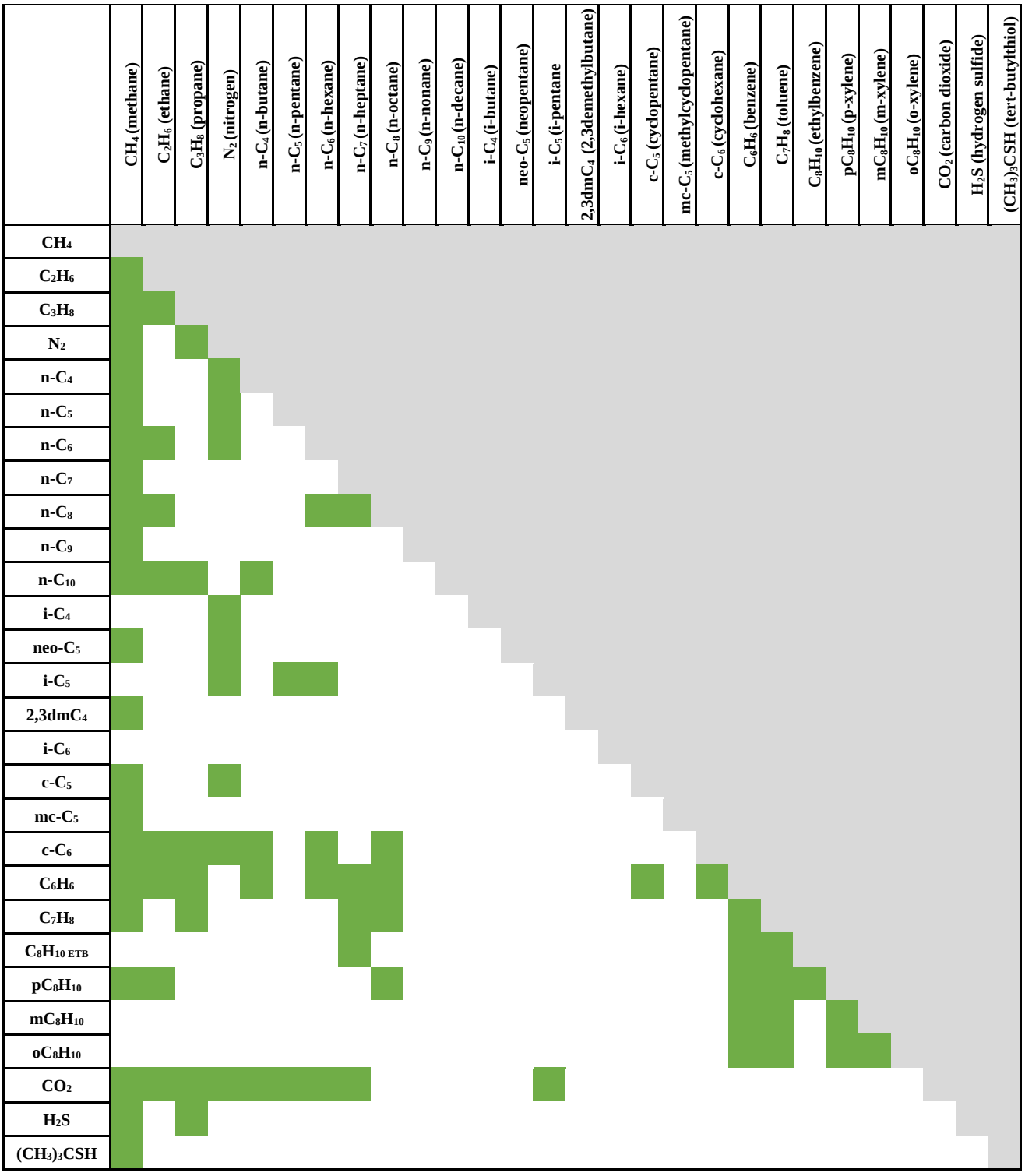

2.3.1 Methane + solid former binary systems

Natural gas is mainly composed of methane, thus the systems containing methane are the most investigated in the literature. The solubility limits of 21 components in methane are reported in the literature. Nevertheless, this is still not enough for understanding the thermodynamic behavior of natural gas during the liquefaction process and thus optimizing the purification and the liquefaction process (avoiding the oversizing of the purification units while controlling the crystallization risk). On the one hand, the data reported in the literature are generally focused on the high-temperature region, and those occurring at the LNG temperature are scarce; on the other hand, the SFE behavior of systems involving some of the NG components has not been investigated at all and their thermodynamic behavior in the LNG remains completely unknown.

In order to have a better comprehension of the thermodynamic behavior of the LNG mixture (complete evaluation of the solidification conditions of the different potential solid formers), additional experimental measurements are necessary. In the following, a brief review of the SFE of the systems composed by methane and a solid former that have been investigated in the literature.

The methane+carbon dioxide system is well studied in the literature, and a high amount of SLVE and SVE data are reported, however, no data have been found for the SLE (experimental pressure higher than the SLVE pressure). The deep investigation of this system is motivated by its large interest for several industrial processes (cryogenic carbon capture and storage, natural gas liquefaction, biogas liquefaction, etc).
Fig2.1 shows the pressure-temperature diagram of all the available SVE and SLVE literature data involving solid carbon dioxide; the continuous lines correspond to the saturation and the melting loci of pure methane (1) and pure carbon dioxide (2) calculated using REFPROP v10 [40]. Fig2.2 presents the solubility limits of solid CO_2 in liquid methane at the SLVE (filled symbols) and in vapor methane at the SVE (open symbols).

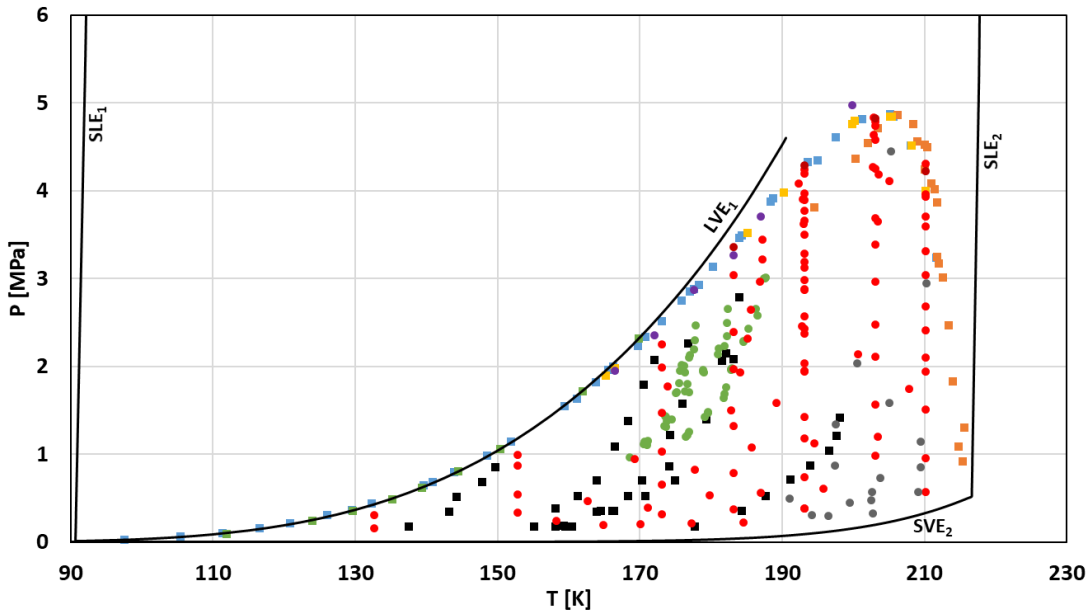

Figure 2.1: pressure–temperature diagram of methane(1)+carbon dioxide (2) system at the SVE and SLVE.
— pure components properties, ■ ref [20], ■ ref [41], ■ ref [42], ■ ref [43], ■ ref [44], ● ref [45], ● ref [46], ● ref [47], ● ref [48], ● ref [49].

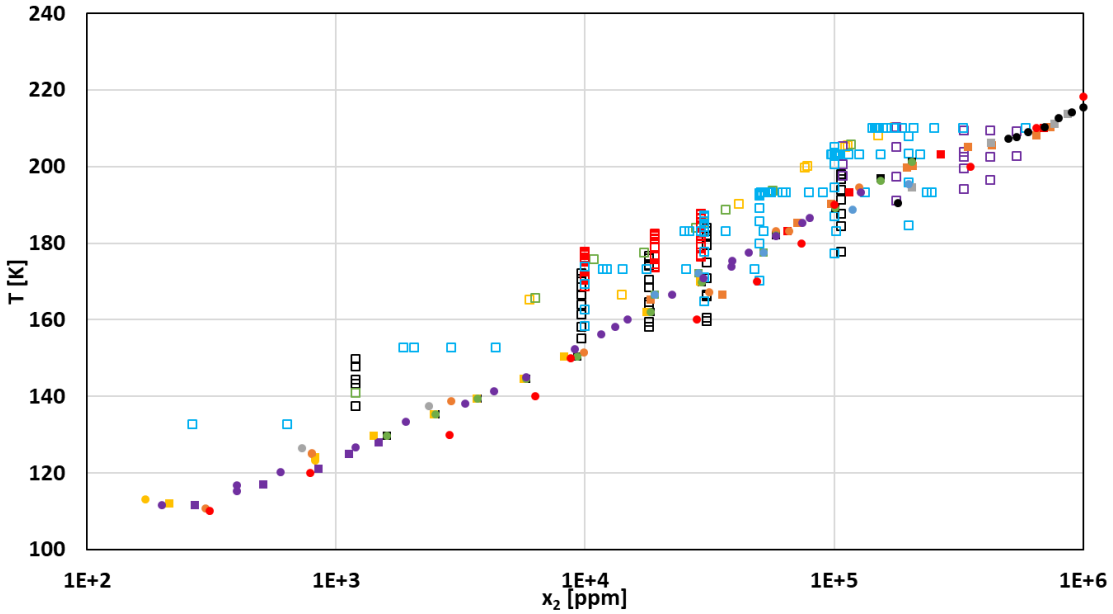

Figure 2.2: temperature-composition diagram of methane(1)+carbon dioxide (2) system at the SVE and SLVE.
SVE: □ ref [20], □ ref [43], □ ref [41], □ ref [45], □ ref [48], □ ref [46].
SLVE: ■ ref [41], ■ ref [42], ■ ref [43], ■ ref [44], ■ ref [47], ■ ref [49], ■ ref [50], ■ ref [51] ● ref [52], ● ref [53], ● ref [54], ● ref [55], ● ref [56], ● ref [57], ● ref [58], ● ref [59].

The solubility limits of the light n-alkanes in liquid methane have also been deeply studied in the literature, and the available literature data involving solid n-alkanes from n-butane up to n-octane are presented in Fig2.3. Based on the solubility limits reported in the literature, it can be stated that the n-alkanes do not present any solidification risk during the LNG production (at least up to n-heptane) since their concentrations in the feed gas (after the natural gas liquids recovery) are lower than their solubility limits (at the LNG temperature (110 K). Besides n-octane, the other n-alkanes have a solubility limits higher than 100 ppm). Among the reported literature data, some disagreements can be pointed out. The solubilities of n-butane reported in refs [18] and [36] are not in good agreement between each other and present an absolute deviation of more than 32%. Concerning the solubility limits of n-pentane, the data reported in [18] and [59] do not agree with the data of the other references. For the methane+n-hexane system, some of the data reported in [60] (data at temperatures lower than 155 K) are not in agreement with the other references. The solubility limits of n-octane in liquid methane reported in [61] present inconsistencies compared to the expected behavior of the solubility limits (the solubility should decrease monotonically for decreasing temperature); further measurements of the methane+n-octane system will therefore be useful to elucidate its behavior at cryogenic temperatures and confirm the low-solubility limits of solid n-octane in liquid methane.

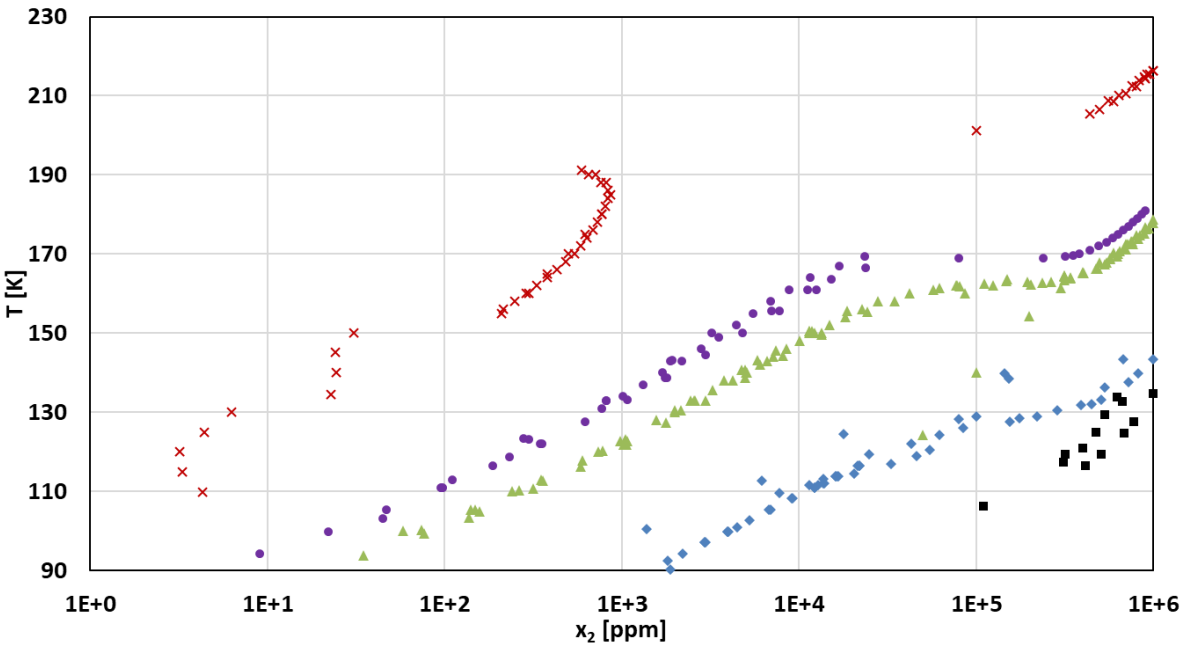

Figure 2.3: temperature-composition diagram of methane(1)+n-alkane (2) system.
■ n-butane refs [18] [36]; ♦ n-pentane refs [50] [59] [36] [62] [63] [18]; ▲ n-hexane refs [52] [64] [63] [65] [66] [37] [60] [31]; ● n-heptane refs [64] [62] [37] [67] [18] [14]; x n-octane refs [52] [16] [68] [15] [61] [69].

The branched and cyclo-alkanes are less studied compared to the n-alkanes. SVE data are reported for methane+neopentane in ref [39]; The experimental values of the solubility limits of neopentane, 2,3-dimethylbutane, and cyclo-pentane in liquid methane are reported in reference [59]; in addition, SLE and SLVE data of methane+cyclo-hexane system are reported in refs [64] and [68] respectively. The investigation of the solid-fluid equilibrium behavior of these components allows the evaluation of the effect of the isomerism and the pure component properties (heat of fusion, triple point temperature, etc) on the solubility limits of the alkanes in methane. The scarcity of the data dealing with these components suggests performing additional measurements in order to improve the knowledge of the thermodynamic behavior of the systems involving these components. The available literature data accounting for the solubilities of branched and cyclo-alkanes in methane are presented in Fig2.4.

Aromatic compounds are of high interest for the natural gas industry, since they are systematically present in raw natural gas, and their concentration changes depending on the origin of the NG. Few references are available in the literature concerning these components; the methane+benzene system is highly studied but most of the literature works report data on the high-temperature region (the triple point temperature of benzene is 278.5 K) and account usually for the benzene-rich liquid phase. The solubility limits of solid benzene in liquid methane are presented in refs [37], [65], [70], and [71]; unfortunately, the data from these references present some inconsistencies. SLE and SLVE data of the methane+toluene system are presented only in reference [37] that reports SLE and SLVE data. Recently Siahvashi and coworkers have investigated the SLVE of the methane+p-xylene system [72]; these measurements are focused on the high-temperature SLVE branch (the one originating from the triple point of p-xylene and ending on an upper critical endpoint, as presented in section 2.5.1), thus are related to the solubility of solid p-xylene in liquid phase rich in p-xylene; these SLVE data are not representative of the conditions encountered in the natural gas liquefaction process, for which the liquid phase is a methane-rich mixture. The analysis of these available data shows that the aromatic compounds present a very low solubility in methane at cryogenic conditions and present a high potential risk to form solid phases during the liquefaction process. All the literature data dealing with the solubility limits of aromatic compounds (BTEX: Benzene, Ethylbenzene, Toluene, and Xylenes) in methane are shown in Fig2.5.

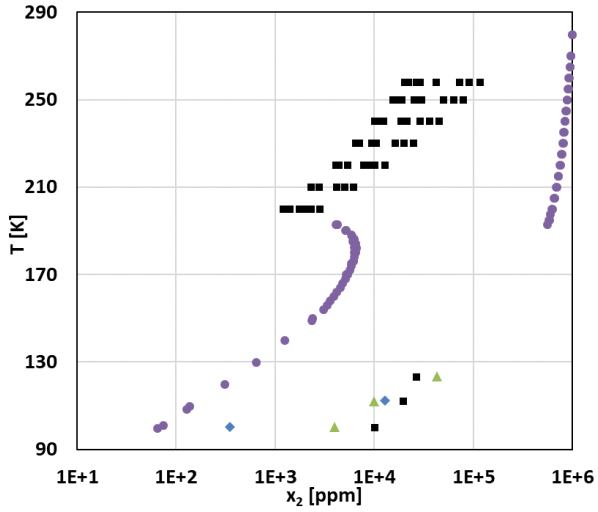

Figure 2.4: temperature-composition diagram of methane(1)+iso-alkane/cycloalkane(2) system.
■ neopentane refs [39] [59]; ♦ cyclopentane ref [59]; ▲ 2,3-dimethylbutane ref [59]; ● cyclohexane refs [64] [68].

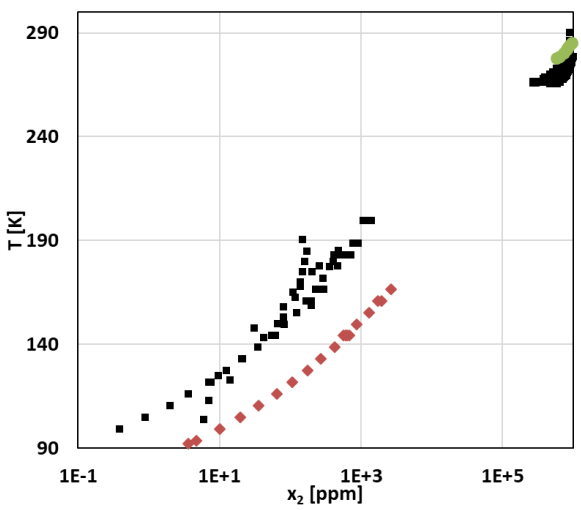

Figure 2.5: temperature-composition diagram of methane(1)+BTEX(2) binary system.
■ benzene refs[37] [65] [70] [71] [73] [74] [21]; ♦ toluene ref [37]; ● p-xylene ref [72].

In addition to the families cited above, sulfur compounds (sulfides and thiols) are generally present in raw natural gas. Except hydrogen sulfide (H_2S) for which two references exist in the literature [13], and [54], no data are presented for the other components belonging to this family of components. Since these components are extremely harmful, several restrictions exist to limit their concentration in the sold LNG (the concentration limits depend on the local market), thus a severe purification process is needed to meet these limitations. Despite these low-concentration limits imposed by the NG trade, the concentration of these components in the natural gas leaving the purification units and feeding the liquefaction unit may be higher than their solubility limits in LNG and thus present a risk of solid formation. Further experimental investigations could be then useful for giving insights into the solidification risk of the sulfur components in the LNG mixtures.

Several components can be found in the liquefied natural gas but are not present in the raw NG. It is the case of components voluntary added for odorizing the NG in order to detect any eventual leak (for instance, tert-butylthiol, which is used in the USA, has been investigated by Kuebler and McKinley [38]; in France, it is tetrahydrothiophene (THT) which is used as an odorant for the NG). In addition, some other components are mixed to NG following the different processes upstream of the liquefaction (for instance, amines, glycols, methanol, etc).

2.3.2 Other solvent + solid former binary systems

Methane is not the only component that can be considered as a solvent when evaluating the solidification risk in LNG production, but also ethane, propane, and nitrogen are considered as solvent since their triple point temperatures are lower than the target temperature of the LNG. The data concerning these systems are very useful for the evaluation of the influence of the presence of a small amount of these solvents on the solubility limits of the solid formers in methane.

The general tendency that can be inferred from the analysis of the available literature data is that the solid formers of interest in the context of natural gas liquefaction are more soluble in ethane and propane, and less soluble in nitrogen compared to methane. This suggests that the presence of ethane and propane may increase the solubility limit of the solid formers while the presence of nitrogen decreases the solubility limits. In addition, the solubilities measurements involving ethane, propane, or nitrogen as solvent are crucial for the tuning of the models used for the representation of the thermodynamic behavior of LNG mixtures.

Solubilities of solid n-hexane and n-heptane in liquid ethane are reported in ref [62], Kohn et al. reported SLVE of the n-octane+ethane mixture [75], and Liu et al. reported SLVE of cyclohexane+ethane system [76]. Regarding the aromatic compounds, solubilities of benzene are reported in refs [16] and [76] and those of p-xylene in ref [72]. The solubility limits of solid CO_2 in ethane are reported by Jensen and Kurata [77].

The solubility limits of the solid formers in ethane are presented in Fig2.6. Unlike the different systems presented in Fig2.6, the solubility limits of cyclohexane in liquid ethane presents a sharp slope change at approximately 180 K; this is due to the change on the crystalline structure of the cyclohexane at this temperature and the enthalpy change at this solid-solid transition is much higher than the one at the solid-liquid transition.

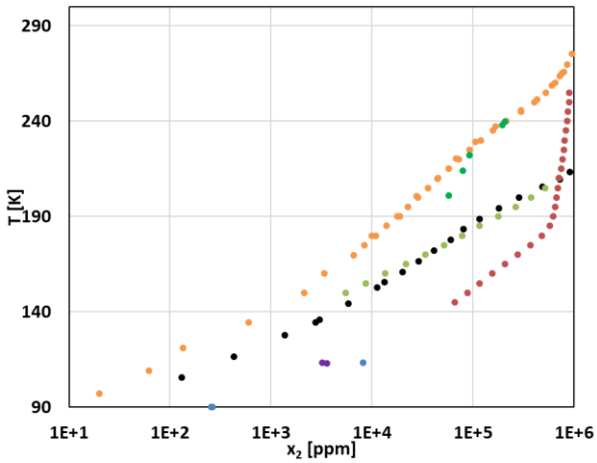

Figure 2.6: temperature-composition diagram of ethane(1)+solid former (2)binary mixture.
● carbon dioxide ref [77]; ● benzene refs [16] [76]; ● p-xylene ref [72]; ● n-hexane ref [62];
● cyclohexane ref [76]; ● n-heptane ref [62]; ● n-octane ref [75].

The solubility limit of n-pentane, n-hexane, and n-heptane in liquid propane at 113.15 K are reported in ref [62], whereas the SLVE of propane+benzene, and propane+cyclohexane systems have been studied by Chen et Luks [78]. the SLE data of the propane+benzene and propane+toluene systems are reported by Neumann et al. [79] and Teller and Knapp [80] respectively. Jensen and Kurata reported the SLVE of the carbon dioxide+propane system[77]. Finally, few data of propane+hydrogen sulfide are also given in ref [54].

The solubility limits of the solid formers in propane are presented in Fig2.7.

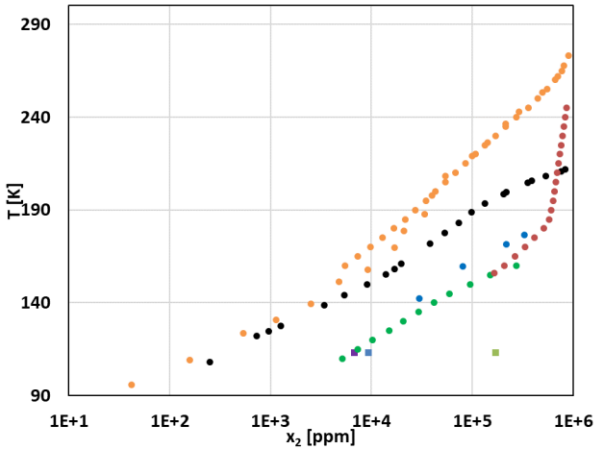

Figure 2.7: temperature-composition diagram of propane(1)+solid former (2)binary mixture.
● carbon dioxide ref [77]; ●benzene refs [78] [79]; ● toluene ref [80]; ● cyclohexane ref [78];
■ n-pentane ref [62]; ■ n-hexane ref [62]; ■ n-heptane ref [62].

Szczepaniec-Cieciak and Kurdziel reported the solubility limits of n-butane and i-butane in liquid nitrogen [81], those of n-pentane, i-pentane, and cyclopentane at 77.4 K in [82], and those of n-hexane and cyclo-hexane at 77.4 K in [83]. The SVE data of nitrogen+neopentane system have been reported in ref [39].

Finally, the solubility limits of benzene in liquid nitrogen are reported in ref [71], and those of carbon dioxide are reported by Yakimenko et al. [84] and Sonntag and van Wylen [85] and [86].

The solubility limits of the solid former in nitrogen are presented in Fig2.8.

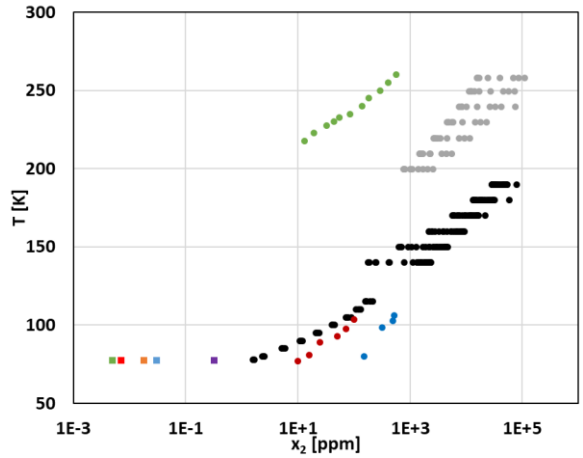

Figure 2.8: temperature-composition diagram of nitrogen(1)+solid former (2)binary mixture.
● carbon dioxide ref [84] [85] [86]; ● neopentane ref [39]; ● benzene ref [71] ; ● n-butane ref [81]; ● i-butane ref [81]; ■ n-pentane ref [82]; ■ i-pentane ref [82] ; ■ cyclopentane ref [82]; ■ n-hexane ref [83]; ■ cyclohexane ref [83]

.

A summary of the collected SLE, SVE, and SLVE data of all the systems investigated in this work is given in appendix A.

2.4 Modeling of the solid-fluid phase equilibrium

2.4.1 Equilibrium condition

The thermodynamic equilibrium of a heterogeneous and closed system containing "N_c" components and composed by "Φ" phases is given by the equality of the temperature "T" (thermal equilibrium), the pressure "P" (mechanical equilibrium), and the chemical potential "μ" (chemical equilibrium) for each component in all the phases of the system.

$$\begin{gathered} \forall\, i \in [1,N_c] \text{ and } \forall\, j \in [1, \Phi] \\ T^j = T^{\Phi} \\ P^j = P^{\Phi} \\ \mu_i^j(T^j, P^j, \overrightarrow{x^j}) = \mu_i^{\Phi}(T^{\Phi}, P^{\Phi}\overrightarrow{x^{\Phi}}) \end{gathered} \tag{2.1}$$

The chemical potential of a given component of the mixture (species "*i*") in a given phase corresponds to the energy variation induced by the variation of the amount (number of moles) of this species in this phase. The thermodynamic equilibrium of a mixture is reached when the variation of the energy induced by the displacement of any quantity of each species from one phase to another is equal whatever the sense. The

chemical potential allows the evaluation of the tendency of the species to migrate and move from one phase to another.

In order to quantify the chemical potential of a component "*i*" in a given phase using the classical variables; Gibbs-Duhem proposed the following relation:

$$SdT - vdP + \sum_{i=1}^{N} n_i \mu_i = 0 \tag{2.2}$$

For each species in the phase, the Eq2.3 holds:

$$d\mu_i = v_i dP - s_i dT \tag{2.3}$$

The isothermal integration of Eq2.3 for an ideal gas $\left(v_i = \frac{RT}{P}\right)$ between a reference state (indicated in the following by the superscript *ref*) and a given state leads to:

$$\begin{aligned} \mu_i - \mu_i^{ref} &= \int_{P^{ref}}^{P} v_i dP \\ \mu_i - \mu_i^{ref} &= RT ln\left(\frac{P}{P^{ref}}\right) \end{aligned} \tag{2.4}$$

To give a valid expression even for dense phases, Lewis introduced in 1908 the concept of the fugacity. The ratio $\frac{\boldsymbol{P}}{\boldsymbol{P^{ref}}}$ becomes then $\frac{\boldsymbol{f}}{\boldsymbol{f^{ref}}}$ (for ideal gas f = P, and for a mixture of ideal gases $f_i = y_i P$). Introducing the fugacity in Eq2.4 and considering a system at thermal and mechanical equilibrium results in a new thermodynamic equilibrium condition written in terms of fugacity (iso-fugacity condition).

$$\forall\ i \in [1, N_c] \text{ and } \forall\ j \in [1,\ \Phi\ ] \qquad \hat{f}_i^{\,j}(T, P, \overrightarrow{x^j}) = \hat{f}_i^{\,\Phi}(T, P, \overrightarrow{x^\Phi}) \tag{2.5}$$

In the case of solid-fluid equilibrium, Eq2.5 becomes

$$\forall\ i \in [1, N_c] \qquad \hat{f}_i^{\,s}(T, P, \overrightarrow{x^s}) = \hat{f}_i^{\,f}(T, P, \overrightarrow{x^f}) \tag{2.6}$$

2.4.2 Resolution of the iso-fugacity condition

As reported above, the thermodynamic equilibrium of a given system requires respecting the iso-fugacity condition for each component "*i*" in all the phases at equilibrium. Two main approaches are often used for the resolution of such a condition: the symmetric and the asymmetric approach.

- ***The symmetric (residual) approach,*** known as the "φ-φ" approach, consists of evaluating the fugacities in terms of fugacity coefficients calculated from an Equation of State (EoS). This approach is widely used when dealing with the vapor-liquid equilibrium.

- ***The asymmetric (excess) approach,*** known as the "γ-φ" approach, is usually used when dense phases are involved in the equilibrium. The activity coefficient "γ" of a given component in a dense phase is evaluated by means of excess Gibbs Energy models.

The application of the two mentioned approaches for the resolution of the iso-fugacity condition between two phases "α" and "β" leads to Eq2.7 and Eq2.8.

φ- φ approach		**γ- φ approach**	
$x_i \varphi_i^{\alpha} P = y_i \varphi_i^{\beta} P$	(2.7)	$x_i \, \gamma_i^{\alpha} \, f_i^{ref} = y_i \varphi_i^{\beta} P$	(2.8)

The asymmetric approach involves the fugacity of the component *i* in a reference state. Two main reference states are used to represent f_i^{ref}; the first one considers as the reference state the pure component "*i*" taken at the same P-T condition of the real mixture (Raoul's law), and the second one considers as the reference state the mixture at infinite dilution (Henry's law).

2.4.3 Review of the models dealing with SFE

The modeling of the phase equilibria involving solid phases is particularly complex. The selection of the suitable model for representing a given system depends on the nature of the solid phase (pure, solid solution, etc), the nature of the components involved in the studied system, and the scientific or industrial application. A deep review of the different methods and attempts dealing with the representation of phase equilibria involving solid phases has been presented by Campestrini in ref [29].

In this work, a particular interest is given to the approaches dealing with the modeling of the solid-fluid equilibria involving pure solid phase (complete immiscibility in the solid phase); this hypothesis is widely adopted when investigating systems of interest for the LNG production. In the following, a description of the two main methods used in the literature for the representation of such systems is given.

2.4.3.1 Empirical correlations for the solubility calculation

Among the first works on the modeling of the solid-fluid equilibria at cryogenic temperature in the context of natural gas liquefaction, the one carried out by the research group of Kohn and Luks in the Seventies of the last century during their collaboration with the Gas Processor Association (GPA) can be taken as a reference [16]. The authors developed correlations for the calculation of the solubility of some hydrocarbons and CO_2 in the LNG and NGL mixtures. The GPA has long adopted these correlations as reference equations for estimating the solubility limit of certain solid formers in LNG mixtures.

For developing these correlations, the authors started by considering the ideal solution behavior for evaluating the ideal solubility based on the infinite dilution hypothesis; then, the authors introduced corrections to this ideal solubility by means of factors based on the activity coefficient of the liquid phase. An excess Gibbs free energy model was then used for the evaluation of the activity coefficient; this model used two empirical parameters that were regressed on the available experimental data of the binary mixtures.

The correlation was developed for the calculation of the solubility limits of the solid former in the liquid phase at the solid-liquid-vapor equilibrium. Since they are continuous expressions, one of their main limitations is the investigation of the binary systems characterized by a non-continuous SLVE line (such as methane+benzene system). In addition, the scarcity of experimental measurements dealing with the SLVE of the binary mixtures (data from the triple point of the solid former down to the cryogenic temperatures) and the absence of a pressure-dependent term in these correlations reduce their accuracy and restrict their range of application.

2.4.3.2 The classical approach for the SLE

The thermodynamic modeling of the SLE of pure components requires the resolution of the iso-fugacity condition (Eq2.6), this passes through the quantification of the fugacity of the pure component in the solid phase and in the fluid phase. The main used method in the literature for the calculation of the fugacity of the pure component in the solid phase is the so-called "Classical Approach" (CA).

The classical approach is a method that allows calculating the fugacity of a pure component in the solid phase starting from its fugacity in the subcooled liquid phase by using a Correcting Factor (CF).

$$f_0^s(T,P) = f_0^l(T,P) * CF \tag{2.9}$$

The first attempt for defining the correcting factor was reported by Prausnitz who proposed a CF based on the properties of the solid former at its triple point (Prausnitz's expression neglects the pressure effect and considers the non-temperature dependence of the heat capacity change upon melting) [87]. The full expression of the CF can be derived using rigorous thermodynamic relations based on the Fundamental Property Relations or the Gibbs State Function applied at the SLE of the pure component.

For the reader's convenience, the mathematical development and the steps leading to the final expression of the fugacity of a pure component in the solid phase by means of the classical approach (Eq2.10) are presented in appendix B.

$$f_0^s(T,P) = f_0^l(T,P)\exp\left[\frac{\Delta H_{T_tP_t}^{s\to l}}{RT}\left(\frac{T}{T_t}-1\right)+\frac{\Delta C_{P_{T_tP_t}}^{s\to l}}{R}\left(\frac{T_t}{T}-1-ln\left(\frac{T_t}{T}\right)\right)-\frac{\Delta V_{T_tP_t}^{s\to l}}{RT}(P-P_t)\right] \quad (2.10)$$

Where, $f_0^s(T,P)$ is the fugacity of the pure component in the solid phase at a given Temperature (T) and Pressure (P), $f_0^l(T,P)$ is the fugacity of the pure component in the subcooled liquid phase at T and P. $\Delta H_{T_tP_t}^{s\to l}, \Delta C_{P_{T_tP_t}}^{s\to l}, \Delta V_{T_tP_t}^{s\to l}$ are respectively the enthalpy, the heat capacity, and the volume change upon melting taken at the triple point temperature (T_t) and pressure (P_t), and *R* is the gas constant.

Preston and Prausnitz used a simplified form of Eq2.10 (they neglected the terms on $\Delta C_{P_{T_tP_t}}^{s\to l}$ and $\Delta V_{T_tP_t}^{s\to l}$) to represent the solubility of several solid former in cryogenic solvents at the SLE [88]; the authors used Scatchard's equation for evaluating the properties of the liquid phases.

In 1978, Soave [89] used the classical approach for modeling the SLE of CO_2 + light hydrocarbons binary mixtures. In his work, Soave used the Soave Redlich Kwong Equation of State (SRK EoS) for the representation of the properties of the fluid phase and neglected the pressure effect when calculating the fugacity of a pure component in the solid phase. In addition, $\Delta H^{s\to l}$ and $\Delta C_p^{s\to l}$ have been regressed on the sublimation data of the CO_2 in order to improve the representation of the pure CO_2 saturation properties.

Garcia and Luks investigated the possibility of mapping out the SLVE loci of different homologous series of binary mixtures (ethane+n-alkanes and carbon dioxide+n-alkanes binary mixtures) [90]. The classic approach was coupled with the van der Waals EoS for the representation of the SLVE conditions.

Rodrigues-Reartes et al. used a similar expression to the one in Eq2.10 for investigating the solid-fluid and the solid-fluid-fluid equilibrium of pure components and binary asymmetric mixtures [91]. The authors used a linear temperature dependence of the $\Delta C_p^{s\to l}$. In addition, instead of using the properties of the pure component at its triple point (as in Eq2.10), they used four adjustable parameters; three of them have been regressed on the SLE of the pure component and the last one has been regressed on the binary mixture data in order to obtain an agreement between the calculated and the measured solubilities. In a recent work, the same research group correlated the parameters used for the representation of the SLE of n-alkanes in methane to the carbon number of the n-alkanes [92].

Campestrini and Stringari made an inventory of the existing literature data for the methane+n-alkanes binary mixtures (up to n-triacontane) [93]. In the light of this review, they assessed the capability of three fluid phase models (The Predictive Peng Robinson EoS (PPR78 EoS), the Predictive Soave Redlich Kwong EoS (PSRK EoS), and the Peng Robinson EoS (PR EoS) with constant value of the binary interaction parameter) when coupled with a simplified form of Eq2.10 to represent the solubility limits of the investigated systems.

Baker and coworkers developed a software for the prediction of the solidification risk in cryogenic natural gas [94]. The authors used the full expression given in Eq2.10 coupled with the PR EoS; binary interaction parameters (k_{ij}) have been regressed on the available SFE data.

Aside from the examples cited above, several literature works used the classical approach for representing the SFE. In ref [19] the CA has been coupled with the UNIFAC model for the modeling of the SLE of organic compounds. De Hemptinne used the CA with the PR EoS for the evaluation of the crystallization risk of benzene in the LNG mixture [95]. In addition, phase equilibria including the solid phase for methane+carbon dioxide have been investigated by means of the CA in ref [96].

2.5 Classification of the phase diagram including solid phase

Van Konynenburg and Scott proposed in 1980 a classification of the different global phase diagrams of binary mixtures when considering only the fluid phases; the van der Waals equation of state was used for generating the possible phase diagrams and five different types have been obtained [97]. Subsequently, several authors reported additional global phase diagrams and more extensive-classifications.

Kohn and Luks proposed a classification of the global phase diagram including the solid phases and considering a total or partial immiscibility in the solid phases [16]. Four different global phase diagrams are reported in ref [16] and are representative of a large number of the systems involved in the natural gas mixtures. These global phase diagrams are described in the following in order to give a better comprehension of the thermodynamic behavior of the systems investigated in this thesis.

2.5.1 Type A phase diagram

The qualitative pressure-temperature diagram for type A reported by Kohn and Luks is shown in Fig2.9; considering only the fluid phases, this type of phase diagram corresponds to the type III according to the classification of the van Konynenburg and Scott.

Besides the saturation, the melting, and the sublimation curves of the pure components, the type A is characterized by the following loci:

- Two separate critical lines; the first one originates at the critical point of the component 2 (heaviest compounds) and ending at the Upper Critical End-Point 2 (UCEP2), and the second one originates at the critical point of the component 1 (lightest compound) and ends at the Upper Critical End-Point 1 (UCEP1)

- A quadruple point that corresponds to a Solid$_1$-Solid$_2$-Liquid-Vapor Equilibrium (S_1S_2LVE). The existence of this quadruple point is due to considering a total or partial immiscibility of the components 1 and 2 in the solid phases.
- A three-phase Solid$_2$-Liquid$_2$(component2-rich liquid)-Vapor Equilibrium (S_2L_2VE) line originating at the triple point of the component 2 and ending at the UCEP2.
- A three-phase Solid$_2$-Liquid$_1$(component1-rich liquid)-Vapor Equilibrium (S_2L_1VE) line originating at the UCEP1 and ending at the quadruple point (S_1S_2LVE).
- A three-phase Solid$_1$-Liquid-Vapor Equilibrium (S_1LVE) line originating at the triple point of the component 1 and ending at the quadruple point (S_1S_2LVE).
- A three-phase Solid$_1$-Solid$_2$-Vapor Equilibrium (S_1S_2VE) line originating at the quadruple point (S_1S_2LVE) and developing in the low-temperature-low-pressure region.
- A three-phase Solid$_1$-Solid$_2$-Liquid Equilibrium (S_1S_2LE) line originating at the quadruple point (S_1S_2LVE) and developing in the high-pressure region.

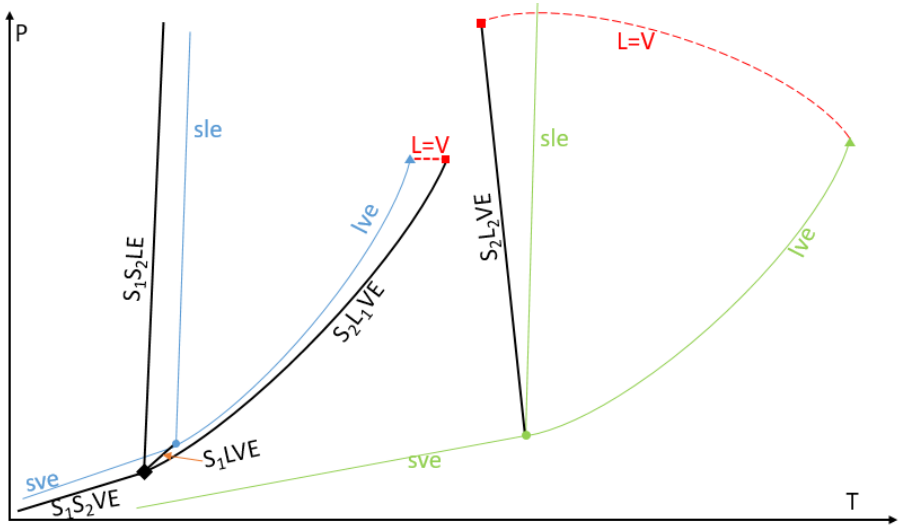

Figure 2.9: qualitative P-T diagram of a binary system having a global phase diagram of type A

2.5.2 Type B phase diagram

The qualitative pressure-temperature diagram for type B reported by Kohn and Luks is shown in Fig2.10; considering only the fluid phases, this type of phase diagram corresponds to the type III according to the classification of the van Konynenburg and Scott.

Besides the saturation, the melting, and the sublimation curves of the pure components, the type B is characterized by the following loci:

- Two separate critical lines, the first one originates at the critical point of the component 2 (heaviest compound) and ends at the UCEP2 the second one originates at the critical point of the component 1 (lightest compound) and ends at the UCEP1.
- Two quadruple points: the warmer corresponds to a $Solid_2$-$Liquid_1$(component1 rich liquid)-$Liquid_2$(component2 rich liquid)-Vapor Equilibrium ($S_2L_1L_2VE$) and the colder corresponds to a $Solid_1$-$Solid_2$-Liquid-Vapor Equilibrium (S_1S_2LVE).
- A three-phase $Solid_2$-$Liquid_2$(component2-rich liquid)-Vapor Equilibrium (S_2L_2VE) line originating at the triple point of the component 2 and ending at the warmer quadruple point ($S_2L_1L_2VE$).
- A three-phase $Solid_2$-$Liquid_1$(component1-rich liquid)-Vapor Equilibrium (S_2L_1VE) line originating at the warmer quadruple point ($S_2L_1L_2VE$) and ending at the colder quadruple point (S_1S_2LVE).
- A three-phase $Liquid_1$(component1-rich liquid)-$Liquid_1$(component1 rich liquid)-Vapor Equilibrium (L_1L_2VE) line originating at the warmer quadruple point ($S_2L_1L_2VE$) and ending at UCEP1.
- A three-phase $Solid_2$-$Liquid_1$(component1-rich liquid)-$Liquid_2$(component2 rich liquid) Equilibrium ($S_2L_1L_2E$) line originating at the warmer quadruple point ($S_2L_1L_2VE$) and ending at the UCEP2.
- A three-phase $Solid_1$-Liquid-Vapor Equilibrium (S_1LVE) line originating at the triple point of the component 1 and ending at the colder quadruple point (S_1S_2LVE).
- A three-phase $Solid_1$-$Solid_2$-Vapor Equilibrium (S_1S_2VE) line originating at the colder quadruple point (S_1S_2LVE) and developing in the low-temperature-low-pressure region.
- A three-phase $Solid_1$-$Solid_2$-Liquid Equilibrium (S_1S_2LE) line originating at the colder quadruple point (S_1S_2LVE) and developing in the high-pressure region.

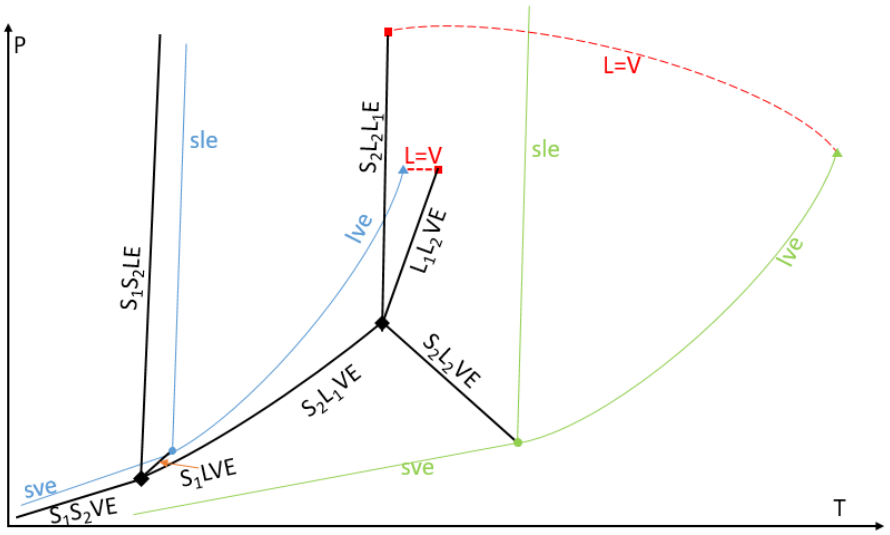

Figure 2.10: qualitative P-T diagram of a binary system having a global phase diagram of type B

2.5.3 Type C phase diagram

The qualitative pressure-temperature diagram for type C reported by Kohn and Luks is shown in Fig2.11; considering only the fluid phases, this type of phase diagram corresponds to the type V according to the classification of the van Konynenburg and Scott.

Besides the saturation, the melting, and the sublimation curves of the pure components, the type C is characterized by the following loci:

- Two separate critical lines, the first one originates at the critical point of the component 2 (heaviest compounds) and ends at the lower Critical End-Point (LCEP), the second one originates at the critical point of the component 1 (lightest compound) and ends at the Upper Critical End-Point (UCEP).
- A quadruple point corresponding to a $Solid_1$-$Solid_2$-Liquid-Vapor Equilibrium (S_1S_2LVE). The existence of this quadruple point is due to the considering of the total or partial immiscibility of the components 1 and 2 in the solid phases.
- A three-phase $Solid_2$-LiquidVapor Equilibrium (S_2LVE) line originating at the triple point of the component 2 and ending at the quadruple point (S_1S_2LVE).
- A three-phase $Liquid_1$(component1 rich liquid)-$Liquid_2$($component_2$ rich liquid)-Vapor Equilibrium (L_1L_2VE) line originating at the lower critical end-point and ending at the upper critical end-point.
- A three-phase $Solid_1$-Liquid-Vapor Equilibrium (S_1LVE) line originating at the triple point of the component 1 and ending at the colder quadruple point (S_1S_2LVE).

- A three-phase Solid$_1$-Solid$_2$-Vapor Equilibrium (S_1S_2VE) line originating at the colder quadruple point (S_1S_2LVE) and developing in the low-temperature-low-pressure region.
- A three-phase Solid$_1$-Solid$_2$-Liquid Equilibrium (S_1S_2LE) line originating at the colder quadruple point (S_1S_2LVE) and developing in the high-pressure region.

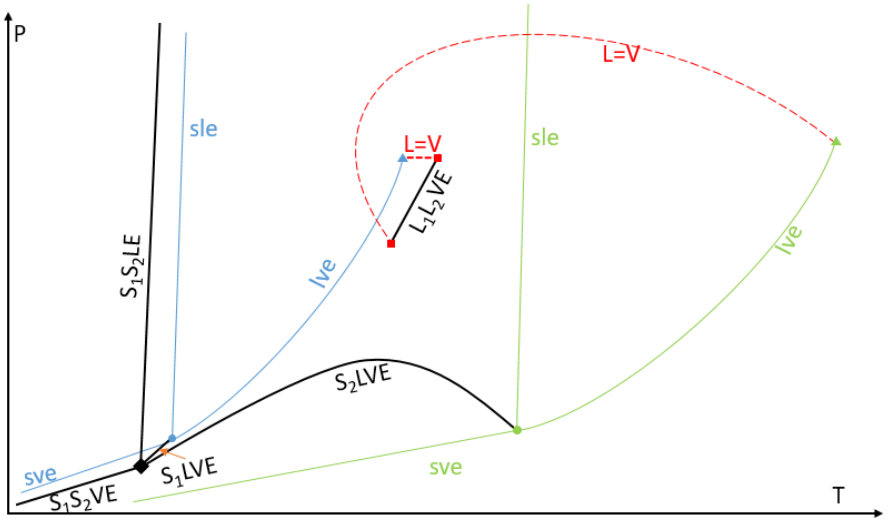

Figure 2.11: qualitative P-T diagram of a binary system having a global phase diagram of type C

2.5.4 Type D phase diagram

The qualitative pressure-temperature diagram for type D reported by Kohn and Luks is shown in Fig2.12; considering only the fluid phases, this type of phase diagram corresponds to the type I according to the classification of the van Konynenburg and Scott.

Besides the saturation, the melting, and the sublimation curves of the pure components, the type C is characterized by the following loci:

- A continuous critical line relating the critical points of the component 1 and 2.
- A quadruple point corresponding to a Solid$_1$-Solid$_2$-Liquid-Vapor Equilibrium (S_1S_2LVE). The existence of this quadruple point is due to the considering of the total or partial immiscibility of the components 1 and 2 in the solid phases.
- A three-phase Solid$_2$-Liquid-Vapor Equilibrium (S_2LVE) line originating at the triple point of the component 2 and ending at the quadruple point (S_1S_2LVE).
- A three-phase Solid$_1$-Liquid-Vapor Equilibrium (S_1LVE) line originating at the triple point of the component 1 and ending at the colder quadruple point (S_1S_2LVE).

- A three-phase Solid$_1$-Solid$_2$-Vapor Equilibrium (S_1S_2VE) line originating at the colder quadruple point (S_1S_2LVE) and developing in the low-temperature-low-pressure region.
- A three-phase Solid$_1$-Solid$_2$-Liquid Equilibrium (S_1S_2LE) line originating at the colder quadruple point (S_1S_2LVE) and developing in the high-pressure region.

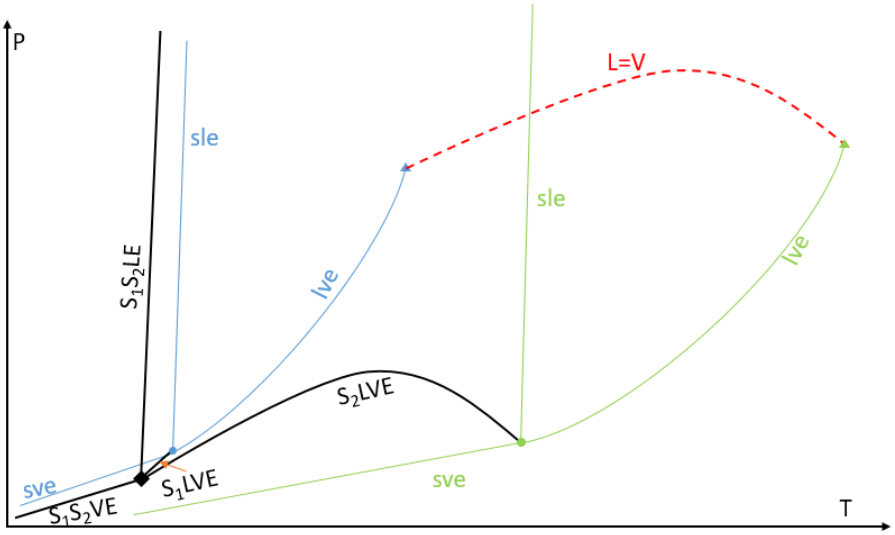

Figure 2.12: qualitative P-T diagram of binary system having a global phase diagram of type D

References

[1] C. Song, Q. Liu, S. Deng, H. Li, Y. Kitamura, Cryogenic-based CO_2 capture technologies: State-of-the-art developments and current challenges, Renewable and Sustainable Energy Reviews, vol. 101, 265-278, 2019.

[2] M. J. Tuinier, M. van Sint Annaland, G. J. Kramer, J. A. M. Kuipers, Cryogenic CO_2 capture using dynamically operated packed beds, Chemical Engineering Science, vol. 65, N°1, 114-119, 2010.

[3] M. Jensen, Energy Process Enabled by Cryogenic Carbon Capture.

[4] X. Pan, D. Clodic, J. Toubassy, CO_2 capture by antisublimation process and its technical economic analysis, Greenhouse Gas Sci Technol, vol. 3, N°1, 8-20, 2013.

[5] A. S. Holmes J. M. Ryan, cryogenc distillative separation of acid gases from methane.

[6] E. R. Thomas R. D. Denton, Conceptual studies for CO_2/natural gas separation using the controlled freeze zone (CFZ) process, Gas Separation & Purification, vol. 2, N°2, 84-89, 1988.

[7] A. Hart N. Gnanendran, Cryogenic CO_2 capture in natural gas, Energy Procedia, vol. 1, N°1, 697-706, 2009.

[8] C.-F. Song, Y. Kitamura, S.-H. Li, K. Ogasawara, Design of a cryogenic CO_2 capture system based on Stirling coolers, International Journal of Greenhouse Gas Control, vol. 7, p. 107-114, mars 2012.

[9] R. H. Brown, J. P. Lebreton, J. H. Waite, Éd., Titan from Cassini-Huygens. Dordrecht Heidelberg: Springer, 2009.

[10] V. De Stefani, A. Baba-Ahmed, D. Richon, A review of experimental methods for solid solubility determination in cryogenic systems, Cryogenics, vol. 44, N°9, 631-641, 2004.

[11] A. Siahvashi, S. Z. S. Al-Ghafri, J. H. Oakley, T. J. Hughes, B. F. Graham, E. F. May, Visual Measurements of Solid–Liquid Equilibria and Induction Times for Cyclohexane + Octadecane Mixtures at Pressures to 5 MPa, J. Chem. Eng. Data, vol. 62, N° 9, 2896-2910, 2017.

[12] G. T. Hefter R. P. T. Tomkins, The experimental determination of solubilities, Wiley, 2003.

[13] J. P. Kohn F. Kurata, Heterogeneous phase equilibria of the methane-hydrogen sulfide system, AIChE J, vol. 4, N°2, 211-217, 1958.

[14] J. P. Kohn, Heterogeneous phase and volumetric behavior of the methanen-heptane system at low temperatures, AIChE J, vol. 7, N°3, 514-518, 1961.

[15] J. P. Kohn W. F. Bradish, Multiphase and Volumetric Equilibria of the Methane- n -Octane System at Temperatures between -110°C and 150°C, J. Chem. Eng. Data, vol. 9, N°1, 5-8, 1964.

[16] J. P. Kohn and K. D. Luks, Solubility of hydrocarbons in cryogenic LNG and NGL mixtures, GPA R- 22 76, 1976.

[17] K. H. Lee J. P. Kohn, Heterogeneous phase equilibrium in the ethane-n-dodecane system, J. Chem. Eng. Data, vol. 14, N°3, 292-295, 1969.

[18] F. Kurata, Solubility of heavier hydrocarbons in liquid methane, GPA RR-14, 1975.

[19] A. Jakob, R. Joh, C. Rose, J. Gmehling, Solid-liquid equilibria in binary mixtures of organic compounds, Fluid Phase Equilibria, vol. 113, N°1-2, 117-126, 1995.

[20] G. M. Agrawal R. J. Laverman, Phase Behavior of the Methane-Carbon Dioxide System in the Solid-Vapor Region, in Advances in Cryogenic Engineering, K. D. Timmerhaus, Éd. Boston, MA: Springer US, 1995, 327-338.

[21] A. Siahvashi, S. ZS. Al Ghafri, E. F. May, Solid-fluid equilibrium measurements of benzene in methane and implications for freeze-out at LNG conditions, Fluid Phase Equilibria, vol. 519, 2020.

[22] F. J. Verónico-Sánchez, O. Elizalde-Solis, A. Zúñiga-Moreno, L. E. Camacho-Camacho, C. Bouchot, Experimental Procedure for Measuring Solid–Liquid–Gas Equilibrium in Carbon Dioxide + Solute, J. Chem. Eng. Data, vol. 61, N°10, 3448-3456, 2016.

[23] L. F. S. Souza, S. Z. S. Al Ghafri, O. Fandiño, M. Trusler, Vapor-liquid equilibria, solid-vapor-liquid equilibria and H2S partition coefficient in (CO2 + CH4) at temperatures between (203.96 and 303.15) K at pressures up to 9 MPa, Fluid Phase Equilibria, vol. 522, 2020.

[24] C. A. McConville al., Peritectic phase transition of benzene and acetonitrile into a cocrystal relevant to Titan, Saturn's moon, Chem. Commun., vol. 56, N°88, 13520-13523, 2020.

[25] X. Wang, Y. Zhao, X.g Dong, X. Yao, J. Wang, H. Gu, M. Gong, Investigation on solid-liquid equilibrium for trifluoromethane (R23) plus difluoromethane (R32) binary system, International Journal of Refrigeration, vol. 126, 238-245, 2021.

[26] A. Baba-Ahmed, P. Guilbot, D. Richon, New equipment using a static analytic method for the study of vapour–liquid equilibria at temperatures down to 77 K, Fluid Phase Equilibria, vol. 166, N°2, 225-236, 1999.

[27] V. De Stefani, A. Baba-Ahmed, A. Valtz, D. Meneses, D. Richon, Solubility measurements for carbon dioxide and nitrous oxide in liquid oxygen at temperatures down to 90 K, Fluid Phase Equilibria, vol. 200, N°1, 19-30, 2002.

[28] V. De Stefani, A. Baba-Ahmed, D. Richon, Experimental determination of carbon dioxide and nitrous oxide co-solubility in liquid oxygen, Fluid Phase Equilibria, vol. 207, N°1-2, 131-142, 2003.

[29] D. Houssin-Agbomson, C. Coquelet, P. Arpentinier, F. Delcorso, D. Richon, Equilibrium Data for the Oxygen + Propane Binary System at Temperatures of (110.22, 120.13, 130.58, and 139.95) K, J. Chem. Eng. Data, vol. 55, N°10, 4412-4415, 2010.

[30] D. Houssin-Agbomson, C. Coquelet, D. Richon, P. Arpentinier, Equipment using a "static-analytic" method for solubility measurements in potentially hazardous binary mixtures under cryogenic temperatures, Cryogenics, vol. 50, N°4, 248-256, 2010.

[31] P. Stringari, P. Theveneau, C. Coquelet, G. Lauermann, Solubility measurements of solid n-hexane in liquid methane at cryogenic temperature.

[32] S. Langé, L. A. Pellegrini, P. Stringari, C. Coquelet, Experimental determination of the solid-liquid-vapor locus for the CH_4-CO_2-H_2S system and application to the design of a new low-temperature distillation process for the purification of natural gas.

[33] S. Langè, M. Campestrini, P. Stringari, Phase behavior of system methane + hydrogen sulfide, AIChE J, vol. 62, N°11, 4090-4108, 2016.

[34] M. Riva P. Stringari, Experimental Study of the Influence of Nitrogen and Oxygen on the Solubility of Solid Carbon Dioxide in Liquid and Vapor Methane at Low Temperature, Ind. Eng. Chem. Res., vol. 57, N°11, 4124-4131, 2018.

[35] H. Diez-y-Riega, D. Camejo, A. E. Rodriguez, C. E. Manzanares, Unsaturated hydrocarbons in the lakes of Titan: Benzene solubility in liquid ethane and methane at cryogenic temperatures, Planetary and Space Science, vol. 99, 28-35, 2014.

[36] G. P. Kuebler, C. McKinley, Solubility of solid n-Butane and n-Pentane in liquid Methane, Adv. Cryog. Eng., 21, 509-515, 1976.

[37] G. P. Kuebler, C. McKinley, Solubility of Solid Benzene, Toluene, n-Hexane, and n-Heptane in Liquid Methane, in Advances in Cryogenic Engineering, K. D. Timmerhaus, Éd. Boston, MA: Springer US, 320-326, 1995.

[38] G. P. Kuebler, C. McKinley, Solubility of solid tert-butylmercaptan in liquid methane and an LNG mixture, 1980.

[39] G. L. Baughman, S. P. Westhoff, S. Dincer, D. D. Duston, A. J. Kidnay, The solid + vapor phase equilibrium and the interaction second virial coefficients for argon +, nitrogen +, methane +, and helium + neopentane I. Experimental, The Journal of Chemical Thermodynamics, vol. 6, N°12, 1121-1132, 1974.

[40] E.W. Lemmon, I.H. Bell, M.L. Huber, M.O. McLinden, NIST Standard Reference Database 23, Reference Fluid Thermodynamic and Transport Properties - REFPROP, DLL version number Version 10.0, Applied Chemicals and Materials Division, 2018.

[41] J. A. Davis, N. Rodewald, F. Kurata, Solid-liquid-vapor phase behavior of the methane-carbon dioxide system, AIChE J, vol. 8, N°4, 537-539,1962.

[42] H. G. Donnelly D. L. Katz, Phase Equilibria in the Carbon Dioxide–Methane System, Ind. Eng. Chem., vol. 46, N°3, 511-517, 1954.

[43] Fred. Kurata K. Un. Im, Phase equilibrium of carbon dioxide and light paraffins in presence of solid carbon dioxide, J. Chem. Eng. Data, vol. 16, N°3, 295-299, 1971.

[44] T. Shen, T. Gao, W. Lin, A. Gu, Determination of CO_2 Solubility in Saturated Liquid CH_4+N_2 and CH_4+C_2H_6 Mixtures above Atmospheric Pressure, J. Chem. Eng. Data, vol. 57, N°8, 2296-2303, 2012.

[45] T. T. Le M. A. Trebble, Measurement of Carbon Dioxide Freezing in Mixtures of Methane, Ethane, and Nitrogen in the Solid−Vapor Equilibrium Region, J. Chem. Eng. Data, vol. 52, N°3, 683-686, 2007.

[46] Pikaar, M. J., A Study of Phase Equilibria in Hydrocarbon−CO2 System, Ph.D. Thesis, University of London, London, 1959.

[47] Sterner, C. J., Phase Equilibria in the CO_2-Methane Systems, 467-474, 1964.

[48] L. Zhang, R. Burgass, A. Chapoy, B. Tohidi, E. Solbraa, Measurement and Modeling of CO_2 Frost Points in the CO_2-Methane Systems, J. Chem. Eng. Data, vol. 56,N° 6, 2971-2975, 2011.

[49] Mraw S.C.; Hwang S.-C.; Kobayashi R, The Vapor-Liquid Equilibrium of the CH_4-CO_2 System at Low Temperatures. GPA Research Rep, 1-18, 1977.

[50] Boyle, G. J., Shell Res. LTD., Thornton Res. Centre, 1987.

[51] Brady C.J.; Cunningham J. R.; Wilson G.M., 1982, GPA RR-62.

[52] J. Brewer F. Kurata, Freezing points of binary mixtures of methane, AIChE J., vol. 4, N°3, 317-318, 1958.

[53] Chang HL.; Kobayashi R. J., Chem. Eng. Data, 1967, 12(4), 517.

[54] Cheung H Zander EH, Solubility of carbon dioxide and hydrogen sulfide in liquid hydrocarbons at cryogenic temperatures, Chem Eng Progress Symp, Series 88.

[55] T. Gao, T. Shen, W. Lin, A. Gu, Y. Ju, Experimental Determination of CO_2 Solubility in Liquid CH_4/N_2 Mixtures at Cryogenic Temperatures, Ind. Eng. Chem. Res., vol. 51, N°27, 9403-9408, 2012.

[56] Sparks K.A.; Sloan E. D., 1983, GPA RR-71.

[57] Streich, M., "N2 Removal from Natural Gas", Hydrocarbon Process, 49, 86-88 ?1970.

[58] Voss, G., Ph.D. Thesis, Technical University of Berlin, Berlin, Germany, 1975.

[59] G. T. Preston, E. W. Funk, J. M. Prausnitz, Solubilities of hydrocarbons and carbon dioxide in liquid methane and in liquid argon, J. Phys. Chem., vol. 75, N°15, 2345-2352, 1971.

[60] Beck L.A., Solubility, density, and freezing point data for solutions of methane in n-hexane, MS Thesis, University of Kansas, 1956.

[61] Teller M., Diss TU Berlin, 1982, as reported in Solid-liquid equilibrium data collection, vol VIII, Knapp H.; Teller, M.; Langhorst R., ed DECHEMA Chemistry data series, DECHEMA 1985.

[62] Morlet J, Morlet J., Rev. Inst. Fr. Pet., 127-143, 1963, Rev. Inst. Fr. Pet., 127-143, 1963.

[63] R. Scott, Solid-Liquid Phase Equilibria in the Mixtures Methane+n-Hexane and Methane+n-Pentane.

[64] Neumann A.; Mann R.; Kaeltetech. Klim. 1970, 6, 182-184.

[65] K.D. Lucks, J.D. Hottovy, J.P. Kohn, Three phase solid-liquid-vapor equilibriums in the binary hydrocarbon systems methane-hexane and methane-benzene, Journal of Chemical and Engineering data, 1981.

[66] J. Shim J. P. Kohn, Multiphase and Volumetric Equilibria of Methane-n-Hexane Binary System at Temperatures Between -110°C and -150°C., J. Chem. Eng. Data, vol. 7, N°1, 3-8,1962.

[67] D. L. Tiffin, K. D. Luks, J. P. Kohn, Solubility Enhancement of Solid Hydrocarbons in Liquid Methane due to the Presence of Ethane, in Advances in Cryogenic Engineering, K. D. Timmerhaus, Éd. Boston, MA: Springer US, 538-543, 1978.

[68] J. P. Kohn, K. D. Luks, P. H. Liu, D. L. Tiffin, Three-phase Solid-Liquid-Vapor Equilibria of the Binary Hydrocarbon Systems Methane-n-Octane and Methane-Cyclohexane.

[69] Papahronis, B.T., Solubility, volumetric and freezing point data for mixtures of methane in n-octane, MS Thesis, University of Kansas, 1954.

[70] Neumann A.; Mann R.; Von Szalghary W.-D., Kaeltetech. Klim. 1972, 24, 143-149.

[71] Teller M., Knapp H., 1985, as reported in Solid-liquid equilibrium data collection, vol VIII, Knapp H.; Teller, M.; Langhorst R., ed DECHEMA Chemistry data series,.

[72] A. Siahvashi, S. ZS. Al Ghafri, T. J. Hughes, B. F. Graham, S. H. Huang, E. F. May, Solubility of p-xylene in methane and ethane and implications for freeze-out at LNG conditions, Experimental Thermal and Fluid Science, vol. 105, 47-57, 2019.

[73] M. P. W. M. RijkersM. MalaisJ. de Swaan Arons, Experimental determination of the phase behavior of binary mixtures of methane + benzene: Part I. Vapor + liquid, solid benzene + liquid, solid benzene + vapor and solid benzene + liquid + vapor equilibria, Fluid Phase Equilibria, 327-342, 1992.

[74] T. J. Hughes, M. E. Kandil, B. F. Graham, K. N. Marsh, S. H. Huang, E. F. May, Phase equilibrium measurements of (methane + benzene) and (methane + methylbenzene) at temperatures from (188 to 348) K and pressures to 13 MPa, The Journal of Chemical Thermodynamics, vol. 85, 141-147, 2015.

[75] J. P. Kohn, D. Luks, P. H. Liu, Three-phase Solid-Liquid-Vapor Equilibria of Binary-n-Alkane Systems (Ethane-n-Octane, Ethane-n-Decane, Ethane+n-Dodecane).

[76] P. H. Liu, K. D. Luks, J. P. Kohn, Three-phase solid-liquid-vapor equilibria of the systems ethane-benzene, ethane-cyclohexane, and ethane-trans-decalin, J. Chem. Eng. Data, vol. 22, N°2, 220-221, 1977.

[77] R. H. Jensen F. Kurata, Heterogeneous phase behavior of solid carbon dioxide in light hydrocarbons at cryogenic temperatures, AIChE J., vol. 17, N°2, 357-364, 1971.

[78] W.-U. Chen K. D. Luks, Three-phase Sotid-Liquid-Vapor Equilibria of the Binary Hydrocarbon Systems Propane-Benzene, Propane-Cyclohexane, n-Butane-Benzene, n-ButaneCyclohexane, n-Butane-n-Decane, and n-Butane-n-Dodecane.

[79] Neumann A; Schippler B; Chem. Ing. Tech. 50, 1978.

[80] Teller M., Knapp H., cryogenics; 1984 471-476; *as reported in Solid-liquid equilibrium data collection, vol VIII, Knapp H.; Teller, M.; Langhorst R., ed DECHEMA Chemistry data series.*

[81] E. Szczepaniec-Cieciak, V. A. Kondaurov, S. M. Melikova, Study on the solubility light alkanes in liquid nitrogen, Cryogenics, vol. 20, N°1, 48-51, 1980.

[82] E. Szczepaniec-Cieciak, M. Krzeczkowska, L. Ulman, K. Nagraba, Solubility of pentane, 2-methylbutane, and cyclopentane in liquid nitrogen at 77.4 K, J Solution Chem, vol. 23, N°4, 501-509, 1994.

[83] E. Szczepaniec-Cieciak, M. Kurdziel, L. Ulman, Solubility of hex-1-ene, hexane and cyclohexane in liquid nitrogen, J. Chem. Soc., Faraday Trans. 1, vol. 85, N°9, 2695, 1989.

[84] N. P. Yakimenko, M. B. Glukh Iomtev, R. I. Abramova, Solubility of Solid Carbon Dioxide in Liquid Nitrogen. Russ.J.Phys.Chem, vol 49,116-117, 1975.

[85] R. E. Sonntag, G. J. Van Wylen, The solid-vapor equilibrium of carbon dioxide-nitrogen, Adv. Cryog. Eng, 7, 99-105, 1962.

[86] R. E. Sonntag, G. J. Van Wylen, Solid-vapor equilibrium of the carbon dioxide-nitrogen system at pressures to 200 atmospheres, Adv. Cryog. Eng, 9, 197-206, 1963.

[87] J. M. Prausnitz, R. N. Lichtenthaler, E. G. de Azevedo, Molecular thermodynamics of fluid-phase equilibria, 3. ed. Upper Saddle River, NJ: Prentice-Hall PTR, 1999.

[88] G. T. Preston J. M. Prausnitz, Thermodynamics of Solid Solubility in Cryogenic Solvents, Ind. Eng. Chem. Proc. Des. Dev, vol. 9, N°2, 264-271, 1970.

[89] G. S. Soave, Application of the redlich-kwong-soave equation of state to solid-liquid equilibria calculations, Chemical Engineering Science, vol. 34, N°2, 225-229, 1979.

[90] D. C. Garcia K. D. Luks, Patterns of solid–fluid phase equilibria: new possibilities? Fluid Phase Equilibria, vol. 161, N°1, 91-106, 1999.

[91] S. B. Rodriguez-Reartes, M. Cismondi, M. S. Zabaloy, Computation of solid–fluid–fluid equilibria for binary asymmetric mixtures in wide ranges of conditions, The Journal of Supercritical Fluids, vol. 57, N°1, 9-24, 2011.

[92] N. G. Tassin, S. B. Rodríguez Reartes, M. S. Zabaloy, M. Cismondi, Modeling of solid-fluid equilibria of pure n-alkanes and binary methane + n-alkane systems through predictive correlations, The Journal of Supercritical Fluids, vol. 166, 2020.

[93] M. Campestrini P. Stringari, Solubilities of solid n-alkanes in methane: Data analysis and models assessment, AIChE J, vol. 64, N°6, 2219-2239, 2018.

[94] C. Baker al., Advanced predictions of solidification in cryogenic natural gas and LNG processing, The Journal of Chemical Thermodynamics, vol. 137, 22-33, 2019.

[95] J.-C. de Hemptinne, Benzene crystallization risks in the LIQUEFIN liquefied natural gas process, Proc. Safety prog., vol. 24, N°3, 203-212, 2005.

[96] K. Carter K. D. Luks, Extending a classical EOS correlation to represent solid–fluid phase equilibria, Fluid Phase Equilibria, vol. 243, N°1-2, 151-155, 2006.

[97] P.H. van Konynenburg, R.L. Scott, Critical lines and phase equilibria in binary van der Waals mixtures, Phil. Trans. R. Soc. Lond. A, vol. 298, N°1442, 495-540, 1980.

Chapter 3:

Low-temperature measurements

Résumé du chapitre 3 en français

Trois appareillages différents ont été utilisé dans cette thèse et présenté dans ce chapitre ; ces appareillages permettent d'étudier les équilibres de phase solide-fluide et fluide-fluide à basse-température. Deux appareillages utilisent l'azote liquide comme réfrigérant et permettent de travailler à des températures allant de la température ambiante jusqu'à 77 K. Le troisième appareillage utilise un bain d'éthanol liquide et permet de travailler à des températures allant de la température ambiante jusqu'à 173 K. Les mesures expérimentales réalisées en utilisant ces trois appareillages ont fait appel à deux méthodes expérimentales différentes : la méthode statique-analytique et la méthode synthétique-indirecte.

La méthode statique-analytique a été utilisé pour mesurer les limites de solubilité du benzène, ethylbenzène, p-xylène, m-xylène, et o-xylène dans le méthane à 3 et 6 MPa. L'influence de la présence de l'éthane ou de l'azote sur la solubilité de benzène et du p-xylène dans le méthane a été aussi évalué en utilisant cette méthode. Cette étude a permis de fournir des informations cruciales qui permettent d'optimiser les procédés de purification de liquéfaction du gaz naturel ; ceci permettra d'éviter le surdimensionnement ou le sous-dimensionnement des unités de purification.

La solubilité du tétrahydrothiophène (THT) dans le méthane liquide a également été mesurée à 3 et 6 MPa en utilisant la méthode statique-analytique. Le THT est ajouté avant l'injection du gaz naturel dans le réseau de distribution français pour donner une odeur particulière au gaz pour faciliter la détection d'éventuelles fuites. La connaissance des limites de solubilité du THT dans le méthane est primordiale pour l'évaluation de son risque de cristallisation lors d'éventuelle production du GNL à partir du gaz du réseau.

Une étude approfondie des équilibres de phases à basse température du système méthane+néopentane a été menée dans cette thèse en utilisant la méthode statique-analytique et la méthode synthétique-indirect. Les équilibres solide-liquide ont été mesurés à des températures allant de 99 K à 163 K et à des pressions allant jusqu'à 6 MPa. De plus, la courbe d'équilibre solide-liquide-vapeur a été étudié à partir de la température du point triple du néopentane (256,5 K) jusqu'à 144 K. En plus de ces mesures expérimentales en présence de phase solide, les équilibres liquide-vapeur à plusieurs isothermes ont été réalisé pour compléter la compréhension du comportement thermodynamique global de ce système.

3 Low-temperature measurements

Among others research field, the laboratory "Center of Thermodynamics of Processes" (Laboratory where I done my PhD) has been developing an exciting research activity aiming at studying and understanding the low-temperature phase equilibria, especially those involving molecular solid phases. Since the end of the 90's, this has led several industrial and academic collaborations. Among these collaborations, a Joint Industry Project (JIP) founded by Engie, Shell, and Linde was launched in 2018 for the investigation of the crystallization risk in LNG production; this thesis is a part of this project.

The deep bibliographic research performed in this thesis has allowed the identification of several systems that have not been investigated yet in the literature or for which the existing data are scarce or inconsistent. To tackle this lack of knowledge, several experimental campaigns have been performed to produce original data and investigate the Solid-Fluid Equilibrium (SFE) of some systems of interest. In the context of this thesis, the solubility limits of benzene, ethylbenzene, m-xylene, o-xylene, p-xylene, tetrahydrothiophene and neopentane in methane have been measured; in addition, the effect of the presence of some ethane or nitrogen on the solubility limits of benzene, p-xylene and neopentane in methane has been evaluated.

Seeing that this thesis was carried out in a framework of a project sponsored by industrial partners, most of the data measured during these three years are subject to confidentiality agreement and thus not disclosed here. However, a summary of all the investigated systems is given in Tab3.2. In addition, a detailed description and deep analysis of the low-temperature thermodynamic behavior of the methane+neopentane system is presented in section 3.6.

3.1 Apparatuses

Three different apparatuses have been used in this work for carrying out low-temperature solid-fluid and fluid-fluid equilibria. Two apparatuses (referred to as **apparatus1** and **apparatus2** in this manuscript) use liquid nitrogen as refrigerant and allow working at temperatures ranging from the room temperature down to 77 K. The third apparatus (referred to as **apparatus3** in this manuscript) uses a liquid ethanol bath and allows working at temperatures ranging from the room temperature down to 173 K (the use of another fluid allows working in a different temperature range).

3.1.1 Apparatuses using liquid nitrogen

The apparatus1 was developed and built at the CTP in the context of the thesis of Baba Ahmed in order to study the thermodynamic behavior of systems of interest for the cryogenic air separation [1]. Subsequently, this apparatus has been used for the measurement of the phase equilibria including solid phases; for instance, De Stefani et al. used this apparatus for measuring the solubility and the co-solubility of solid carbon dioxide

and nitrous oxide in liquid oxygen [2] [3]; the solubilities of solid n-hexane in liquid methane have been measured by Stringari and coworkers [4]; Langé et al. measured the SLVE locus of the methane+carbon dioxide+hydrogen sulfide system [5], and recently Riva and Stringari used this apparatus to study the influence of the presence of nitrogen and oxygen on the solubility of solid carbon dioxide in vapor and liquid methane [6]. The flow diagram of the apparatus1 is shown in Fig3.1.

The apparatus2 was built in 2017 (before the beginning of my thesis), and it has been conceived trying to provide some improvements compared to the old one. This apparatus has been validated by comparing original Solid-Liquid Equilibrium (SLE) values of methane+n-hexane system with those previously obtained with appatus1. The schematic flow diagram of the apparatus2 is shown in Fig3.2.

Even if the apparaus2 presents some improvements and modifications compared the apparatus1, the two apparatuses are similar with respect to the working principle. Given the similarities between the two apparatuses, a common description of both apparatuses is given in the following. Nevertheless, details concerning the differences between the two apparatuses are also provided.

Each apparatus consists of a Hastelloy Equilibrium Cell (EC) placed inside a Brass Shell (BS), which is surrounded by a Heating Resistance (HR); the HR is connected to a PID (Proportional, Integral, and Derivative) regulator. The brass shell together with the equilibrium cell are immersed in a Cryostat (Cr) filled partially with liquid nitrogen. The cryostat is at atmospheric pressure thanks to a nitrogen vapor vent (VN_2 vent) which avoids *(i)* the accumulation of the vapor nitrogen (generated by the evaporation of Liquid Nitrogen (LN_2) and moving upward in the Cr) around the EC and *(ii)* the resulting heating of this accumulating vapor nitrogen because of the heaters of the EC. As a result, the heat generated by the EC is permanently evacuated by the vented vapor nitrogen (VN_2 vent) which thus reduces the thermal stratification in the cryostat.

The EC of the appartus1 has a volume of 40cc; it is equipped with two platinum resistance thermometer Pt-100 probes placed on its top and bottom part, thus allowing the evaluation of the presence of eventual temperature gradient within the cell. The temperature probes are not in contact with the fluid inside the EC but placed in the body of the EC. The experimental temperature is obtained as the average of the values given by the two Pt-100 probes after calibration.

The EC of the apparatus2 has a volume of 48 cc; it is equipped with five platinum resistance thermometer Pt-100 probes (T1-T5). Four of them (T1-T4) are placed on the top and the bottom sides of the brass shell (as shown in Fig3.2, the probes are placed in the top-right, top-left, bottom-right, and bottom-left parts of the EC); this allows the quantification of an eventual vertical and radial temperature gradient. The last one

(T5) is placed directly inside the cell and is in permanent contact with the fluid within the EC. The experimental temperature is taken as the one given by the probe inside the EC after calibration.

The apparatus1 is equipped with one pressure transducer, Druck [0-16 MPa], maintained at a constant temperature of 323.15 K and connected to the EC using a tube with an inner diameter of 0.5 mm. The apparatus2 is equipped with two pressure transducers. The first one (P1), Keller [0-30MPa], is connected to the cell using a 0.2 mm tube, and placed inside a Teflon shell maintained at a constant temperature of 323.15 K. The second one (P2), Kulite [0-20MPa] is placed on the top flange of the EC without tubing.

It is interesting to point out that the presence of a temperature probe inside the EC and a pressure transducer directly on the upper flange of the EC is one of the main modifications and improvements of apparatus2 compared to apparatus1. The Kulite transducer is equipped with a membrane that is in direct contact with the fluid, thus allows measuring the pressure of the fluid without the need of a circuit relating the EC to an external pressure transducer; as a consequence, the dead volume is reduced and there is no risk of solid formation in the tubes and consequent blockage of the circuit. The temperature probe inside the cell (T5) is in direct contact with the fluid phase, thus allows measuring the temperature inside the EC and reduces the experimental temperature uncertainties; in addition, this sensor is more sensitive to the temperature changes occurring during the formation of the solid phase.

Each apparatus is equipped with a Data Acquisition Unit (DAU) allowing reading and recording the values measured by the temperature probes and the pressure transducers. Each DAU is connected to a computer and controlled using an appropriate software.

Two ROLSI® samplers (Rapid OnLine Sampler injector) [7] are placed on the upper flange of the EC of both apparatus1 and apparatus2 and allow withdrawing some µL of the fluid phase within the EC thanks to the 0.13mm capillary connecting each ROLSI® sampler to the EC. The two capillaries are of different length and allow taking samples at the bottom and the top of the EC, this allows the simultaneous evaluation of potential two different fluid phases within the EC (as in the case for instance of for Solid-Liquid-Vapor Equilibrium (SLVE) or Solid-Liquid-Liquid-Equilibrium (SLLE) conditions). Two separate heating resistances are placed on the capillaries in order to keep them at a temperature slightly higher than the one of the EC in order to avoid solid formation inside the capillaries. The samplers are equipped with a heating chamber allowing the vaporization of the samples. Carrier gas (Helium is used in this work) is continuously injected inside the transfer line that connects the ROLSI® to the separation column placed inside the oven of the Gas Chromatography (GC), and the GC detectors: Thermal Conductivity Detector (TCD) and Flame Ionization Detector (FID).

Two Loading Lines (LNs) are installed on the upper part of the EC of each apparatus and allow the feeding of the components involved in the mixture to be studied. The LNs are also connected to a vacuum pump that allows evacuating the EC before the loading of the mixture.

A stirring system is used to enhance the heat and the mass transfer within the equilibrium cell. The rotary movement generated by an external motor is transferred to a stirring bar (magnetic) placed inside the cell by means of a gear system and an external permanent magnet.

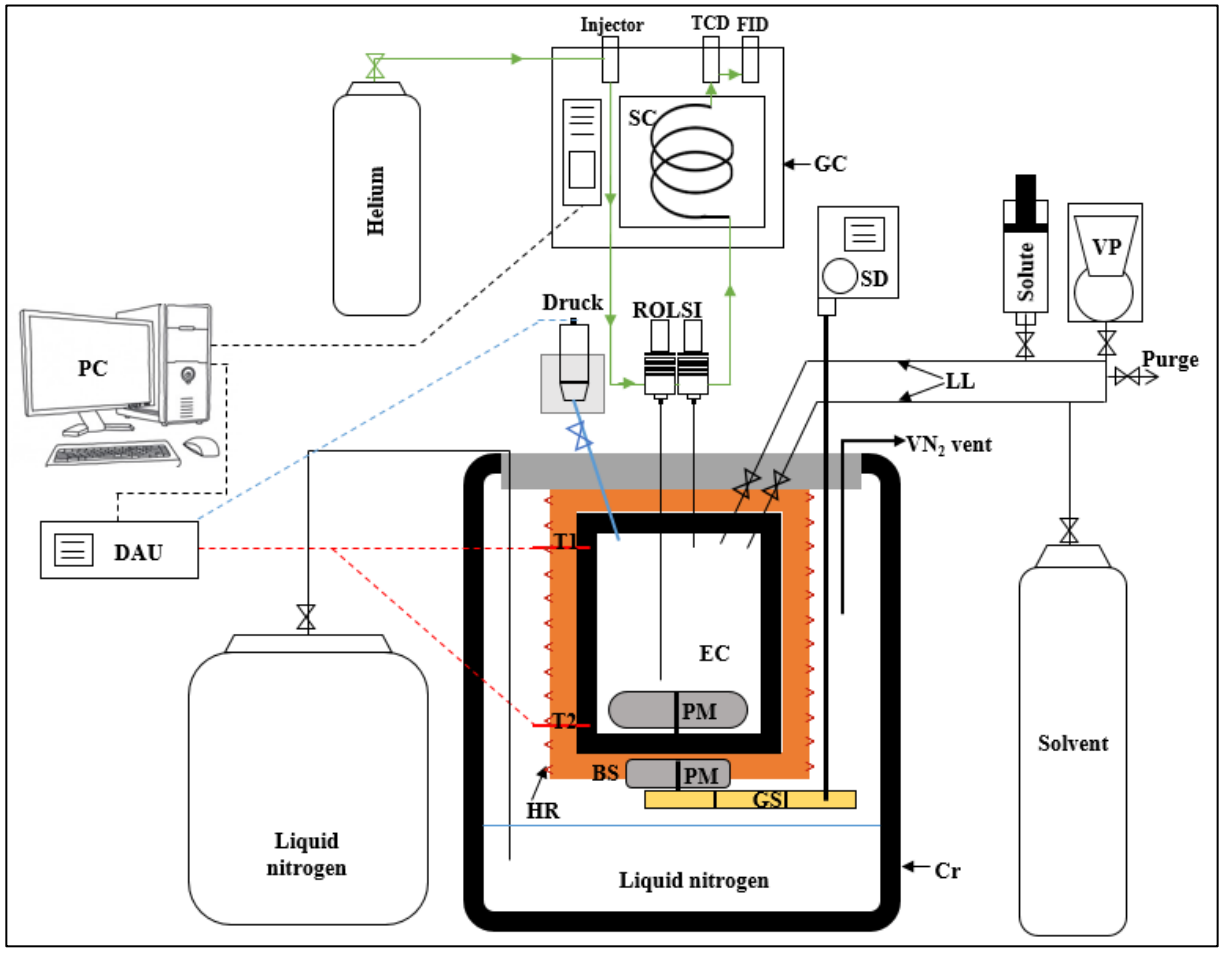

Figure 3.1: flow diagram of the apparatus1

BS: *brass shell,* ***Cr:*** *cryostat,* ***DAU:*** *data acquisition unit,* ***Druck:*** *pressure transducer, type Druck,* ***EC:*** *equilibrium cell,* ***FID:*** *flame ionization detector,* ***GC:*** *gas chromatograph,* ***GS:*** *gear system,* ***HR:*** *heating resistance,* ***LL:*** *loading lines,* ***PC:*** *personal computer,* ***PM:*** *permanent magnet,* ***ROLSI®:*** *rapid on-line sampler injector,* ***SD:*** *stirring device,* ***SC*** *separation column,* ***TCD:*** *thermal conductivity detector,* ***Ti:*** *temperature probes,* ***VP:*** *vacuum pump.*

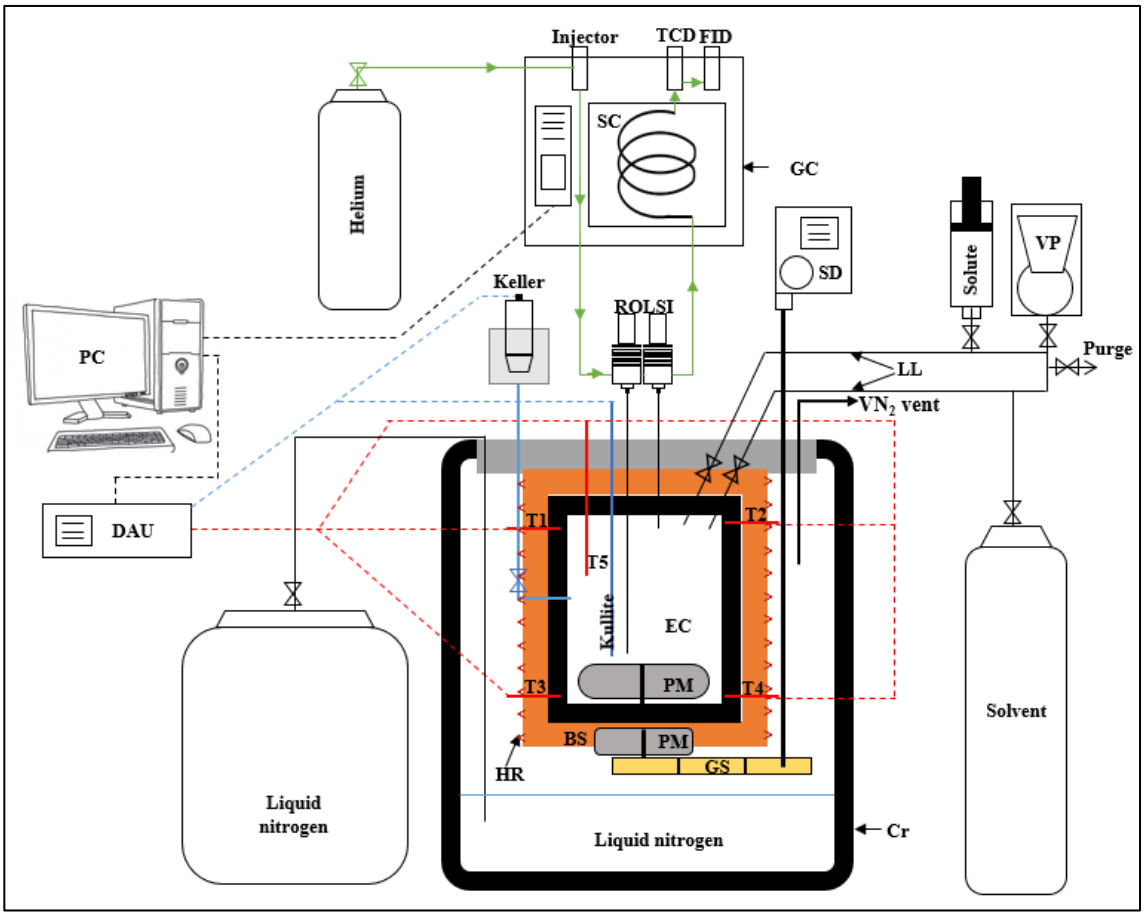

Figure 3.2: flow diagram of the apparatus2

BS: *brass shell,* ***Cr:*** *cryostat,* ***DAU:*** *data acquisition unit,* ***EC:*** *equilibrium cell,* ***FID:*** *flame ionization detector,* ***GC:*** *gas chromatograph,* ***GS:*** *gear system,* ***HR:*** *heating resistance,* ***Keller:*** *pressure transducer, type Keller,* ***Kullite:*** *pressure transducer, type Kullite,* ***LL:*** *loading lines,* ***PC:*** *personal computer,* ***PM:*** *permanent magnet,* ***ROLSI®:*** *rapid on-line sampler injector,* ***SD:*** *stirring device,* ***SC*** *separation column,* ***TCD:*** *thermal conductivity detector,* ***Ti:*** *temperature probes,* ***VP:*** *vacuum pump.*

3.1.2 Apparatus using liquid ethanol bath

The apparatus3 is similar to the one presented in ref [8] and uses the static-analytic method for the determination of the fluid composition. The flow diagram of apparatus3 is presented in Fig3.3.

The equilibrium cell (EC) is composed of a sapphire tube and two Hastelloy flanges and has a volume of 30 cc. The flanges are placed on the top and the bottom ends of the sapphire tube and screwed to each other. The EC is completely immersed in a thermo-regulated liquid bath (LB) maintained at constant temperature thanks to a temperature regulator. The bath is filled with liquid ethanol and allows working at temperatures from the room temperature down to 173 K (other liquids could be used to work at higher temperatures).

Two platinum resistance thermometers Pt-100 probes (T1 and T2) are placed in the top and the bottom flange respectively; this allows evaluating the eventual temperature gradient within the EC. The experimental temperature is taken as the average of the temperature of the two probes after calibration. The EC is equipped with two pressure transducers (PT) (Keller [0-5 MPa] and Keller [0-20 MPa]). Depending on the investigated pressure range, the corresponding pressure transducer is used for measuring the pressure of the system. These sensors are connected to a data acquisition unit for the pressure and temperature reading and recording.

Three loading lines (two placed on the top flange and one in the bottom flange) allow connecting the EC to the bottles containing the solvent and the solute, and the vacuum pump.

Two ROLSI® samplers are used for withdrawing samples of the fluids within the EC. Each ROLSI® is connected to the EC using a capillary allowing the sampling of the liquid or the vapor phase (capillaries of different length are used). The samples are vaporized in the heating chamber of the ROLSI® and transferred to the GC thanks to the carrier gas continuously circulating in the transfer line. A column placed inside the oven of the GC allows separating the components involved in the sample and then analyzed thanks to the TCD and FID.

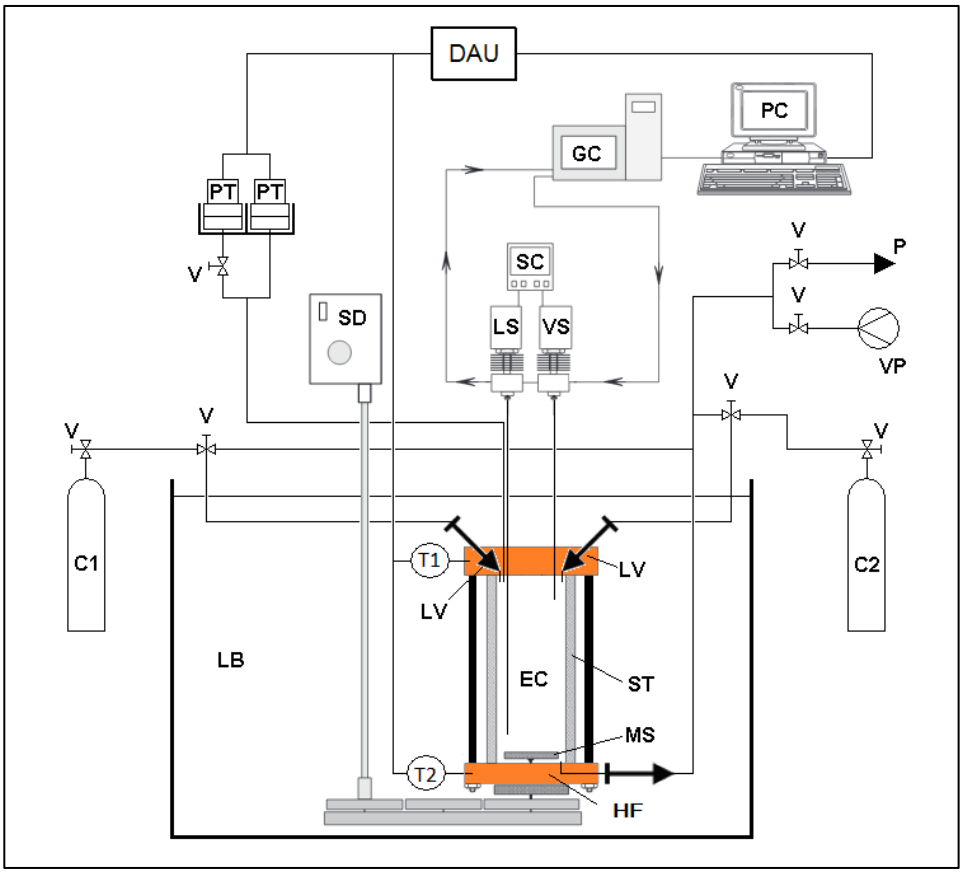

Figure 3.3: flow diagram of the apparatus3

***C1**: component1, **C2**: component2, **DAU**: data acquisition unit, **EC**: equilibrium cell, **GC**: gas chromatograph, **LB**: liquid bath, **LS**: liquid ROLSI® sampler, **VS**: vapor ROLSI® sampler, **LV**: loading valve, **MS**: magnetic stirrer; **P**: Purge, **PC**: personal computer, **PP**: platinum resistance thermometer probe, **PT**: pressure transducer, **SC**: sample controller, **SD**: stirring device, **ST**: sapphire tube, **TR**: temperature regulator, **HF**: Hastelloy flange, **V**: valve, **VP**: vacuum pump.*

3.2 Calibration

The calibration of the different sensors and detectors is one of the crucial steps when performing experimental works. Indeed, the temperature probes or the pressure transducers provide values that are usually slightly far from the real experimental values. Therefore, the use of correcting polynomials relating the recorded value to the real one is mandatory. The correcting polynomials are obtained by calibrating the different devices against standard equipment.

3.2.1 Temperature probes calibration

A 25 Ω reference platinum probe (Pt25, Hart Scientific, reference uncertainty u_{ref} = 8 mK) has been used for the calibration of the platinum resistance thermometer Pt-100 probes used in the apparatus1 and apparatus3. The reference platinum resistance thermometer was calibrated by the Laboratoire National

d'Essais de Paris following the ITS90 (1990 International Temperature Scale) protocol. The calibration of the temperature probes used in apparatus1 was made at 5 different temperatures (288.8, 273.8, 254.9, 217, and 77.4 K); the corresponding calibration polynomials (first order) are shown in Fig3.4a and Fig3.4b. The temperature probes used within the apparatus3 were calibrated at several temperatures using the liquid ethanol bath (the temperature probes together with the reference platinum resistance thermometer are immersed in the liquid ethanol bath); the calibration diagram of these probes is given in Fig3.5a and Fig3.5b.

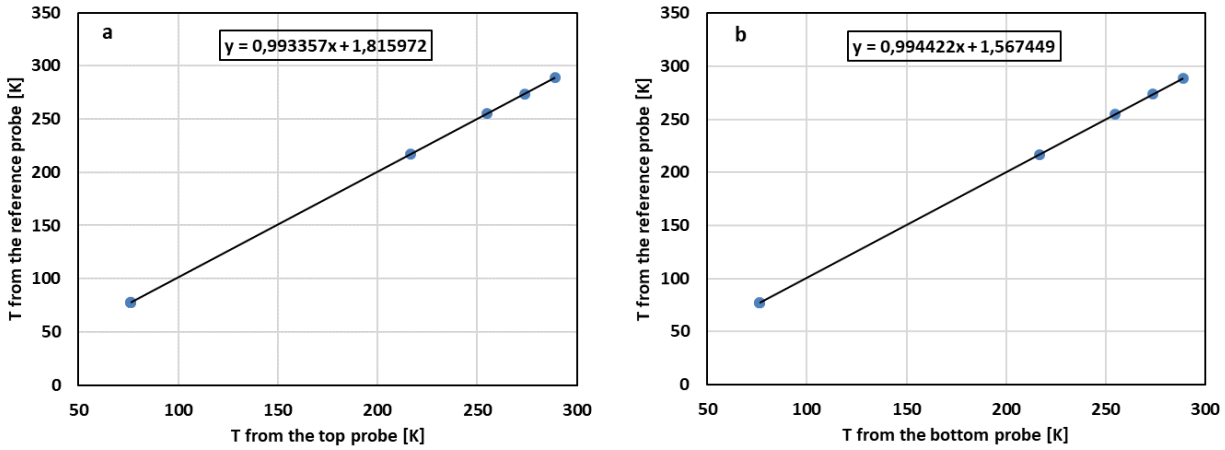

Figure 3.4: calibration diagram of the temperature probes used in the apparatus1

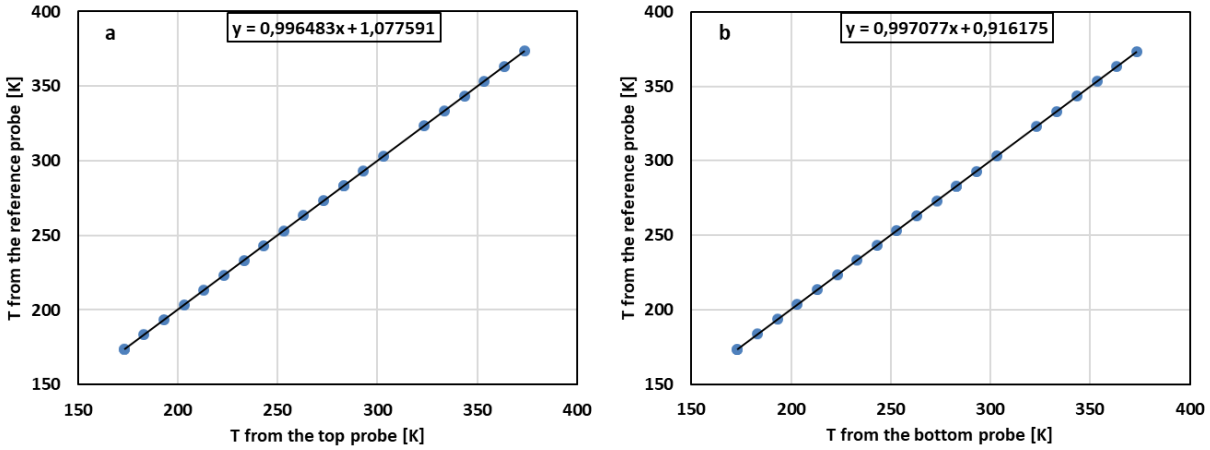

Figure 3.5: calibration diagram of the temperature probes used in the apparatus3

The five platinum resistance thermometer Pt-100 probes used within the apparatus2 have been calibrated by the "Laboratoire Commun de Metrologie LNE-CNAM" against a standard thermometer. Each temperature probe was calibrated at 5 temperatures, 273.15, 253.15, 233.15, 193.15, and 77.15 K. The calibration diagram and the corresponding polynomial of the temperature probe placed inside the EC (T5 in Fig3.2) is shown in Fig3.6. This probe is the one used for the experimental temperature measurements.

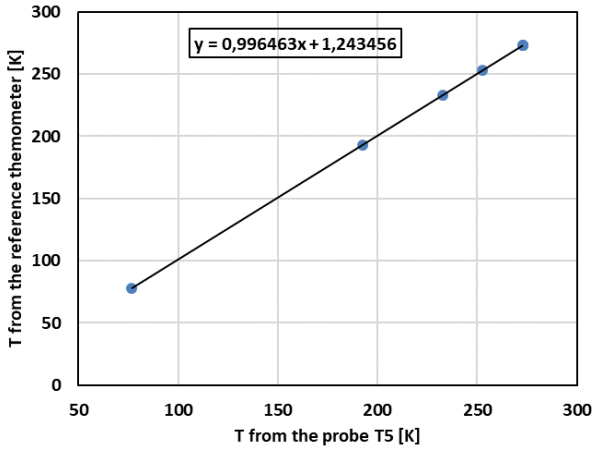

Figure 3.6: calibration diagram of the temperature probe (T5) placed inside the apparatus2

3.2.2 Pressure transducer calibration

All the pressure transducers used within the three apparatuses (the Druck of the apparatus1, the Keller and Kulite of the apparatus2, and the Keller [0-5 MPa] and [0-20 MPa] used within the apparatus3) have been calibrated using a PACE 5000 modular pressure controller (Desgranges & Huot, reference uncertainty u_{REF} = 0.09 kPa). The calibration diagram of these pressure transducers are given in Figs3.7-9

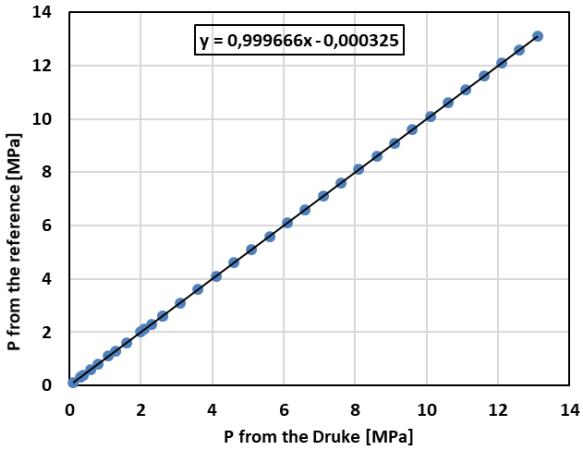

Figure 3.7: calibration diagram of the pressure transducer used in the apparatus1 (Druck)

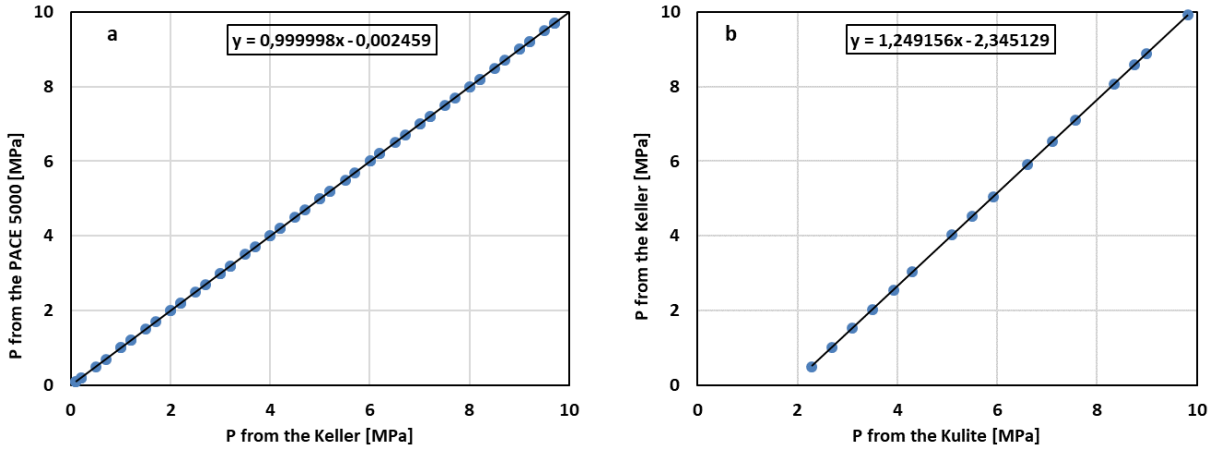

Figure 3.8: calibration diagram of the pressure transducer used in the apparatus2 (a = Keller, b = Kullite)

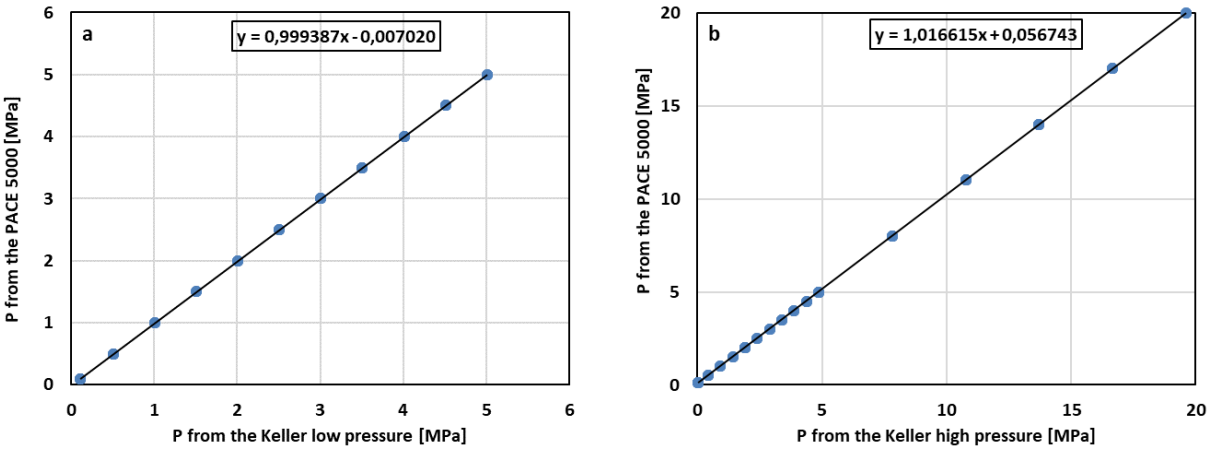

Figure 3.9: calibration diagram of the pressure transducer used in the apparatus3 a = low pressure (0 – 5 MPa) , b = high pressure (0 – 20 MPa)

3.2.3 GC detectors calibration

Each sample withdrawn from the EC is vaporized and transferred to the GC where the components involved in the sample are separated in the separation column placed inside the oven of the GC and transferred separately to the GC detectors (TCD and FID). When these components pass throughout the TCD or the FID, the signal emitted by this latter deviates from the baseline and forms a peak as shown in Fig3.10 (a typical GC analysis of binary system); the surface of each peak is representative of the amount of the corresponding component. The calibration of the response of the detectors allows relating the peak's surface to the mole number of the corresponding component. The detector's response is specific to the analyzed component, so the calibration is done separately for all the components involved in the mixture.

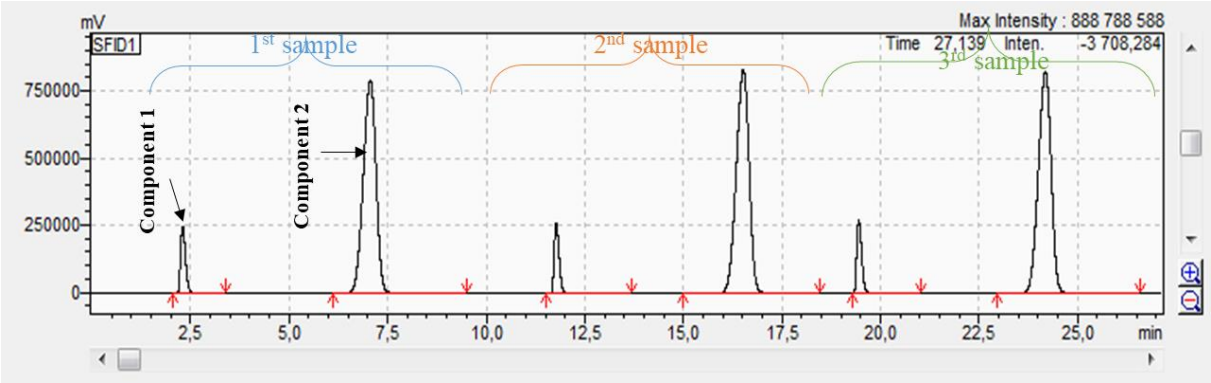

Figure 3.10: example of the signal emitted by the GC detector

For the calibration, a known volume (number of moles) of the given component is injected into the GC using a manual or an automatic syringe; this generates a peak having a surface that corresponds to the number of moles injected to the GC. Additional injections are carried out using different volumes until covering a large mole number range. In order to evaluate the repeatability of the injection, each volume is injected three/four times. The mole numbers (calculated starting from the density of the given component for liquids or assuming the ideal behavior in case of gases) are plotted as a function of the peak's surfaces and the calibration polynomial is then determined as the mathematical expression that relates the mole number to the pick's surface. The calibration diagrams of the TCD with methane and of the FID with o-xylene are shown in Fig3.11a and Fig3.11b respectively.

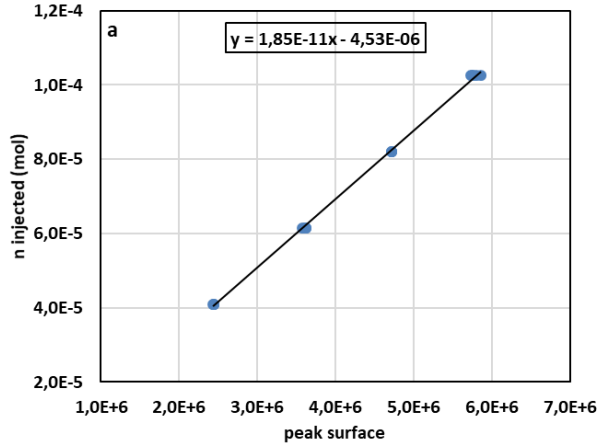

Figure 3.11a: calibration diagram of the TCD with methane

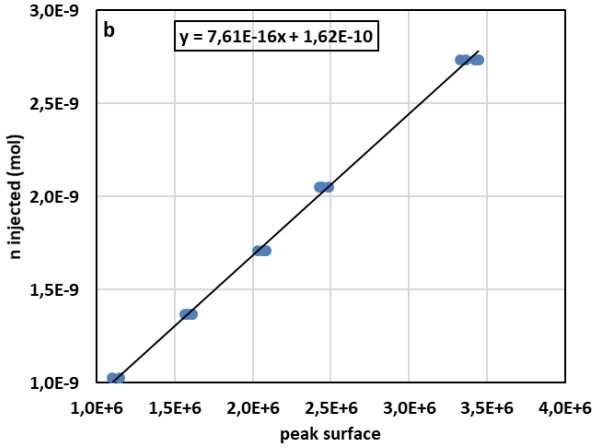

Figure 3.11b: calibration diagram of the FID with o-xylene

3.3 Uncertainty calculation

For any measured property "*M*", it is mandatory to associate the measured value to an interval taking into account the uncertainty affecting this property "*u(M)*".

$$M - u(M) < \boldsymbol{M} < M + u(M) \tag{3.1}$$

The uncertainty related to the experimental values is the result of combining all the sources of uncertainty affecting this experimental property. The combination formula is given in Eq3.2.

$$u(M)] = \sqrt{\sum_i [u_i(M)]^2} \tag{3.2}$$

To give more confidence to the reported experimental value, a coverage factor "*k*" is usually used. Without the coverage factor (*k* = 1), the degree of confidence of the measured value does not exceed 68.28%; however, the highest is the value of *"k"* the highest is the degree of confidence of the experimental measurement (for instance, 90% for *k*=1.645, 95.45 for *k*=2, 99% for k= 2.576, and 99.73% for *k*=3).

A coverage factor of 2 is used for the calculation of the uncertainty concerning the experimental points presented in this work.

$$U\ (M) = k * u(M) \tag{3.3}$$

3.3.1 Uncertainties on the experimental pressure and temperature

Three different sources of uncertainty affect the experimental pressure and temperature. The first one is given by the accuracy of the reference device used for the calibration of the measurement device *(u_{ref})*, the second one is related to the use of the calibration polynomial for correcting the read values *(u_{cal})*, and the last one is given by the repeatability of the recorded values since the experimental value is taken as the average of several records *(u_{rep})*.

The formula allowing the calculation of the uncertainty related to the experimental Pressure (M =P) or temperature (M = T) is given in Eq3.4.

$$u(M)] = \sqrt{[u_{ref}(M)]^2 + [u_{cal}(M)]^2 + [u_{rep}(M)]^2} \tag{3.4}$$

- ***Uncertainty related to the reference device (u_{ref}):***

  The platinum resistance thermometer Pt-100 probes used within apparatus1 and apparatus3 are calibrated against the 25 Ω reference platinum probe having a reference uncertainty u_{ref} (T) = 8 mK.

The platinum resistance thermometer Pt-100 probes used within the apparatus2 are calibrated using a standard thermometer with u_{ref}(T) = 5 mK. All the pressure transducers used in this work are calibrated using the PACE 5000 modular pressure controller (Desgranges & Huot) with u_{ref}(P) = 0.09 kPa. The reference uncertainties are summarized in the third column of Tab3.1.

- ***Uncertainty related to the calibration polynomial (u_{cal}):***

  This uncertainty is calculated assuming a rectangular dispersion of errors with a factor $\sqrt{3}$ as shown in Eq3.5, where b_M is the maximum absolute deviation between the reference value and the one calculated using the calibration polynomial. The maximum deviation (b_M) and the uncertainty related to the calibration (u_{cal}) of the temperature probes and the pressure transducers used within the three apparatuses are gathered in the fourth and fifth columns of Tab3.1.

$$u_{cal}(M) = \frac{b_M}{\sqrt{3}} \tag{3.5}$$

- ***Uncertainty related to the repeatability of the measurement (u_{rep}):***

  The experimental pressure or temperature is taken as the average of several recorded values, the uncertainty related to the repeatability of the recorded values is given by the Eq3.6, where σ_M is the standard deviation of the recorded values after calibration, and N_v is the number of the recorded values.

$$u_{rep}(M) = \frac{\sigma_M}{\sqrt{N_v}} \tag{3.6}$$

For the measurements carried out using apparatus1 and apparatus3, the experimental temperature is taken as the average of the temperatures given by the top and the bottom probes after calibration. The experimental uncertainty of the temperature is given by Eq3.7.

$$u(T) = \sqrt{\left[\frac{u(T_1)}{2}\right]^2 + \left[\frac{u(T_2)}{2}\right]^2} \tag{3.7}$$

Table 3.1: summary of the source of the uncertainty affecting the experimental pressure and temperature.

Apparatus	Sensor	u_{ref}	b_M	u_{cal}
Apparatus1	T1	8 Mk	0.1 K	0.06 K
	T2		0.1 K	0.06 K
	Druck	0.09 kPa	1.6 kPa	0.92 kPa
Apparatus2	T5	5 mK	16 Mk	9 mK
	Keller	0.09 kPa	0.85 kPa	0.49 kPa
	Kulite		11.8 kPa	6.83 kPa
Appratus3	T_1	8 mK	20.78 mK	12 mK
	T_2		15.59 mK	9 mK
	Keller [0-5MPa]	0.09 kPa	0.4 kPa	0.23 kPa
	Keller [0-20MPa]		1.8 kPa	1.04 kPa

3.3.2 Uncertainty on the experimental composition

The calculation of the uncertainty affecting the molar composition of each component involved in a given mixture depends on the method used for the determination of the composition. In this work, all the experimental compositions are determined using the GC analysis of the fluid samples whatever the experimental protocol; in such a case, the molar composition uncertainty can be associated with four main sources.

- ***Use of the calibration polynomial "f" for the calculation of the mole number (u_{cal}):*** for a given sample of the fluid, the mole number of each component is calculated from the surface of the corresponding pick of the gas chromatography analysis using the appropriate calibration polynomial *f*; this generates an uncertainty that is given in Eq3.8.

$$u_{cal}(n_i) = \sqrt{\sum_{j=1}^{w}\left[\left(\frac{\partial f}{\partial a_j}\right)u(a_j)\right]^2} \tag{3.8}$$

  Where *w* is the order of the polynomial *f*, a_j is the j^{th}-order coefficient and $u(a_j)$ is the corresponding uncertainty.

- ***Purity of the chemicals (u_{pur}):*** The chemicals used for the experiments present always some impurities. The purity (P_u) of each component is generally given by the supplier. The uncertainty taking into account the presence of these impurities is calculated using Eq.3.9.

$$u_{pur}(n_i) = \frac{1 - P_{u,i}}{\sqrt{3}} \tag{3.9}$$

- ***The repeatability of the measurement (u_{rep}):*** the experimental composition of a fluid phase is obtained as the average of the composition of a certain number of samples of this phase. The error related to the repeatability of the composition of these samples is given in Eq.3.10.

$$u_{rep}(x_i) = \frac{\sigma_{x_i}}{\sqrt{N_s}} \tag{3.10}$$

  Where σ_{x_i} is the standard deviation of the composition of component *i*, and N_s is the number of the samples.

- ***Calculation of the mole fraction from the mole number (u_{for}):*** the use of the mathematical formula for calculating the mole fraction starting from the mole number of each component induces propagation of the uncertainties related to the mole number calculation (u_{pur}, u_{cal}). The propagation of the uncertainty can be evaluated using Eq3.11.

$$u_{for}(x_i) = \sqrt{\sum_{j=1}^{N_c}\left[\left(\frac{\partial x_i}{\partial n_j}\right)\left(u_{cal}(n_j) + n_j\, u_{pur}(n_j)\right)\right]^2} \tag{3.11}$$

For binary mixtures:

$$u_{for}(x_1) = u_{for}(x_2)$$
$$= \sqrt{\left[x_2 x_1 u_{pur}(n_1) + \frac{x_2}{n_T} u_{cal}(n_1)\right]^2 + \left[x_2 x_1 u_{pur}(n_2) + \frac{x_1}{n_T} u_{cal}(n_2)\right]^2} \tag{3.12}$$

The final uncertainty on the composition is calculated combining only the uncertainty related to the repeatability of the measurements and the one related to the calculation of the mole fraction from the mole number seeing that the uncertainty related to the use of the calibration polynomial and the purity of the chemicals are already used for the calculation of $u_{for}(x_i)$.

$$u(x_i) = \sqrt{[u_{rep}(x_i)]^2 + u_{for}(x_i)^2} \tag{3.13}$$

3.4 Experimental procedure

Two main techniques have been used for measuring the solubility limits of the systems investigated in this PhD thesis; the "static-analytic method" and the "synthetic-indirect method".

The synthetic methods are commonly used when the analytic methods are not suitable. In many cases and especially when dealing with phase equilibria involving solid phases, the synthetic and the analytic methods become complementary. The synthetic methods are more suitable for the investigation of the high solubility region, and their accuracy decreases with decreasing solubility limits; to the contrary, the analytic-methods are more suitable for the investigation of the low-solubility region.

In the following, a general description of the different steps allowing the measurement of phase equilibria involving solid phases by means of static-analytic or synthetic-indirect methods is given. Depending on the studied system some modification can be required to adapt the experimental protocol.

3.4.1 The static analytic method

The experimental procedure allowing the measurement of the solid-fluid phase equilibria using the static-analytic method can be described as it follows (referring to apparatus1 and apparatus2:

- **Loading of the equilibrium cell:** the equilibrium cell and the loading lines are evacuated at ambient temperature thanks to the vacuum pump. Once no impurities remain in the EC, the solute is

introduced into the EC, and then a quantity of the solvent is added. When dealing with the static-analytic method, the exact knowledge of the global composition is not required; however, the amount of the solute (solid former) must be higher than its solubility limit at the target pressure and temperature; this limit can be estimated using a thermodynamic model or by assuming the ideal behavior (the ideal solubility is higher than the real solubility).

- **Reaching the target pressure and temperature**: once the EC has been filled with the components involved in the mixture, liquid nitrogen is filled into the cryostat, and then the target temperature is set on the PID regulator controlling the heating resistance. The balance between the cold originating from the vapor nitrogen and the heat provided by the heating resistance allows working at temperatures ranging from ambient temperature down to liquid nitrogen temperature. When the target temperature is achieved, the pressure of the system within the EC can be adjusted by adding some solvent. The system is maintained under stirring and kept at this temperature until reaching the thermodynamic equilibrium.
- **Sampling and analysis of the fluid phase:** depending on the equilibrium temperature and pressure, Solid-Vapor Equilibrium (SVE), Solid-Liquid Equilibrium (SLE), or Solid-Liquid-Vapor Equilibrium (SLVE) occurs within the cell since the mixture is oversaturated with respect to the solid former solubility limit. The ROLSI® samplers are used to withdraw fluid-phase (liquid or vapor) samples; the samples are vaporized in the heating chamber of the ROLSI® and transferred to the GC for analysis thanks to the carrier gas circulating in the transfer line. A suitable column inside the oven of the GC allows separating the components of the sample and then the amount of this component is analyzed thanks to the GC detectors (TCD or FID). The mole number of each component is calculated starting from the GC's peak by using the corresponding calibration polynomial. Additional samples are withdrawn until having more than six repeatable molar composition of the given fluid phase.

Once the experimental point (solubility limit) is entirely defined (P, T, x and/or y) at a given target temperature and pressure, a new target temperature is set on the PID regulator. The steps described above are repeated until covering all the desired temperature range or the global composition of the solid former is lower than its solubility limit; the cell is then emptied and evacuated, before carrying out addition experiment campaigns using new mixture containing sufficient solute.

Seeing that most of the systems investigated in this work present very low-solubility limits, the static analytic-method has been widely used.

3.4.2 The synthetic-indirect method

Unlike the static-analytic method, the synthetic-indirect method requires the exact knowledge of the global composition of the mixture to be studied, and each experimental point entails the emptying, the evacuation, and then the loading of the EC. The indirect procedure has been used in this work for the investigation of the SLVE of the methane+neopentane system.

The key step when dealing with this method is the preparation of a mixture of known composition. This can be made following at least three different methods:

- **The weighing of the amount of the components involved in the mixture:** in this case, the mixture is prepared in an external Auxiliary Cell (AC), which is then connected to the EC. The mixture is prepared commonly at ambient temperature and at pressure as high as a monophasic state occurs within the auxiliary cell. First, the AC is evacuated and weighed (m_1), then the solute is introduced into the auxiliary cell and then the auxiliary cell (filled with the solute) is weighed (m_2); finally, the solute is added into the auxiliary cell until reaching pressure allowing having a monophasic phase in the auxiliary cell and a final weighing is then carried out (m_3). Starting from m_1, m_2, and m_3, the mass of the solute can be calculated as $m_{solute} = m_2 - m_1$, and the masse of the solvent is given as $m_{solvent} = m_3 - m_2$.

  Once the mass of the solvent and the solute introduced into the auxiliary cell are determined, their respective mole number (n) is calculated as the ratio $n=m/M$ where M is the molar mass of the given pure component.
- **Use of PVT properties of the pure components:** this method allows preparing the mixture directly inside the equilibrium cell, the cells containing the pure component being connected separately to the EC. The method is based on the Pressure-Volume-Temperature (PVT) measurement before and after the feeding of the EC.

  The method allowing the calculation of the mole number introduced into the equilibrium cell depends on the type of the auxiliary cell containing the pure component:

  i) *The auxiliary cell has a constant volume (v).* The pressure and the temperature of the auxiliary cell are measured before and after the loading of the EC. Knowing the molar density (ρ) of the pure component in the AC at the P-T condition before and after the feeding of the EC, and the volume of the auxiliary cell, the mole number inside the AC can be calculated before and after the filling of the EC using the following equation $n = v \times \rho$. The mole number introduced into the equilibrium cell is given by the difference between the mole number in the auxiliary cell before and after the loading of the EC.

ii) *The auxiliary cell is of variable-volume type.* In this case, the auxiliary cell is maintained at constant pressure and temperature and then the volume (v) of the component introduced into the cell is given by the change in the volume of the auxiliary cell. Starting from this volume change (Δv) and knowing the molar density of the fluid (ρ), the mole number introduced into the EC is calculated as $n = \Delta v \times \rho$.

- **Use of GC analysis:** if the experimental apparatus is equipped with a sampling system, the global composition of the studied mixture can be evaluated using GC analysis if the studied mixture is in a monophasic state at the loading pressure-temperature condition. The loading procedure is similar to the one used when preparing the mixture in an auxiliary cell by means of the weighing method. A given amount of the solute is loaded into the EC, then, the solvent is added until reaching pressure as high as a monophasic phase occurs within the EC. Thanks to the sampling device, several samples are withdrawn and analyzed in order to determine the composition of the fluid phase within the EC.

Once the mixture of known composition is prepared and loaded, the EC is cooled and the pressure-temperature conditions are continuously recorded. The pressure is plotted as a function of the temperature in a $P=f(T)$ diagram. The solid phase formation induces a change in the slope of such a diagram.

3.5 Summary of the studied systems

The bibliographic research performed in this work has pointed out some critical systems that are useful to study in order to evaluate their solubility limits in methane-rich mixture and thus their crystallization risk in LNG production. The selection of the mixtures to be investigated was driven by their scientific interest (different global phase diagrams) and also by their industrial impact (provide adequate purification limits allowing the optimization of the purification process, thus increasing the safety and the profitability of the LNG plants).

Among all the natural gas components, the aromatic compounds are one of the main solid formers that present a high solidification risk at cryogenic temperatures, this obliges LNG companies to adopt strict purification limits concerning these components. The solubility limits of benzene, ethylbenzene, p-xylene, m-xylene, and o-xylene in methane rich-mixture have been measured at the two nominal pressures of 3 and 6 MPa (which are representative of the pressure condition within the natural gas liquefaction train, one pressure lower than the critical pressure of the LNG mixture and one higher than critical pressure of the LNG mixture) using the static-analytic method. In addition, the effect of the presence of ethane on the solubility limits of benzene and p-xylene has been evaluated by measuring their solubility limits in the methane+ethane mixture (90%_10% mol/mol) at a nominal pressure of 6 MPa; and the presence of nitrogen

on the solubility limits of benzene in methane has been also evaluated thanks to the study of its solubility limits in the methane+nitrogen mixture (90%_10% mol/mol) at a nominal pressure of 6 MPa.

The SLE and SLVE of the methane+neopentane system have been measured down to 100 K; the influence of the presence of ethane or nitrogen has been also evaluated thanks to the evaluation of the SLVE of neopentane+methane+ethane and neopentane+methane+nitrogen ternary mixtures. The investigation of the solubility limits of neopentane has motivated by its triple point properties, which are usually a good indication of the expected solubility limits. Indeed, the higher is the triple point temperature and the heat of fusion, the lower is the solubility limits. In this regard, neopentane has a high triple point temperature (256.5 K, [9]) and a low heat of fusion upon melting (3.26 kJ/mol, [9]): this put in competition the effect of these two properties.

In addition to the above-described systems involving components naturally present in natural gas, the solubility of tetrahydrothiophene (THT) in liquid methane at 3 and 6 MPa has been also measured. The THT is not a constituent of the raw natural gas, rather it is added in very small quantities to the gas injected into the French natural gas distribution networks to facilitate the detection of gas leaks thanks to its particular odor. The knowledge of the solubility limits of THT in liquid methane is mandatory in case of LNG production starting from the gas circulating on the distribution network.

To sum up, the systems investigated in this work are gathered in Tab3.2. The number of the experimental points (N_p), the temperature, the pressure, and the solute composition are given in the second, third, fourth, and fifth column; the experimental apparatus and the experimental method followed for the SFE measurement are given in the sixth and the seventh column.

Table 3.2: summary of systems studied in this PhD thesis

System	N_p	T range [K]	P range [MPa]	Apparat-us	Method
Methane+benzene	29	104.5 – 262.9	2.8 – 6.4	1	Static-analytic
Methane+ethylbenzene	24	108.5 – 170.2	2.9 – 6.5	1	Static-analytic
Methane+p-xylene	33	129.9 – 273.2	2.8 – 7.2	1 &3	Static-analytic
Methane+o-xylene	21	122.9 – 241.2	2.8 – 6.6	2	Static-analytic
Methane+m-xylene	24	104.5 – 217.4	1.9 – 6.4	2	Static-analytic
Methane+neopentane	31	98.8 – 253	0.2 – 6.2	1 & 3	Static-analytic & Synthetic-indirect
Methane+THT	20	111.4 – 169.9	2.1 – 6.3	2	Static-analytic
Methane+ethane+benzene	13	102.2 – 264.3	5.9 – 6.9	1	Static-analytic
Methane+ethane+neopentane	13	101.1 – 249.2	0.02 – 1.6	1	Synthetic-indirect
Methane+ethane+p-xylene	11	127.9 – 264.3	5.8 – 6.6	1	Static-analytic

Methane+nitrogen+benzene	20	113.5 – 264.1	5.7 – 6.3	1	Static-analytic
Methane+nitrogen+neopentane	14	161.2 – 246.1	0.9 – 2.9	1	Synthetic-indirect

3.6 Methane+neopentane system

3.6.1 Literature review

The first experimental campaigns aiming to understand the thermodynamic behavior of the methane+neopentane system have been carried out in 1971 by Williams and Prodany [10] and Rogers and Prausnitz [11]. In ref [10], VLE data at 344, 377, and 410 K have been reported, while VLE and critical measurements at 298 K are reported in ref [11]; both references used the static-analytic method for the measurement of the liquid and the vapor phase compositions at equilibrium. These data are presented in Fig3.12.

The literature works dealing with phase equilibria involving solid neopentane are those of Preston et al. [12], Baughman et al. [13], and Siahvashi et al. [14].

In ref [12], a visual equilibrium cell made of a thick-walled Pyrex tube was used; two copper flanges were sealed to this tube by the pure indium welding procedure. The EC was placed in a cylindrical cavity located in the upper end of a copper bar; this latter is partially immersed in a liquid nitrogen bath. Two heaters, placed on the copper tube, allowed balancing the excess refrigeration coming from the liquid nitrogen. The EC was equipped with a movable liquid-sampling probe, and with a vapor inlet and outlet that allowed recirculating the vapor phase within the EC and stirring the liquid phase. No pressure measurement device was installed on the cell; therefore, the reported data should correspond to SLVE since the vapor phase was recirculated. The volatility difference between methane and neopentane suggests that the vapor phase can be assumed as pure methane, thus the experimental pressure can be approximated by the saturation pressure of pure methane.

A single-pass flow method was used by Baughman and coworkers for the investigation of the solubility limits of solid neopentane in vapor or supercritical methane at temperatures ranging from 257.9 down to 199.99 K [13]. The experimental apparatus consisted of a 7-trays equilibrium cell, which was immersed in a liquid bath that uses a mixture of carbon tetrachloride and chloroform (50% in volume). The bath temperature was obtained by balancing the excess refrigeration coming from a controlled flow rate of liquid nitrogen passing through the bath in a coiled heat exchanger with two electric heaters. Firstly, liquid neopentane was introduced into the equilibrium cell, and the temperature was decreased down to the target temperature; then, methane was fed into the bottom of the EC and allowed to flow in a cross-flow pattern across the trays. A metering valve was used for adjusting the flow rate of methane and controlling the

pressure within the EC. The equilibrium vapor leaving the top of the cell was transferred to gas chromatographic analysis in order to determine its composition. The SVE data presented in ref [13] are presented in Fig3.13a.

Recently, Siahvashi and coworkers used a visual high-pressure sapphire cell to measure the solubility limits of solid neopentane in methane [14]. The EC was placed inside an environmental chamber with operating temperatures ranging from 88 K up to 473 K. The EC cell was equipped with a copper cold finger controlled with Peltier modules; the temperature of the copper finger was kept slightly lower than the other parts of the EC; this allowed confining the solid formation in a small place and then facilitated its detection. The authors used two techniques for investigating this system; firstly, the thermodynamic behavior (SVE, SLE, and SLVE) of synthetic mixtures prepared inside the EC has been investigated; then, the SVE points of a commercial mixture made of 2036 ppm of neopentane in methane have been measured at different pressures and temperatures. The SVE data reported in ref [14] are presented in Fig3.13a, while the SLE and the SLVE are presented in Fig3.13b together with the data presented in ref [12].

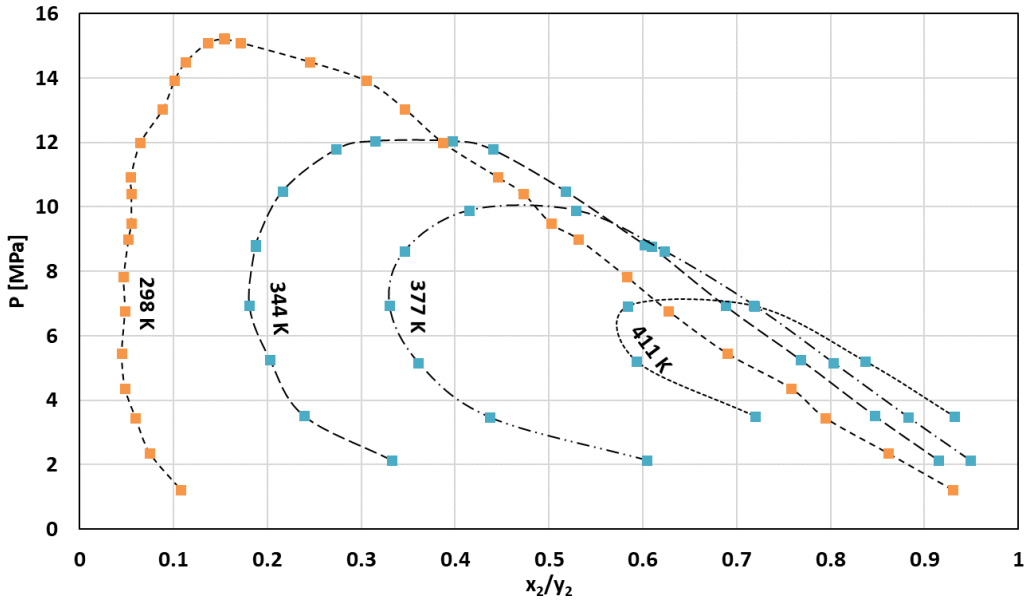

Figure 3.12: literature VLE data of the (1)methane+(2)neopentane system at temperatures from 298 K up to 411 K

■ ref [10]; ■ ref [11], --- guide for the eyes of the reader

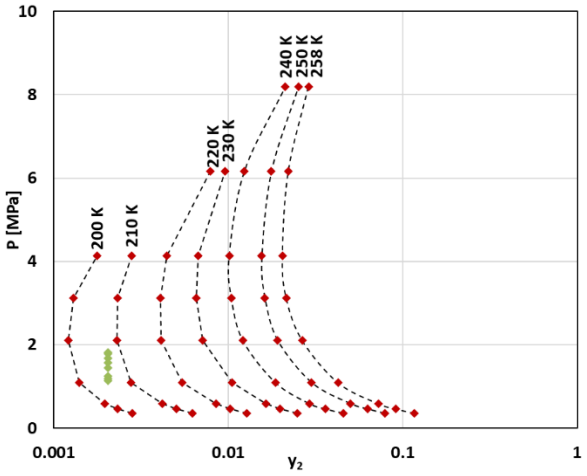

Figure 3.13a: literature SVE data of the (1)methane+(2)neopentane system
♦ ref [13], ♦ ref [14]
--- guide for the eyes of the reader

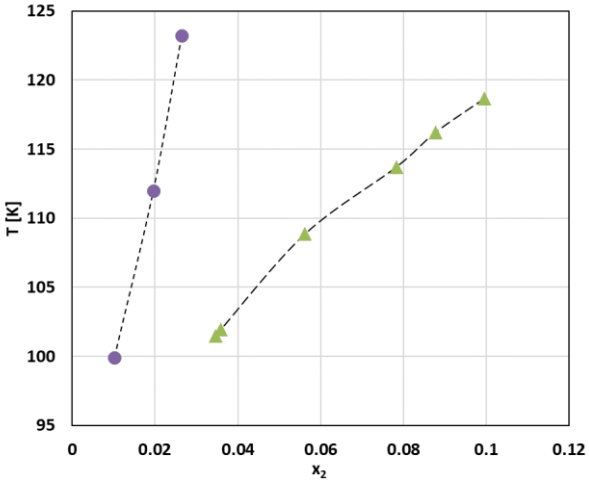

Figure 3.13b: literature SLE and SLVE data of the (1)methane+(2)neopentane system
● ref [12], ▲ ref [14],
--- guide for the eyes of the reader

To sum up, all the available literature values accounting for fluid-fluid and solid-fluid phase equilibria of methane+neopentane system are gathered in Tab3.3 and presented in the pressure-temperature diagram of Fig3.14. The saturation lines of methane and neopentane are calculated by means of the GERG2008 Equation of State as implemented in REFPROP v.10 [15]; whereas the melting curves of methane and neopentane are represented by vertical lines located at their respective triple-point temperatures.

Table 3.3: summary of the available literature data of the methane(1)+neopentane(2) system

T range [K]	P range [MPa]	x_2 range	y_2 range	N	Kind of data	Ref
344 – 411	2.1 – 12.1	0.40 – 0.95	0.18 – 0.72	18	VLE	[10]
298.15	1.2 – 15.1	0.17 – 0.93	0.04 – 0.14	16	VLE	[11]
	15.2	0.155		1	CP	
99.9 – 123.2		0.01 – 0.026		3	SLVE	[12]
200 – 257.9	0.36 – 8.2		0.0012 – 0.17	57	SVE	[13]
101.5 – 234.2	0.3 – 10.9	0.0347 – 0.5269	0.002036	16	SLE, SVE, SLVE	[14]

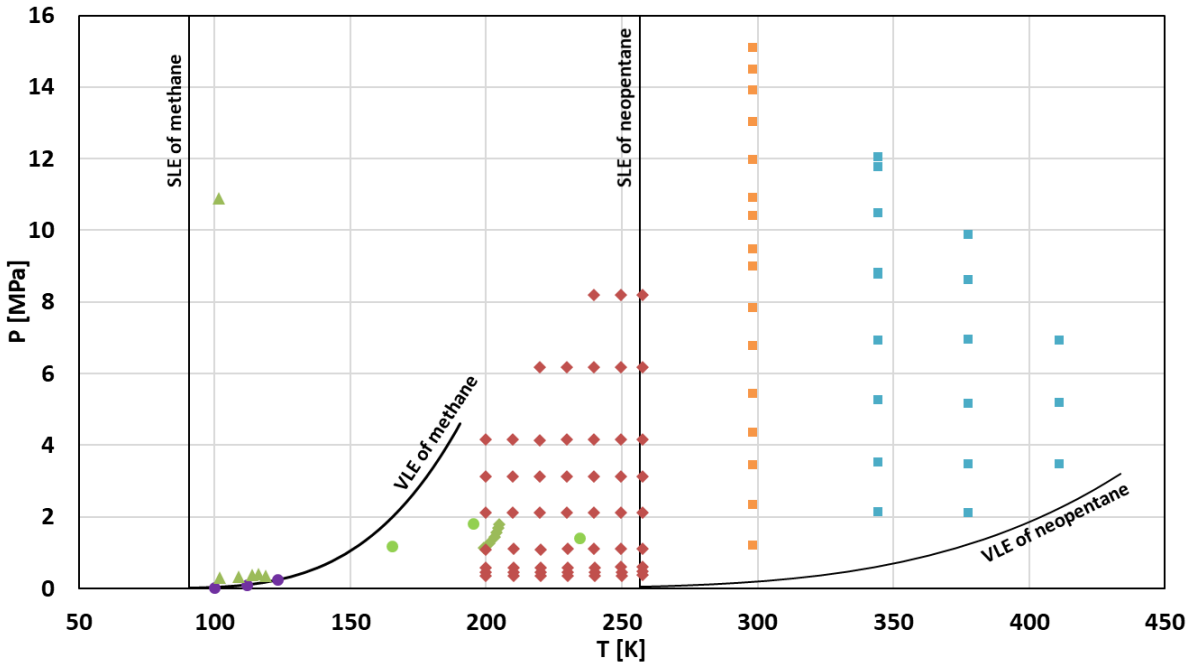

Figure 3.14: pressure-temperature diagram of the available literature data of the methane+neopentane system

VLE: ■ ref [10], ■ ref [11]; SVE: ♦ ref [13], ♦ ref [14]; SLVE: ● ref [12], ● ref [14]; SLE : ▲ ref [14]
— melting and saturation curve of pure methane and pure neopentane.

The analysis of all the available literature data allows highlighting some inconsistencies and disagreements concerning the quantitative and the qualitative thermodynamic behavior of the methane+neopentane system.

The low-temperature solubility limits of solid neopentane in liquid methane reported in Preston et al. [12] and Siahvashi et al. [14] are not in good agreement. Indeed, the solubility limits reported in [14] are much higher than those reported in [12] (see Fig3.13).

Based on the Fig3.14, and focusing on the temperatures ranging from the triple point temperature of neopentane down to the critical point temperature of methane, an inconsistency between the qualitative thermodynamic behavior (global phase diagram) inferred from the data reported by Baughman et al. [13] and those reported by Siahvashi et al. [14] can be pointed out.

- On the one hand, the three SLVE data reported by Siahvashi et al. [14] (represented in Fig3.14 by green filled circles) suggest a continuous locus of the SLVE that originates at the triple point temperature of neopentane and develops toward the low-temperature region; the SLVE curve reaches a maximum pressure that does not exceed 2 MPa. This behavior (continuous SLVE curve) can be associated with the global phase diagram of type D according to the classification of Kohn and Luks [16]. This implies that for pressures higher than the SLVE locus only the SLE or VLE

may occur depending on the global composition of the mixture, whereas only the SVE may occur for pressures lower than the SLVE locus. The qualitative pressure-composition (P-x) diagram at constant temperature located in the above-mentioned region is given in Fig3.15a.

- On the other hand, the high-pressure SVE reported by Baughman et al. (represented in Fig3.14 by red filled diamonds) suggest that the liquid phase is not stable for temperatures lower than the triple point temperature of neopentane and pressures at least as high as the maximum pressure reported for each isotherm in ref [13]. This thermodynamic behavior can be associated with the global phase diagram of type A according to the classification of Kohn and Luks [16]. Based on this information, the qualitative P-x diagram at temperatures ranging from the triple point temperature of neopentane down to the critical point temperature of methane is presented in the Fig3.15b.

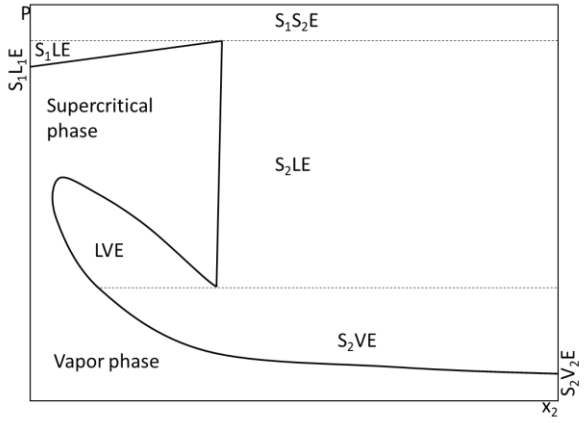

Figure 3.15a: qualitative pressure-composition diagram of the (1)methane+(2)neopentane system as inferred from the data of Siahvashi et al. [14]

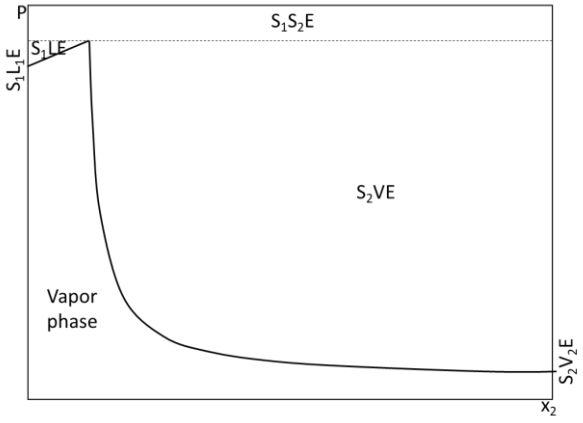

Figure 3.15b: qualitative pressure-composition diagram of the (1)methane+(2)neopentane system as inferred from the data of Baughman et al. [13]

3.6.2 Chemicals and apparatuses

The information concerning the chemicals used in this work are gathered in Tab3.4.

Table 3.4: identification number, purities, and suppliers of the chemicals used in this work.

Chemical name	CAS number	Purity "*Pu*"	Source
Methane	74-82-8	0.99995	MESSER
neo-pentane	463-82-1	0.99	AIR LIQUIDE

Two apparatuses have been used for the investigation of the low-temperature thermodynamic behavior of the methane+neopentane system. The apparatus1 described in section 3.1.1 has been used for the measurement of the SLVE and the SLE using the synthetic-indirect and static-analytic methods respectively.

The apparatus3 described in section 3.1.2 has been used to carry out SLVE and VLE following the static-analytic method.

3.6.3 SLE and SLVE measurements

At the beginning of this PhD thesis, the only available data involving solid neopentane were those reported by Baughman et al. [13] and Preston et al. [12]. From ref [13], it can be inferred that for temperatures ranging from the triple point temperature of neopentane and down to the lowest temperature investigated in this reference (200 K) and for pressure at least as high as the maximum pressures reported in this reference (8 MPa), the methane +neopentane system is at SVE or in a monophasic vapor state, depending on the global composition. This means that the liquid phase is not stable at these P-T conditions.

Based on this information, three experimental campaigns have been carried out for investigating the thermodynamic behavior of the methane+neopentane system at low temperatures in the presence of solid neopentane.

i) ***The first experimental campaign*** aimed at measuring the SLE at temperatures ranging from 150 K down to 100 K and at pressures between 2 and 6 MPa. The apparatus1 has been used following the static-analytic method described in section 3.4.1 for measuring the SLE. Certain quantities of neopentane and methane were introduced separately into the EC at ambient temperature, then, the system was cooled down to the target temperatures. At each target temperature, methane was added until reaching the target pressure. The system was kept at this P-T condition and continuously stirred for avoiding any thermal or composition stratification within the EC. The ROLSI® sampler was used to withdraw liquid samples at the SLE, which were transferred to the GC analysis in order to determine the liquid composition. During the sampling, the P-T conditions of the system were recorded. Each experimental point (P, T, x) was considered as properly defined after having obtained more than 6 samples with a repeatable composition (no increasing or decreasing tendency is observed). Additional experimental points are carried out at lower temperatures following the same procedure. The values obtained during this first campaign are given in the first part of Tab3.5.

ii) ***The second experimental campaign*** aimed at investigating the temperature region slightly lower than the triple point temperature of neopentane. Seeing the high solubility limits obtained in the first campaign, and the modeling results that are not in agreement with the data reported by Baughman et al. [13] (see chapter4 of this manuscript), apparatus3 has been used in order to investigate the thermodynamic behavior of methane+neopentane system at temperatures from 228 K up to 232 K, in order to make an end to the uncertainties on the thermodynamic behavior of this system and elucidate the disagreement between the modeling results, the data from ref [14] and the data from ref [13].

The EC was filled with a certain amount of neopentane and methane, and the system was cooled until reaching the target temperature (between 228 K and 232 K). Thanks to the visual window it was possible to detect all the phase equilibrium transitions during the cooling of the system.

- Firstly, the system was at VLE at the loading condition.
- The decreasing temperature led to a transition from VLE to SLVE (the phase change has been visually observed and followed by a change in the slope of the P-T curve). This is a proof that the liquid phase is stable at temperatures lower than the triple point temperature of neopentane, thus the data reported by Baughman et al. in ref [13] are partially or totally inconsistent with the kind of phase equilibria reported in this reference (SVE). It is worth noticing that the data of Siahvashi et al. [14] has not been yet published when this experimental work was carried out.

At the SLVE, the ROLSI® samplers were used to withdraw fluid samples, which were analyzed using the GC. Since the liquid level in the EC was very high, it was not possible to sample the vapor phase. Thus, only the compositions of the liquid phase at the SLVE were determined in this experimental campaign. The corresponding data are presented in the second part of Tab3.5.

iii) ***The third experimental campaign*** aimed at investigating the SLVE loci from the triple point temperature of neopentane down to 100 K. The apparatus1 was used following the synthetic-indirect method (described in section 3.4.2) for the measurement of the solidification temperature of mixtures of know composition. First, a given amount of neopentane was introduced into the EC, and then methane was added until reaching a pressure as high as the system within the equilibrium cell was at the supercritical condition. The ROLSI® sampler was used for sampling the mixture within the EC in order to determine its global composition. The system was then cooled and the P-T conditions are continuously recorded; the system reached firstly a VLE and then a SLVE. A change in the slope of the P-T diagram was noticed at the transition from VLE to SLVE.

This first cooling (high cooling rate) was used to locate approximately the P-T condition of the solid phase formation. Once the temperature range of the transition was identified, a second cooling procedure was carried out. For avoiding the overcooling of the system, the cooling of the system was carried out following decreasing temperature stages; for each stage, the system was kept at constant temperature for more than 1 hour and then the temperature of a new stage was imposed following a cooling rate of 1 K/hour. The solidification condition of the studied mixture was determined as the intersection point of the two trend curves which represent the P-T condition of the stages achieved in the VLE and the SLVE region respectively. Once the solidification temperature of the given mixture is determined, the EC is emptied and filled with a new mixture.

An example of the P-T diagram following several cooling stages corresponding to the system (18.64%methane+81.36%neopentane) is showed in Fig3.16. The stages accounting for the VLE conditions are represented by blue open circles while those accounting for the SLVE are represented by red open circles; the P-T condition of the transition between the VLE and the SLVE (temperature of the solid phase appearance) is represented by a black filed square. The data obtained in this experimental campaign are presented in the third part of Tab3.5.

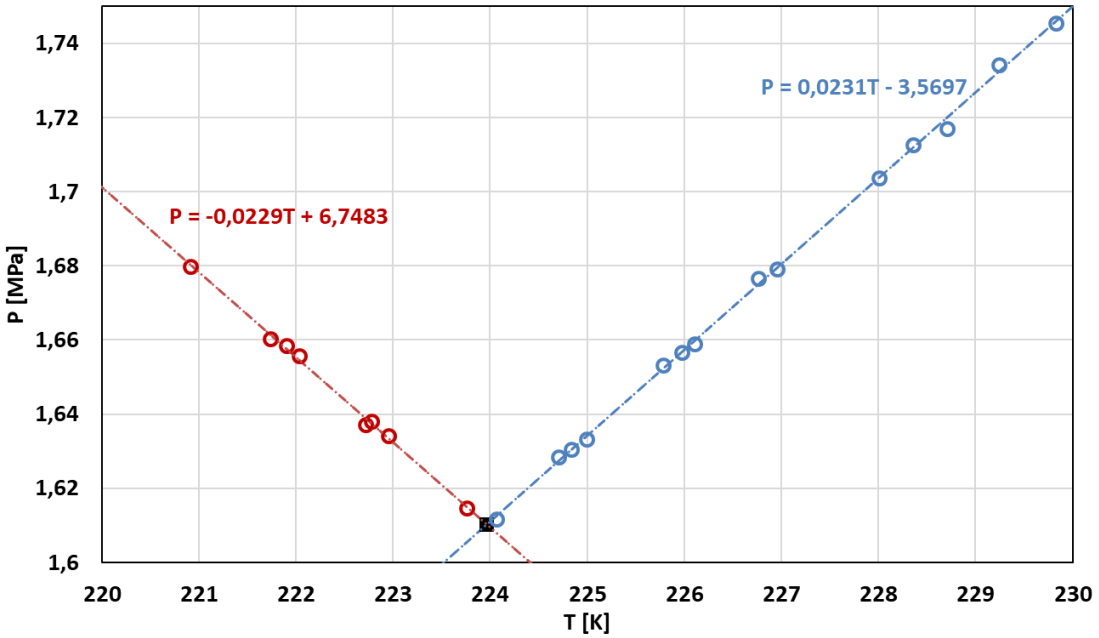

Figure 3.16: pressure-temperature variation during the transition between the VLE to SLVE of the methane+neopentane system (18.64%/81.36%).
■ VLE to SLVE; ○VLE; ○ SLVE

The SLE and the SLVE measurements obtained from the three experimental campaigns are gathered in Tab3.5. The experimental temperature, pressure, and neopentane composition are given in the second, fourth, and sixth columns while the corresponding expanded uncertainties (a coverage factor k = 2 is used) are given in the third, fifth, and seventh columns. The kind of data and the experimental method (Static-Analytic (S-A) and Synthetic-Indirect (S-I)) used for each experimental point are given in the eighth and ninth columns respectively.

Table 3.5: SLE and SLVE measurements of the methane(1)+neopentane(2) system

Exp campaign	T [K]	U(T) [K]	P [bar]	U(P) [bar]	x_2,z_2 [mol/mol]	Urel(x_2,z_2) [%]	STATE	Exp method
1	162.84	0.05	3.662	0.006	0.3748	1.84	SLE	S-A
	162.63	0.04	2.104	0.007	0.3754	1.71	SLE	S-A
	162.60	0.04	4.862	0.005	0.3712	2.26	SLE	S-A
	161.58	0.04	3.644	0.007	0.3679	1.68	SLE	S-A
	160.76	0.04	2.454	0.004	0.3631	1.66	SLE	S-A
	126.12	0.06	6.011	0.015	0.1543	1.96	SLE	S-A
	123.87	0.08	5.564	0.018	0.1382	2.71	SLE	S-A
	115.42	0.04	3.624	0.002	0.0895	1.39	SLE	S-A
	113.77	0.04	2.966	0.004	0.0762	1.30	SLE	S-A
	113.42	0.06	5.950	0.015	0.0770	2.34	SLE	S-A
	99.39	0.04	6.196	0.002	0.0358	2.17	SLE	S-A
	125.86	0.06	2.947	0.008	0.1543	1.65	SLE	S-A
	98.84	0.06	3.589	0.004	0.0327	3.69	SLE	S-A
2	231.85	0.06	1.354	0.002	0.8740	2.64	SLVE	S-A
	229.00	0.07	1.446	0.003	0.8601	2.31	SLVE	S-A
	228.25	0.05	1.471	0.002	0.8566	2.60	SLVE	S-A
	228.10	0.05	1.519	0.004	0.8527	2.02	SLVE	S-A
3	253.03	0.18	0.212	0.003	0.9849	0.02	SLVE	S-I
	249.63	0.21	0.455	0.003	0.9629	0.19	SLVE	S-I
	240.56	0.11	0.935	0.002	0.9104	0.31	SLVE	S-I
	230.38	0.17	1.405	0.002	0.8537	0.49	SLVE	S-I
	220.94	0.15	1.698	0.004	0.7938	0.59	SLVE	S-I
	212.56	0.11	1.849	0.003	0.7385	0.78	SLVE	S-I
	202.86	0.09	1.880	0.004	0.6752	1.02	SLVE	S-I
	194.07	0.12	1.823	0.005	0.6203	1.03	SLVE	S-I
	184.15	0.04	1.672	0.002	0.5485	1.29	SLVE	S-I
	175.40	0.07	1.493	0.003	0.4842	1.32	SLVE	S-I
	170.29	0.07	1.385	0.003	0.4465	1.61	SLVE	S-I
	166.45	0.04	1.252	0.004	0.4181	1.78	SLVE	S-I
	155.93	0.09	0.876	0.002	0.3412	2.22	SLVE	S-I
	142.44	0.05	0.521	0.004	0.2527	3.08	SLVE	S-I

The solubility limits of solid neopentane in liquid methane at SLE and SLVE measured in this work are presented in Fig3.17. The data accounting for the first campaign are presented by filled black tringles, those accounting for the second campaign are presented by filled grey circles, and those measured during the third campaign are presented by filled black circles. Despite the use of two different experimental apparatuses and following two different experimental procedures (static-analytic and synthetic-indirect methods), the

measured values obtained after the three experimental campaigns are in good agreement, showing the reproducibility of the results.

As illustrated in Fig. 3.17, the data obtained from the 1st campaign (liquid composition at SLE conditions measured using the static-analytic method) and those from the 2nd campaign (liquid composition at SLVE (measured using the static-analytic method) are in quite good agreement with the evolution of the experimental values obtained from the 3rd campaign (global composition of the mixture investigated using the synthetic-indirect method). This means that the liquid composition (not measured) at the SLVE conditions obtained in the 3rd campaign should be very similar to the global composition of the mixture (measured value before cooling), thus it can be concluded that the volume occupied by the vapor phase inside the equilibrium cell at the SLVE conditions measured during the 3rd campaign was negligible. As a consequence, for the SLVE obtained in the 3rd campaign, the liquid phase composition at SLVE conditions can be approximated by the value of the global composition of the mixture loaded into the EC.

Despite the pressure difference between the data measured during the 1st campaign (SLE) and those measured during the 3rd campaign (SLVE), the liquid composition obtained from these two experimental campaigns are very similar. Thus, the pressure effect (in the range investigated in this work) on the solubility of solid neopentane in liquid methane can be neglected, especially at very low temperatures.

The experimental SLVE pressures and temperatures shown in Fig3.18 can be represented by a continuous locus originating at the triple point temperature of neopentane and extending in the low temperature region down to 140 K. Starting from the triple point of neopentane and for decreasing temperatures, the SLVE pressure first increases until reaching a maximum value of about 1.9 MPa at 202.9 K, then decreases monotonically for tower temperatures.

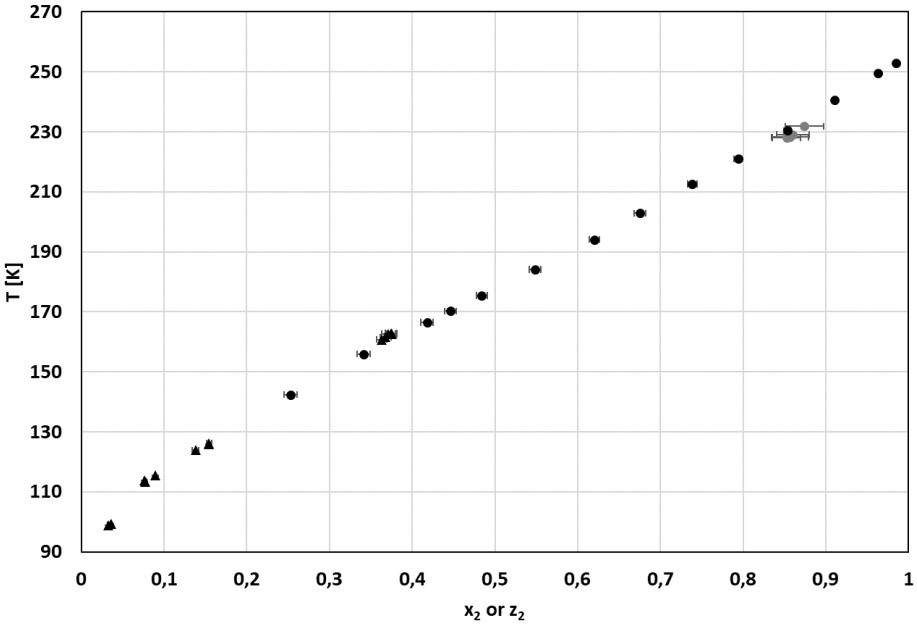

Figure 3.17: temperature-composition diagram of the (1)methane+(2)neopentane system at the SLE and SLVE.

SLE: ▲ 1st campaign; SLVE: ● 2nd campaign ● 3rd campaign

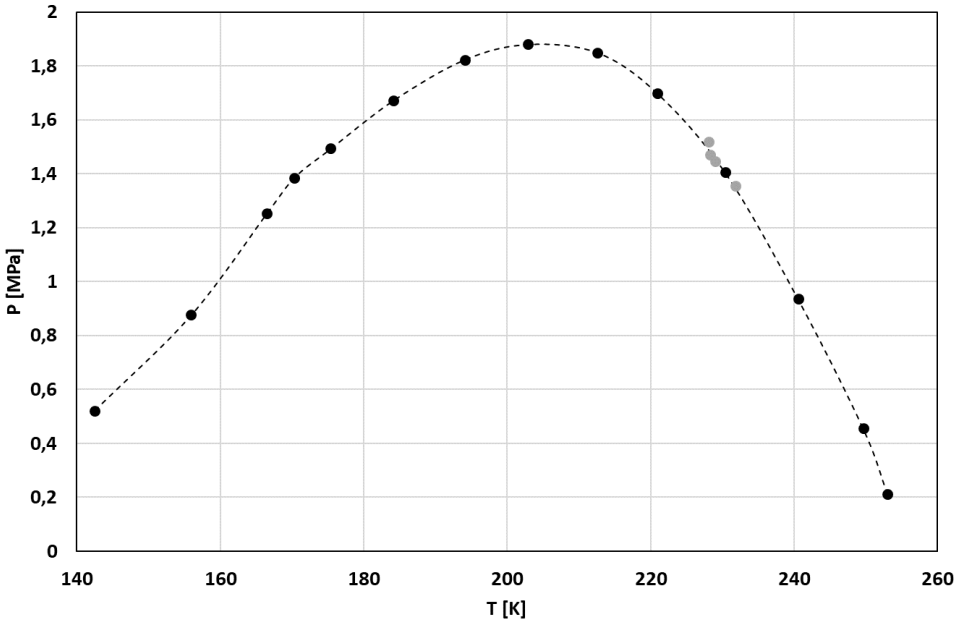

Figure 3.18: measured pressure-temperature SLVE conditions of the (1)methane+(2)neopentane system.

● 2nd campaign; ● 3rd campaign;

--- guide for the eyes of the reader

3.6.4 Low-temperature VLE measurements

In the quest of deeper investigation of the low-temperature phase equilibrium behavior of the methane+neopentane system, several experimental campaigns have been carried out for measuring the

vapor-liquid equilibrium at temperatures from 344 K down to 213 K using the apparatus3 described in section 3.1.2 by means of the static-analytic method.

For temperatures lower than the room temperature, liquid ethanol was used as a thermo-regulated bath.

The EC together with the loading lines were evacuated and the temperature of the bath was set at room temperature. A certain amount of neopentane and methane was loaded into the equilibrium cell. The system was cooled until reaching the target temperature and the pressure of the system was adjusted by adding some methane until the pressure of the system was slightly higher than the SLVE pressure at the target temperature. The phase equilibrium was assumed to be achieved when the pressure and temperature readings were stabilized to within their instrument uncertainty for at least 10 minutes.

Once the equilibrium was reached, the ROLSI® samplers were used for withdrawing samples from the liquid and the vapor phases. The samples were transferred to the GC and analyzed thanks to the TCD detector. The pressure and the temperature within the equilibrium cell were continuously recorded. After having five/six samples with a repeatable composition for both phases (no increasing or decreasing trend is observed for the obtained composition), the experimental point (T,P,x,y) was supposed properly defined. A new experimental point at higher pressure was then investigated by adding some methane in the EC. The process was repeated until having a satisfactory description of the pressure-composition diagram at the target temperature.

For VLE measurements at temperatures higher than the room temperature (298 K, and 344 K), water was used as a liquid bath instead of ethanol because the normal boiling point of water is higher than the one of ethanol.

The results of these experimental campaigns are gathered in Tab3.6 (T= 213, 230,243, and 253 K) and Tab3.7 (T= 263, 274, 298, and 345 K). The VLE data are gathered according to the nominal temperature of each experimental campaign, which is the average of the temperatures of all the experimental points accounting for the corresponding target temperature. The experimental temperature (T), pressure (P), liquid and vapor composition (x_1, and y_1, 1=methane) are reported in the first, third, sixth, and ninth column; their corresponding expanding uncertainties are reported in the second, fourth, seventh and the tenth column (a coverage factor k=2 is used for the uncertainty calculation). The number of the liquid and vapor samples (N_x and N_y) are reported in the fifth and the eighth column. The data listed in Tab3.6 and Tab3.7 are presented in Fig3.19 and Fig3.20 respectively.

Table 3.6. experimental VLE of the (*1*)methane+(2)neo-pentane system from 213 K up to 253 K.

T [K]	$U_{rel}(T)$ [%]	P [MPa]	$U_{rel}(P)$ [%]	N_x	x_1 [mol/mol]	$U_{rel}(x_1)$ [%]	N_y	y_1 [mol/mol]	$U_{rel}(y_1)$ [%]
Nominal temperature 212.59 K									
212.65	0.02	2.000	0.04	5	0.2702	2.81	5	0.9959	0.02
212.60	0.03	3.002	0.02	9	0.3987	2.39	6	0.9972	0.02
212.68	0.02	3.794	0.02	7	0.4977	2.03	6	0.9971	0.01
212.61	0.03	4.591	0.03	5	0.5966	1.72	5	0.9966	0.01
212.69	0.02	5.385	0.04	6	0.6928	1.35	7	0.9954	0.02
212.50	0.02	6.000	0.05	8	0.7727	0.98	6	0.9935	0.03
212.59	0.04	6.521	0.12	6	0.8451	0.67	8	0.9899	0.04
212.66	0.03	6.879	0.08	10	0.9021	0.40	5	0.9823	0.07
212.49	0.03	6.997	0.09	6	0.9347	0.28	5	0.9723	0.11
212.46	0.02	7.008	0.03	5	0.9416	0.24	5	0.9686	0.13
Nominal temperature 230.20 K									
230.18	0.02	1.593	0.08	8	0.1713	3.51	7	0.9913	0.04
230.09	0.02	2.964	0.05	6	0.3113	2.97	8	0.9935	0.03
230.13	0.02	4.178	0.05	7	0.4253	2.40	16	0.9934	0.03
230.11	0.02	5.385	0.04	7	0.5329	1.86	6	0.9923	0.03
230.10	0.02	6.616	0.03	6	0.6369	1.43	7	0.9895	0.04
230.10	0.02	7.622	0.03	7	0.7216	1.09	6	0.9843	0.07
230.18	0.02	8.410	0.03	11	0.7925	0.83	13	0.9760	0.10
230.27	0.02	9.072	0.03	7	0.8684	0.53	8	0.9525	0.20
230.16	0.02	9.135	0.03	5	0.8830	0.47	5	0.9433	0.23
230.28	0.03	9.185	0.07	6	0.8928	0.44	5	0.9382	0.25
230.37	0.02	9.197	0.04	6	0.8961	0.43	7	0.9345	0.27
230.44	0.02	9.221	0.05	5	0.9042	0.40	5	0.9283	0.29
Nominal temperature 242.97 K									
242.99	0.02	1.155	0.12	7	0.1067	4.01	6	0.9803	0.08
242.92	0.02	2.596	0.06	6	0.2378	3.52	6	0.9881	0.05
243.03	0.02	4.004	0.03	6	0.3546	2.68	5	0.9889	0.05
243.00	0.02	5.539	0.04	6	0.4741	2.19	6	0.9876	0.05
242.90	0.02	6.994	0.03	6	0.5765	1.66	6	0.9844	0.07
242.96	0.03	8.366	0.03	7	0.6736	1.33	6	0.9780	0.09
242.91	0.02	9.529	0.02	6	0.7606	1.00	6	0.9648	0.15
242.90	0.02	10.419	0.02	6	0.8504	0.65	8	0.9300	0.29
242.94	0.02	10.506	0.03	6	0.8718	0.54	6	0.9141	0.35
243.14	0.03	10.539	0.06	6	0.8822	0.55	5	0.9042	0.40
Nominal temperature 253.34 K									
253.27	0.01	0.457	0.14				7	0.9161	0.41
253.34	0.01	0.781	0.18	8	0.0619	4.17	5	0.9517	0.21

253.33	0.01	2.525	0.12	8	0.2045	4.08	11	0.9809	0.08
253.36	0.01	4.066	0.05	7	0.3257	3.10	8	0.9836	0.07
253.31	0.01	5.634	0.06	7	0.4374	2.76	8	0.9828	0.08
253.33	0.02	7.200	0.03	5	0.5386	2.01	5	0.9794	0.09
253.32	0.02	8.684	0.02	5	0.6347	1.62	5	0.9721	0.14
253.34	0.01	10.117	0.02	5	0.7274	1.16	5	0.9546	0.19
253.38	0.02	11.142	0.02	6	0.8117	0.80	5	0.9249	0.39
253.39	0.02	11.333	0.03	5	0.8404	0.69	5	0.9094	0.37

Table 3.7: experimental VLE of the (*1*)methane+(2)neo-pentane system from 263 K up to 345 K.

T **[K]**	***U*$_{rel}$*(T)*** **[%]**	***p*** **[MPa]**	***U*$_{rel}$ *(p)*** **[%]**	***N*$_x$**	***x*$_1$** **[mol/mol]**	***U*$_{rel}$ *(x*$_1$*)*** **[%]**	***N*$_y$**	***y*$_1$** **[mol/mol]**	***U*$_{rel}$ *(y*$_1$*)*** **[%]**
Nominal temperature 263.25 K									
263.24	0.01	0.476	0.17	6	0.0332	3.97	6	0.8848	0.47
263.25	0.02	1.027	0.13	7	0.0753	4.33	6	0.9453	0.22
263.24	0.02	2.631	0.12	6	0.1989	3.65	6	0.9718	0.12
263.26	0.01	3.982	0.05	6	0.2939	3.21	6	0.9740	0.12
263.26	0.01	5.731	0.06	6	0.4072	2.45	9	0.9738	0.11
263.23	0.01	7.559	0.06	9	0.5168	1.98	7	0.9703	0.14
263.23	0.01	9.165	0.04	9	0.6120	1.60	6	0.9607	0.18
263.23	0.01	10.253	0.03	7	0.6779	1.37	5	0.9499	0.25
263.25	0.01	11.326	0.02	7	0.7504	1.04	6	0.9292	0.30
263.24	0.01	11.905	0.02	7	0.8049	0.83	7	0.9029	0.39
263.34	0.02	12.046	0.04	5	0.8315	0.70	5	0.8792	0.48
Nominal temperature 274.18 K									
274.36	0.03	1.004	0.05	8	0.0706	1.86	6	0.9136	0.17
274.22	0.01	2.022	0.06	8	0.1392	1.69	7	0.9512	0.10
274.24	0.01	3.756	0.06	8	0.2497	1.51	11	0.9641	0.07
274.21	0.01	5.512	0.04	6	0.3559	1.26	11	0.9659	0.07
274.14	0.01	7.600	0.27	6	0.4752	1.04	6	0.9620	0.08
274.22	0.01	9.520	0.22	5	0.5824	0.84	6	0.9513	0.10
274.22	0.02	11.575	0.18	6	0.7009	0.58	7	0.9202	0.16
274.25	0.01	12.287	0.16	6	0.7570	0.47	10	0.8929	0.21
274.00	0.01	12.503	0.16	6	0.7926	0.40	6	0.8680	0.27
273.97	0.01	12.541	0.16	11	0.8117	0.36	6	0.8582	0.28
Nominal temperature 298.18 K									
298.18	0.01	0.811	0.07	8	0.0395	1.89	13	0.7652	0.45
298.16	0.01	1.502	0.06	18	0.0817	1.81	7	0.8610	0.27
298.19	0.01	3.236	0.10	6	0.1820	1.63	14	0.9171	0.17
298.18	0.02	6.048	0.33	7	0.3370	1.33	7	0.9315	0.14
298.20	0.01	9.042	0.22	7	0.4878	1.00	7	0.9240	0.17

298.21	0.01	11.873	0.17	6	0.6381	0.72	7	0.8860	0.23
298.21	0.01	12.577	0.16	7	0.6879	0.60	7	0.8612	0.28
298.20	0.02	12.856	0.16	6	0.7169	0.54	6	0.8414	0.31
298.21	0.01	12.951	0.15	6	0.7314	0.52	5	0.8296	0.34
298.20	0.01	12.994	0.15	10	0.7406	0.50	6	0.8156	0.37
297.99	0.02	13.024	0.16	7	0.7500	0.48	8	0.8055	0.39
Nominal temperature 344.52 K									
344.52	0.01	0.981	0.06				6	0.3405	1.26
344.52	0.01	2.228	0.06	6	0.0859	1.76	7	0.6608	0.65
344.51	0.01	4.031	0.04	6	0.1742	1.60	6	0.7698	0.45
344.53	0.01	6.047	0.33	7	0.2696	1.41	9	0.8048	0.40
344.51	0.01	8.038	0.25	6	0.3682	1.22	5	0.8086	0.39
344.53	0.01	10.204	0.20	9	0.4784	1.03	6	0.7858	0.44
344.52	0.01	11.098	0.18	9	0.5351	0.93	6	0.7593	0.49
344.51	0.01	11.641	0.17	6	0.5874	0.83	7	0.7202	0.56
344.52	0.01	11.741	0.17	7	0.6059	0.80	6	0.7037	0.60
344.52	0.01	11.775	0.17	7	0.6169	0.78	6	0.6893	0.62

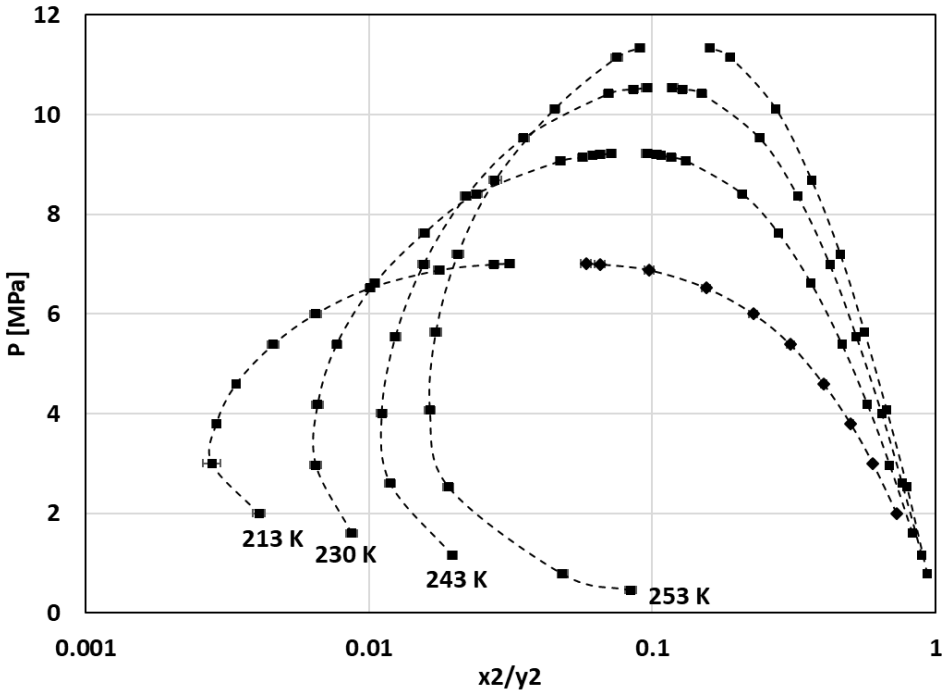

Figure 3.19: experimental VLE data from 213 K up to 253 K for the (1)methane+(2)neopentane system
--- guide for the eyes of the reader

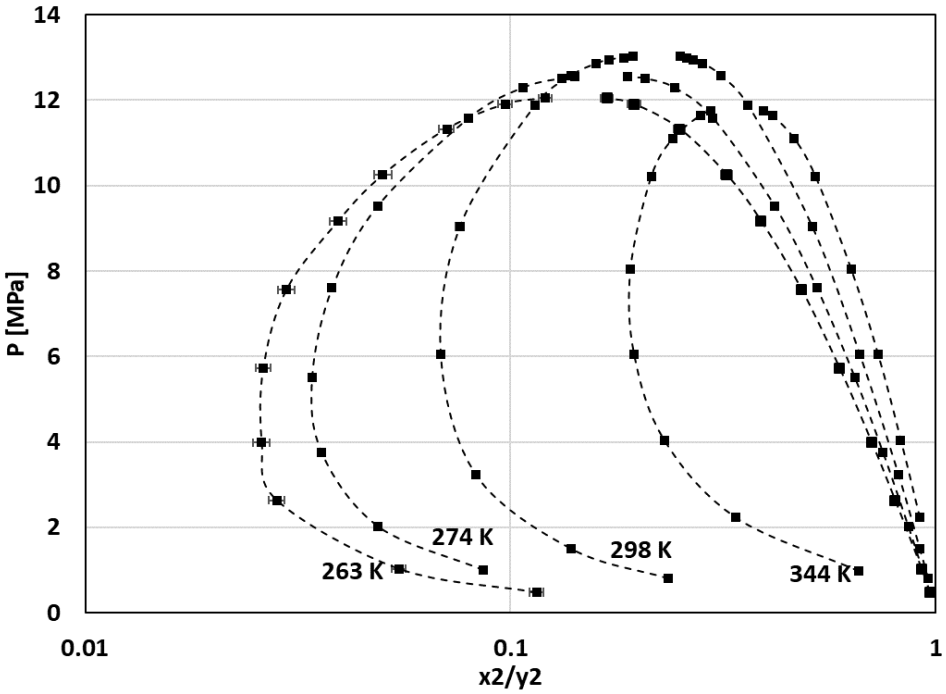

Figure 3.20: experimental VLE data from 263 K up to 344 K for the (1)methane+(2)neopentane system
--- guide for the eyes of the reader

3.6.5 Discussion

Fig3.21 shows a comparison between the data obtained in this thesis and those from the literature (refs [14] and [12]); the SLE and the SLVE data obtained in this work are in very good agreement with those presented by Siahvashi et al. [14] even if different kind of apparatuses and experimental procedures have been used. One experimental point reported as SLVE in ref [14] at 234.24 K (z_2 = 0.5269) is not in agreement with the other data. This may be explained by the fact that the liquid composition of this experimental point cannot be approximated by the global composition (to the contrary to the data obtained in this work for which this approximation has been proved by comparing the data from the 2nd and 3rd campaigns, see section 3.6.3). Seeing the high agreement between the values obtained in this work and those reported by Siahvashi and coworkers in the very low-temperature region (temperatures lower than 130 K), it can be stated that the data reported by Preston et al. [12] underestimate the solubility of solid neopentane in liquid methane.

Despite the high triple point temperature of neopentane, its solubility limit in liquid methane is relatively high (higher than 6% at the LNG temperature, around 110 K). It can then be stated that neopentane does not present any risk of solidification during LNG production (its concentration in the gas feeding the liquefaction train is usually much lower than 6%).

The effect of the pressure on the solubility of solid neopentane in liquid methane at the SLE is negligible. Indeed, the SLE data reported by Siahvashi et al. (filled green triangles) and those obtained in this thesis (black filled triangles) has been measured at different pressures, but this does not induce any significant effect on the composition of the saturated liquid phase (see Fig3.21).

The SLVE locus investigated in this work cover a large temperature range and the experimental values are in good agreement with two of the three experimental points reported by Siahvashi et al. [14]; once again, the pressure of the experimental point at 234.24 K corresponding to $z_2 = 0.5269$ is slightly far from the data measured in this work. The continuous locus of the SLVE between the triple point temperature of neopentane down to low temperatures is a proof that the liquid phase can be stable for temperatures lower than the triple point temperature of neopentane contrary to what can be inferred from the data of Baughman et al. [13]. It can be stated that the global phase diagram of the methane+neopentane system is of type D according to the classification of Kohn and Luks [16] and not of type A as it can be inferred from the data reported in ref [13].

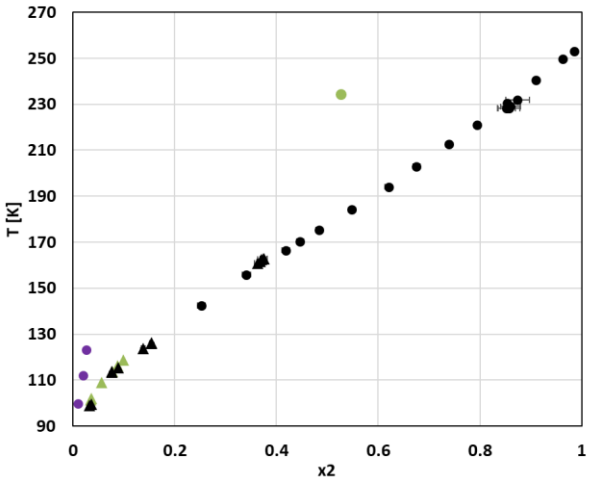

Figure 3.21: solubility of solid neopentane in liquid methane at the SLVE and SLE
SLVE: ● ref [12]; ● ref [14]; ● this work
SLE: ▲ ref [14] ▲ this work

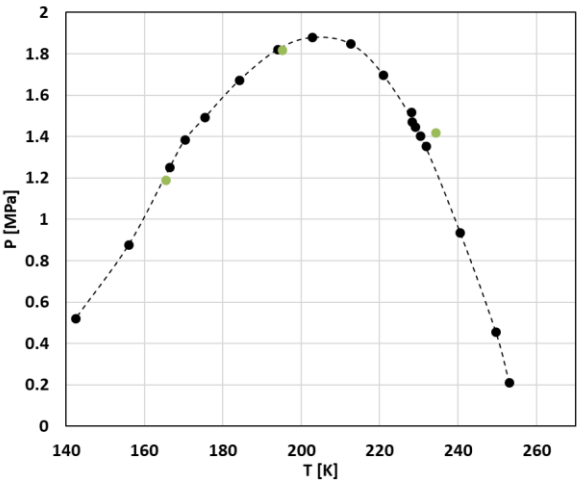

Figure 3.22: pressure-temperature loci of the SLVE of methane+neopentane system
● ref [12]; ● ref [14]; ● this work,
--- guide for the eyes of the reader

Fig3.23a shows a comparison between the data reported by Baughman et al. [13], Siahvashi et al. [14] and those obtained in this work in pressure-temperature diagram. According to this figure, some of the data reported in ref [13] correspond to the vapor composition in equilibrium with a neopentane-rich liquid phase (VLE) instead of neopentane solid phase (SVE). To demonstrate, the experimental points at a given temperature reported in ref [13] that are located at pressures higher than the SLVE pressure could not be representative of SVE data since the SLVE locus represents the upper boundary conditions of the existence of the SVE. As a consequence, these SVE data placed behind the SLVE locus are actually representative of

VLE conditions, thus some of the data given in ref [13] deal with the composition of the vapor phase at VLE rather than SVE.

Thanks to SLVE data obtained in this thesis, it has been possible to distinguish the VLE data among the SVE data and then assign the right kind of equilibrium for the values reported by Baughman and coworkers. Such sorting is graphically presented in the Fig3.23b, where red filled squares are used to represent the values accounting for VLE data, while red filled diamonds are used to represent the values accounting for SVE.

In Fig3.23a-b, the melting conditions of the pure neopentane are represented by the vertical red line at its triple point temperature.

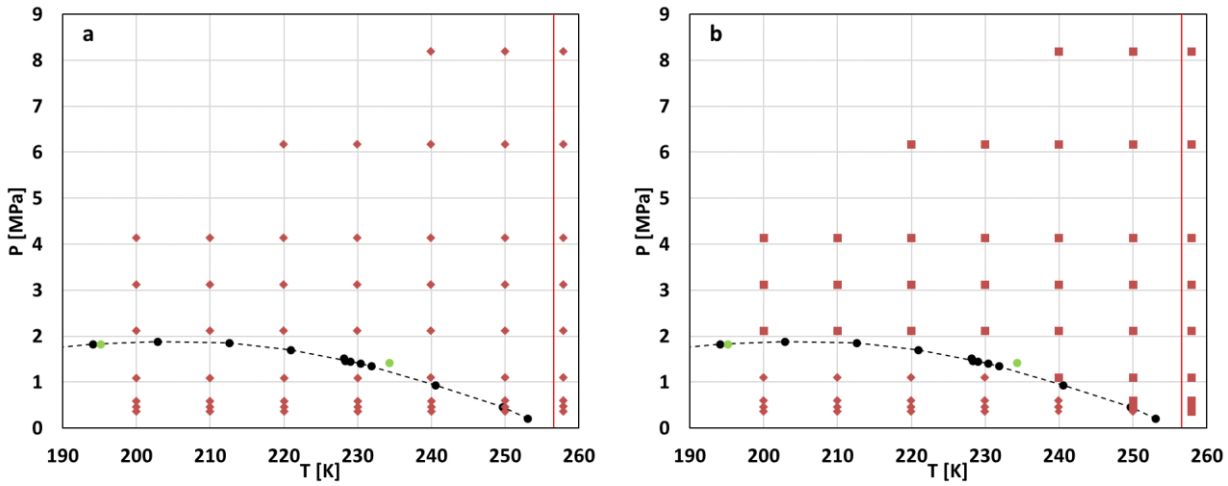

Figure 3.23: pressure-temperature diagram of the methane+neopentane system between 190 and 260 K
♦ ■ ref [13]; ● SLVE ref [14]; ● SLVE this work, — melting line of neopentane

The VLE data measured in this work at temperatures ranging from 253 K down to 213 K are an additional proof of the stability of the liquid phase at temperatures lower than the triple point temperature of neopentane and that a part of the data presented in ref [13] are VLE data instead of SVE data. Figs3.24-27 show the comparison between the VLE data obtained in this work and the vapor composition reported by Baughman and coworkers. Even if the set of data are not exactly at the same temperatures (except the isotherm at 230 K presented in Fig3.25), a quite good agreement can be noticed among the data at similar temperatures.

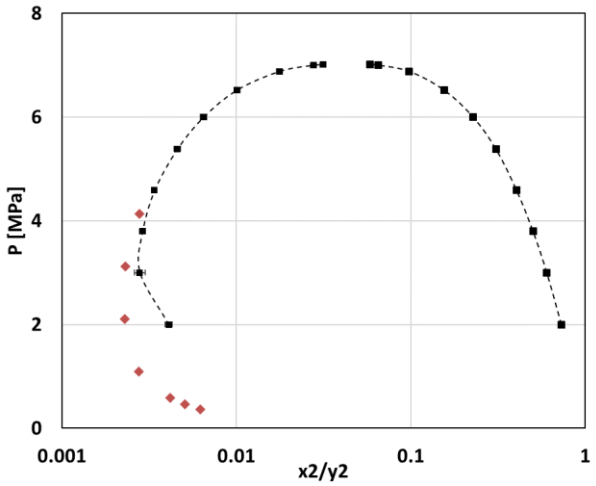

Figure 3.24: pressure-composition diagram of the methane+neopentane system at 213 K.
♦ SVE at 210 K ref [13]; ■ VLE this work;
--- guide for the eyes of the reader

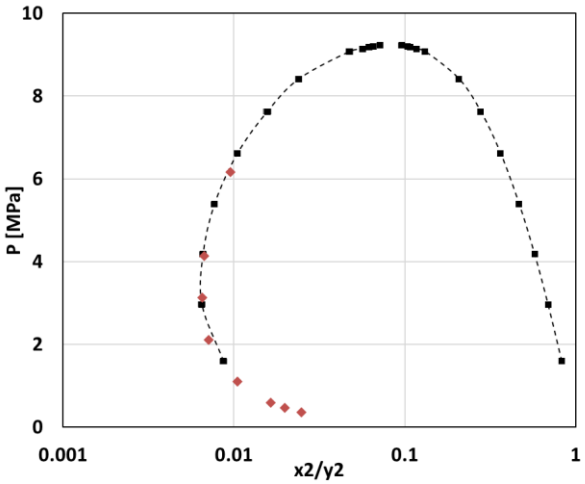

Figure 3.25: pressure-composition diagram of the methane+neopentane system at 230 K.
♦ SVE at 230 K ref [13]; ■ VLE this work;
--- guide for the eyes of the reader

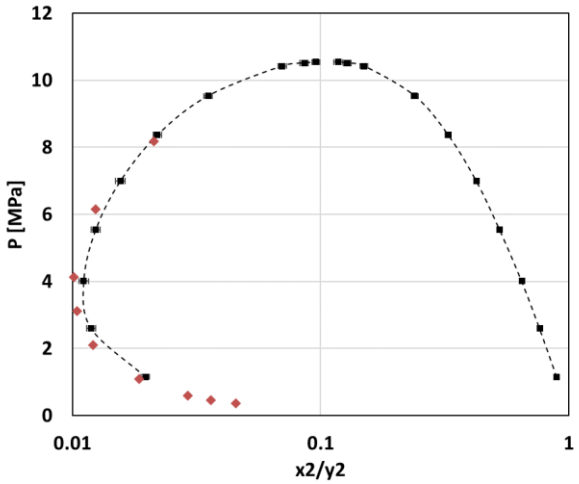

Figure 3.26: pressure-composition diagram of the methane+neopentane system at 243 K.
♦ SVE at 240 K ref [13]; ■ VLE this work;
--- guide for the eyes of the reader

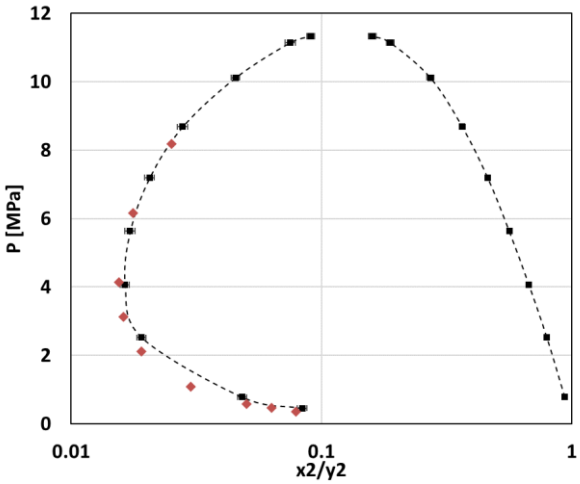

Figure 3.27: pressure-composition diagram of the methane+neopentane system at 253 K.
♦ SVE at 250 K ref [13]; ■ VLE this work;
--- guide for the eyes of the reader

Figs3.28-29 show a comparison between the VLE obtained in this work and those from refs [11] and [10] at 298.15 K and 344.5 K respectively. The data measured in this work are not in agreement with those obtained by Williams and Prausnitz [11], especially for the vapor composition and the near-critical region. However, a quite good agreement can be noticed between the data obtained in this work at 344.5K and those from Williams and Prodany [10].

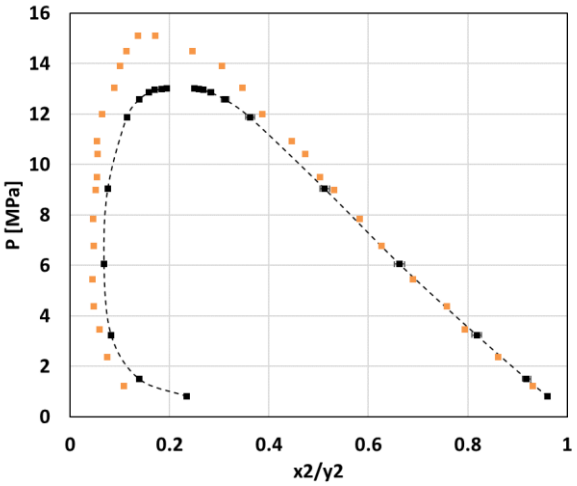

Figure 3.28: pressure-composition diagram of the methane+neopentane system at 298.15 K.
VLE data: ■ ref [11]; ■ this work.
--- guide for the eyes of the reader

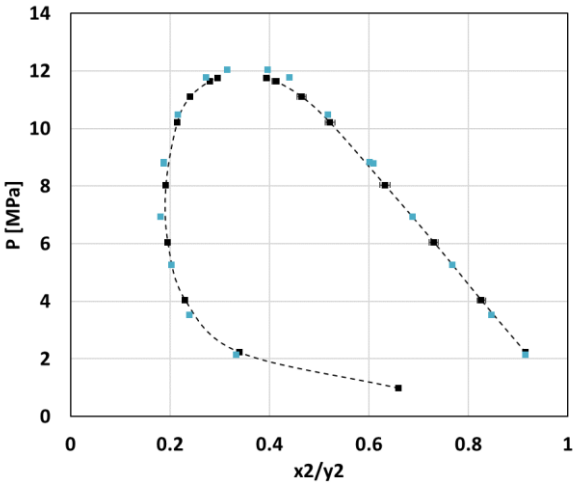

Figure 3.29: pressure-composition diagram of the methane+neopentane system at 344.5 K.
VLE data: ■ ref [10]; ■ this work.
--- guide for the eyes of the reader

To sum up, all the experimental data reported in the literature and those obtained in this thesis are presented in the pressure-temperature diagram in Fig3.30. In the light of the information given in Fig3.30, we can consider that the qualitative and the quantitative low-temperature thermodynamic behavior of the methane+neopentane system is well defined. However, additional SVE and VLE in the temperature region from 200 K down to low temperatures are required for the complete quantitative description of the low-temperature phase equilibria of the methane+neopentane system.

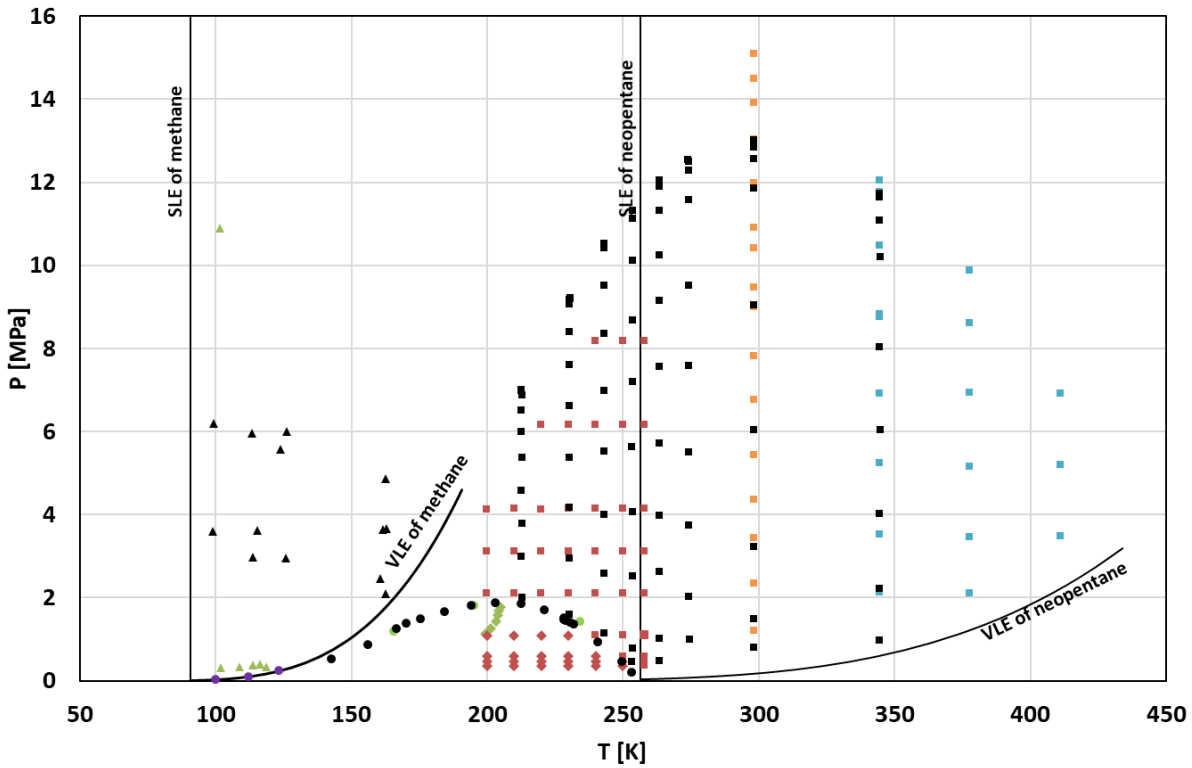

Figure 3.30: pressure-temperature diagram of the available literature data of the methane+neopentane system

VLE: ■ ref [10], ■ ref [11], ■ this work; SVE: ♦ ref [13], ♦ ref [14];
SLVE: ● ref [14], ● this work; SLE : ▲ ref [14], ▲ this work.
─ melting and saturation curve of pure methane and pure neopentane.

3.7 Conclusion

Three experimental apparatuses are presented in this work and have been used for the investigation of the low-temperature phase equilibria of systems of interest for the natural gas liquefaction. Two experimental procedures have been used: on the one hand, the static-analytic method has been used for measuring the low solubility limits at SLE or SVE (compositions down to 1 ppm have been obtained thanks to this method); on the other hand, the synthetic-indirect method was used for investigating the SLVE of systems presenting high solubility limits.

The solubility limits of the main aromatic components known as BTEX (Benzene, Toluene, Ethylbenzene, and Xylenes) in methane have been measured at 3 and 6 MPa (toluene was not investigated in this work since data are available in the literature [17]). In addition, the effect of the presence of ethane or nitrogen on the solubility limits has been evaluated. The solubility of benzene in methane+ethane and methane+nitrogen mixture and the solubility of p-xylene in methane+ethane have been measured. This investigation allowed

defining the adequate purification limits of the aromatic components in LNG production, a very important information that was still missing in the scientific and the technical literature.

The solubility of tetrahydrothiophene (THT) in liquid methane has been also measured at 3 and 6 MPa. THT is added before the injection of the natural gas in the French distribution network to provide a particular smell to the gas for facilitating the detection of leaks. The knowledge of the solubility limits of THT in liquid methane is of high interest for the production of the LNG starting from the gas circulating in the distribution network.

A deep investigation of the low-temperature phase equilibria of the methane+neopentane system has been carried out in this thesis. SLE have been measured in the temperature region from 163 K down to 99 K at pressure up to 6 MPa. In addition, the SLVE locus has been investigated from the triple point temperature of neopentane (256.5 K) down to 144 K. For decreasing temperatures, the SLVE pressure increases from the triple-point of neopentane until reaching a maximum value of about 1.9 MPa at 202.9 K and then decreases for lower temperatures. The data measured in this work are in good agreement with those published recently by Siahvashi and coworkers and confirmed that the data reported by Preston and coworkers underestimate the solubility limits of solid neopentane in liquid methane. A solubility limits higher than 6 % has been obtained at LNG temperature (110 K), this allows stating that neopentane does not present any solidification risk in LNG production since its composition in the feed gas is lower than this solubility limit.

Thanks to this deep investigation, it can be stated that the global phase diagram of methane+neopentane system is of type D according to the classification of Kohn and Luks [16], contrary to what can be inferred from the SVE data reported by Baughman and coworkers (these data suggest a global phase diagram of type A). Based on this finding, it is possible to state that a part of the data reported by Baughman and coworkers are vapor composition at VLE (data at pressures higher than the SLVE pressure) and not at SVE.

In order to provide more information about the low-temperature VLE of the methane+neopentane system, experimental campaigns have been carried out following the static-analytic method at temperature down to 213 K. The results are in quite good agreement with the vapor composition reported by Baughman and coworkers.

Some additional SVE and VLE at lower temperatures are required to have a complete quantitative and qualitative comprehension of the low-temperature thermodynamic behavior of the methane+neopentane system.

References

[1] A. Baba-Ahmed, P. Guilbot, D. Richon, New equipment using a static analytic method for the study of vapour–liquid equilibria at temperatures down to 77 K, Fluid Phase Equilibria, vol. 166, N° 2, 225-236, 1999.

[2] V. De Stefani, A. Baba-Ahmed, A. Valtz, D. Meneses, D. Richon, Solubility measurements for carbon dioxide and nitrous oxide in liquid oxygen at temperatures down to 90 K, Fluid Phase Equilibria, vol. 200, N° 1, 19-30, 2002.

[3] V. De Stefani, A. Baba-Ahmed, D. Richon, Experimental determination of carbon dioxide and nitrous oxide co-solubility in liquid oxygen, Fluid Phase Equilibria, vol. 207, N° 1-2, 131-142, 2003.

[4] P. Stringari, P. Theveneau, C. Coquelet, G. Lauermann, Solubility measurements of solid n-hexane in liquid methane at cryogenic temperature, 91st Annual GPA Convention, New Orleans, USA, 2012.

[5] S. Langé, L. A. Pellegrini, P. Stringari, C. Coquelet, Experimental determination of the solid-liquid-vapor locus for the CH4-CO2-H2S system and application to the design of a new low-temperature distillation process for the purification of natural gas, 94th GPA Convention Proceedings, 207-238, 2015.

[6] M. Riva, P. Stringari, Experimental Study of the Influence of Nitrogen and Oxygen on the Solubility of Solid Carbon Dioxide in Liquid and Vapor Methane at Low Temperature, Ind. Eng. Chem. Res., vol. 57, N° 11, 4124-4131, 2018.

[7] P. Guilbot, A. Valtz, H. Legendre, D. Richon, Rapid on-line sampler-injector: a reliable tool for HT-HP sampling and on-line GC analysis, Analysis, vol. 28, N°5, 426-431, 2000,.

[8] E. Boonaert, A. Valtz, J. Brocus, C. Coquelet, Y.Beucher, F.de Carlan, J-M. Fourmigué, Vapor-liquid equilibrium measurements for 5 binary mixtures involving HFO-1336mzz(E) at temperatures from 313 to 353 K and pressures up to 2.735 MPa, International Journal of Refrigeration, vol. 114, 210-220, 2020.

[9] J. S. Chickos, W. E. Acree, J. F. Liebman, Estimating Solid–Liquid Phase Change Enthalpies and Entropies, Journal of Physical and Chemical Reference Data, vol. 28, N°6, p. 1535-1673, 1999.

[10] B. Williams, N. W. Prodany, Vapor-liquid equilibriums in methane-hydrocarbon systems, J. Chem. Eng. Data, vol. 16, N°1, 1-6, 1971.

[11] B. L. Rogers, J. M. Prausnitz, High pressure vapor-liquid equilibria for argon+neopentane and methane+neopentane.

[12] G. T. Preston, E. W. Funk, J. M. Prausnitz, Solubilities of hydrocarbons and carbon dioxide in liquid methane and in liquid argon, J. Phys. Chem. vol. 75, N°15, 2345-2352, 1971.

[13] G. L. Baughman, S. P. Westhoff, S. Dincer, D. D. Duston, A. J. Kidnay, The solid + vapor phase equilibrium and the interaction second virial coefficients for argon +, nitrogen +, methane +, and helium + neopentane I. Experimental, J. Chem. Thermodynamics, vol. 6, N°12,1121-1132, 1974.

[14] A. Siahvashi, S. Z. S. Al Ghafri, X. Yang, D. Rowland, E. F. May, Avoiding costly LNG plant freeze-out-induced shutdowns: Measurement and modelling for neopentane solubility at LNG conditions, Energy, vol. 217, 119331, 2021.

[15] E.W. Lemmon, I.H. Bell, M.L. Huber, M.O. McLinden, NIST Standard Reference Database 23, Reference Fluid Thermodynamic and Transport Properties - REFPROP, DLL version number Version 10.0, Applied Chemicals and Materials Division, 2018.

[16] J. P. Kohn and K. D. Luks, Solubility of hydrocarbons in cryogenic LNG and NGL mixtures, GPA R- 22 76, 1976.

[17] G. P. Kuebler, C. McKinley, Solubility of Solid Benzene, Toluene, n-Hexane, and n-Heptane in Liquid Methane, in Advances in Cryogenic Engineering, K. D. Timmerhaus, Éd. Boston, MA: Springer US, 320-326, 1995.

Chapter 4:

New insights into the modeling of the SFE

Résumé du chapitre 4 en français

Le chapitre 4 est consacré à l'investigation des possibilités d'amélioration de la représentation des équilibres de phase à basses températures et en particulier ceux incluant les phases solides moléculaires. L'approche utilisée pour la modélisation des équilibres solides-fluides est basée sur le couplage d'un modèle pour les phases fluides (ici l'équation d'état de Peng Robinson a été utilisé) et un modèle permettant de calculer la fugacité des composés en phase solide (les phases solides sont considérées comme étant pures).

Dans un premier temps, un algorithme basé sur la minimisation de l'écart entre le coefficient d'activité calculé par l'équation d'état et le coefficient d'activité pseudo-expérimental calculé à partir de la composition de la phase liquide en équilibre avec la phase solide a été développé et décrit dans ce chapitre. Cet algorithme a été utilisé pour régresser le k_{ij} optimal pour chaque point expérimental pour plusieurs mélanges d'intérêts pour la liquéfaction du gaz naturel. Le résultat du travail de régression a montré que les k_{ij} régressés tendent vers une valeur constante à basses températures, cela signifie qu'un k_{ij} constant (pas de dépendance en température) pourra être suffisant pour avoir une modélisation correcte et précise des équilibres solide-fluide des systèmes étudier dans ce travail.

Dans un deuxième lieu, la continuité du k_{ij} entre les équilibres fluide-fluide et solide-fluide a été évalué. Pour cela, le k_{ij} (constant) régressé sur les données solide-fluide de chaque mélange binaire a été utilisé pour prédire les équilibres fluide-fluide à des températures proches de la température triple du composé le plus lourd dans le mélange. Les résultats de ces prédictions ont montré un accord satisfaisant par rapport aux données expérimentales et ont montré des déviations comparables à celles obtenues quand les modèles PPR78 et PSRK EoSs (deux modèles largement utilisés pour la représentation des équilibres fluide-fluide) ont été utilisé.

Une fois la constance du k_{ij} à basses températures et sa continuité entre les équilibres fluide-fluide et solide-fluide a été démontré, la possibilité d'utiliser les données fluide-fluide à des températures proches de la température triple du composé le plus lourd pour régresser un k_{ij} constant et l'utiliser pour prédire les équilibres solide-fluide a été évalué. Les résultats obtenus sur les différents systèmes étudiés dans cette thèse ont été très satisfaisants et en accord avec les données expérimentales.

À la fin de ce chapitre, une modélisation complète du diagramme de phases du système méthane+néopentane a été réalisé. Cette étude vient compléter, d'une part, les mesures expérimentales présentées dans le chapitre 3 pour ce système et, d'autre part, appliquer et confirmer les différentes conclusions tirer du travail de modélisation (constance et continuité du k_{ij}).

4. New insights into the modeling of the SFE

The experimental investigation of phase equilibria is time-consuming and cannot cover all the pressure-temperature-composition range of industrial and scientific applications. Nevertheless, the experimental data are mandatory for the development of the thermodynamic models and therefore the tuning of their parameters in order to improve their accuracy.

In this chapter, some possibilities of improving the modeling of the phase equilibria involving solid phases are presented; firstly, the modeling approach for the Solid-Fluid Equilibria (SFE) that consists of coupling of the classical approach initiated by Prausnitz [1] and a cubic equation of state is described, then the use of an algorithm based on pseudo-experimental activity coefficients for the regression of the optimal k_{ij} for the Solid-Liquid (SLE) and the Solid-Liquid-Vapor Equilibrium (SLVE) is presented. In the light of the obtained values of the k_{ij}, the capability of a constant k_{ij} to accurately represent SFE is evaluated. In addition, the continuity of k_{ij} for a given binary mixture crossing the triple point temperature of the heaviest component (passing from Fluid-Fluid Equilibria (FFE) to the SFE) is investigated; in case of validity of this hypothesis, FFE data can be used for the regression of a k_{ij} allowing the accurate representation of SFE. The possibility of predicting SFE data of several systems using k_{ij} regressed on the FFE is then presented and discussed.

Finally, a deep modeling investigation of the thermodynamic behavior of the methane+neopentane system is presented. This modeling work completes the large experimental investigation of this system presented in chapter 3.

NB: for the reader's convenience, the different algorithms allowing the calculation of the phase equilibria involving solid phases are presented in appendixD.

4.1 Modeling Framework

4.1.1 Solid-phase fugacity of a pure component

According to the classical approach initiated by Prausnitz, the fugacity of a given component in the pure solid phase can be calculated as a shifting of its fugacity in the subcooled liquid phase [1].

The mathematical relation between the two fugacities (in the pure solid and the liquid phase) can be obtained from the classical thermodynamic relations thanks to a simple quantification of the total Gibbs free energy variation at the melting condition, which, in turn, is related to the enthalpy and the entropy variations upon melting.

The expression of the fugacity of a given component in the pure solid phase is given in Eq4.1; and the fugacity of this component in the pure subcooled liquid phase is calculated using an equation of state (for the reader's convenience, the mathematical development and the steps leading to the final expression of the fugacity of a given component in the pure solid phase are presented in appendix A).

$$f_0^s(T,P) = f_0^l(T,P)\, exp\left[\frac{\Delta H_{T_tP_t}^{s\to l}}{RT}\left(\frac{T}{T_t}-1\right)+\frac{\Delta C_{P_{T_tP_t}}^{s\to l}}{R}\left(\frac{T_t}{T}-1-ln\left(\frac{T_t}{T}\right)\right)-\frac{\Delta V_{T_tP_t}^{s\to l}}{RT}(P-P_t)\right] \quad (4.1)$$

In Eq.4.1, $f_0^s(T,P)$ is the fugacity of the pure component in the solid phase at given Temperature (T) and Pressure (P), $f_0^l(T,P)$ is the fugacity of the pure component in its subcooled liquid phase, $\Delta H_{T_tP_t}^{s\to l}$, $\Delta C_{P_{T_tP_t}}^{s\to l}$, $\Delta V_{T_tP_t}^{s\to l}$ are respectively the latent heat of fusion, the heat capacity change and volume change upon melting, taken at the triple point temperature (T_t) and pressure (P_t), and *R* is the universal gas constant.

The terms on the right-hand side of the Eq4.1 have not the same importance; the weights of the second and third terms are much smaller than the one of the first term, but they improve the consistency of the pure solid phase fugacity expression and allow taking into account the pressure-dependence. Nevertheless, several authors have proposed to use a simplified form of Eq4.1 by neglecting the second and the third terms. In addition, $\Delta H_{T_tP_t}^{s\to l}$ is more available in the literature than $\Delta C_{P_{T_tP_t}}^{s\to l}$ and $\Delta V_{T_tP_t}^{s\to l}$.

Two main assumptions are made when developing Eq4.1, the temperature-dependence of $\Delta C_{P_{T,P}}^{s\to l}$ and $\Delta V_{T,P}^{s\to l}$ upon melting are neglected. It means that the values of these two experimental properties can be assumed equal to the values at the triple point of the considered component or at any other melting point.

In the case of components presenting a solid-solid transition (phase,α to phase,β), it is necessary to take into account the enthalpy change during the transition from solid phase α to β ($\Delta H_{T_{tr}P_{tr}}^{s^\alpha\to s^\beta}$). In such a case, the fugacity of a given component in the pure solid phase at a temperature lower than the solid-solid transition temperature is calculated using Eq.4.2 (when neglecting the heat capacity and the molar volume changes at the solid-solid transition temperature).

$$\begin{aligned} f_0^s(T,P) = f_0^l(T,P)\exp\Bigg[&\frac{\Delta H_{T_tP_t}^{s^\alpha\to l}}{RT}\left(\frac{T}{T_t}-1\right)+\frac{\Delta H_{T_{tr}P_{tr}}^{s^\alpha\to s^\beta}}{RT}\left(\frac{T}{T_{tr}}-1\right)\\ &+\frac{\Delta C_{P_{T_tP_t}}^{s^\alpha\to l}}{R}\left(\frac{T_t}{T}-1-ln\left(\frac{T_t}{T}\right)\right)-\frac{\Delta V_{T_tP_t}^{s^\alpha\to l}}{RT}(P-P_t)\Bigg] \end{aligned} \quad (4.2)$$

The melting pressure of a pure component can be calculated by applying the iso-fugacity condition to Eq4.1.

$$\frac{\Delta H_{T_tP_t}^{s\to l}}{RT}\left(\frac{T}{T_t}-1\right)+\frac{\Delta C_{P_{T_tP_t}}^{s\to l}}{R}\left(\frac{T_t}{T}-1-ln\left(\frac{T_t}{T}\right)\right)-\frac{\Delta V_{T_tP_t}^{s\to l}}{RT}(P-P_t)=0 \tag{4.3}$$

$$P=P_t+\frac{\Delta H_{T_tP_t}^{s\to l}}{\Delta V_{T_tP_t}^{s\to l}}\left(\frac{T}{T_t}-1\right)+\frac{\Delta C_{P_{T_tP_t}}^{s\to l}}{\Delta V_{T_tP_t}^{s\to l}}T\left(\frac{T_t}{T}-1-ln\left(\frac{T_t}{T}\right)\right) \tag{4.4}$$

Thanks to Eq4.4, the melting pressure of a pure component at a given temperature can be calculated using its triple point properties. Fig4.1 shows a comparison between the experimental melting conditions (filled points) of some alkanes and the calculated conditions (solid lines) obtained using Eq4.4 in a certain temperature range. Despite considering the constant value for the heat capacity and the volume change upon melting, the calculated pressures are in quite good agreement with the literature values reported in ref [2]. Except for iso-pentane for which an Average Absolute Deviation (AAD) of 12.42 % was obtained, all the others investigated hydrocarbons present an AAD of less than 8%.

The properties of the pure components used within Eq4.4 and the AAD between the calculated and the literature melting pressures are gathered in Tab4.1.

Table 4.1: summary of the melting properties of the investigated pure components.

Pure Component	T range [K]	P range [MPa]	N_p	Ref	$\Delta H_{T_tP_t}^{s\to l}$ J/mol	Ref	$\Delta C_{P_{T_tP_t}}^{s\to l}$ J/(mol K)	Ref	$\Delta V_{T_tP_t}^{s\to l}$ m^3/mol	Ref	AAD %
iso-pentane	113-151	0.1-300	7	[2]	5150	[3]	32.194	[4]	$7.3\ 10^{-6}$	[2]	12.42
n-pentane	143-184	0.1-300	7	[2]	8393	[3]	39.525	[4]	$9.4\ 10^{-6}$	[2]	5.03
n-hexane	177-225	0.1-300	7	[2]	13080	[3]	43.538	[4]	$14.7\ 10^{-6}$	[2]	7.39
cyclohexane	279-397	0.1-300	6	[2]	2677	[3]	14.63	[4]	$5.3\ 10^{-6}$	[2]	7.59
n-heptane	182-225	0.1-300	7	[2]	14040	[3]	53.317	[4]	$13\ 10^{-6}$	[2]	4.84
n-octane	216-269	0.1-300	7	[2]	20740	[3]	50.008	[4]	$20.1\ 10^{-6}$	[2]	5.34
n-decane	243-294	0.1-300	7	[2]	28720	[3]	52.274	[4]	$24\ 10^{-6}$	[2]	6.57

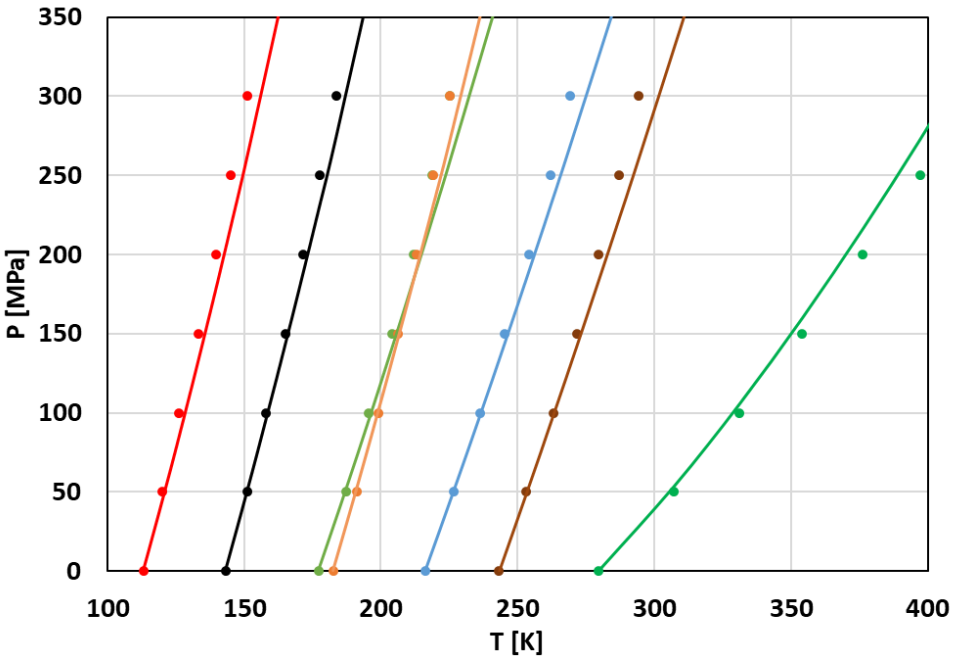

Figure 4.1: comparison of the literature melting lines (ref [2]) and the calculations obtained using Eq4.4
● *iso-pentane;* ● *n-pentane;* ● *n-hexane;* ● *n-heptane;* ● *n-octane;* ● *n-decane;* ● *cyclohexane;*

4.1.2 Solid-fluid equilibria of mixture

The modeling of the solid-fluid equilibrium at given pressure and temperature requires the resolution of the iso-fugacity condition for all the components involved in the solid and fluid phases.

$$\hat{f}_i^s\left(T,P,\overrightarrow{x^s}\right) = \hat{f}_i^f\left(T,P,\overrightarrow{x^f}\right) \tag{4.5}$$

The fugacity of the component "*i*" in the solid phase, $\hat{f}_i^s\left(T,P,\overrightarrow{x^s}\right)$ can be calculated as a function of its fugacity in the pure solid phase at the same P-T condition, $f_{0,i}^s(T,P)$, its composition, x_i^s, and its activity coefficient, γ_i^s.

$$\hat{f}_i^s\left(T,P,\overrightarrow{x^s}\right) = x_i^s\gamma_i^s f_{0,i}^s(T,P) \tag{4.6}$$

The solid phases encountered when dealing with LNG mixtures are commonly considered as pure solids (total immiscibility in the solid phase). This assumption allows assuming the ideal behavior of the solid phase, $x_i^s = 1$ and $\gamma_i^s = 1$. Applying this assumption to Eq.4.6 yields the new iso-fugacity condition given in Eq4.7

$$f_{0,i}^s(T,P) = \hat{f}_i^f\left(T,P,\overrightarrow{x^f}\right) \tag{4.7}$$

The fugacity of the component "*i*" in the pure solid phase ($f_{0,i}^{s}(T,P)$) can be now calculated using Eq4.1 (or Eq4.2, depending on the presence or not of the solid-solid transition in the investigated temperature range), and its fugacity in the fluid phase is calculated using a fluid-phase model. In this work, the Peng Robinson Equation of State (PR EoS) [5] is used; the functional form and the different parameters of the PR EoS are reminded in Appendix C.

4.1.3 Pseudo-experimental activity coefficients from solid-phase fugacity

In the case of solid-liquid equilibrium, the fugacity of the component "*i*" in the liquid phase can be calculated using the excess approach. Therefore, the new equilibrium condition at the SLE is given in Eq4.8:

$$f_{0,i}^{s}(T,P) = x_i^l \gamma_i^l f_{0,i}^{l}(T,P) \tag{4.8}$$

Introducing Eq.4.1 into Eq4.8 and making some mathematic operations, the activity coefficient of the component "*i*" in the liquid phase in equilibrium with the pure solid phase at given pressure and temperature can be calculated using Eq4.9.

$$\gamma_i^l = \frac{1}{x_i^l}\exp\left[\frac{\Delta H_{T_tP_t}^{s\to l}}{RT}\left(\frac{T}{T_t}-1\right)+\frac{\Delta C_{P_{T_tP_t}}^{s\to l}}{R}\left(\frac{T_t}{T}-1-ln\left(\frac{T_t}{T}\right)\right)-\frac{\Delta V_{T_tP_t}^{s\to l}}{RT}(P-P_t)\right] \tag{4.9}$$

Seeing that all the properties involved in the calculation of the activity coefficient of the component "*i*" in the liquid phase can be obtained from experimental values, γ_i^l can be considered as a pseudo-experimental (p-exp) value.

$$\gamma_i^l = \gamma_i^{p-exp} \tag{4.10}$$

For the solid formers concerned by a solid-solid transition, the pseudo-experimental activity coefficient at temperatures lower than the solid-solid transition temperature is calculated using Eq4.11.

$$\gamma_i^{p-exp} = \frac{1}{x_i^l}\exp\left[\frac{\Delta H_{T_tP_t}^{s^\alpha\to l}}{RT}\left(\frac{T}{T_t}-1\right)+\frac{\Delta H_{T_{tr}P_{tr}}^{s^\alpha\to s^\beta}}{RT}\left(\frac{T}{T_{tr}}-1\right)+\frac{\Delta C_{P_{T_tP_t}}^{s^\alpha\to l}}{R}\left(\frac{T_t}{T}-1-ln\left(\frac{T_t}{T}\right)\right)-\frac{\Delta V_{T_tP_t}^{s^\alpha\to l}}{RT}(P-P_t)\right] \tag{4.11}$$

4.2 k_{ij} regression using a pseudo-experimental activity coefficient

In order to improve the representation of the phase equilibria involving pure solid phases when coupling the cubic equation of state with the classical approach, the binary interaction parameters (k_{ij}) used within the van der Waals mixing rule have been regressed by means of an algorithm based on a pseudo-experimental activity. The algorithm used for the regression of the k_{ij} is given in Fig4.2.

Each pseuds-experimental activity coefficient is calculated starting from the experimental liquid composition at the solid-liquid or solid-liquid-vapor equilibrium using Eq4.9 (or Eq4.11).

The algorithm presented in Fig.4.2 has been applied for the regression of reliable k_{ij} of several binary mixtures following three different scenarios:

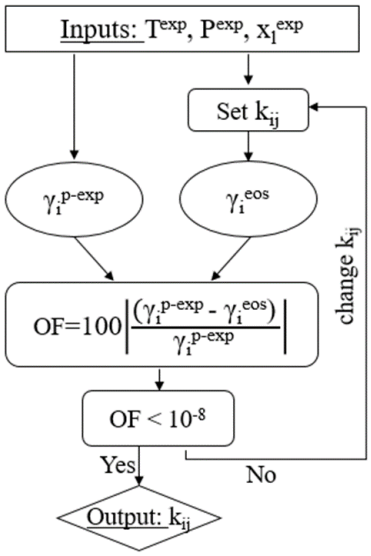

Figure 4.2: algorithm for the regression of the k_{ij} using a pseudo-experimental activity coefficient

In a first scenario, a reliable value of k_{ij} is regressed for each experimental point; thus, the obtained k_{ij} is the unique value that makes the model reproducing exactly the pseudo-experimental activity coefficient of a given experimental point (T,P,x). Fig4.3 shows the variation of the regressed k_{ij} on the SLE and the SLVE as a function of the temperature for 12 systems (methane+carbon dioxide, methane+benzene, methane+toluene, methane+n-pentane, methane+n-hexane, methane+n-heptane, ethane+carbon dioxide, ethane+n-octane, ethane+benzene, propane+carbon dioxide, propane+benzene, and propane+toluene).

Based on the results presented in Fig4.3, it can be noticed that for each binary mixture, the k_{ij} are almost constant in a wide temperature range. This allows inferring that a constant value of the binary interaction parameter could be sufficient for accurately describing the temperature dependence of the pseudo-experimental activity coefficients obtained from SLE and SLVE data.

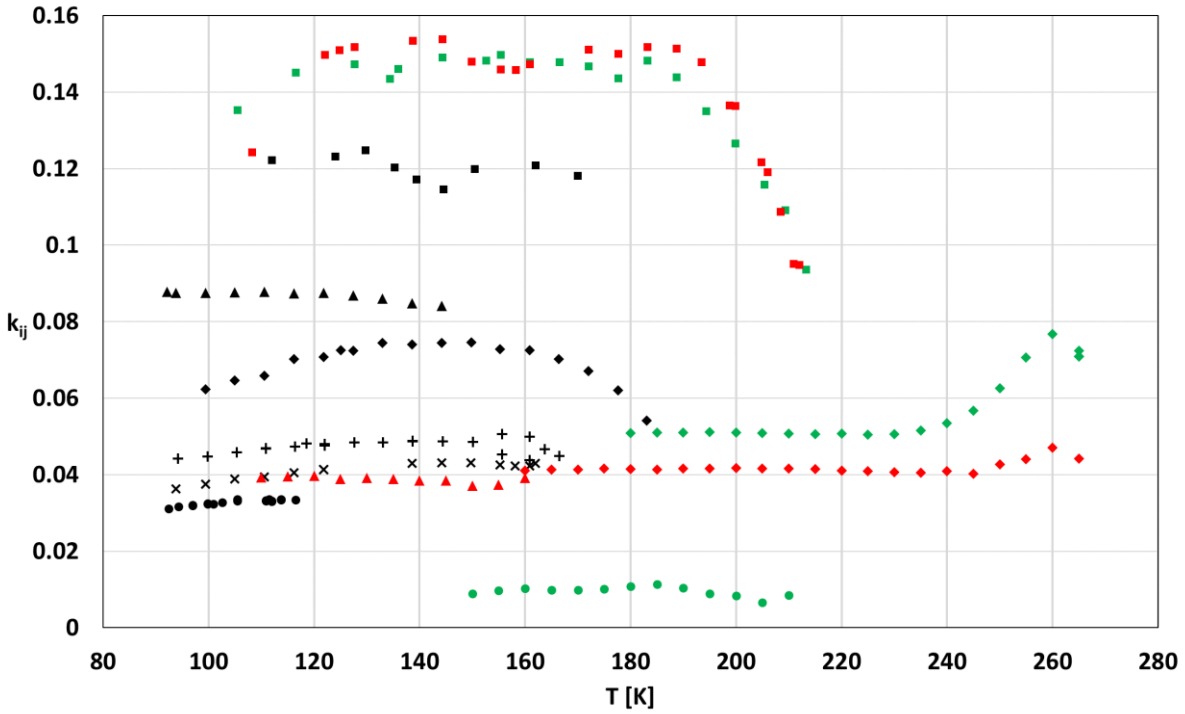

Figure 4.3: regressed k_{ij} against SLE (and/or SLVE) data of several binary mixtures as a function of temperature

■ *methane+carbon dioxide;* ● *methane+n-pentane;* x *methane+n-hexane;* ✚ *methane+n-heptane;*
♦ *methane+benzene;* ▲ *methane+toluene;*
■ *ethane+carbon dioxide;* ♦ *ethane+benzene;* ;● *ethane+n-octane;*
■ *propane+carbon dioxide;* ♦ *propane+benzene;* ▲ *propane+toluene.*

In order to stress the result obtained in the first scenario (reliable k_{ij} for the modeling of the SLE and SLVE are almost constant), two additional regression scenarios have been carried out. The second scenario is based on the regression of one constant value of k_{ij} that allows having the minimum average absolute deviation between the activity coefficients calculated using the PR EoS and the pseudo-experimental activity coefficients calculated using Eq4.9 (or Eq4.11) for all the available literature data of a given binary system. The third scenario considers a linear variation of the k_{ij} with respect to temperature, $k_{ij}=a + b \times T$, and the parameters "a" and "b" have been regressed to obtain the best agreement between the pseudo-experimental and the calculated activity coefficient of a given binary system (all the available data for the given system have been used for the regression work).

The Objective Function (OF) used in the 2nd and 3rd scenarios is given in Eq4.12, where N_P is the number of literature values. The values of the OF obtained for all the experimental points of the different investigated systems are presented in the fifth and sixth columns of Tab4.2. The use of the k_{ij} obtained in the 2nd and 3rd scenarios provides an acceptable representation of the literature data. The deviations between the pseudo-experimental activity coefficients calculated using the liquid equilibrium compositions reported in the

literature and the activity coefficients calculated using the PR EoS among all the investigated system do not exceed 21%. In addition, very similar results have been obtained when using a constant k_{ij} or a linear temperature-dependent k_{ij}. This outcome confirms that the use of a constant value of k_{ij} is a valid choice when dealing with the modeling of phase equilibria involving solid phases, at least for the systems investigated in this work.

$$OF = \frac{1}{N_p}\sum_{j}^{N_p} 100 \left| \frac{\gamma_j^{EoS} - \gamma_j^{p-exp}}{\gamma_j^{p-exp}} \right| \tag{4.12}$$

Table 4.2: comparison of the results when using constant k_{ij} and linear temperature dependence k_{ij}

System	N_p	T range [K]	P range [MPa]	OF (%)	
				k_{ij} =Constant	k_{ij} =a+bT
Methane+carbon dioxide	145	90.9 – 218.3	0.012 – 32.47	21.15	21.08
Methane+n-butane	11	113.3 – 129	0.09 – 0.14	1.22	1.20
Methane+n-pentane	40	92.4 – 139.8	0.15 – 10.4	3.23	2.06
Methane+n-hexane	63	90.9 – 178.7	0.00026 – 13.2	7.68	7.53
Methane+n-heptane	56	94.2 – 181	0.37 – 9.58	8.14	7.93
Methane+benzene	63	99.4 – 292.2	0.005 – 7.81	10.07	9.90
Methane+toluene	20	92.1 – 166.4	5.8 – 13.4	9.53	3.9
Ethane+carbon dioxide	19	105.4 – 213.2	0.0005 – 0.56	5.29	5.06
Ethane+benzene	39	97.2 – 275.2	< 1	13.76	6.46
Ethane+n-octane	13	150 – 210	0.01 – 0.16	1.30	1.11
Propane+carbon dioxide	22	108.2 – 212	< 0.4	9.44	9.35
Propane+benzene	42	95.7 – 273.2	< 0.18	19.67	9.24
Propane+toluene	11	110 – 160	< 0.0008	2.37	1.59
Nitrogen+carbon dioxide	165	78 – 190	0.51 – 20.27	5.57	4.24

4.3 Constant k_{ij} for the modeling of the SFE

On the basis of the results obtained in the different regression scenarios, it can be considered that the choice of using constant k_{ij} instead of linear temperature-dependent k_{ij} is sufficient for the accurate representation of the phase equilibria involving solid phase when coupling the classical approach with the PR EoS.

In order to deeply analyze the reliability of the modeling of solid-fluid equilibria using constant k_{ij}, some systems are investigated and presented in the following sections.

4.3.1 Methane+benzene

The thermodynamic behavior of the methane+benzene system in the presence of solid benzene has been widely studied in the literature. SLE data have been reported by Kuebler and McKinley [6] and Siahvashi et al. [7], SLVE data have been reported by Luks et al. [8] and Rijkers et al. [9], while SVE data have been reported by Rijkers et al. [9], Hughes et al. [10] and Siahvashi et al. [7]. The lack of the experimental pressure in the data reported by Neumann et al. [11] and Teller et al. [12] does not allow to link these data to a specific kind of equilibrium (either SLE or SLVE).

The SLE and the SLVE presented in refs [6], [7], and [8] have been used for calculating the pseudo-experimental activity coefficients and then a constant of k_{ij} has been regressed and a value of 0.0707 has been obtained. Fig4.4 shows the comparison between the calculated and the experimental solubility limits of solid benzene in liquid methane reported in ref [6]. The PR EoS with constant k_{ij} coupled with the solid phase fugacity from Eq4.1 provides a good representation of the literature data, an AAD of less than 12% has been obtained. This AAD value corresponds to about 0.3 ppm at the LNG temperature. The AAD obtained using the constant k_{ij} is comparable to the experimental uncertainties encountered when dealing with the experimental investigation of such a system at cryogenic conditions.

In ref [7], Siahvashi and coworkers have reported the melting pressure-temperature conditions of two commercial mixtures (x_2=0.001012 and x_2=0.000199, where x_2 is the global composition of benzene in the mixture). Fig4.5 shows the comparison between these data and the modeling results obtained using the PR EoS with constant k_{ij} coupled with the classical approach. The model is in good agreement with the data reported by Siahvashi and coworkers and provides an AAD between the experimental solidification temperatures and the calculated ones of 0.5% for the mixture where x_2=0.001012, and 1.6% for the mixture where x_2=0.000199.

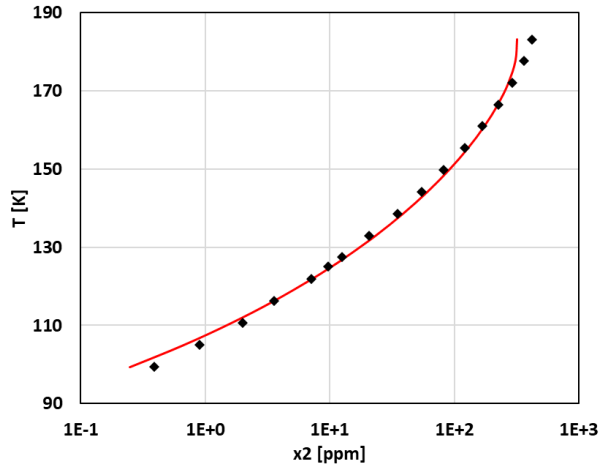

Figure 4.4: solubility limits of solid benzene(2) in liquid methane(1) at 5.41 MPa.
♦ *ref* [6]*;*
— *PR EoS with constant k_{ij} coupled with the CA*

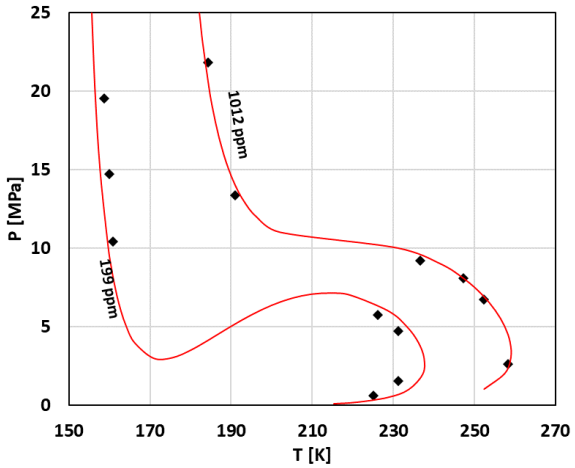

Figure 4.5: solidification conditions of two mixtures of (1)methane+(2)benzene at different pressures
♦ *ref* [7]*;*
— *PR EoS with constant k_{ij} coupled with the CA*

4.3.2 Methane+n-heptane

The phase equilibria of the methane+n-heptane system involving solid n-heptane are reported in refs [6] [13], and [14]. Kuebler and McKinley measured the solubility of solid n-heptane in liquid methane at temperatures ranging from 166.5 K down to 94.2 K[6]; Tiffin et al. reported in ref [13] a complete study of the SLVE locus (from the triple point of n-heptane down to 131 K) together with the quadruple point, Solid-Liquid-Liquid-Vapor Equilibrium ($S_2L_1L_2VE$), of this system; Neumann and Mann measured the solubility limits of solid n-heptane in liquid methane at temperatures from 150 K down 103 K [14]; the absence of the pressure does not allow determining the kind of the equilibrium of these data (SLE or SLVE). The data from refs [6] and [13] have been used to regress a constant k_{ij} and a value of 0.0475 has been obtained.

The use of this value leads to represent the solubility limits from ref [6] with an AAD of 7.91% and those from ref [13] with an AAD of 7.56%. The pressures of the SLVE reported in ref [13] are represented with an AAD of 4.91 %. Concerning the quadruple point reported in [13], the average absolute deviation between the modeling results and the literature data is 0.86% for the pressure, 0.45% for the temperature, 8.13% for the n-heptane-rich liquid phase composition, and 45.84% for the methane-rich liquid phase composition. The comparison between the literature data and the modeling results using a constant k_{ij} are presented in Figs4.6-8.

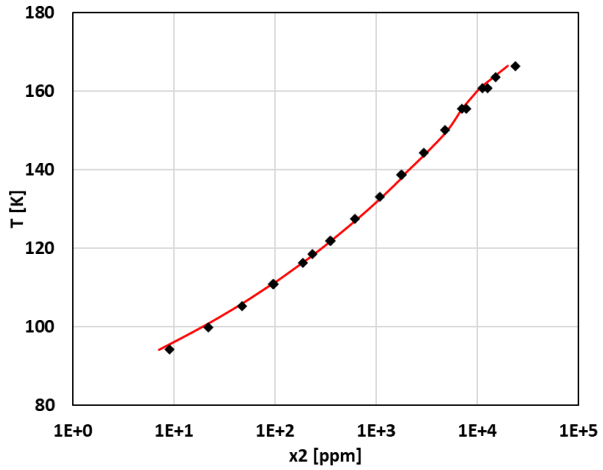

Figure 4.6: solubility limits of solid n-heptane(2) in liquid methane(1)at the SLE
♦ *ref* [6]; — *PR EoS with constant k_{ij} coupled with the CA*

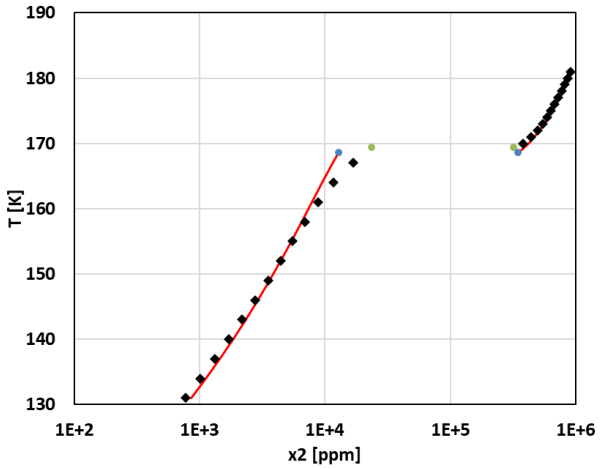

Figure 4.7: solubility limits of solid n-heptane(2) in liquid methane(1) at the SLVE.
♦ *ref* [13];
— *PR EoS with constant k_{ij} coupled with the CA*
quadruple point: ● *ref* [13]; ● *PR EoS with constant k_{ij}*

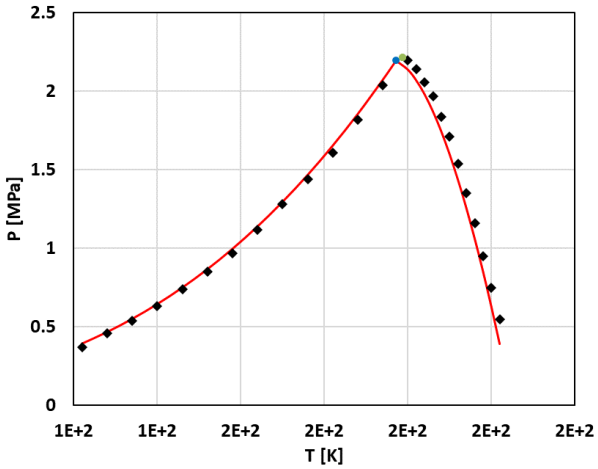

Figure 4.8: pressure-temperature SLVE loci of the methane+n-heptane system.
♦ *ref* [13];
— *PR EoS with constant k_{ij} coupled with the CA*
quadruple point: ● *ref* [13]; ● *PR EoS with constant k_{ij}*

4.3.3 Ethane+n-octane

The SLVE data of the ethane+n-octane system have been reported by Kohn et al. [15]. These data have been used for regressing a constant k_{ij} and a value of 0.0098 has been obtained. The liquid compositions at the SLVE are presented in Fig4.9 by filled black diamonds and compared to the modeling results obtained using a constant k_{ij} regressed against the pseudo-experimental activity coefficient calculated starting from the values reported in ref [15]. Although the data extend over temperatures ranging from 210 K down to 150 K, the use of non-temperature dependent k_{ij} provides a very good representation of the solubility limits of n-

octane in liquid ethane. The AAD between the experimental and the calculated solubility limits of n-octane in liquid ethane is 1.42%.

Fig4.10 shows the pressure-temperature diagram of the SLVE of the ethane+n-octane system. For decreasing temperatures from the triple point temperature of n-octane, the SLVE pressure reported in ref [15] increases until reaching a maximum value at 200 K, then it decreases for lower temperatures; the same behavior has been obtained when using the PR EoS with constant k_{ij} (red line) coupled with the CA. The SLVE pressures tend to reach the saturation pressures of ethane (green dashed line) at low temperatures (lower than 170 K), in this temperature region, the vapor composition at the SLVE can be considered as pure ethane.

Despite the qualitatively correct representation of the SLVE locus, the modeling results underestimate the literature values for temperatures higher than 195 K and overestimate the literature values for lower temperatures. The maximum pressure given by the model and reported in the literature are at approximately the same temperature (200 K); however, the calculated pressure at this temperature is relatively lower than the value reported in ref [15] (0.142 MPa and 0.165 MPa respectively). The PR EoS with constant k_{ij} coupled with the Eq4.1 for solid n-octane represents the SLVE pressures reported in ref [15] with an AAD of 13.9%.

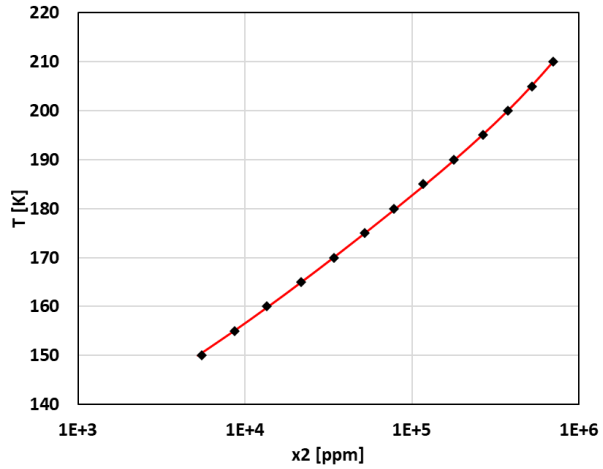

Figure 4.9: solubility limits of solid n-octane(2) in liquid ethane(1) at the SLVE.
♦ *ref* [15]*;*
— *PR EoS with constant k_{ij} coupled with the CA*

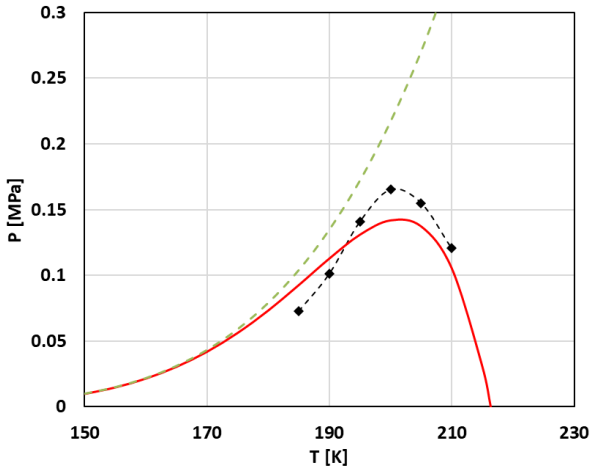

Figure 4.10: pressure-temperature SLVE locus of the ethane+n-octane system.
♦ *ref* [15]*;* — *PR EoS with constant k_{ij} coupled with the CA;* - - - *saturation line of pure ethane*

4.3.4 Propane+cyclohexane

Chen et al. have reported SLVE data of the propane+cyclohexane system from 245 K down to 156 K in ref [16]. These data have been used for regressing a constant k_{ij} and a value of 0.0116 has been obtained

The data reported in ref [16] are presented in Fig4.11 together with the modeling results obtained when using the PR EoS with constant k_{ij} and coupled with the CA. Seeing that cyclohexane is concerned by a solid-solid transition at 186.09 K [17], Eq4.1 has been coupled with the PR EoS for the iso-fugacity condition for temperatures higher than the temperature of the solid-solid transition, whereas Eq4.2 has been used instead of Eq4.1 for lower temperatures.

The use of the constant value of k_{ij} provides a very good representation of the literature data and presents an AAD of 2.13% on the molar composition (solubility limit). Concerning the SLVE pressure, the modeling results are not in agreement with the literature data, and a high AAD has been obtained (68.07%). It is worth noticing that no reliable k_{ij} (values from -0.15 up to 0.15) has been found for the accurate representation of the SLVE pressures reported in ref [16].

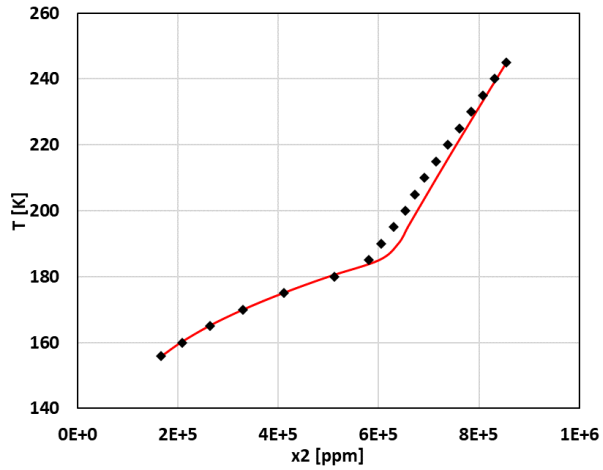

Figure 4.11: solubility limits of solid cyclohexane(2) in liquid propane(1) at the SLVE.
♦ *ref* [16]*;*
— *modeling*

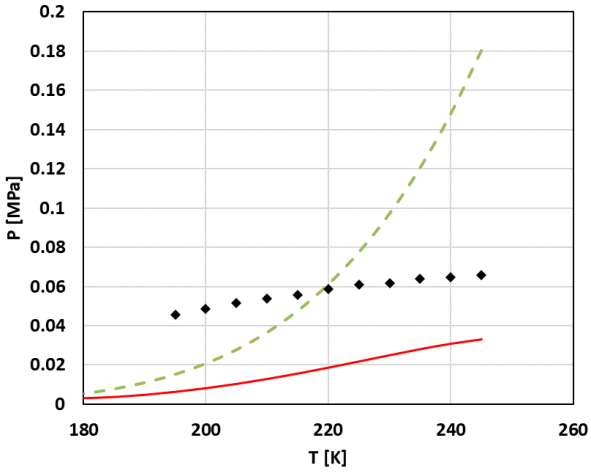

Figure 4.12: pressure-temperature SLVE locus of the propane+cyclohexane system.
SLVE: ♦ *ref* [16]*;* — *modeling*
Saturation line of pure propane: --- *PR EoS*

The comparison of the SLVE pressures with the saturation pressures of pure propane (Fig4.12) questions the reliability of the pressure values from ref [16]. The literature SLVE pressures cross the saturation line of pure propane at approximately 220 K, thus the SLVE pressures are higher than the saturation pressures of pure methane. This could mean that the propane+cyclohexane system could exist in the vapor phase for pressures higher than the saturation pressure of pure propane (the more volatile component). In such a case, the cyclohexane composition in the vapor phase is higher than the liquid phase composition, seeing that the vapor compositions are not reported in ref [16], it is difficult to elucidate the disagreement between the behavior inferred from the literature data and the one from the model; nevertheless, from the author point of view, and based on the investigation of similar systems, it can be stated that the behavior inferred from the modeling is more representative of the real behavior. To make more insight into the two different

behaviors (as inferred from the model and from the literature data), qualitative pressure-composition diagrams at a temperature lower than 220 K are shown in Fig4.13 and Fig4.14.

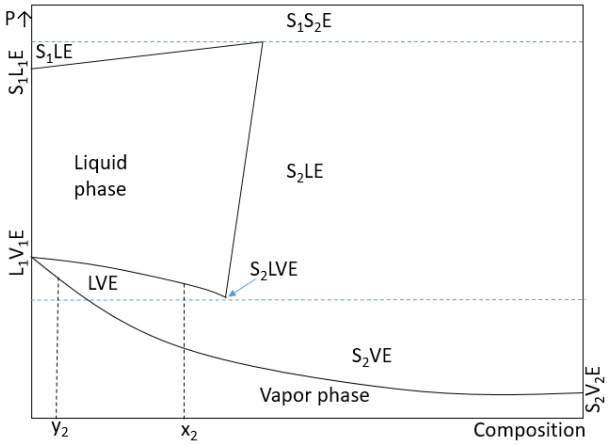

Figure 4.13: pressure-composition diagram of the propane(1)+cyclohexane(2) at a temperature lower than 220 K as inferred from the modeling results

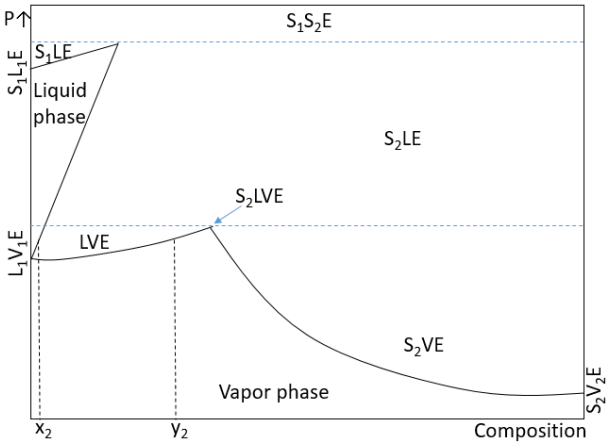

Figure 4.14: pressure-composition diagram of the propane(1)+cyclohexane(2) at a temperature lower than 220 K as inferred from the data reported in ref [16]

4.4 On the continuity of the k_{ij} between SFE and FFE

For evaluating the continuity of the binary interaction parameter when passing from SFE to FFE, the k_{ij} regressed on the pseudo-experimental activity coefficients calculated starting from the liquid phase composition at the SLE and SLVE presented in the previous section have been used to predict the fluid-fluid equilibria of some binary mixtures of interest for the LNG production. These predictions have been compared to the predictions obtained when using the two widely used models, the predictive Peng Robinson EoS (PPR78 EoS) [18] and the predictive Soave Redlich Kwong EoS (PSRK EoS) [19] (as implemented in Simulis thermodynamic software) and the literature FFE data of some binary mixtures.

Tab4.3 presents a comparison of the capability of the three models to predict the Liquid-Vapor Equilibrium (LVE) and/or the Liquid-Liquid Equilibrium (LLE) compositions of several systems at temperatures close to the triple point temperature of the heaviest component of the considered binary systems. The comparison between the models and the literature data has been evaluated through the AAD calculated using Eq4.13.

$$AAD = \frac{100}{N_p}\sum_{i=1}^{N_P}\left[\left|\frac{x_1^{cal}-x_1^{exp}}{x_1^{exp}}\right| + \left|\frac{x_2^{cal}-x_2^{exp}}{x_2^{exp}}\right| + \left|\frac{y_1^{cal}-y_1^{exp}}{y_1^{exp}}\right| + \left|\frac{y_2^{cal}-y_2^{exp}}{y_2^{exp}}\right|\right] \quad (4.13)$$

N_p is the number of the experimental points, x and y are the composition of the liquid and the vapor phase, respectively (the experimental and the calculated compositions are represented using the superscript *exp* or *cal*).

Table 4.3: comparison between the PR EoS with k_{ij} regressed on SLE and SLVE, the PPR78 EoS, and the PSRK EoS for the representation of low-temperature FFE.

System	T_t^* [K]	Ref	N_p	T range [K]	P range [MPa]	AAD [%]		
						PR EoS	PPR78 EoS	PSRK EoS
Methane+n-butane	134.6	[20]	12	144.3 –166.5	0.1 – 1.7	51.23	40.45	50.08
		[21]	14	166.5 – 177.6	0.3 – 3.1	43.08	20.35	32.39
Methane+n-pentane	143.46	[22]	19	176.2 –199.9	0.1 – 4.1	33.28	35.57	52.16
		[23]	36	177.6 – 198.2	0.3 – 4.4	98.51	84.50	73.74
Methane+n-heptane	182.56	[24]	13	185	0.3 – 6.2	22.16	19.00	8.65
		[25]	5	170 – 190	2.3 – 4.5	13.31	3.65	36.43
Methane+benzene	278.5	[26]	16	273 – 293	4.9 – 39.2	39.64	36.96	85.86
		[10]	6	278.15	2.3 – 7.8	71.44	86.69	98.68
Methane+toluene	178	[27]	7	188.7	0.7 – 20.7	50.24	55.31	120.63
		[10]	9	188.1 – 198.1	2 – 11.5	61.31	61.18	174.21
Methane+carbon dioxide	216.58	[28]	37	209.3 – 223.7	1.5 – 6.5	36.23	20.62	16.22
		[29]	25	230	0.9 – 9.1	32.57	19.07	22.03
Ethane+benzene	278.5	[30]	7	298.15	0.7 – 3.8	22.06	18.87	20.38
Ethane+n-octane	216.2	[31]	64	273.2 – 373.2	0.4 – 5.3	46.72	47.2	45.46
		[32]	18	318.2 – 338.2	1.5 – 6.8	29.51	29.36	37.61
Ethane+carbon dioxide	216.58	[33]	23	207 – 210	0.3 – 0.9	34.34	36.57	25.76
		[34]	8	207	0.3 – 0.5	31.09	14.07	26.6
Propane+benzene	278.5	[35]	6	37.8	0.1 – 1.1	23.57	27.17	30.05
Propane+carbon dioxide	216.58	[36]	289	210.9 – 349.8	0.06 – 5.9	7.92	8.03	8.18
		[29]	29	230	0.2 – 0.9	41.56	48.56	30.35
		[37]	14	253.15	0.2 – 1.8	30.39	19.34	9.01
Propane+cyclohexane	279.7	[38]	7	313	0.2 – 1.3	6.01	6.2	18.91
Nitrogen+carbon dioxide	216.58	[39]	21	218.2 – 232.8	1.3 – 13.9	16.15	15.82	18.37
		[40]	11	220 – 240	1.5 – 16.7	17.54	18.57	14.32
		[41]	11	250	2.6 – 14	9.9	9.81	14.47
Overall result						27.34	24.79	27.50

[*] *T_t: is the triple point temperature of the heaviest component in the binary mixture taken as the average of all the values reported in the NIST chemistry webbook website.*

In the following, some binary systems have been selected for deeply discussing the capability of the PR EoS with a constant value of k_{ij} regressed on the pseudo-experimental activity coefficients calculated from the SLE and the SLVE to represent the fluid-fluid equilibria at temperatures close to the triple point temperature of the heaviest component in the binary mixture. In addition, the obtained results are compared to those obtained when using the PPR78 EoS and the PSRK EoS.

4.4.1 Methane+benzene

The vapor-liquid equilibria of the methane+benzene system at temperatures close to the triple point temperature of benzene are reported by Stepanova et al. at 273.15 K and 293.15 K [26], and by Hughes et al. at 278.15 K [10]. The PR EoS with constant k_{ij} regressed on the SLE and the SLVE data, the PPR78 EoS, and the PSRK EoS are used for predicting these VLE data of this system and the results are compared to literature data. Despite the use of a constant k_{ij} regressed on the SLE and SLVE data, the PR EoS provides a satisfactory prediction compared to the PPR78 EoS and PSRK EoS; the average absolute deviation between the modeling results and the literature values are given in Tab4.3.

The comparison between the literature values and the model's predictions at 273.15 K and 293.15 K is shown in Figs4.15-16. The choice of the k_{ij} significantly affects the prediction of the critical locus; indeed, the use of the three models provides comparable results in the low-pressure region, however the difference among the modeling results increases by increasing pressure.

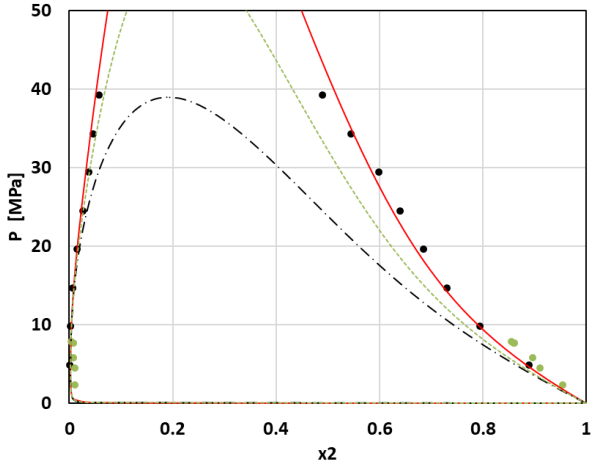

Figure 4.15: pressure-composition of the methane(1)+benzene(2) system at the VLE at 273.15K.
● *ref* [26]; ● *ref* [10]
— *PR EoS;* - - - *PPR78 EoS;* - - - *PSRK EoS*

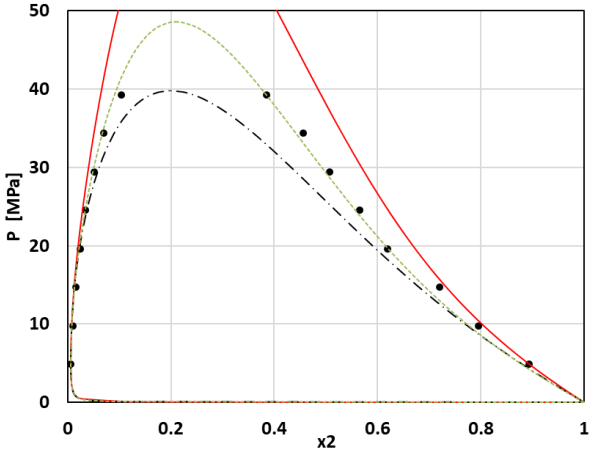

Figure4.16: pressure-composition of the methane(1)+benzene(2) system at the VLE at 293.15K.
● *ref* [26];
— *PR EoS;* - - - *PPR78 EoS;* - - - *PSRK EoS*

4.4.2 Methane+n-pentane

The low-temperature VLE data of the methane+n-pentane system have been reported by Chu et al. at temperatures down to 176.2 K [22], and Kahre at temperatures down to 177.6 K [23]. The comparison between the modeling results obtained using the three models and the literature values is presented in Figs4.17-20.

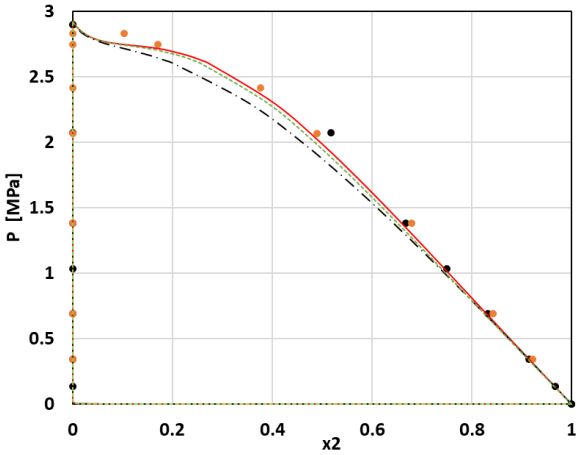

Figure 4.17: pressure-composition of the methane(1)+n-pentane(2) system at the VLE at 176.2K

● *ref* [22]; ● *ref* [23]

— *PR EoS;* - - - *PPR78 EoS;* - - - *PSRK EoS*

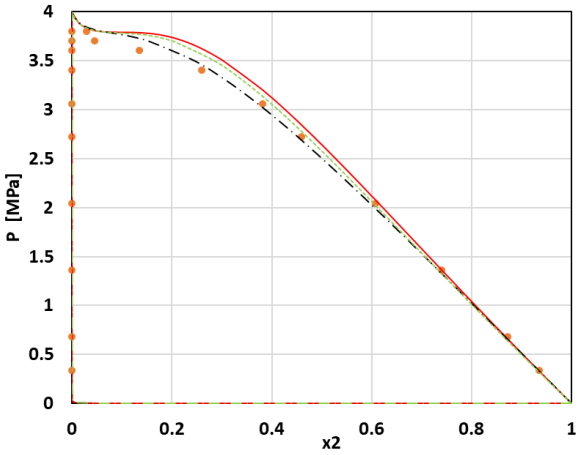

Figure 4.18: pressure-composition of the methane(1)+n-pentane(2) system at the VLE at 185.95K

● *ref* [23]

— *PR EoS;* - - - *PPR78 EoS;* - - - *PSRK EoS*

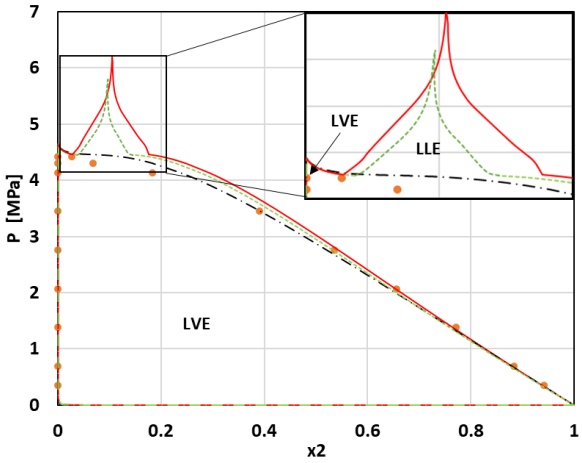

Figure 4.19: pressure-composition of the methane(1)+n-pentane(2) system at the VLE at 190.95K

● *ref* [23]

— *PR EoS;* - - - *PPR78 EoS;* - - - *PSRK EoS*

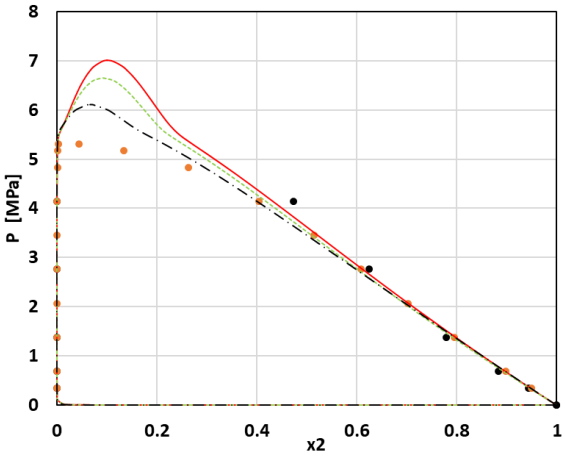

Figure 4.20: pressure-composition of the methane(1)+n-pentane(2) system at the VLE at 198.15K

● *ref* [22]; ● *ref* [23]

— *PR EoS;* - - - *PPR78 EoS;* - - - *PSRK EoS*

Even though the lowest temperature isotherm, investigated here, is 33 K higher than the triple point temperature of n-pentane (143.46 K), the use of the PR EoS with constant k_{ij} regressed on the SFE data provides very similar results compared to the PPR78 EoS and the PSRK EoS as it can be observed from the AADs gathered in Tab4.3 and Fig4.17-18. The three models give an acceptable prediction of the liquid composition; however, the predicted vapor composition is a little far from the literature values independently from the used model. In addition, the predicted thermodynamic behavior at pressures close to the critical pressure of methane (4.6 MPa) presents some divergence compared to the behaviors reported in the

literature, especially for the isotherms close to the critical point of methane. At this condition, the PR EoS with constant k_{ij} from the SFE and the PPR78 EoS predict either a liquid-liquid equilibrium or a vapor-liquid equilibrium (depending on the global composition). This disagreement can be expected seeing the difficulties of cubic EoSs to reproduce the critical thermodynamic behavior of such a system whose behavior is close to the one of methane+n-hexane that is concerned by a liquid demixing in this region. Nevertheless, a stability test must be carried out to confirm the reliability of these modeling results.

4.4.3 Ethane+n-octane

The VLE behavior of the ethane+n-octane system has not been investigated in the temperature region close to the triple point temperature of n-octane (216.4 K); nevertheless, VLE data are reported by Rodrigues et al. at temperatures from 273 K up to 373 K [31], and by Weng and Lee at temperatures from 313 K up to 338 K [32]. Even if these literature data are not at temperatures close to the triple point temperature of the n-octane, the modeling results obtained when using the PR EoS with constant k_{ij} regressed on the SFE are in quite good agreement with the literature data as it can be observed in Figs4.21-22. Furthermore, the predictions are very similar to the one obtained when using the PPR78 EoS or the PSRK EoS.

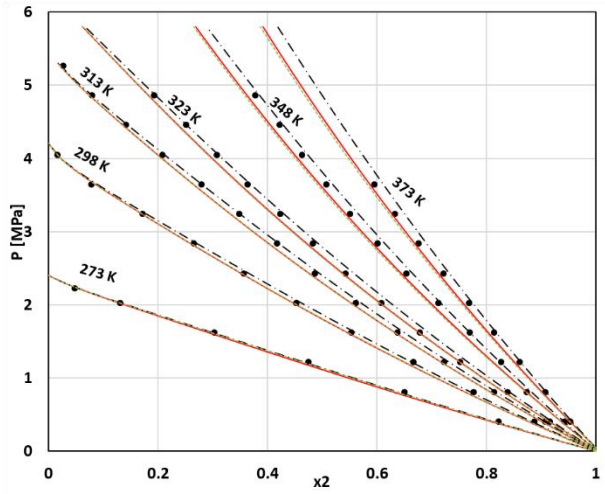

Figure 4.21: pressure-liquid composition of the ethane(1)+n-octane(2) system at the VLE.
● *ref* [31]
— *PR EoS;* - - - *PPR78 EoS;* - - - *PSRK EoS*

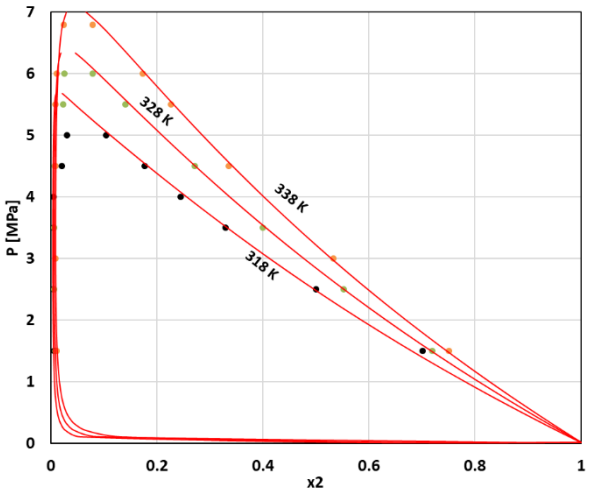

Figure4.22: pressure-composition of the ethane(1)+n-octane(2) system at the VLE.
● *ref* [32]*;*
— *PR EoS*

4.4.4 Propane+cyclohexane

The only data accounting for VLE of the propane+cyclohexane system are reported by Richon et al. at 313 K, 393 K, and 473 K in ref [38]. The use of a constant k_{ij} regressed on the SLVE data within the PR 78 EoS for the prediction of the VLE data gives satisfactory results. The model represents the literature data with an AAD of 6.01% while the use of PPR78 and PSRK provides an AAD of 6.2% and 18.91% respectively.

This result consolidates the fact that the use of constant k_{ij} can be sufficient for the modeling of the phase equilibria over a large range of temperatures for this system.

The comparison between the literature data and the modeling results using the three models is given in Figs4.23-24. The results from the three models are almost overlapped which means that the PR EoS with constant k_{ij} regressed on the SLVE data is able to represent the VLE data as well as the models whose parameters have been regressed with respect only to FFE (PPR78 and PSRK).

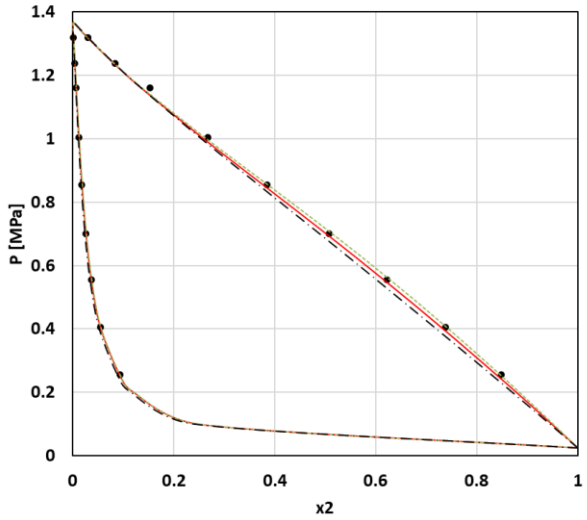

Figure 4.23: pressure-composition of the propane(1)+cyclohexane(2) system at the VLE at 313K.
● *ref* [38]
— *PR EoS;* - - - *PPR78 EoS;* - - - *PSRK EoS*

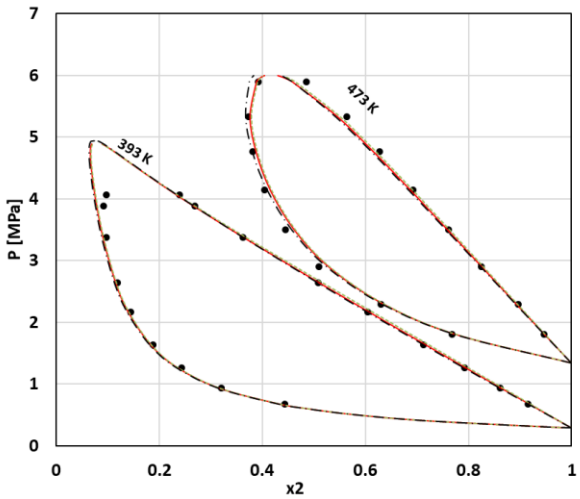

Figure 4.24: pressure-composition of the propane(1)+cyclohexane(2) system at the VLE at 393K and 473K.
● *ref* [38]
— *PR EoS;* - - - *PPR78 EoS;* - - - *PSRK EoS*

From the analysis of results summarized in Tab4.3 and those presented in Figs4.15-24, it can be concluded that the k_{ij} values regressed on pseudo-experimental activity coefficients obtained from SLE and the SLVE data provide a satisfactory prediction of fluid-fluid equilibrium, at least at temperatures close to the triple point temperature of the heaviest component (the modeling results are similar to those obtained when applying the PPR78 EoS and the PSRK EoS). For pressure-temperature conditions far from the critical region, the use of the PR EoS with constant k_{ij} appears to be a valid choice for the accurate representation of the phase equilibria, at least for the systems involved in the LNG production.

4.5 Prediction of the SFE using k_{ij} from FFE

The results obtained in the previous section showed that the k_{ij} is continuous when passing from the fluid-fluid equilibria to the solid-fluid equilibria (the same k_{ij} provide a satisfactory representation of the SFE and the low-temperature FFE); in addition, a constant value of the k_{ij} could be sufficient for the accurate

representation of the phase equilibria over a large range of temperature (FFE and SFE). Based on these observations, the possibility of accurately predicting the phase equilibria involving solid phases using a constant k_{ij} regressed on the fluid-fluid equilibria at temperatures close to the triple point temperature of the solid former is evaluated in this section.

Several binary systems presenting FFE at temperatures close to the triple point temperature of the heaviest component have been investigated and a constant value of the k_{ij} has been regressed on the FFE for each binary system. Each k_{ij} has then been used within the PR EoS for evaluating the possibility of accurately predicting the phase equilibria involving the solid phases when coupled with the classical approach for calculating the fugacity of the solid former in the solid phase (considering the solid phase as pure). The PR EoS with constant k_{ij} has been compared to the PPR78 EoS that uses a temperature-dependent k_{ij} (The PPR78 EoS has been also coupled with the classical approach). This comparison is not performed for evaluating the capability of the PPR78 EoS to predict the SFE, seeing that this model is developed for predicting the fluid-fluid equilibria, but for showing that the extrapolation of the temperature-dependent k_{ij} to low temperatures could be unsafe and can lead to inaccurate values.

4.5.1 Methane+carbon dioxide

The study of the thermodynamic behavior of the methane+carbon dioxide system is of high interest for several applications; this motivated several research groups to carry out experimental measurements for investigating the thermodynamic behavior of this system.

Vapor-liquid equilibria have been reported by Donnelly et al. [28], Webster and Kidnay [29], Kaminishi et al. [42], Neumann and Walch [43], Davalos et al. [44], Mraw et al. [45], Somait and Kidnay [46], Al-Sahhaf et al. [40], Xu et al. [47], Bian et al. [48], Wei and Brown [34], Sauza et al. [49], Petropoulou et al. [50] and Nasir et al. [51]. The data reported in these references cover almost all the temperature range between the triple point and the critical point of carbon dioxide (216.58 K and 304.18 K).

Fig4.25 shows the k_{ij} values regressed against the data reported in the above-cited references. The k_{ij} shows a tendency to reach a constant value at temperatures lower than 270 K. This behavior consolidates the conclusion drawn in the previous sections: *i)* a constant k_{ij} is sufficient for the accurate modeling of the solid-fluid phase equilibria, and *ii)* this value is continuous when crossing the triple point of the solid former and provides an accurate representation of the fluid-fluid equilibria in this temperature region.

The red line in Fig4.25 shows the constant k_{ij} regressed on the VLE data at temperatures lower than 270 K, whereas the dashed green line shows the k_{ij} as calculated from the PPR78 EoS.

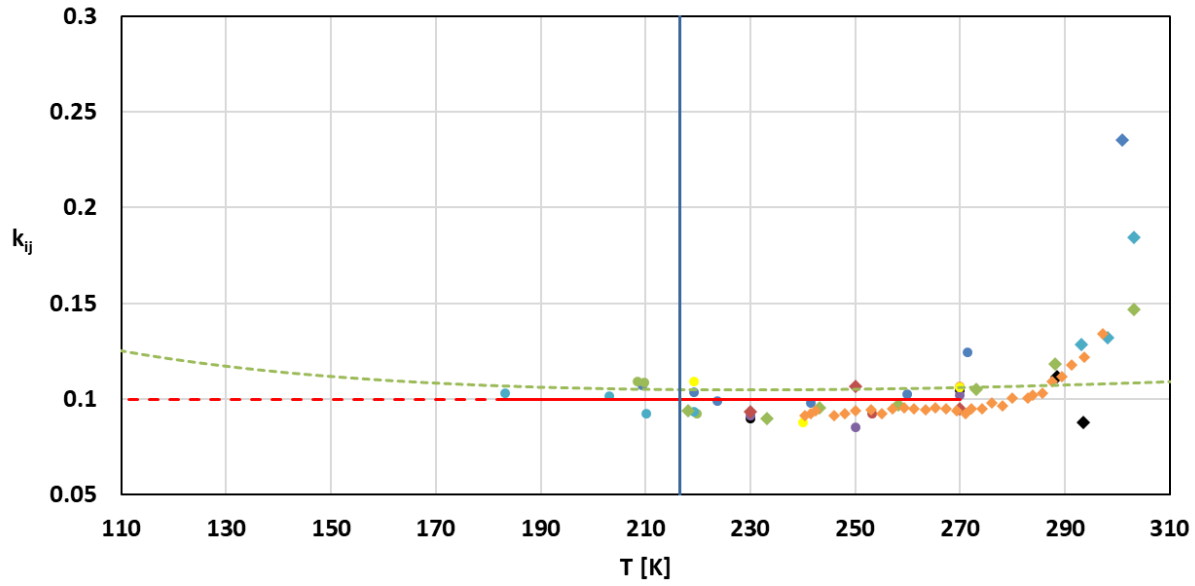

Figure 4.25: variation of the k_{ij} regressed on the VLE data of the methane+carbon dioxide system as a function of temperature.

kij regressed with respect to each data set : ● *ref* [29]; ● *ref* [28]; ● *ref* [42]; ● *ref* [43]; ● *ref* [44]; ● *ref* [45]; ● *ref* [46]; ● *ref* [40]; ♦ *ref* [47]; ♦ *ref* [48]; ♦ *ref* [34]; ♦ *ref* [49]; ♦ *ref* [50]; ♦ *ref* [51]

— *constant k_{ij} regressed on the low-temperature VLE data (T<270 K);* - - - *k_{ij} from PPR78 EoS*

— *triple point temperature of carbon dioxide*

For evaluating the possibility of predicting the SFE using k_{ij} regressed on the FFE, these two k_{ij} (the one from the PPR78 EoS and the constant k_{ij} regressed for the PR EoS on VLE data at temperatures lower than 270 K) have been used for calculating the phase equilibria of the methane+carbon dioxide system in the presence of solid carbon dioxide.

Figs4.26-27 show the comparison between the solubility limits of the solid carbon dioxide in liquid methane and the pressure-temperature locus of the SLVE reported in the literature and the modeling results obtained when coupling the solid phase fugacity from the classical approach with the PR EoS. The red continuous line corresponds to the prediction obtained using a constant k_{ij} regressed on the VLE (T<270 K), while the dashed green line shows the prediction obtained when using the PPR78 EoS.

According to Figs4.26-27, it is possible to state that the use of both models provides a good representation of the SLE and the SLVE. Despite the use of the PPR78 EoS at temperatures lower than its validity domain, it provides a good representation of the SLVE data; this is due to the small variation of the k_{ij} from the PPR78 EoS at low-temperature, see Fig4.25.

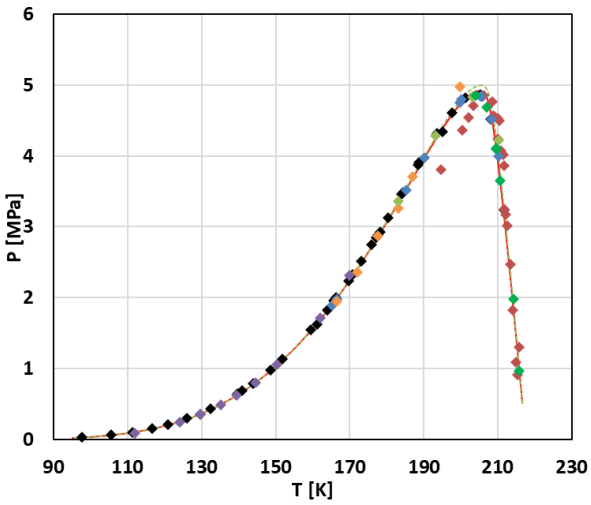

Figure 4.26: solubility limits of solid carbon dioxide in liquid methane at the SLVE

♦ *ref* [52]; ♦ *ref* [28]; ♦ *ref* [53]; ♦ *ref* [54]; ♦ *ref* [55]; ♦ *ref* [45]

— *PR EoS;* - - - *PPR78 EoS*

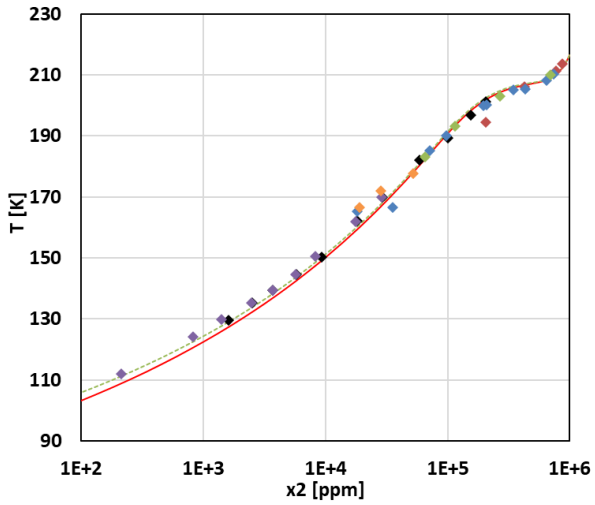

Figure 4.27: SLVE locus of the methane+carbon dioxide system

♦ *ref* [52]; ♦ *ref* [28]; ♦ *ref* [53]; ♦ *ref* [54]; ♦ *ref* [55]; ♦ *ref* [45]; ♦ *ref* [49]

— *PR EoS;* - - - *PPR78 EoS*

4.5.2 Methane+toluene

The VLE of the methane+toluene system have been investigated by El-Bishlawi and Spencer [56], Lin et al. [27], Rabe [24], Legret et al. [57], Srivatsan et al. [58], Hughes et al. [10], and Chang et al. [59]. The LLE data have been reported by Hughes et al. [10] and by Lin et al. [27]. In this work, optimal k_{ij} have been regressed for each isotherm in order to minimize the difference between the literature data and the values calculated using the PR EoS, and the obtained values are presented in Fig4.28. As shown in Fig4.28, the k_{ij} regressed on the data of Chang et al. [59] deviate from the other values, and this is due to the disagreement observed between these data and those reported in the other references.

Despite some scattering on the values of the regressed k_{ij}, it can be noticed that they tend to reach a constant value, especially at temperatures close to the triple point temperature of toluene. A constant k_{ij} is consequently regressed with respect to all the literature data, except those reported in ref [59], and a value of 0.085 has been obtained. This constant value has been used within the PR EoS for representing the FFE at temperatures slightly higher than the triple point temperature of toluene and compared to the PPR78 and the PSRK EoS.

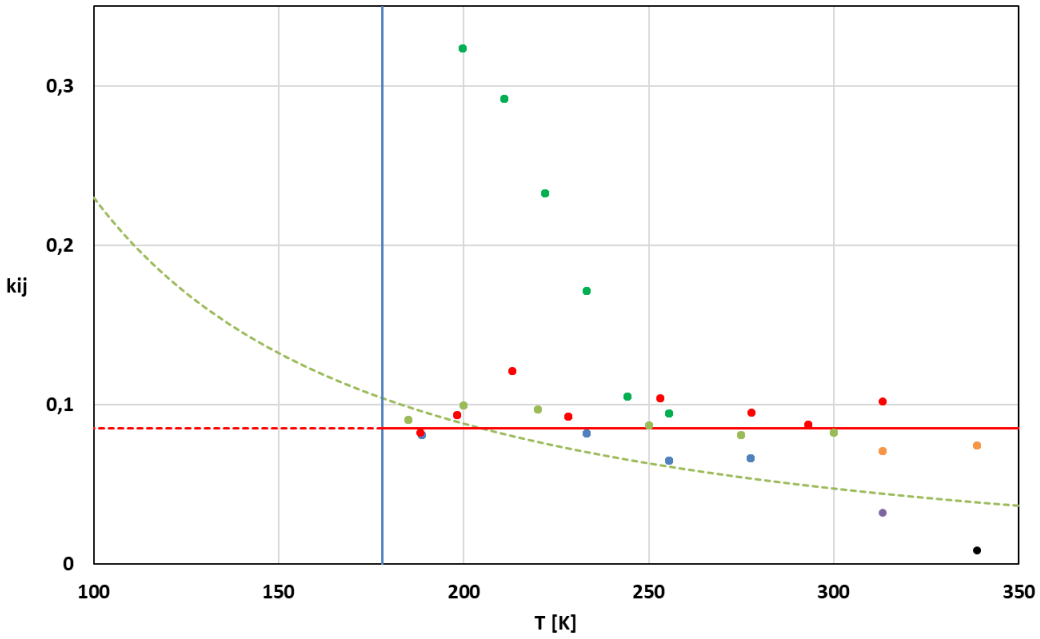

Figure 4.28: variation of the k_{ij} regressed on the VLE and LLE data of the methane+toluene system as a function of temperature.

kij regressed with respect to each FFE dataset: ● *ref* [56], ● *ref* [27], ● *ref* [24], ● *ref* [57], ● *ref* [10], ● *ref* [59], ● *ref* [58]*;*

— *constant* k_{ij} *regressed on all the FFE data;* - - - k_{ij} *from PPR78 EoS;*

— *triple point temperature of toluene*

The use of constant k_{ij} leads to representing the data collected in this work with an AAD of 23.34%, whereas the predictions of the PPR78 EoS and the PSRK EoS represent the literature data with an AAD of 21.54% and 41.14%, respectively. The PR EoS with constant k_{ij} provides comparable results to those obtained from the PPR 78 EoS (which uses a temperature-dependent k_{ij}). However, a large deviation between the models and the literature values has been noticed in the critical region; for each temperature investigated in this work, the models provide a fairly high value of the critical pressure. The comparison between the predicted and the experimental fluid-fluid phase equilibria are given in Figs4.29-31.

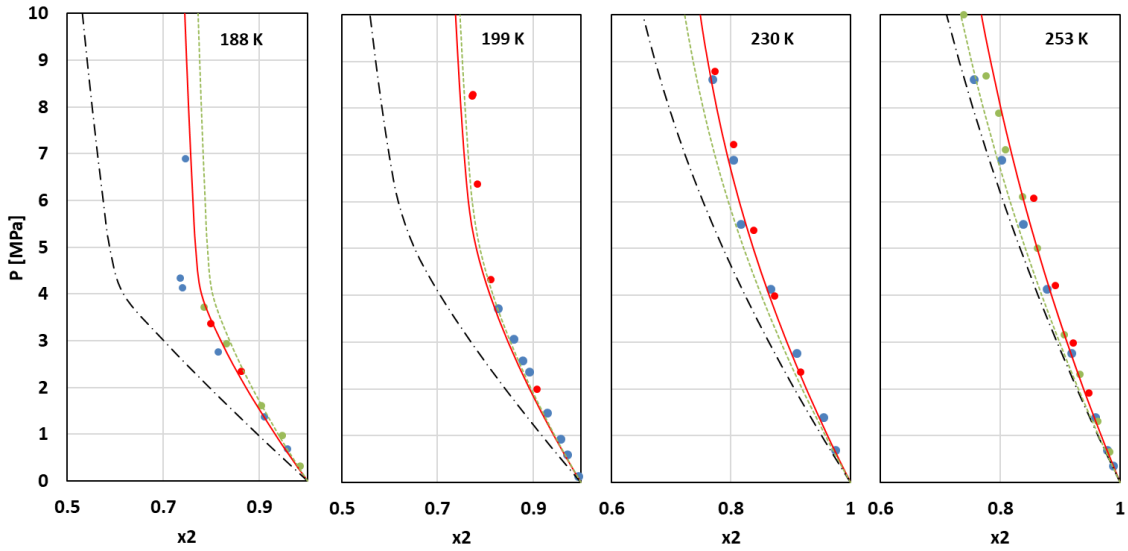

Figure 4.29: pressure-composition phase diagram of the methane(1)+toluene(2) system
● *ref* [27], ● *ref* [24], ● *ref* [10]*;*
— *PR EoS with constant* k_{ij}*;* - - - *PPR78 EoS;* - - - *PSRK EoS*

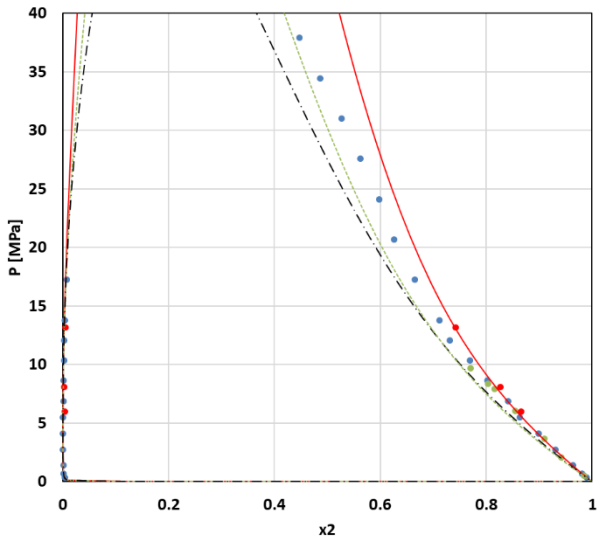

Figure 4.30: pressure-composition phase diagram of the methane(1)+toluene(2) system at 277K.
● *ref* [27], ● *ref* [24], ● *ref* [10]*;*
— *PR EoS with constant* k_{ij}*;* - - - *PPR78 EoS;*
- - - *PSRK EoS.*

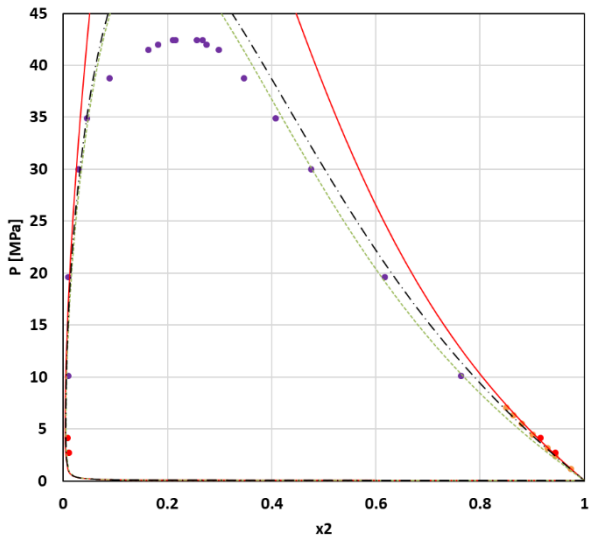

Figure 4.31: pressure-composition phase diagram of the methane(1)+toluene(2) system at 313K.
● *ref* [58], ● *ref* [57], ● *ref* [10]*;*
— *PR EoS with constant* k_{ij}*;* - - - *PPR78 EoS;*
- - - *PSRK EoS.*

The SLE of methane(1)+toluene(2) system have been reported by Kuebler and McKinley in ref [6]; in addition, Chang and Kobayashi [59] reported the quadruple point Solid-liquid-Liquid-Vapor Equilibrium ($S_2L_2L_1VE$), and some data on the three phases boundaries, the Solid,2-Liquid,1-Vapor (S_2L_1VE), the

Solid,2-Liquid,2-Vapor (S_2L_2VE) and the Liquid,1-Liquid,2-Vapor (L_1L_2VE) (L_2 refers to the toluene-rich liquid and L_1 refers to the methane-rich liquid).

The PR EoS with the constant k_{ij} regressed on the FFE, the PPR78 and the PSRK EoSs have been coupled with the classical approach for predicting the solubility limits of solid toluene in liquid methane at 8.4 MPa. The modeling results are compared to those reported in ref [6] and presented in Fig4.32. A very good prediction has been obtained when using the PR EoS with the constant value of k_{ij} regressed on the low-temperature FFE; the obtained AAD on the solubility limits is lower than 18%. On the contrary, the use of the PPR78 EoS or PSRK EoS leads to a very high deviation with respect to the literature data (the predicted solubility limits are several orders of magnitude lower or higher than the experimental data). The PPR78 and the PSRK EoSs have been used here in order to point out the potential large deviation that can be encountered when using these fluid-models at low temperatures; the extrapolation of the k_{ij} used in the PPR78 EoS (temperature-dependent) or the mixing rules used in the PSRK to very low temperatures (far from their validity area) may provide a poor quantitative and qualitative results.

The PR EoS with the constant k_{ij} is used for the calculation of the thermodynamic behavior of the methane+toluene system in the quadruple point region, as illustrated in Fig4.33. The results are in quite good agreement with the literature S_2L_1VE, S_2L_2VE, and L_1L_2VE data reported in ref [59]; the temperature and the pressure of the quadruple point of the system have been predicted with a deviation of less than 2 K and 0.1 MPa (1.15% and 4.3% respectively).

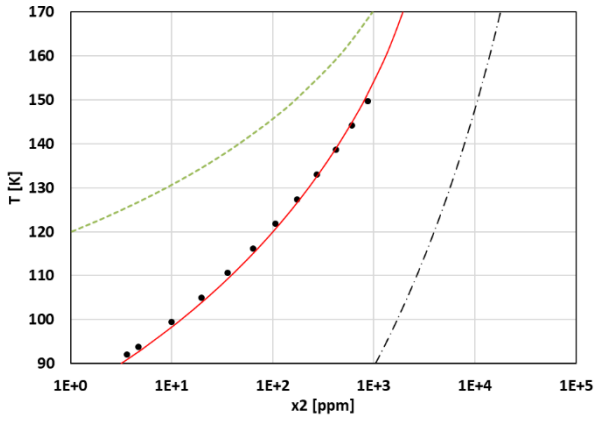

Figure 4.32: solubility limits of solid toluene(2) in liquid methane at 8.4 MPa

● *ref* [6]; — *PR EoS with constant* k_{ij} *;*
- - - *PPR78 EoS;* - - - *PSRK EoS.*

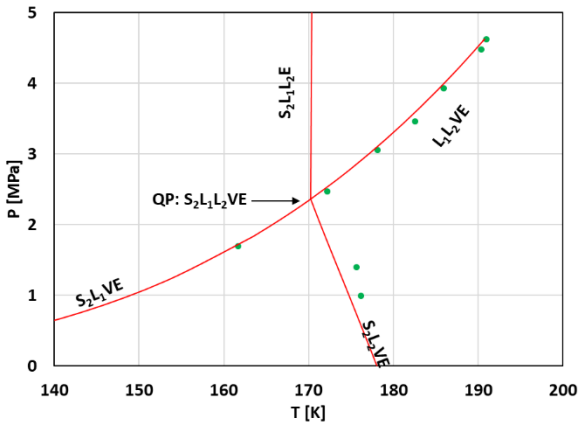

Figure 4.33: near quadruple point behavior of the methane+toluene system

● *ref* [59], — *PR EoS with constant* k_{ij}

4.5.3 Ethane+benzene

Only one set of VLE data has been found for the ethane+benzene system [30], these data have been used for regressing a reliable k_{ij} when using the PR EoS and a value of 0.0434 has been obtained. This model has been coupled with the classical approach for modeling the SLVE reported by Liu et al. in ref [60], and solubility limits of solid benzene in liquid ethane reported by Neumann et al. in ref [61]. The modeling results together with the literature values are presented in Figs4.34-35.

Despite the use of only one set of VLE data for regressing the k_{ij}, the predicted SLE and SLVE behavior using this constant k_{ij} is in good agreement with the literature data. The model reproduces the solubility limits reported in refs [60] and [61] with an AAD of 20.62% and 22.8% respectively; the pressures of the SLVE reported in ref [60] are represented with an AAD of 3.66%.

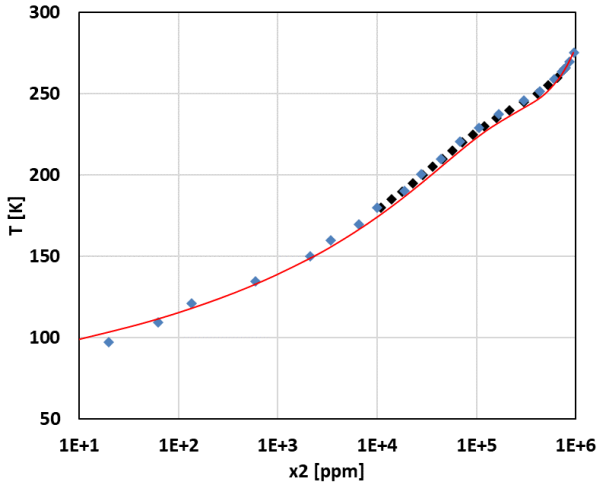

Figure 4.34: solubility limits of solid benzene(2) in liquid ethane at the SLVE.
♦ *ref* [60], ♦ *ref* [61], — *PR EoS with constant* k_{ij}

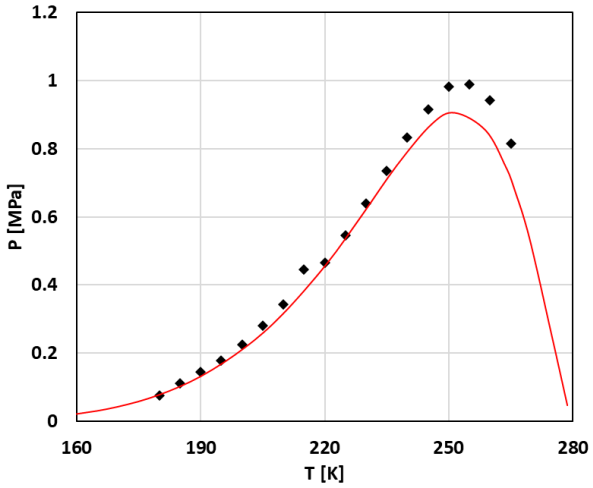

Figure 4.35: pressure-temperature loci of the SLVE of the ethane+benzene system.
♦ *ref* [60], — *PR EoS with constant* k_{ij}

4.5.4 Nitrogen+carbon dioxide

The vapor-liquid equilibria of the nitrogen+carbon dioxide system are deeply investigated in the literature; examples are the works of Krichevskii et al. [62], Al-Sahhaf et al. [40], Bian et al. [48], Brown et al. [41], Muirbrook [63], Somait and Kidnay [46], Xu et al. [47], Yucelen and Kidnay [64], and Zenner and Danna [39]. For each isotherm reported in the above-cited references, an optimal value of the k_{ij} has been regressed to accurately represent the literature data when the PR EoS is used; the obtained values are presented in Fig4.36. Similarly to the methane+carbon dioxide system, the regressed k_{ij} show a tendency to reach a constant value at temperature lower than 290 K. On the basis of this observation, a constant value of the k_{ij} has been regressed against all the VLE data at temperatures lower than 290 K and a value of -0.015 has been

obtained. In Fig4.28 the constant k_{ij} regressed on the low-temperature VLE is presented using a continuous red line, and the one from the PPR78 EoS is presented using a green dashed line. In addition, the extrapolations to low temperatures are also shown in Fig4.36 as dashed lines; the fact of using a temperature-dependent expression for k_{ij} from PPR78 EoS leads to sharply increasing values of the k_{ij} for decreasing temperatures.

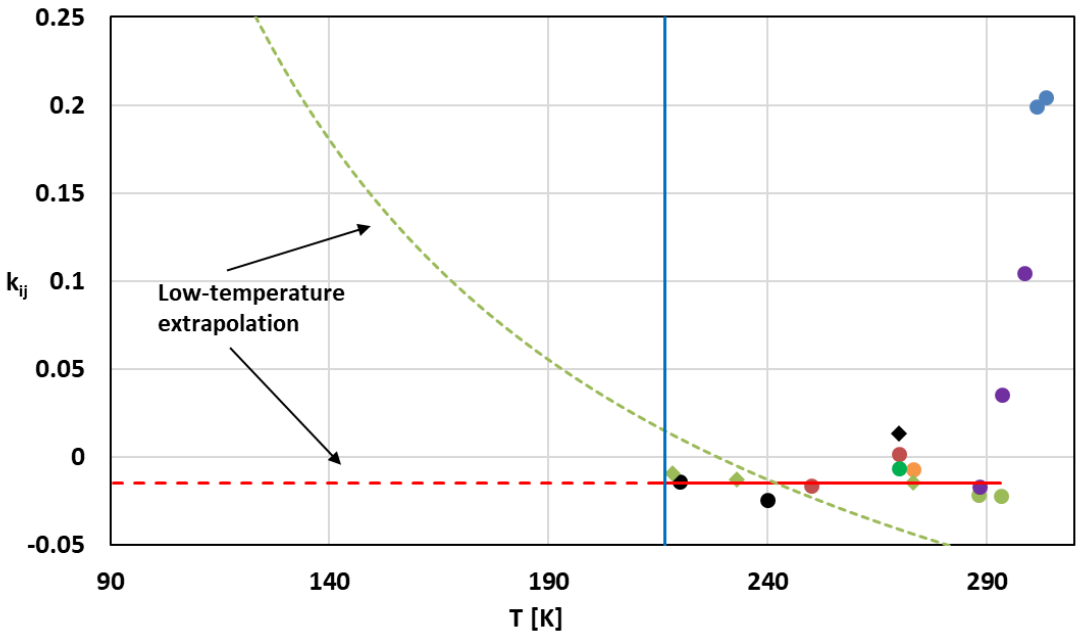

Figure 4.36: variation of the k_{ij} regressed on the VLE data of the nitrogen+carbon dioxide system as a function of temperature

kij regressed with respect to each VLE data set: ● *ref* [40], ● *ref* [48], ● *ref* [41], ● *ref* [62], ● *ref* [63], ● *ref* [46], ● *ref* [47], ♦ *ref* [64], ♦ *ref* [39],

— *k_{ij} regressed on the low-temperature VLE data (T<290 K);* - - - *k_{ij} from PPR78 EoS;*

— *triple point temperature of carbon dioxide*

The two models (PR EoS with constant k_{ij} from VLE data and the PPR78 EoS) have been coupled with the classical approach and used for predicting the solubility limits of solid carbon dioxide in nitrogen and compared to the literature data.

Fig4.37 shows the comparison between the modeling results and the literature SVE data from 190 K down to 140 K measured by Sontag and van Wylen [65] [66]. The use of the constant k_{ij} regressed on the VLE data allows representing the literature vapor composition at the SVE with an AAD of 7.44 %, while the use of the PPR78 EoS leads to an AAD of 11.12 %.

For each isotherm, the variation of the composition of the CO_2 in the saturated vapor (gas) phase decreases for increasing pressure until reaching a local minimum at a pressure close to the critical pressure of nitrogen;

then, the composition (the solubility limit in the supercritical nitrogen) increases for increasing pressure. This behavior is more pronounced for temperatures closer to the critical temperature of nitrogen.

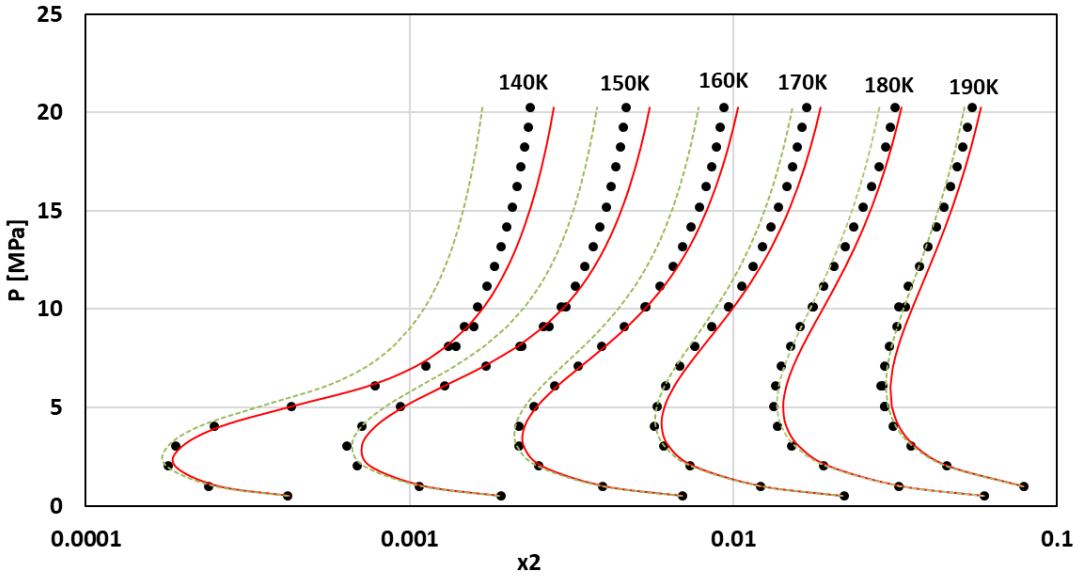

Figure 4.37: evolution of the solubility of carbon dioxide(2) in supercritical nitrogen as a function of the pressure

● *refs* [65] [66]; — *PR EoS;* - - - *PPR78 EoS*

Figs4.38-39 show the global temperature-composition diagram of the nitrogen+carbon dioxide system at 4 and 9 MPa respectively. For the VLE, the fluid phase model is used and a flash at constant pressure and temperature is performed for calculating the liquid and the vapor compositions. For the SVE and the SLE, the fluid phase model is coupled with the classical approach in order to solve the isofugacity condition of the solid former in the fluid phase (liquid or vapor) and in the solid phase. The red continuous line and the green dashed line represent respectively the modeling results obtained when using the PR EoS with constant k_{ij} obtained from the VLE data and the PPR78 EoS. The black-filled diamonds represent the SLE data reported by Yakimenko et al. in ref [67]; the black points represent the SVE data reported in ref [65], while the black-filled squares represent VLE data taken at pressures close to 4 and 9 MPa from the above-cited references.

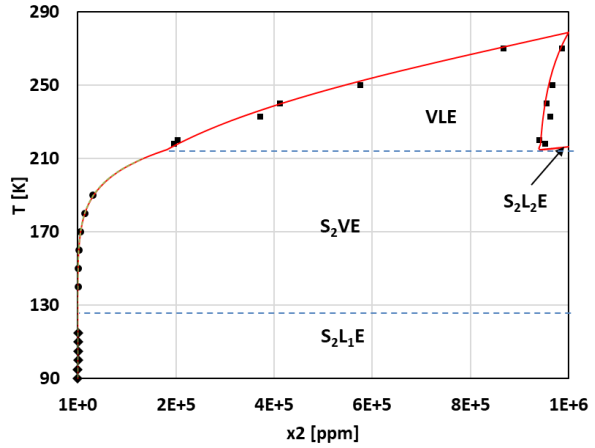

Figure 4.38: global temperature-composition diagram of the nitrogen(1)+carbon dioxide(2) at 4 MPa.

SLE: ♦ *ref* [67]*; SVE:* ● *refs* [65] [66]*; VLE:* ■ *ref*

— *PR EoS;* - - - *PPR78 EoS*

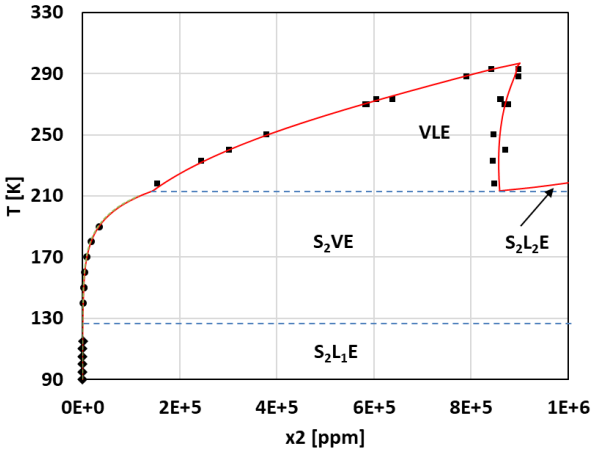

Figure 4.39: global temperature-composition diagram of the nitrogen(1)+carbon dioxide(2) at 9 MPa.

SLE: ♦ *ref* [67]*; SVE:* ● *refs* [65] [66]*; VLE:* ■ *ref*

— *PR EoS;* - - - *PPR78 EoS*

Seeing that the two models are overlapped in Figs4.38-39, a zoom has been made on the SVE and the SLE region and presented in Figs4.40-41 and a logarithmic scale has been used for the x-axis; this allows appreciating the difference between the modeling results obtained when using the two models. The quality of the prediction obtained using the PPR78 EoS decreases by decreasing temperature, this is due to the sharply increasing k_{ij} for decreasing temperatures of this model (as shown in Fig4.36). On the other hand, the PR EoS with constant k_{ij} regressed on VLE data provides a high-quality prediction for both the SVE and the SLE data.

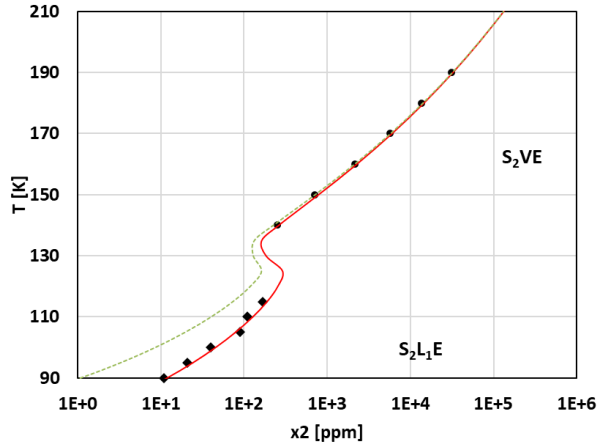

Figure 4.40: temperature-composition diagram of the nitrogen(1)+carbon dioxide(2) at the SVE and SLE at 4 MPa.

SLE: ♦ *ref* [67]*; SVE:* ● *refs* [65] [66]*;*

— *PR EoS;* - - - *PPR78 EoS*

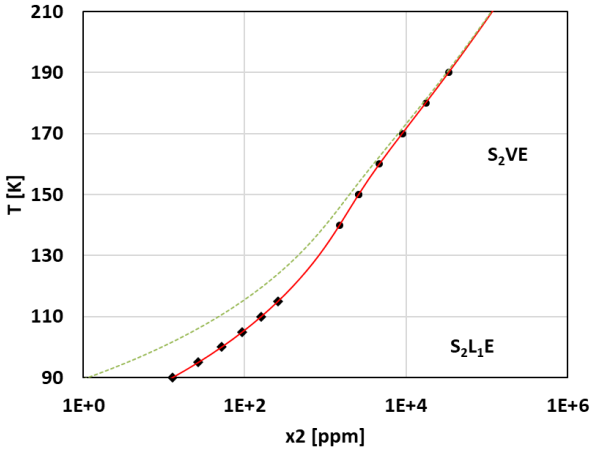

Figure 4.41: temperature-composition diagram of the nitrogen(1)+carbon dioxide(2) at the SVE and SLE at 9 MPa.

SLE: ♦ *ref* [67]*; SVE:* ● *refs* [65] [66]*;*

— *PR EoS;* - - - *PPR78 EoS*

According to Figs4.40-41, the predicted solubility limit of solid carbon dioxide in liquid or vapor nitrogen at 9 MPa is monotonically decreasing for decreasing temperatures. On the contrary, at 4 MPa, for decreasing temperatures, the solubility first decreases until reaching a local minimum, then increases for decreasing temperature until reaching a local maximum before regaining its decreasing trend for lower temperatures. This *"S"* shape occurs approximately between 115 K and 135 K and is due to the rapidly increasing density of the fluid phase in the near-critical region of nitrogen (126.2 K and 3.4 MPa), which makes the effect of the density on the solubility (solubility limits increases for increasing densities) prevailing on the effect of the temperature (solubility limits decreases for decreasing temperatures). This behavior has not been observed at 9 MPa because the pressure of the system is much higher than the critical pressure of nitrogen; thus the density increases less rapidly than at 4 MPa when crossing the critical temperature region of nitrogen. This behavior has been successfully observed and measured in this work for different systems (methane+benzene, methane+p-xylene, metane+o-xylene, and methane+m-xylene systems).

4.6 Methane+neopentane system

The conclusions drawn in the previous sections, namely *i)* the continuity of the k_{ij} between the fluid-fluid equilibria and the solid-fluid equilibria, and *ii)* the capability of the PR EoS with a constant value of the k_{ij} to accurately represent the phase equilibria at temperatures far from the critical region are applied for the modeling of the global thermodynamic behavior of the methane(1)+neopentane(2) system.

The methane+neopentane has been deeply investigated in this work; indeed, several VLE, SLE, and SLVE data have been measured and reported in chapter 3. In the following, the VLE data obtained in this work are used for regressing a constant k_{ij} used within the PR EoS, which is subsequently used for predicting the global phase diagram of the methane+neopentane system (the PR EoS is coupled with the classical approach for the prediction of the SFE). In addition, the modeling results are compared to the experimental data obtained in this work and reported in the literature.

4.6.1 Regression of the k_{ij} on the VLE data

The VLE data of the methane+neopentane system reported in the literature [68] [69] and those measured in this thesis have been firstly used for regressing the optimal k_{ij} for each isotherm, and the obtained values are presented in Fig4.42.

The regressed k_{ij} show a tendency to reach a constant value at temperatures far from the critical temperature of the neopentane (for temperatures lower than 350 K, the k_{ij} is almost constant); this endorses the conclusions that have been drawn in the previous sections, which state that a constant k_{ij} could be sufficient for the accurate modeling of the phase behavior of a given system far from the critical region.

Based on this result, a constant k_{ij} has been regressed using only the VLE measurements obtained in this work at temperatures lower than 300 K, and a value of -0.00156 has been obtained. Even if the VLE from ref [68] are at temperatures lower than 300 K, this set of data has not been used for the regression of the constant k_{ij} because the optimal k_{ij} obtained for this dataset deviates from the constant shape, and this is due to the disagreement between the data reported in ref [68] and those obtained in this work.

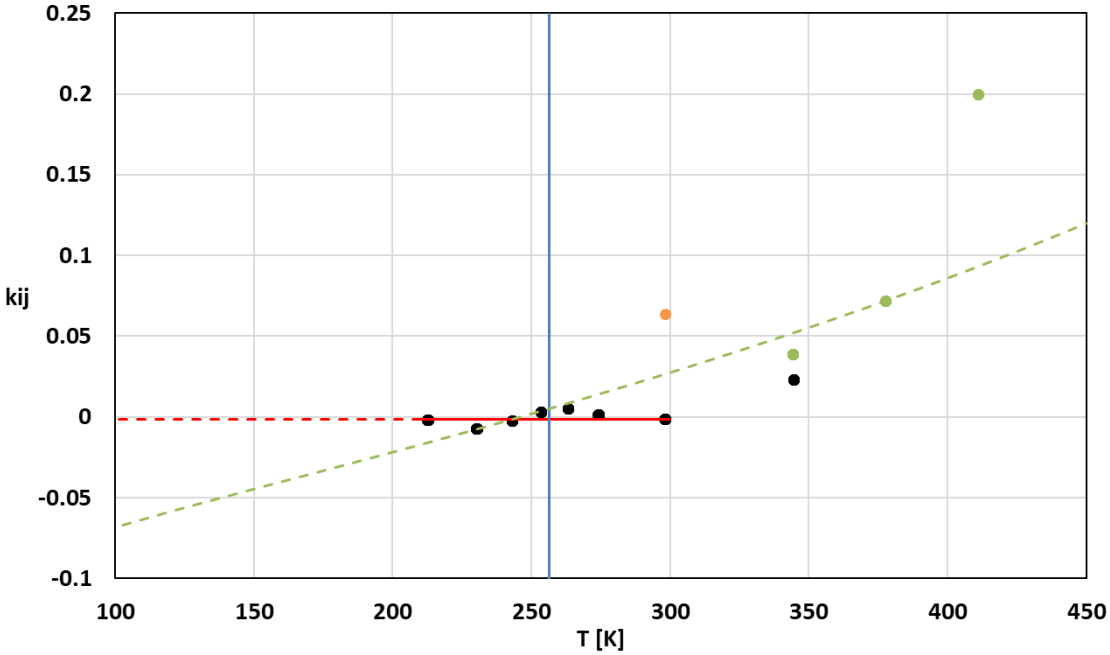

Figure 4.42: variation of the k_{ij} regressed on the VLE data of the methane+neopentane system as a function of temperature.

kij regressed with respect to each VLE dataset: ● *this work,* ● *ref* [68], ● *ref* [69]
— k_{ij} *regressed on the low-temperature VLE data (T<300K);* - - - k_{ij} *from PPR78 EoS;*
— *Triple point temperature of neopentane*

4.6.2 Modeling of the VLE

The constant k_{ij} regressed on the VLE data at temperatures lower than 300 K (measured in this work) has been used within the PR EoS for representing the phase equilibria of the methane+neopentane, and the results are compared to the experimental values in Figs4.43-50.

The pressure-composition diagrams in Figs4.43-46 have been completed by adding the phase equilibria involving solid neopentane since the experimental temperatures of the corresponding VLE are lower than the triple point temperature of neopentane. It is worth noticing that the phase equilibria involving solid neopentane have been calculated by coupling the PR EoS with the classical approach (Eq4.1).

For the isotherms at temperatures lower than the triple point temperature of neopentane (Figs4.43-46), three scenarios have been found depending on the global composition and the pressure of the system:

- For pressures lower than the SLVE pressure, the system is either at SVE or in the monophasic vapor phase.
- For pressures higher than the SLVE pressure, the system can be at SLE, LVE, or in the liquid or vapor phase. The two fluid phases are replaced by the supercritical phase for pressures higher than the critical pressure of the mixture
- At the SLVE pressure, the system is either at SLVE or vapor phase.

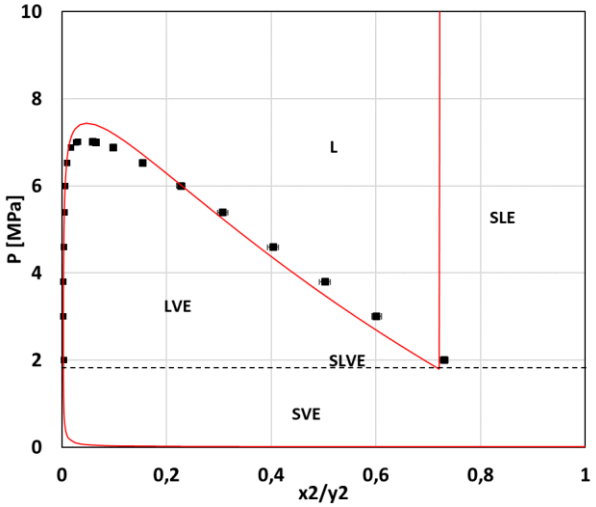

Figure 4.43: temperature-composition diagram of the methane(1)+neopentane(2) system at 213 K.
■ *this work,* — *PR EoS*

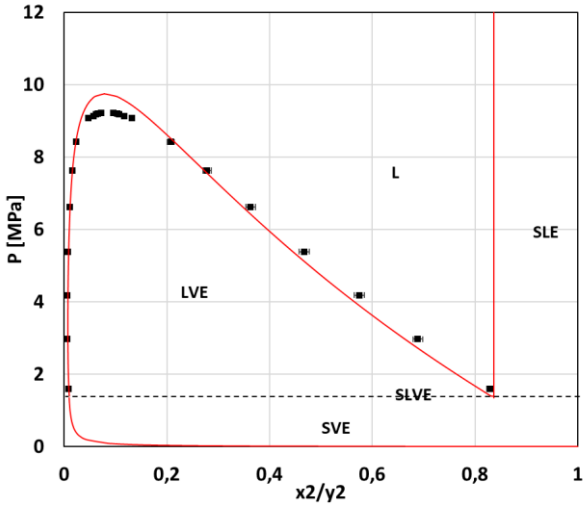

Figure 4.44: temperature-composition diagram of the methane(1)+neopentane(2) system at 230 K.
■ *this work,* — *PR EoS*

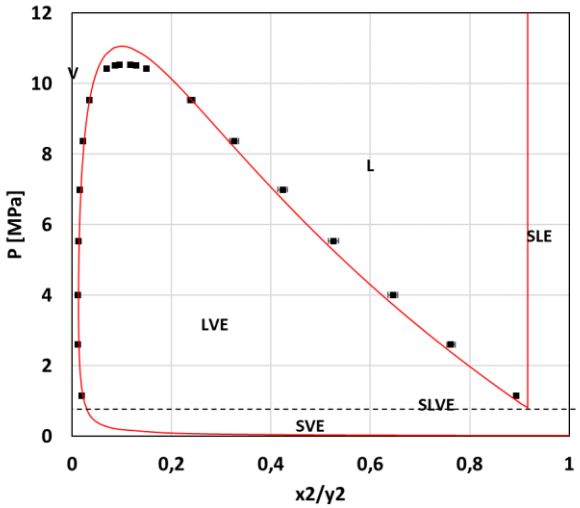

Figure 4.45: temperature-composition diagram of the methane(1)+neopentane(2) system at 243 K
■ *this work,* — *PR EoS*

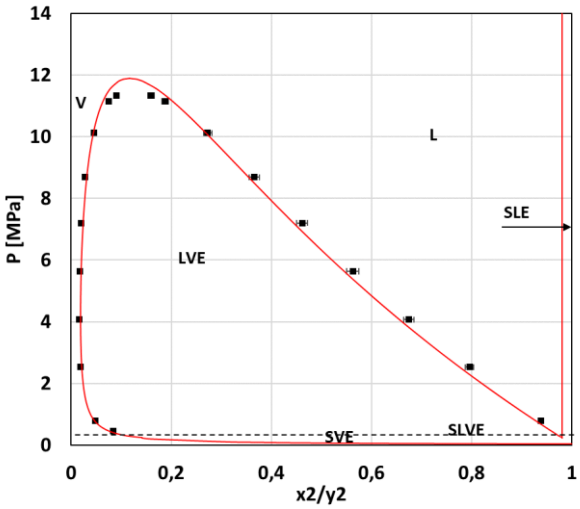

Figure 4.46: temperature-composition diagram of the methane(1)+neopentane(2) system at 253 K
■ *this work,* — *PR EoS*

For temperatures higher than the triple point of neopentane (Figs4.47-50), the system can be at VLE in the vapor, in the liquid phase, or in the supercritical phase, depending on the pressure and the global composition.

The use of the PR EoS with a constant value of k_{ij} allows representing the composition of the VLE data measured in this work with an AAD of 29.16%, while the use of the PPR78 EoS and the PSRK gives an AAD of 30.52% and 39.09% respectively.

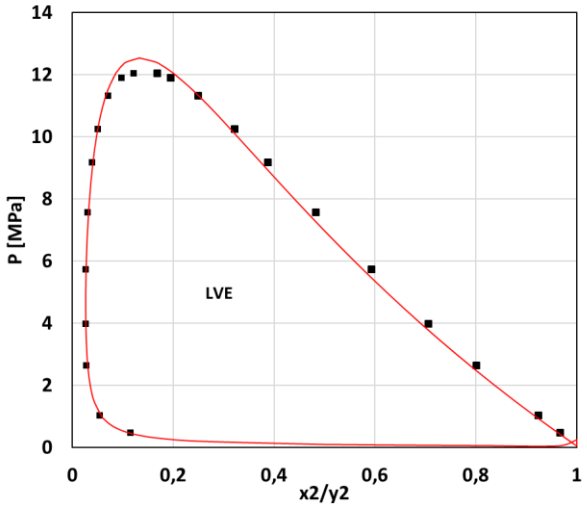

Figure 4.47: temperature-composition diagram of the methane(1)+neopentane(2) system at 263 K.
■ *this work,* — *PR EoS*

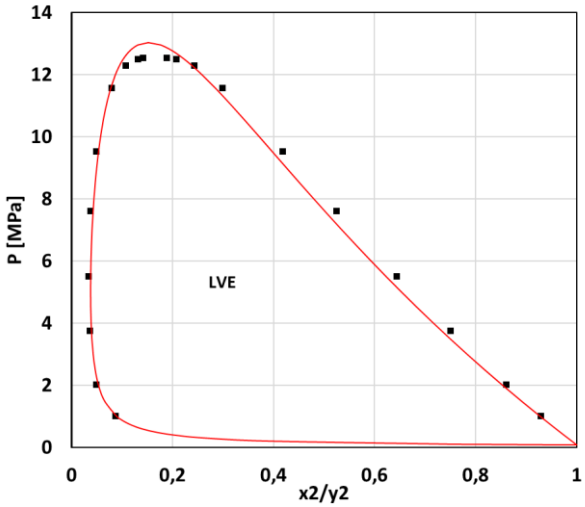

Figure 4.48: temperature-composition diagram of the methane(1)+neopentane(2) system at 274 K.
■ *this work,* — *PR EoS*

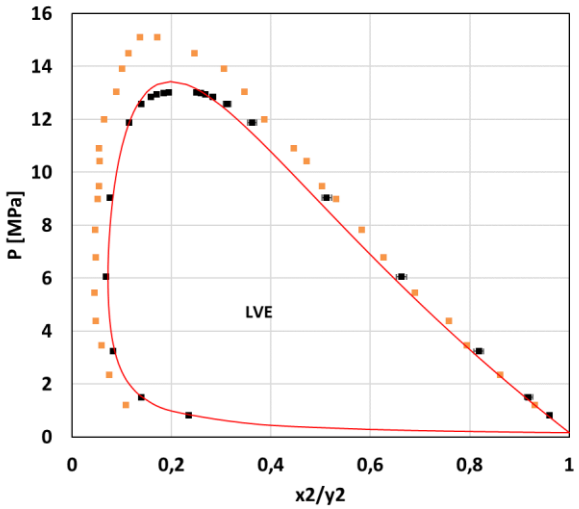

Figure 4.49: temperature-composition diagram of the methane(1)+neopentane(2) system at 298 K.
■ *this work,* ■ *ref* [68], — *PR EoS*

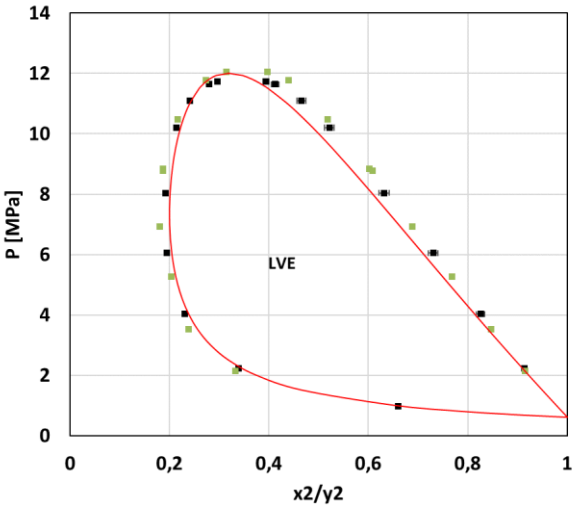

Figure 4.50: temperature-composition diagram of the methane(1)+neopentane(2) system at 344 K.
■ *this work,* ■ *ref* [69], — *PR EoS*

4.6.3 Global phase diagram of the methane+neopentane system

The experimental investigation carried out in this thesis of the phase equilibria of the methane+neopentane system in the presence of solid neopentane has shown that this system presents a continuous locus of the SLVE that extends from the triple point of the neopentane down to the low-temperature region. Furthermore, the critical points reported in ref [70] show a continuous critical line that links the critical points of pure methane and neopentane. Based on this information, it has been concluded in chapter3 that, from the experimental point of view, the global phase diagram of the methane+neopentane system is of type I according to the classification of van Konynenburg and Scott (only the fluid phases are considered) [71], and of type D in the classification of Kohn and Luks (the solid and the fluid phase are considered) [72].

The PR EoS with constant k_{ij} has been coupled with the classical approach (Eqs4.1-2) for modeling the global phase diagram of the methane+neopentane system. The pure component properties used for the modeling work have been taken from Simulis Thermodynamic Software [73] and are summarized in Tab4.4. Seeing that this work focuses on temperatures as low as 80 K, only neopentane presents a solid-solid transition in this temperature range, thus its properties at the solid-solid transition are given in Tab4.4.

Table 4.4: summary of the properties of methane and neopentane used in the modeling work.
ω : acentric factor, T_t, P_t : triple-point temperature and pressure, T_c, P_c : critical-point temperature and pressure, $\boldsymbol{\Delta H^{SLE}_{T_tP_t}}$: heat of fusion at the triple point, T_{tr}: temperature of the solid-solid transition, $\boldsymbol{\Delta H^{SSE}_{T_{tr}P_{tr}}}$: heat of fusion at the solid-solid transition.

Component	ω	T_t K	P_t MPa	$\boldsymbol{\Delta H^{SLE}_{T_tP_t}}$ kJ/mol	T_c K	P_c MPa	T_{tr} K	$\boldsymbol{\Delta H^{SSE}_{T_{tr}P_{tr}}}$ kJ/mol
CH_4	**0.01142**	**90.694**	**0.011696**	**0.9414**	**190.56**	**4.5992**		
neopentane	**0.1961**	**256.6**	**0.035401**	3.26	**433.74**	**3.196**	**140.0**	**2.58**

All the phase boundaries accounting for the fluid-fluid equilibrium (saturation line of pure methane and neopentane and the critical line of the mixture) have been calculated following the algorithms implemented in Simulis Thermodynamic Software [73] and are presented in the phase diagram given in Fig4.51. The calculated critical line is a continuous curve relating the critical points of pure methane and neopentane. Since no other critical loci have been obtained in the pressure-temperature range investigated in this work, the global phase diagram of the methane+neopentane system when considering only the fluid phase corresponds to the type I in the classification of van Konynenburg and Scott [71].

As shown in Fig4.51 the critical line given by the model is in quite good agreement with the values reported in ref [70].

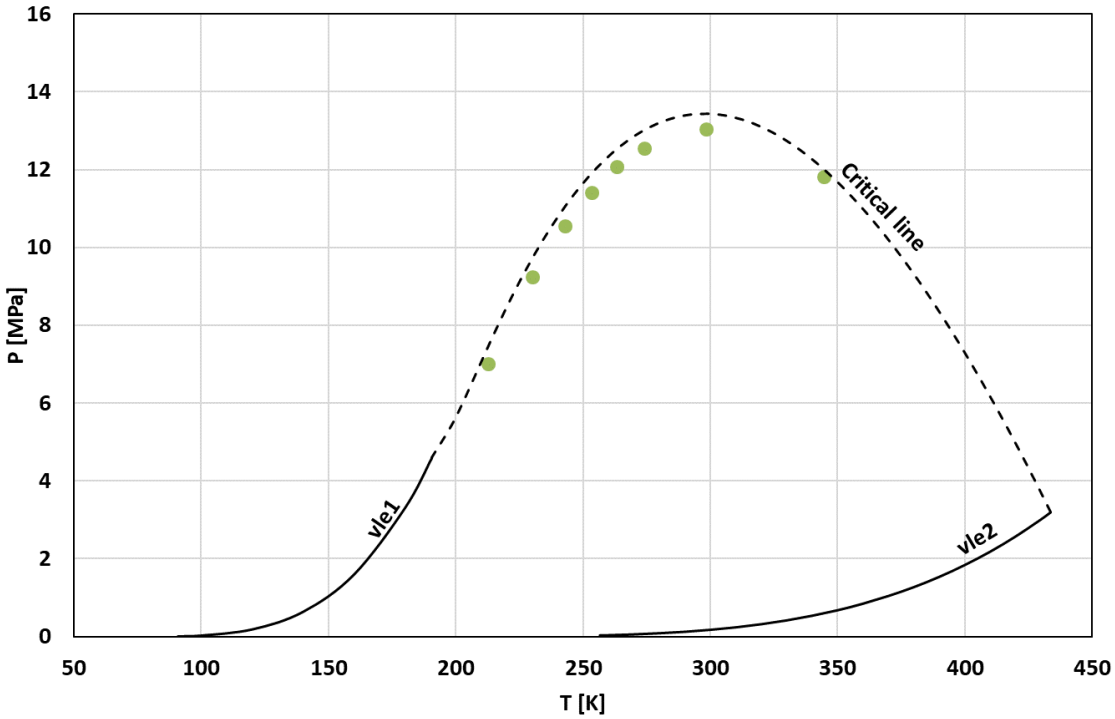

Figure 4.51: pressure-temperature diagram of the methane(1)+neopentane(2) system.
vle1: saturation line of methane, vle2: saturation line of neopentane;
● *critical point ref* [70].

The phase boundaries involving the solid phases are calculated by solving the isofugacity condition between the solid and the fluid phases. The fugacity of each component in the liquid and the vapor phase is calculated using Eqs4.14-15, respectively. In the temperature range investigated in this work, neopentane(2) is concerned by a solid-solid transition (solid structure α to solid structure β) at 140 K; this entails the use of two different equations for calculating its fugacity in the solid phase, depending on the investigated temperature; Eq4.16 is used for temperatures higher than 140 K, while Eq4.17 is used for lower temperatures. The fugacity of methane(1) in the solid phase is calculated using Eq4.18. The terms involving the heat capacity and the volume change upon melting are neglected.

$$\hat{f}_i^l(T,P,\vec{x}) = x_i \hat{\varphi}_i^l P \tag{4.14}$$

$$\hat{f}_i^v(T,P,\vec{y}) = y_i \hat{\varphi}_i^v P \tag{4.15}$$

$$f_{0,2}^{s,\alpha}(T,P) = f_{0,2}^{l}(T,P)\exp\left[\frac{\Delta H_{T_{t,2}P_{t,2}}^{s^{\alpha\to l}}}{RT}\left(\frac{T}{T_{t,2}}-1\right)\right] \tag{4.16}$$

$$f_{0,2}^{s,\beta}(T,P) = f_{0,2}^{l}(T,P)\exp\left[\frac{\Delta H^{s^{\alpha}\to l}_{T_{t,2}P_{t,2}}}{RT}\left(\frac{T}{T_{t,2}}-1\right)+\frac{\Delta H^{s^{\beta}\to s^{\alpha}}_{T_{tr,2}P_{tr,2}}}{RT}\left(\frac{T}{T_{tr,2}}-1\right)\right] \tag{4.17}$$

$$f_{0,1}^{s}(T,P) = f_{0,1}^{l}(T,P)\exp\left[\frac{\Delta H^{s\to l}_{T_{t,1}P_{t,1}}}{RT}\left(\frac{T}{T_{t,1}}-1\right)\right] \tag{4.18}$$

The melting line of methane and neopentane and the solid-solid transition of neopentane are represented by a merely vertical line at their respective triple point temperatures (90.694 K and 256.6 K) and the temperature of the solid-solid transition of neopentane (140 K); this is due to the fact of having neglected the terms involving volume change upon melting for the calculation of the fugacity of the solid phases.

Two quadruple points are encountered when calculating the global phase diagram of the methane+neopentane system. The warmer corresponds to the $Solid_{2,\alpha}$-$Solid_{2,\beta}$-Liquid-Vapor Equilibrium ($S_{2,\alpha}S_{2,\beta}$LVE) and is calculated by solving Eq4.19 at 140 K (seeing that the $Solid_{2,\alpha}$, and $Solid_{2,\beta}$ are considered as made of pure neopentane, the isofugacity condition is solved only with regards to neopentane and so the fugacity of methane in the liquid and the vapor phase is not considered). The colder quadruple point corresponds to the $Solid_1$-$Solid_{2,\beta}$-Liquid-Vapor Equilibrium ($S_1S_{2,\beta}$LVE) and is calculated by solving simultaneously Eqs4.20-21.

$$f_{0,2}^{s,\alpha}(T,P) = f_{0,2}^{s,\beta}(T,P) = \hat{f}_2^{l}(T,P,\vec{x}) = \hat{f}_2^{v}(T,P,\vec{y}) \tag{4.19}$$

$$f_{0,2}^{s,\beta}(T,P) = \hat{f}_2^{l}(T,P,\vec{x}) = \hat{f}_2^{v}(T,P,\vec{y}) \tag{4.20}$$

$$f_{0,1}^{s}(T,P) = \hat{f}_1^{l}(T,P,\vec{x}) = \hat{f}_1^{v}(T,P,\vec{y}) \tag{4.21}$$

The obtained pressure, temperature, and fluid compositions of the two quadruple points are summarized in Tab4.5.

Table 4.5: quadruple point properties of methane+neopentane system obtained by coupling the PR EoS with the classical approach

QP	*T* [K]	*P* [MPa]	x_2	y_2
$S_{2,\alpha}S_{2,\beta}$LVE	140.0	0.3588	0,2467	$1{,}3169\times10^{-6}$
$S_1S_{2,\beta}$LVE	89.7302	0,0103	0,01344	$1{,}8692\times10^{-12}$

The three-phase boundaries encountered when calculating the global phase diagram of the methane+neopentane are:

- The $Solid_{2,\alpha}$-Liquid-Vapor Equilibrium ($S_{2,\alpha}LVE$) line originating at the triple point temperature of neopentane and ending at the warmer quadruple point; the $S_{2,\alpha}LVE$ is obtained by solving Eq4.22.
- The $Solid_{2,\beta}$-Liquid-Vapor Equilibrium ($S_{2,\beta}LVE$) line originating at the warmer quadruple point and ending at the colder quadruple point; the $S_{2,\beta}LVE$ is calculated by solving Eq4.23.
- The $Solid_{2,\alpha}$-$Solid_{2,\beta}$-Liquid Equilibrium ($S_{2,\alpha}S_{2,\beta}LE$) is considered as a vertical line originating at the warmer quadruple point and tending toward the high-pressure region.
- The $Solid_{2,\alpha}$-$Solid_{2,\beta}$-Vapor Equilibrium ($S_{2,\alpha}S_{2,\beta}VE$) is considered as a vertical line originating at the warmer quadruple point and ending at the triple point temperature $solid_{2,\alpha}$-$solid_{2,\beta}$-vapor ($s_{2,\alpha}s_{2,\beta}ve$) of neopentane.
- The $Solid_1$-Liquid-Vapor Equilibrium (S_1LVE) line originating at the triple point temperature of methane and ending at the colder quadruple point; the S_1LVE is calculated by solving Eq4.24.
- The $Solid_1$-$Solid_{2,\beta}$-Liquid Equilibrium ($S_1S_{2,\beta}LE$) is considered as a vertical line originating at the colder quadruple point and tends toward the high-pressure region.
- The $Solid_1$-$Solid_{2,\beta}$-Vapor Equilibrium ($S_1S_{2,\beta}VE$) line originating at the colder quadruple point and tends toward the low-pressure-low-temperature region is calculated by solving Eqs4.25-26 at the same pressure and temperature.

$$f_{0,2}^{s,\alpha}(T,P) = \widehat{f}_2^{l}(T,P,\vec{x}) = \widehat{f}_2^{v}(T,P,\vec{y}) \tag{4.22}$$

$$f_{0,2}^{s,\beta}(T,P) = \widehat{f}_2^{l}(T,P,\vec{x}) = \widehat{f}_2^{v}(T,P,\vec{y}) \tag{4.23}$$

$$f_{0,1}^{s}(T,P) = \widehat{f}_1^{l}(T,P,\vec{x}) = \widehat{f}_1^{v}(T,P,\vec{y}) \tag{4.24}$$

$$f_{0,1}^{s}(T,P) = \widehat{f}_1^{v}(T,P,\vec{y}) \tag{4.25}$$

$$f_{0,2}^{s,\beta}(T,P) = \widehat{f}_2^{v}(T,P,\vec{y}) \tag{4.26}$$

The global phase diagram in the presence of the solid phases is presented in Fig4.52; for the reader's convenience and for appreciating the thermodynamic behavior and the different phase boundaries encountered in the low-temperature-low-pressure region, a zoom is made in the pressure-temperature region of the warmer and the colder quadruple points; the corresponding diagrams are presented in Figs4.53-54.

The obtained global phase diagram is of type D according to the classification of Kohn and Luks [72]. This result is in agreement with the behavior observed during the experimental investigation of this system.

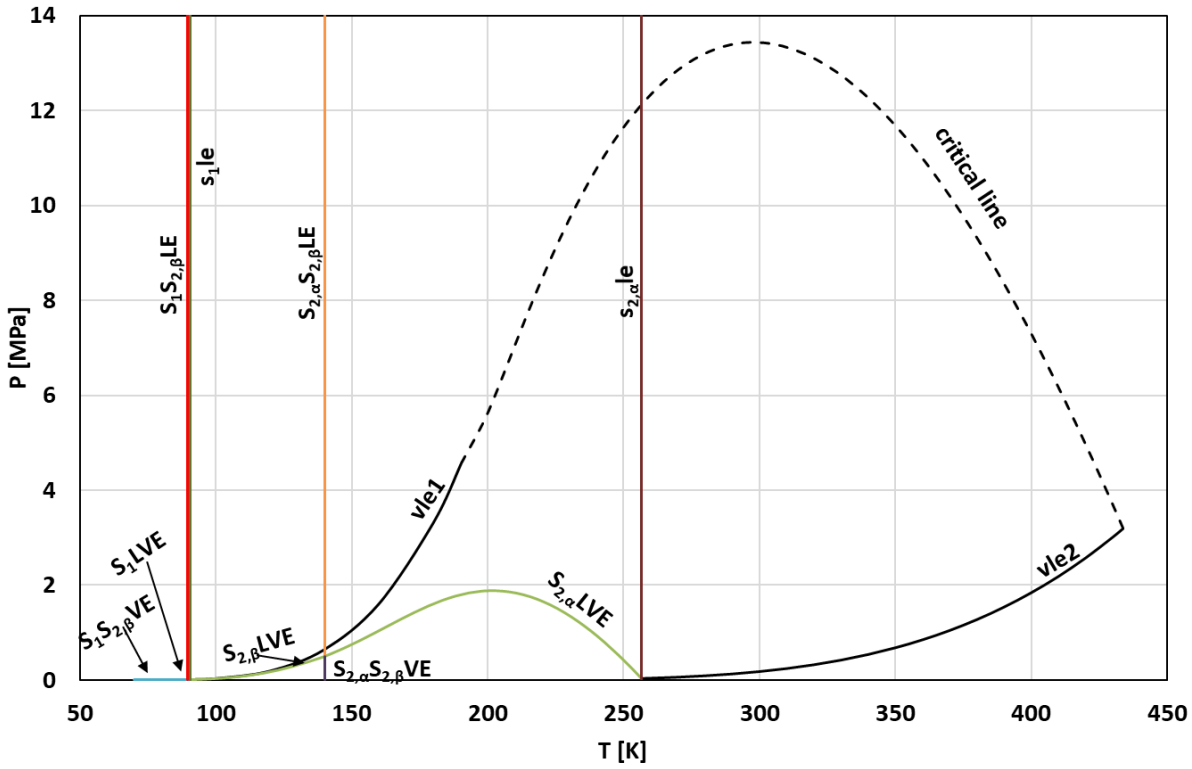

Figure 4.52: global phase diagram of the methane(1)+neopentane(2) system.

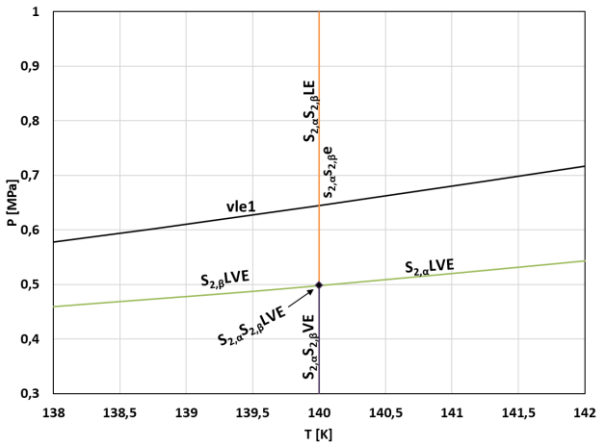

Figure 4.53: focus on the warmer quadruple point pressure-temperature region of the methane(1)+neopentane(2) system.

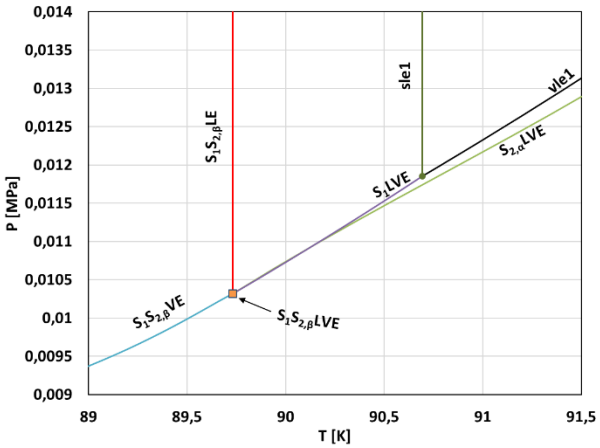

Figure 4.54: focus on the colder quadruple point pressure-temperature region of the methane(1)+neopentane(2) system.

The solubility limits of solid neopentane in liquid methane at the SLE and the SLVE measured in this thesis together with the data reported by Siahvashi et al. in ref [74] are compared to the values predicted when using the PR EoS with constant k_{ij} and presented in Fig4.55. In addition, Fig4.56 shows the comparison between modeling and the experimental values of the SLVE pressure-temperature locus. The use of constant k_{ij} regressed on the low-temperature VLE allows obtaining a very good representation of the phase equilibria involving solid phases; this result confirms what has been observed in section 4.5.

The average absolute deviations between the modeling results and the experimental values are summarized in Tab4.6.

Table 4.6: summary of the AAD between the modeling (PR EoS with a constant kij regressed on the low temperatures VLE coupled with the classical approach) and the experimental data of the methane+neopentane phase equilibria in the presence of solid neopentane.
N_p: number of the experimental point, T^{exp}, $P^{exp,}$ x_2^{exp}: experimental temperature, pressure and neopentane composition, T^{cal}, $P^{cal,}$ x_2^{cal}: calculated temperature, pressure and neopentane composition.

Data	*Ref*	$\frac{1}{N_P}\sum_i^{N_p} 100\left\|\frac{(T^{exp}-T^{cal})}{T^{exp}}\right\|$	$\frac{1}{N_P}\sum_i^{N_p} 100\left\|\frac{(x_2^{exp}-x_2^{cal})}{x_2^{exp}}\right\|$	$\frac{1}{N_P}\sum_i^{N_p} 100\left\|\frac{(P^{exp}-P^{cal})}{P^{exp}}\right\|$
SLE	This work	1.99	10.28	/
	[74]	1.59	9.59	/
SLVE	This work	0.73	2.47	3.89
	[74]	0.52	/	6.09
SVE	[74]	1.58	20.76	/

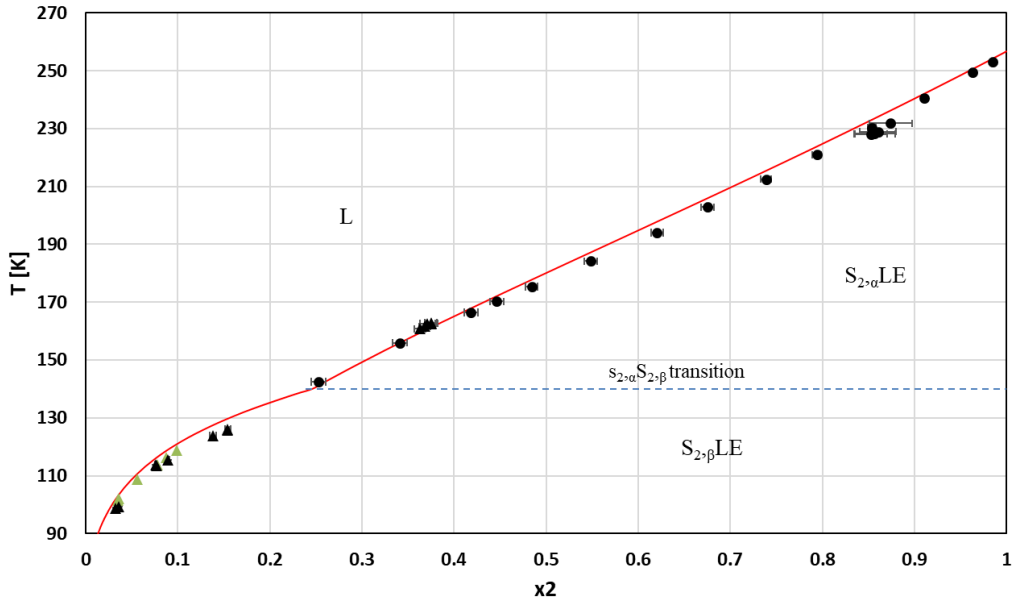

Figure 4.55: solubility of solid neopentane(2) in liquid methane at the $S_{2,\beta}$LE and the $S_{2,\alpha}$LVE $S_{2,\beta}$LVE.
SLVE: ● this work
SLE: ▲ ref [74], ▲ this work
— PR EoS with constant k_{ij} coupled with the classical approach

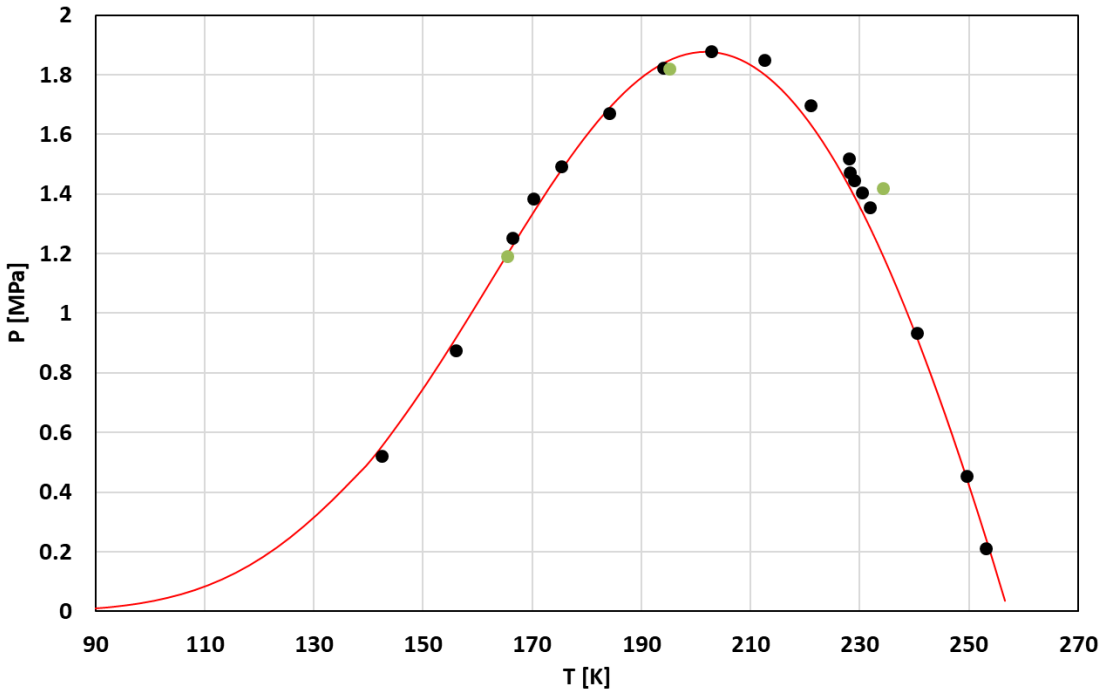

Figure 4.56: pressure-temperature locus of the $S_{2,\alpha}LVE$ $S_{2,\beta}LVE$ of the methane+neopentane system.
SLVE: ● ref [74]; ● this work
— PR EoS with constant k_{ij} coupled with the classical approach

4.7 Conclusion

The modeling work performed in this PhD thesis has been focused on the investigation of the possibilities of improving the representation of the low-temperature phase equilibria, especially those involving solid phases in the context of the natural gas liquefaction. The modeling approach used for the SF(F)E is based on the iso-fugacity condition; the solid phase has been considered as constituted only of the pure component. The fugacity of the solid former in the solid phase is calculated using the classical approach initiated by Prausnitz, while the fugacity of each component involved in the fluid phase is calculated using the PR EoS.

For the regression of the optimal k_{ij} for the SFE, an algorithm based on the pseudo-experimental activity coefficient is presented in this work, the pseudo-experimental activity coefficient is calculated starting from the composition of the saturated liquid phase at the SLE and/or the SLVE. This new algorithm is a valid alternative for the one based on the minimization of the deviation between the calculated and the measured solubility limits.

This algorithm has been used for the regression of the optimal k_{ij} for each experimental point (P,T,x) and the obtained values showed a tendency to reach a constant value; this means that a constant value of the k_{ij}

could be sufficient for the accurate modeling of the phase equilibria involving solid phases, at least for the systems investigated in this work.

In a second time, the continuity of the k_{ij} crossing the triple point temperature of the solid former has been evaluated. For this purpose, the constant k_{ij} regressed on the solid-liquid and solid-liquid-vapor equilibrium of each investigated binary system has been used for predicting the fluid-fluid phase equilibria at temperatures close to the triple point temperature of the solid former. The obtained results have been found in a rather good agreement with the literature data and present a deviation comparable with those obtained when applying the PPR78 EoS and the PSRK EoS (two widely used fluid phase models).

Once the continuity of the k_{ij} between the SFE and the FFE, and its tendency to reach a constant value in the low-temperature region have been demonstrated; the possibility of using the fluid-fluid data at temperatures close to the triple point temperature of the solid former for accurately predicting the phase equilibria involving the solid phase has been investigated. The systems studied in this work have shown that a constant value of k_{ij} regressed on FFE at temperatures close to the triple point temperature of the heaviest component in the binary mixture is a sufficient correction that allows obtaining an accurate prediction of the SFE when the PR EoS is coupled with the classical approach. This outcome allows using a highly supplied FFE database for regressing reliable k_{ij} for the modeling of the phase equilibria over a large range of temperatures (down to cryogenic temperatures).

The review and the modification of the mathematical expression of the k_{ij} calculated through the group contribution method is a very promising perspective for the accurate modeling of the phase equilibrium over a wide temperature range (from the critical temperature of the heaviest component down to the lowest temperature of the existence of the fluid phases). The suitable expression of the k_{ij} is a formula able to represent the variations of k_{ij} in the critical region and tends towards a constant value at low temperatures.

References

[1] J. M. Prausnitz, R. N. Lichtenthaler, et E. G. de Azevedo, Molecular thermodynamics of fluid-phase equilibria, 3.ed. Upper Saddle River, NJ: Prentice-Hall PTR, 1999.

[2] A. Würflinger, Differential thermal analysis under high pressure IV: Low-temperature DTA of solid-solid and solid-liquid transitions of several hydrocarbons up to 3 kbar, Berichte der Bunsengesellschaft für physikalische Chemie, vol. 79, N° 12, 1195-1201, 1975.

[3] A. Weissberger, Techniques of Chemistry: Organic Solvents. Wiley-Interscience, 1970.

[4] Data has been taken as reported in the DIPPR database.

[5] D.-Y. Peng et D. B. Robinson, A New Two-Constant Equation of State, Ind. Eng. Chem. Fund., vol. 15, N° 1, 59-64, 1976.

[6] G. P. Kuebler and C. McKinley, Solubility of Solid Benzene, Toluene, n-Hexane, and n-Heptane in Liquid Methane, in Advances in Cryogenic Engineering, K. D. Timmerhaus, Éd. Boston, MA: Springer US, 320-326, 1995.

[7] A. Siahvashi, S. ZS. Al Ghafri, and E. F. May, Solid-fluid equilibrium measurements of benzene in methane and implications for freeze-out at LNG conditions, Fluid Phase Equilibria, vol. 519, 112609, 2020.

[8] D. Luks, Three-phase Solid-Liquid-Vapor Equilibria of the Binary Hydrocarbon Systems Ethane-2-Methylnaphthalene, Ethane-Naphthalene, Propane-n-Decane, and Propane-n-Dodecane.

[9] M. P. W. M. Rijkers, M. Malais, J. Swaan Arons, Experimental determination of the phase behavior of binary mixtures of methane + benzene: Part I. Vapor + liquid, solid benzene + liquid, solid benzene + vapor and solid benzene + liquid + vapor equilibria, Fluid Phase Equilibria, 327-342, 1992.

[10] T. J. Hughes, M. E. Kandil, B. F. Graham, K. N. Marsh, S. H. Huang, et E. F. May, Phase equilibrium measurements of (methane + benzene) and (methane + methylbenzene) at temperatures from (188 to 348) K and pressures to 13 MPa, The Journal of Chemical Thermodynamics, vol. 85, 141-147, 2015.

[11] Neumann A., Mann R., et von Szalghary W.D., Löslichkeit von festem Benzol in flüssigen Kohlenwasserstoffen, Kältetechnik, Klimatisierung, vol. 24, 145-149, 1992.

[12] Teller M., Knapp H., 1985, as reported in Solid-liquid equilibrium data collection, vol VIII, H. Knapp, M. Teller; Langhorst R., ed DECHEMA Chemistry data series.

[13] Tiffin D.L.; Luks K.D.; Kohn, Tiffin D.L.; Luks K.D.; Kohn J.P., Adv. Cryog. Eng., 23, 538-543, 1978.

[14] Neumann A.; Mann R.; Kaeltetech. Klim, 6, 182-184, 1970.

[15] J. P. Kohn, D. Luks, et P. H. Liu, Three-phase Solid-Liquid-Vapor Equilibria of Binary-n-Alkane Systems (Ethane-n-Octane, Ethane-n-Decane, Ethane-n-Dodecane).

[16] W.-U. Chen et K. D. Luks, Three-phase Solid-Liquid-Vapor Equilibria of the Binary Hydrocarbon Systems Propane-Benzene, Propane-Cyclohexane, n-Butane-Benzene, n-ButaneCyclohexane, n-Butane-n-Decane, and n-Butane-n-Dodecane.

[17] J. G. Aston, George J. Szasz and Herman L. Fink, The Heat Capacity and Entropy, Heats of Transition, Fusion and Vaporization and the Vapor Pressures of Cyclohexane.The Vibrational Frequencies of Alicyclic Ring Systems. J. Am. Chem. Soc, 65, 1135-1139, 1943.

[18] J.-N. Jaubert et F. Mutelet, VLE predictions with the Peng–Robinson equation of state and temperature dependent kij calculated through a group contribution method, Fluid Phase Equilibria, 2004.

[19] T. Holderbaum et J. Gmehling, PSRK: A Group Contribution Equation of State Based on UIVIFAC.

[20] D. G. Elliot, R. J. J. Chen, P. S. Chappelear, et R. Kobayashi, Vapor-liquid equilibrium of methane-butane system at low temperatures and high pressures, J. Chem. Eng. Data, vol. 19, N°1, 71-77, 1974.

[21] L. C. Kahre, Low-temperature K data for methane-butane, J. Chem. Eng. Data, vol. 19, N°1, 67-71, 1974.

[22] T.-C. Chu, R. J. J. Chen, P. S. Chappelear, et R. Kobayashi, Vapor-liquid equilibrium of methane-n-pentane system at low temperatures and high pressures, J. Chem. Eng. Data, vol. 21, N°1, 41-44, 1976.

[23] L. C. Kahre, Low-temperature K data for methane-n-pentane, J. Chem. Eng. Data, vol. 20, N°4, 363-367, 1975.

[24] D. Rabe, Experimental determination of dynamic viscosity and density of binary liquid mixtures of n-heptane with CO2, CH4, C2H6, C3H8 and of toluene with CH4 and C3H8, vol. PhD thesis, Technical University Berlin, Berlin, 1981.

[25] F. M. Llave, K. D. Luks, et J. P. Kohn, Three-phase liquid-liquid-vapor equilibria in the nitrogen-methane-ethane and nitrogen-methane-propane systems, J. Chem. Eng. Data, vol. 32, N°1, 14-17, 1987.

[26] G. S. Stepanova, Y.I. Vybornova, A. S. Velikovskii, G. Delo, Phase equilibria of ternary system methane + n-hexane + benzene: II, N°10, 9-13, 1965.

[27] Y.-N. Lin, S.-C. Hwang, et R. Kobayashi, Vapor-liquid equilibrium of the methane-toluene system at low temperatures.

[28] H. G. Donnelly et D. L. Katz, Phase Equilibria in the Carbon Dioxide–Methane System, Ind. Eng. Chem., vol. 46, N°3, 511-517.

[29] L. A. Webster et A. J. Kidnay, Vapor-Liquid Equilibria for the Methane-Propane-Carbon Dioxide Systems at 230 K and 270 K.

[30] K. Ohgaki, F. Sano, et T. Katayama, Isothermal vapor-liquid equilibrium data for binary systems containing ethane at high pressures, J. Chem. Eng. Data, vol. 21, N°1, 55-58, 1976.

[31] A. B. J. Rodrigues, D. S. McCaffrey, et J. P. Kohn, Heterogeneous phase and volumetric equilibrium in the ethane-n-octane system, journal of chemical and engineering data, vol. 13, N°2, 1968.

[32] W. L. Weng et M. J. Lee, Vapor-liquid equilibrium of the octane/carbon dioxide, octane/ethane, and octane/ethylene systems, J. Chem. Eng. Data, vol. 37, N°2, 213-215, 1992.

[33] T. S. Brown, A. J. Kidnay, et E. D. Sloan, vapor-liquid equilibrium in the carbon dioxide-ethane system.

[34] M.S.W. Wei, T.S. Brown, Vapor + Liquid Equilibria for the Ternary System Methane + Ethane + Carbon Dioxide at 230 K and Its Constituent Binaries at Temperatures from 207 to 270 K, J. Chem. Eng. Data, vol. 40, 726-731, 1995.

[35] J. W. Glanville, B. H. Sage, et W. N. Lacey, Volumetric and Phase Behavior of Propane-Benzene System, industrial and engineering chemistry, vol. 42, N°3, 1950.

[36] J. C. Acosta, E. Hevia, et S. Leipziger, Dew and bubble point measurements for carbon dioxide-propane mixtures.

[37] J. H. Kim et M. S. Kim, Vapor–liquid equilibria for the carbon dioxide + propane system over a temperature range from 253.15 to 323.15 K, Fluid Phase Equilibria, 2005.

[38] D. Richon, S. Laugier, et H. Renon, High-pressure vapor-liquid equilibria for binary mixtures containing a light paraffin and an aromatic compound or a naphthene in the range 313-473 K.

[39] G.H. Zenner, L.I Dana, Liquid-vapor equilibrium compositions of carbon dioxide-oxygen-nitrogen mixtures, Chem. Eng. Prog. Symp, 1963.

[40] T. A. Al-Sahhaf, A. J. Kidnay, et E. D. Sloan, Liquid + vapor equilibriums in the nitrogen + carbon dioxide + methane system.

[41] T.S. Brown, V.G. Niesen, E.D. Sloan, A.J. Kidnay, Vapor-liquid equilibria for the binary systems of nitrogen, carbon dioxide, and n-butane at temperatures from 220 to 344 K. Fluid Phase Equilibria, 7-14, 53, 1989.

[42] G.-I. Kaminishi, Y. Arai, S. Saito, et S. Maeda, vapor-liquid equilibria for binary and ternary systems containing carbon dioxide, J. Chem. Eng. Japan, vol. 1, N°2, 109-116, 1968.

[43] A. Neumann et W. Walch, Dampf/Flüssigkeits-Gleichgewicht CO2/CH4 im Bereich tiefer Temperaturen und kleiner CO2-Molenbrüche: Dampf/Flüssigkeits-Gleichgewicht CO2/CH4 im Bereich tiefer Temperaturen und kleiner CO2-Molenbrüche, Chemie Ingenieur Technik, vol. 40, N°5, 241-244, 1968.

[44] J. Davalos, W. R. Anderson, R. E. Phelps, et A. J. Kidnay, Liquid-vapor equilibria at 250 K for systems containing methane, ethane, and carbon dioxide, J. Chem. Eng. Data, vol. 21, N°1, 81-84, 1976.

[45] S. C. Mraw, S.-C. Hwang, et R. Kobayashi, Vapor-liquid equilibrium of the methane-carbon dioxide system at low temperatures, J. Chem. Eng. Data, vol. 23, N°2, 135-139, 1978.

[46] F. A. Somait et A. J. Kidnay, Liquid-vapor equilibriums at 270.00 K for systems containing nitrogen, methane, and carbon dioxide, J. Chem. Eng. Data, vol. 23, N°4, 301-305, 1978.

[47] N. Xu, J. Dong, Y. Wang, et J. Shi, High pressure vapor liquid equilibria at 293 K for systems containing nitrogen, methane and carbon dioxide, Fluid Phase Equilibria, vol. 81, 175-186, 1992.

[48] B. Bian, Y. Wang, J. Shi, E. Zhao, et B. C.-Y. Lu, Simultaneous determination of vapor-liquid equilibrium and molar volumes for coexisting phases up to the critical temperature with a static method, Fluid Phase Equilibria, vol. 90, N°1, 177-187, 1993.

[49] L. F. S. Souza, S. Z. S. Al Ghafri, O. Fandiño, et M. Trusler, Vapor-liquid equilibria, solid-vapor-liquid equilibria and H2S partition coefficient in (CO2 + CH4) at temperatures between (203.96 and 303.15) K at pressures up to 9 MPa, Fluid Phase Equilibria, vol. 522, 112762, 2020.

[50] E. Petropoulou, E. Voutsas, S. F. Westman, A. Austegard, H. G. J. Stang, et S. W. Løvseth, Vapor - liquid equilibrium of the carbon dioxide/methane mixture at three isotherms, Fluid Phase Equilibria, vol. 462, 44-58, 2018.

[51] Q. Nasir, K. M. Sabil, et K. K. Lau, Measurement of isothermal (vapor + liquid) equilibria, (VLE) for binary (CH 4 + CO 2) from T = (240.35 to 293.15) K and CO 2 rich synthetic natural gas systems from T = (248.15 to 279.15) K, Journal of Natural Gas Science and Engineering, vol. 27, 158-167, 2015.

[52] J. A. Davis, Solid-liquid-vapor phase behavior of the methane-carbon dioxide system, vol. 8, N°4.

[53] D. F. Kurata, Solubility of Solid Carbon Dioxide in Pure Light Hydrocarbons and Mixtures of Light Hydrocarbons.

[54] T. Shen, T. Gao, W. Lin, et A. Gu, Determination of CO2 Solubility in Saturated Liquid CH4 + N2 and CH4 + C2H6 Mixtures above Atmospheric Pressure, J. Chem. Eng. Data, 2012.

[55] C. J. Sterner, Phase Equilibria in the CO2-Methane Systems, in Advances in Cryogenic Engineering, K. D. Timmerhaus, Éd. Boston, MA: Springer US, 467-474, 1961.

[56] M. Elbishlawi et J. R. Spencer, Equilibrium Relations of Two Methane-Aromatic Binary Systems at 150° F., Ind. Eng. Chem., vol. 43, N°8, 1811-1815, 1951.

[57] D. Legret, D. Richon, et H. Renon, Vapor-liquid equilibrium of methane-benzene, methane-methylbenzene (toluene), methane-1,3-dimethylbenzene (m-xylene), and methane-1,3,5-trimethylbenzene (mesitylene) at 313.2 K up to the critical point, J. Chem. Eng. Data, vol. 27, N°2, 165-169, 1982.

[58] S. Srivatsan, W. Gao, K. A. M. Gasem, et R. L. Robinson, Solubility of Methane in Toluene at Temperatures from 313 to 423 K at Pressures to 8.9 MPa, J. Chem. Eng. Data, vol. 43, N°4, 623-625, 1998.

[59] Chang HL.; Kobayashi R. J., Chem. Eng. Data, 1967, 12(4), 517.

[60] P. H. Liu, K. D. Luks, et J. P. Kohn, Three-phase solid-liquid-vapor equilibria of the systems ethane-benzene, ethane-cyclohexane, and ethane-trans-decalin, J. Chem. Eng. Data, vol. 22, N°2, 220-221, 1977.

[61] Neumann A.; Mann R.; Von Szalghary W.-D., Kaeltetech. Klim. 1972, 24, 143-149.

[62] Krichevskii, I. R.; Khazanova, N. E.; Lesnevskaya, L. S.; Sandalova, L. Yu. Khim, Liquid-gas equilibrium in the nitrogen + carbon dioxide system under elevated pressures. Krichevskii, I. R.; Khazanova, N. E.; Lesnevskaya, L. S.; Sandalova, L. Yu. Khim. Prom-st. (Moscow), 38, 169-71, 1962.

[63] Muirbrook, N.K, Experimental and thermodynamic study of the high-pressure vapor-liquid equilibria for the nitrogen-oxygen-carbon dioxide system. Ph.D. Thesis, Univ. Calif., Berkeley (1964).

[64] B. Yucelen et A. J. Kidnay, Vapor−Liquid Equilibria in the Nitrogen + Carbon Dioxide + Propane System from 240 to 330 K at Pressures to 15 MPa, J. Chem. Eng. Data, vol. 44, N°5, 926-931, sept. 1999.

[65] Sonntag, R. E.; Van Wylen, G. J., Solid-vapor equilibrium of the carbon dioxide-nitrogen system at pressures to 200 atmospheres, Adv. Cryog. Eng., 9, 197-206, 1963.

[66] Sonntag, R. E.; Van Wylen, G. J., "The solid-vapor equilibrium of carbon dioxide-nitrogen", Adv. Cryog. Eng, 7, 99-105, 1962.

[67] Yakimenko N.P.; Glukh G.M.; Iomtev M.B.; Abramova R.I., Solubility of Solid Carbon Dioxide in Liquid Nitrogen. Russ.J.Phys.Chem. 49, 116-117, 1975.

[68] B. L. Rogers et J. M. Prausnitz, High pressure vapor-liquid equilibria for argon -I- neopentane and methane + neopentane.

[69] Brymer. Williams et N. W. Prodany, Vapor-liquid equilibriums in methane-hydrocarbon systems, J. Chem. Eng. Data, vol. 16, N°1, 1-6, 1971.

[70] M. Campestrini, A. Valtz, S. Hoceini, P. Stringari, Methane+neo-Pentane system: VLE measurements and modeling of the phase diagram including solid phases. The Journal of Chemical Thermodynamics, 2021.

[71] P.H. van Konynenburg, R.L. Scott, Critical lines and phase equilibria in binary van der Waals mixtures, Phil. Trans. R. Soc. Lond. A, vol. 298, N°1442, 495-540, 980.

[72] J. P. Kohn and K. D. Luks, Solubility of hydrocarbons in cryogenic LNG and NGL mixtures, GPA R- 22 76, 1976.

[73] Simulis Thermodynamics, version 2.0.4, ProSim SA, Lab_ege, France.

[74] A. Siahvashi, S. Z. S. Al Ghafri, X. Yang, D. Rowland, et E. F. May, Avoiding costly LNG plant freeze-out-induced shutdowns: Measurement and modeling for neopentane solubility at LNG conditions, Energy, vol. 217, 119331, 2021.

Chapter 5:

Development of a new equilibrium cell

Résumé du chapitre 5 en français

Un nouvel appareillage a été conçu et construit durant cette thèse pour surmonter certaines des limitations et des inconvénients de nos appareillages existants (gradient de température entre le système d'échantillonnage et la cellule d'équilibre, la pression minimale dans la cellule à garantir pour permettre le prélèvement des échantillons). L'originalité de ce nouvel appareillage réside dans un nouveau système d'échantillonnage. L'appareillage est constitué d'une nouvelle cellule d'équilibre équipée de 4 petites cellules, qui permettent de piéger des volumes constants de la phase fluide à l'équilibre avec une phase solide. Les échantillons piégés sont analysés (un échantillon à la fois) à température ambiante, grâce à un deuxième système d'échantillonnage constitué d'une boucle de prélèvement et d'une vanne Valco (6 orifices 2 positions) après avoir vidé la cellule d'équilibre.

L'appareillage a été validé en réalisant des mesures d'équilibre solide-liquide et solide-liquide-vapeur du système éthane+benzène. Les résultats obtenus sont comparés aux données présentées dans la littérature et un bon accord a été trouvé.

Le choix du système éthane+benzène a été motivé par plusieurs éléments : i) l'incohérence des données SLE de la littérature, ii) les publications récentes qui font état de la présence d'un cocrystal à des températures bien supérieures au point triple de l'éthane, et iii) l'intérêt de ce système dans le processus de production de GNL mais aussi pour comprendre la composition des lacs et des mers sur Titan, la plus grosse lune de Saturne.

5 Development of a new equilibrium cell

The apparatuses presented in section 3 are very efficient and useful for the study of the low-temperatures phase equilibria (whether solid-fluid or fluid-fluid phase equilibria). However, the sampling method used within these apparatuses suffers from the following limitations, which reduce their field of use.

i) A minimum pressure difference between the pressure of the mixture inside the EC and the pressure of the carrier gas in the sampling circuit must be guaranteed. Given the pressure of the carrier gas (usually close to 0.2 MPa), and the pressure drops related to the small diameter of the sampling capillary and the viscosity of the fluid to be sampled, a pressure inside the EC higher than 0.4/0.5 MPa has usually to be guaranteed. This pressure can reach 1 MPa in case of high viscosity (in particular at low temperatures).

ii) The withdrawn of a sample leads to a pressure drop inside the cell, negligible when a gas phase is withdrawn (order of magnitude of some mbar) and more important when a dense phase is withdrawn

(order of magnitude of a hundred of mbar depending on the opening time and the density of the phase). This can lead to composition instability of the fluid phase, especially when the composition is pressure-sensitive.

iii) The sampling device, Rapid OnLine Sampler Injector (ROLSI®), is equipped with a heated chamber allowing the vaporization of the sample (the temperature of the chamber is much higher than the one of the EC). This generates a vertical temperature gradient extending from the ROLSI® to the cell that may affect the composition of the samples with respect to the composition of the fluid within the EC. Consequently, increases the uncertainty of the experimental temperature.

iv) Each couple of the ROLSI®+capillary is designed to work at a certain range of pressure; thus, the investigation of phase equilibria outside this working range requires the use of another couple of the ROLSI®+capillary.

To overcome the above-mentioned limitations, a new equilibrium cell using a new and original sampling system has been conceived, designed, and built. The experimental apparatus has been validated by measuring the solubility limits of solid benzene in liquid ethane at SLE and SLVE; as shown in the following sections, the experimental results are in good agreement with those presented in the literature.

5.1 Description of the apparatus

The apparatus consists of a Hastelloy Equilibrium Cell (EC) equipped with 4 Small Cells (SCs); the volume of the EC is 25 cc and the one of each SC is 0.3 cc. At the solid-liquid (or solid-liquid-vapor) phase equilibrium, each SC allows trapping a constant volume of the equilibrium liquid phase at the equilibrium pressure and temperature. 4 Needle Valves (NVs) installed on the upper flange of the EC allow closing and isolating the SCs. The EC is connected to a 6-ports 2-positions Valco Valve (VV), which is in turn connected to a Gas Chromatograph (GC), a 0.2 cc sampling loop, and a Vacuum Pump (VP). The GC is equipped with a Thermal Conductivity Detector (TCD) and a Flame Ionization Detector (FID).

The equilibrium cell is placed inside a Brass Shell (BS) and covered with a Brass Cap (BC). A heating resistance surrounds the brass shell and a cartridge heater is placed in the brass cap. The two heathers are connected to two separate PID (Proportional, Integral, and Derivative) regulators. The BS together with the EC and the BC are immersed in a Cryostat (Cr) partially filled with liquid nitrogen (LN_2) so that LN_2 never wets the bottom of the EC.

The cryostat is at atmospheric pressure thanks to a nitrogen vapor vent (VN_2 vent) which avoids *(i)* the accumulation of the vapor nitrogen (generated by the evaporation of LN_2 and moving upward in the Cr) around the EC and *(ii)* the resulting heating of this accumulating vapor nitrogen because of the heaters of

the EC. As a result, the heat generated by the EC is permanently evacuated by the vented vapor nitrogen, which reduces the thermal stratification in the cryostat.

The balance between the excess refrigeration originating from the nitrogen vapor and the heat provided by the heating resistance and the heating cartridge of the EC allows regulating the temperature from the room temperature (high LN_2 consumption) down to liquid nitrogen temperature (low LN_2 consumption).

Two platinum resistance thermometer PT100 probes (T1 and T2) are installed in the top and the bottom part of the equilibrium cell; this allows evaluating the eventual presence of vertical temperature gradient within the EC. The temperature probes are not in direct contact with the fluid inside the EC but are placed in the body of the EC. The two PT100 probes have been calibrated against a 25Ω reference platinum probe (Pt25, Hart Scientific), with reference uncertainty u_{ref} = 8 mK. A Pressure transducer (P) (type Druke, range 0-16 MPa) is connected to the EC and allows measuring the pressure of the system within the cell. The pressure transducer was calibrated using a dead weigh balance with reference uncertainty u_{ref} = 1 kPa. These three sensors are connected to a Data Acquisition Unit (DAU) allowing the reading of the pressure-temperature conditions and their recording by means of a special computer software (Bench Ling Data Logger).

The EC is connected to an auxiliary cell containing the solvent (gas phase), and to a variable volume cell containing the solute (liquid at ambient temperature) through the loading line (LL). The LL allows also connecting the EC and the auxiliary cell containing the solvent to the Vacuum Pump (VP).

A magnetic stirring bar is placed inside the EC in order to enhance the heat and mass transfers within the fluid. The rotary movement generated by an external motor (M) is transferred to the stirring bar by means of a Permanent Magnet (PM). The rotation speed is set between 300 and 500 rpm.

The flow diagram of this new apparatus is presented in Fig5.1; the qualitative dimension of the EC and its main parts have been increased for improving the readability of the figure.

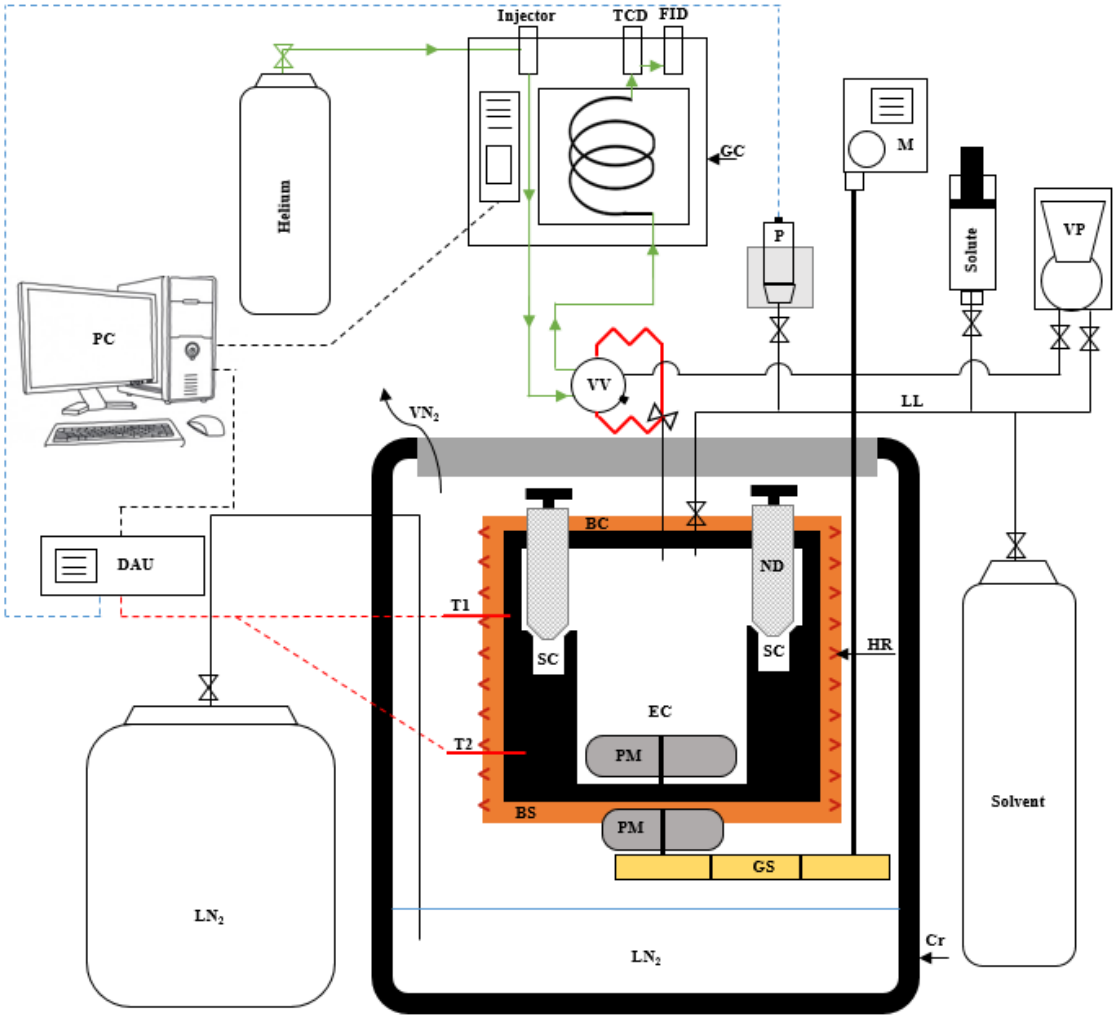

Figure 5.1: flow diagram of the new experimental apparatus

BC: *brass cap,* ***BS:*** *brass shell,* ***Cr:*** *cryostat,* ***DAU:*** *data acquisition unit,* ***EC:*** *equilibrium cell,* ***FID:*** *flame ionization detector.* ***GC:*** *gas chromatograph,* ***GS:*** *gear system,* ***HR:*** *heating resistance,* ***LL:*** *loading lines,* ***LN_2:*** *liquid nitrogen,* ***M:*** *external motor,* ***NV:*** *needle valve* ***P:*** *pressure transducer,* ***PC:*** *personal computer,* ***PM:*** *permanent magnet,* ***SC*** *Small Cell,* ***T1, T2:*** *temperature probes,* ***TCD:*** *thermal conductivity detector,* ***VV:*** *Valco valve,* ***VP:*** *vacuum pump.*

5.2 Experimental protocol

The experimental procedure for evaluating the solubility limits of solids in cryogenic liquids using the apparatus described above can be considered as a static-analytic method since the liquid samples are isolated at the equilibrium pressure and temperature (constant temperature and pressure), and then analyzed at room temperature using GC analysis. To carry out such measurements, four main steps are required: *i)* loading of the EC at room temperature, *ii)* cooling of the system down to the target temperature, *iii)* trapping of the liquid samples and *iv)* analyzing the samples at ambient temperature.

5.2.1 Loading of the EC

The equilibrium cell, the small cells, the loading line, and the sampling system (Valco valve and the sampling loop) are evacuated at ambient temperature. The small cells and the sampling system are then isolated from the equilibrium cell thanks to the needle valves and a three-way valve respectively. A given amount of the liquid solute (benzene) is introduced into the EC through the loading line, and then the solvent (ethane) is added into the EC until reaching a maximum pressure of 3.5 MPa, that is the saturation pressure of pure ethane at ambient temperature. The loaded amount of the solute must corresponds to a global composition higher than the solubility limit at the target pressure-temperature condition.

5.2.2 Cooling of the system down to the target temperature

Once the solute and the solvent are loaded into the EC at ambient temperature, the cryostat is partially filled with liquid nitrogen, and the target temperature is set on the PID regulators. At the target temperature, the system pressure depends on the loaded amounts of the solute and the solvent. Seeing the quantities of the solvent and the solute loaded at ambient temperature, the final pressure at the target temperature correspond usually to a SLVE condition of the ethane+benzene system. Additional ethane is then added in the EC to reach SLE conditions or to raise the level of the liquid phase within the EC at the SLVE over the position of the small cells.

5.2.3 Trapping liquid phase samples using the SCs

One of the small cells is open at the target pressure-temperature condition, and then the SC is fed with the liquid phase. The small cell is kept open for allowing matter exchange with the equilibrium cell, several tests has shown that the equilibrium is reached after two or three hours. For enhancing the matter exchange and the heat transfer within the cell, the stirring is maintained at 300 rpm. Once the equilibrium is reached, the small cell is closed thanks to the corresponding needle valve and then isolated from the EC. Fig5.2 shows a schematic description of the different steps allowing trapping liquid samples using the small cell at the SLVE (the solid phase is represented by red spheres, the liquid phase is represented by the blue color, and the vapor phase is shown by the orange color).

A new target temperature is then set on the PID regulators and a new liquid sample is trapped using another small cell after stabilization of temperature and pressure. The steps are repeated until all the small cells are filled.

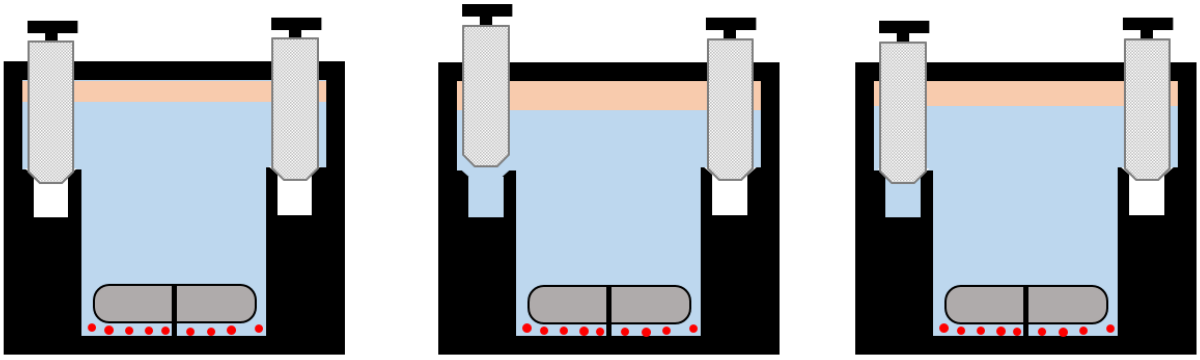

Figure 5.2: schematic description of the different steps allowing trapping liquid phase simples using a SC at the SLVE.

5.2.4 Analysis of the samples

Once all the small cells are filled and isolated. The EC is emptied and warmed up to ambient temperature then the EC is kept under vacuum until no traces of the solute and the solvent remain in the cell. The EC is again isolated and the content of one small cell is released into the EC at ambient temperature. Despite the samples are trapped within each SC in the liquid state at low temperature (samples are then liquids of high density), the pressure in the cell after releasing the content of the SC reaches only several dozen of kPa because of the small volume of the SC compared to the one of the EC. At this P-T condition (low pressure, ambient temperature), the system within the equilibrium cell is in a monophasic vapor phase; otherwise, the composition of the fluid cannot be determined.

The composition of the vapor phase within the EC at ambient temperature (equal to the composition of the liquid phase trapped at cryogenic temperature) is determined using GC analysis, following the three steps presented in Fig5.3. Firstly, the sampling loop is isolated from the EC and evacuated thanks to the vacuum pump (Valco valve in first position). The loop is then isolated from the vacuum pump and is connected to the EC and filled with a certain amount of the vapor phase contained in the EC (Valvo valve still in first position). Finally, the loop is isolated from the EC and the Valco valve is switched to the second position for allowing the transfer of the sample to the GC thanks to the continuous circulation of the carrier gas inside the transfer circuit. The TCD was used for the analysis of ethane and the FID was used for benzene.

The sampling procedure is repeated until having a repeatable composition of at least 6 samples (no increasing or decreasing trend of the fluid composition). The equilibrium cell and all the tubes are then emptied and evacuated before releasing the content of another small cell and performing its analysis.

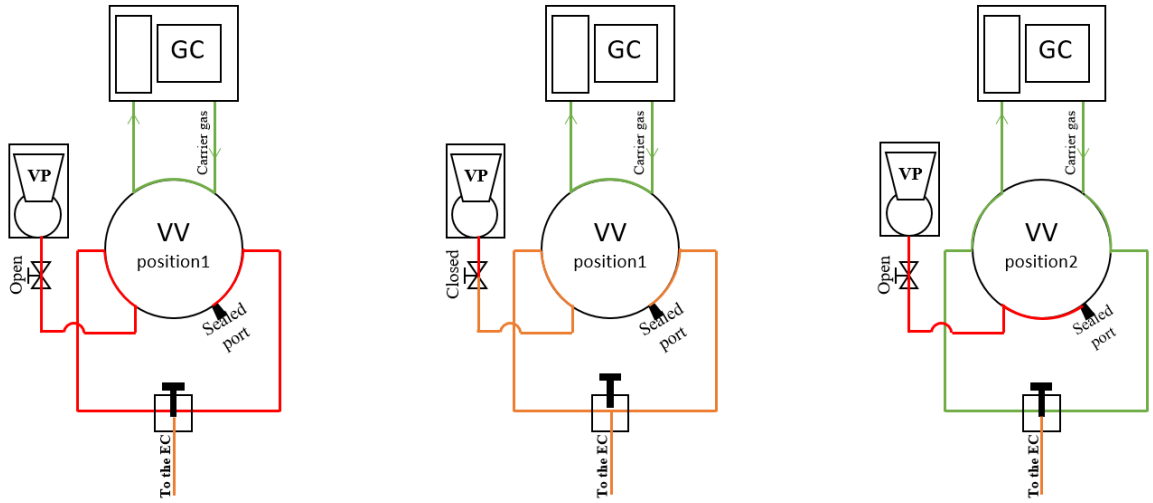

Figure 5.3: schematic description of the different steps allowing the sampling and the analysis of the fluid within the EC using the Valco valve and the sampling loop.

5.3 Uncertainty

The description of the uncertainty calculation is given in section 3.3 of chapter 3; nevertheless, for the reader convenience a brief reminder is given here below.

The uncertainties related to the experimental pressure and temperature are the result of the combination of three sources of uncertainty:

- The use of a reference device for the calibration of the temperature probes or the pressure transducer (the 25Ω reference platinum probe and dead weigh balance), with its own uncertainty (u_{ref}).
- The use of the calibration polynomial (u_{cal}).
- The repeatability of the measurements (u_{rep}).

The mathematical formula allowing the combination of these sources is given in Eq5.1. M represents the pressure (P) or the temperature (T), b_M is the maximum deviation between the reference value of M and the one calculated using the calibration polynomial over the entire calibration range, σ_M is the standard deviation of the recorded values after calibration, and N is the number of the recorded values.

$$u(M) = \sqrt{[u_{ref}(M)]^2 + [u_{cal}(M)]^2 + [u_{rep}(M)]^2} \quad (5.1)$$

$$u(M) = \sqrt{[u_{ref}(M)]^2 + \left[\frac{b_M}{\sqrt{3}}\right]^2 + \left[\frac{\sigma_M}{\sqrt{N}}\right]^2} \quad (5.2)$$

Seeing that the experimental temperature is calculated as the average of the temperatures measured using the top and the bottom probes (T_1 &T_2), the uncertainty on the experimental temperature is calculated as:

$$u(T) = \sqrt{\left[\frac{u(T_1)}{2}\right]^2 + \left[\frac{u(T_2)}{2}\right]^2} \tag{5.3}$$

Concerning the uncertainty affecting the composition of the fluid phase at equilibrium, the main sources of uncertainty are:

- The purity ($P_{u,i}$) of each *i-th* chemical used in the experiment (u_{pur}).

$$u_{pur}(n_i) = \frac{1 - P_{u,i}}{\sqrt{3}} n_i \tag{5.4}$$

- The use of the calibration polynomial for calculating the number of moles from the GC peaks (u_{cal}).

$$u_{cal}(n_i) = \sqrt{\sum_{j=1}^{w} \left[\left(\frac{\partial f}{\partial a_j}\right) u(a_j)\right]^2} \tag{5.5}$$

Where *w* is the order of the polynomial *f*, a_j is the j^{th}-order coefficient and $u(a_j)$ is the corresponding uncertainty.

- The propagation of the uncertainties when calculating the mole fraction *x* of the component *i* starting from the mole number of each component (u_{for}).

$$u_{for}(x_i) = \sqrt{\sum_{j=1}^{N_c} \left[\left(\frac{\partial x_i}{\partial n_j}\right)\left(u_{cal}(n_j) + u_{pur}(n_j)\right)\right]^2} \tag{5.6}$$

Seeing that the system presented here is a binary mixture, Eq5.6 becomes

$$u_{for}(x_1) = u_{for}(x_2) = \sqrt{\left[\frac{x_2}{n_T}(u_{pur}(n_1) + u_{cal}(n_1))\right]^2 + \left[\frac{x_1}{n_T}(u_{pur}(n_2) + u_{cal}(n_2))\right]^2} \tag{5.7}$$

- The repeatability of the measurements (u_{rep}).

$$u_{rep}(x_i) = \frac{\sigma_{x_i}}{\sqrt{N}} \tag{5.8}$$

The uncertainty related to the purity and the calibration are already used for the calculation of the uncertainty related to the errors propagation when calculating the molar composition; thus, the uncertainty related to the molar composition is calculated using Eq5.9.

$$u(x_i) = \sqrt{[u_{for}(x_i)]^2 + [u_{rep}(x_i)]^2} \quad (5.9)$$

5.4 Ethane+benzene system

The study of the phase equilibrium behavior of the ethane+benzene system is of high interest for several industrial and scientific applications. The knowledge of the solubility limits of benzene in liquid ethane is useful for the design and the optimization of natural gas liquefaction plants, seeing that benzene is considered as one of the highest potential solid former and ethane is known to be a better solvent compared to methane (the presence of ethane could enhance the solubility of benzene in the methane-rich mixture). In addition, recent publications dealing with planetary science report that the investigation of the thermodynamic behavior of this mixture is a key point in the quest of the study and the comprehension of the composition of the surface and atmosphere of Titan, the largest moon of Saturn [1] [2] [3] [4].

5.4.1 Literature review

The fluid-fluid phase equilibria of the ethane+benzene system are reported by Kay and Nevens [5], Ohgaki et al. [6], and Reaves et al. [7]. The phase envelops (bubble and dew points) and the critical properties of six mixtures (z_{ethane}=0.192, 0.392, 0.502, 0.723, 0.852, 0.948 mol/mol) have been reported in ref [5] and presented in Fig5.4. In ref [6], a static analytic method is used for measuring vapor-liquid equilibrium at 298.15 K, these data are shown in Fig5.5. The critical properties reported in ref [7] for ethane-rich mixtures, together with the critical points reported in ref [5] are presented in Fig5.6.

According to the Fig5.4, the VLE data of the mixture with z_{ethane}= 0.948 mol/mol present a different behavior compared to the other mixtures; indeed, vapor composition are reported for this mixture at pressures higher than the critical pressure of the mixture. Addition measurements could useful to make more insight into the behavior of this system.

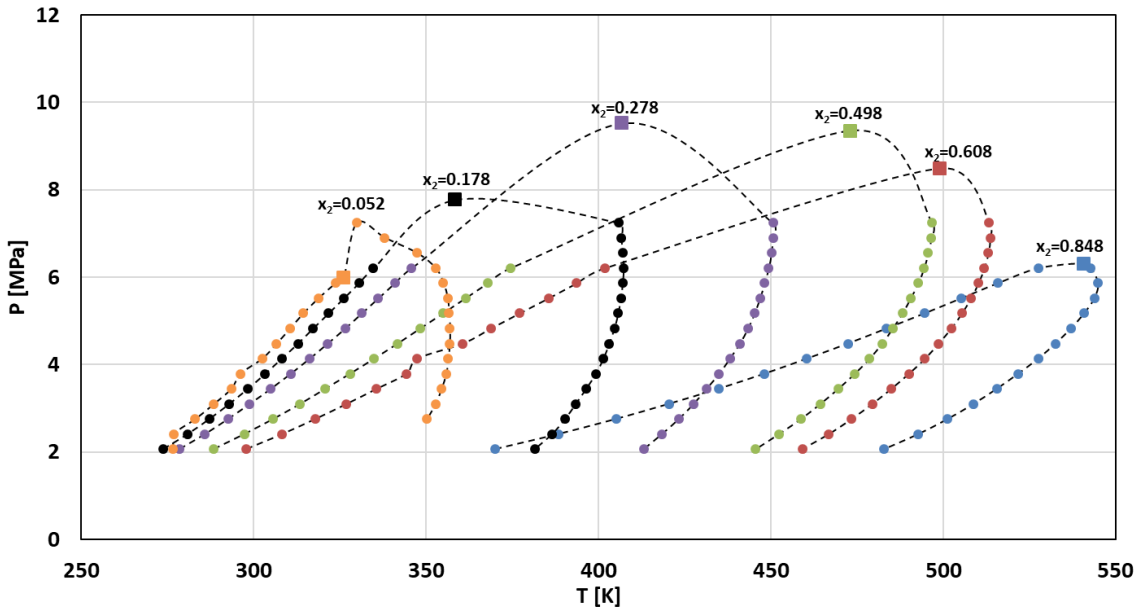

Figure 5.4: phase envelops data of ethane(1)+benzene(2) system
Ref [5] : ● bubble and dew points, ■ critical points, --- guide for the eyes of the reader

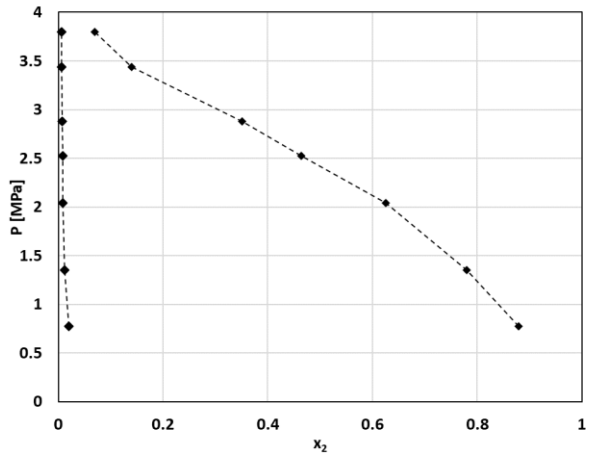

Figure 5.5: pressure-composition diagram of ethane(1)+benzene(2) system at 298.15K
♦ ref [6],
--- guide for the eyes of the reader

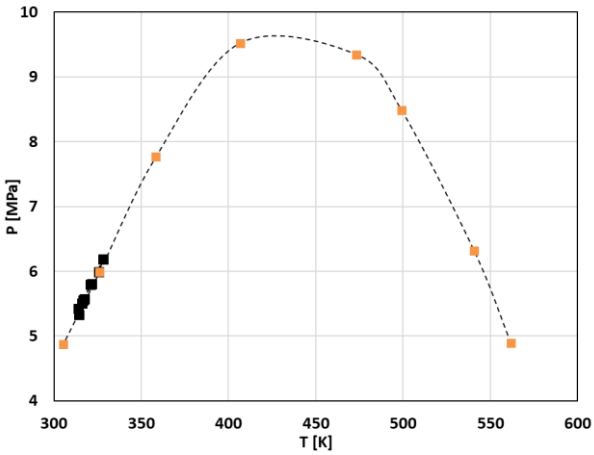

Figure 5.6: critical properties of ethane(1)+benzene(2) system
■ ref [7], ■ ref [5],
--- guide for the eyes of the reader

Neumann et al. reported the solubility limits of solid benzene in liquid ethane at temperatures ranging from the triple point temperature of benzene down to 97 K [8].

The SLVE measurements have been carried out by Liu and coworkers [9]; the authors used a borosilicate glass equilibrium cell for the visual detection of the solid benzene precipitation. The EC is filled with a known amount of the solute (benzene) and the solvent (ethane) and then cooled until the formation of the solid phase. At the crystallization point, the liquid phase composition has been determined stoichiometrically.

Diez-y-Riega and coworkers reported some solubility limits of solid benzene in liquid ethane at cryogenic temperatures (162 K down to 94 K) using the ultraviolet absorption method [4]. The authors used a copper cell equipped with four windows made of Quartz or fused Silica placed symmetrically on each side of the equilibrium cell. Mixtures of known composition were prepared inside the EC at ambient temperature. First, benzene in vapor state (pressure lower than its saturation pressure at ambient temperature) was introduced into the EC and the pressure was recorded, the density of benzene was then calculated assuming ideal gas behavior. Then, ethane was fed into the EC until reaching a pressure of 1 atm (0.101325 MPa) and the mixture was cooled down to 100 K. Additional ethane was then added to the EC until no vapor phase remained in the cell. The composition of benzene was calculated as the ratio between its density and the one of ethane taken at the target temperature. For a given temperature, the integrated absorbance of benzene in liquid ethane for different compositions was recorded. The integrated absorbance is then plotted as a function of the composition of the corresponding mixture. The integrated absorbance reached a constant value for mixtures with compositions higher than the solubility limits of benzene in liquid ethane. In ref [4], the pressure is not given, but seeing the experimental procedure, it can be inferred that the experimental pressure is slightly higher than the saturation pressure of ethane at the experimental temperature.

The literature data concerning the solubility of solid benzene in liquid ethane as a function of temperatures are presented in Fig5.7. A very good agreement can be noticed between the data reported by Neumann et al. [8] (black filled diamonds) and those reported by Liu et al. [9] (green filled squares). Nevertheless, the data reported by Diez-y-Riega et al. [4] (red filled circles) are not in agreement with the data reported in ref [8]; even if the two references tend to approximately the same value at temperatures close to 100 K, the data reported in [4] show much lower solubility limits than the ones reported in [8] for higher temperatures. As a consequence, it can be stated that additional measurements at the cryogenic temperatures are necessary to provide more knowledge on the variation of the solubility limits of solid benzene in liquid ethane.

The pressure-temperature condition of the SLVE loci reported in [9] are presented in fig5.8, the data shows a continuous shape, at least over the studied temperature range. According to the SLVE data, for decreasing temperature the SLVE pressure firstly increases until reaching a maximum of 0.99 MPa at 255 K, then decreases monotonically for lower temperatures.

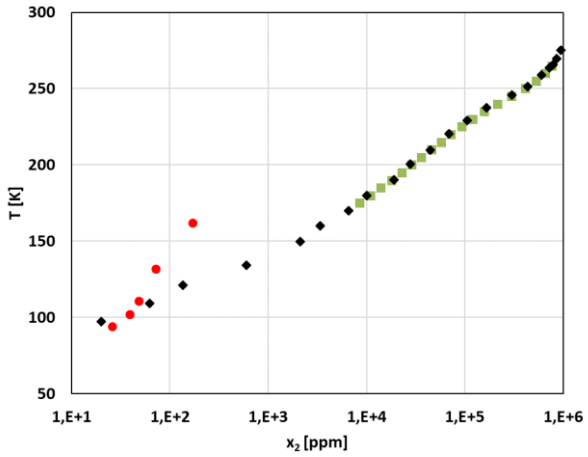

Figure 5.7: solubility limits of solid benzene (2) in liquid methane (1) as a function of temperature.
♦ ref[8], ■ ref [9], ● ref [4]

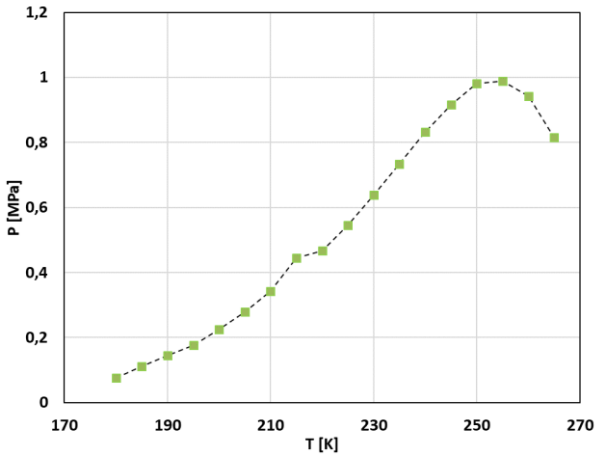

Figure 5.8: SLVE locus of ethane+benzene system.
■ ref [9], --- guide for the eyes of the reader

In the context of the investigation of Titan's surface composition, some literature works report that the ethane+benzene system forms a cocrystal at temperatures much higher than the triple point temperature of ethane [2] [3]. Vu et al. report that the cocrystal is stable at temperatures ranging from 90 K up to 160 K [3], at this temperature, the cocrystal becomes unstable and ethane is liberated and the original structure of pure solid benzene forms. Maynard-Casely et al. report that the cocrystal has a stoichiometric benzene/ethane ratio equal to 3/1 and the cocrystal structure is made of a lattice of benzene hosting ethane molecules [2]; in addition, the authors state that the cocrystal becomes unstable at temperatures higher than 145 K if the system is left at this temperature for sufficient time.

The presence of the cocrystal is a very exciting and challenging information seeing that the investigations of the solid-fluid behavior of such system consider that the solid phase is composed of the pure solid former (benzene), this hypothesis is commonly done when dealing with systems of interest for the natural gas liquefaction. As a consequence, the presence of a cocrystal challenges the global phase diagram of the ethane+benzene system, and the kind of phase equilibrium occurring at low temperatures.

The available literature data of the ethane+benzene system are gathered in Tab5.1. The temperature (T), the pressure (P), and the composition range (x_2 refers to the composition of benzene) are gathered in the first, the second, and the third column; the number of the experimental points (N_p), and the kind of equilibrium are presented in the fourth and the fifth column respectively; while the corresponding reference is presented in the last column.

Table 5.1: summary of the available literature data for the ethane(1)+benzene(2) system

T range [K]	P range [MPa]	x_2 range (%)	N_p	Kind of the data	Reference
273.15 – 545	2.1 – 9.5	5.19 – 84.8	174	VLE & Critical points	[5]
298.15	0.78 – 3.8	0.63 – 87.99	7	VLE	[6]
310.3 – 328.2	51.9 – 61.9	0.9 – 4.8	10	Critical points	[7]
97.2 – 275.2		0.002 – 95	21	SLE	[8]
175 – 265	0.08 – 0.99	8.85 – 76.48	19	SLVE	[9]
94 – 162	> 0.1	0.0026 – 0.017	5	SLE	[4]
90 – 160				Co-crystal	[3]
90 – 145				Co-crystal	[2]

5.4.2 Experimental results

Two experimental campaigns have been carried out for measuring the SLE and the SLVE of the ethane+benzene system. These data together with the corresponding uncertainties are summarized in Tab5.2 (the experimental uncertainties (U) are calculated following the method described in section 5.3; a coverage factor k = 2 is used).

Table 5.2: Summary of the experimental measurement of ethane(1)+benzene(2) system

Experimental campaign	T [K]	U_(T) [K]	P [MPa]	U_(P) [MPa]	x_2 [mol/mol]	U_(x_2) [mol/mol]	Kind of data
1	217.58	0.03	0.958	0.002	0.0463	0.0049	SLE
	217.58	0.03	0.958	0.002	0.0483	0.0051	SLE
	217.58	0.03	0.958	0.002	0.0486	0.0054	SLE
2	192.27	0.03	0.151	0.002	0.0157	0.0017	SLVE
	172.62	0.03	0.052	0.002	0.0055	0.0006	SLVE
	181.46	0.03	0.086	0.002	0.0098	0.0011	SLVE

The first experimental campaign aimed at validating the experimental apparatus and protocol by evaluating the repeatability of the samples trapped in the small cells at the same SLE conditions (same temperature and pressure). For this purpose, the equilibrium cell was fed with the mixture and cooled down to 217.58 K; additional ethane was then added until reaching a pressure of 0.96 MPa: at this P-T condition, the system is at the SLE. Liquid samples are trapped using the small cells and then analyzed at ambient temperature following the steps described in section 5.2 (due to operating issues, the content of one cell has not been analyzed during this first experimental campaign). According to results given in Tab5.2, the compositions of the 3 samples are in good agreement (standard deviation of 2.45%). This result was important since the fact of having a repeatable composition among the different small cells is a proof that no solid benzene has

been trapped when following the experimental procedure described in section5.2, (only the saturated liquid has been trapped inside the SCs).

The second experimental campaign has been carried out in order to investigate the SLVE locus of the mixture (P-T-x conditions). The equilibrium cell was filled at ambient temperature and then cooled down to the target temperature. Once the first target temperature was reached, the system was at SLVE (the experimental temperature and pressure were compared to SLVE data from the literature), but there is any likelihood that the liquid level was not enough to trap the liquid into the SCs because of the amount of matter loaded at ambient temperature in the cell. Additional ethane was then introduced into the EC until reaching a pressure slightly higher than the SLVE pressure (the system is then at SLE), the system is once again cooled until a SLVE occurs (a change in the P-T slope indicates the transition from the SLE to the SLVE). At this new SLVE condition, the liquid phase fills almost the entire EC. The system is kept at this P-T condition and one small cell is used for trapping a liquid sample. The same procedure is used for trapping liquid samples at lower temperatures using the other small cells.

The experimental values obtained in this work are presented in Figs5.9-10. As it can be observed in Fig5.9, the solubility limits of solid benzene in liquid ethane measured in this work are in good agreement with those reported in refs [8] and [9]; in addition, the P-T conditions of the SLVE loci measured in this work at three different temperatures are also in a very good agreement with those presented in ref [9] (as presented in Fig5.10). In spite of these preliminary results, additional measurements are required to provide more insights on the thermodynamic behavior of this system in the low-temperature region (down to the triple point temperature of ethane) to confirm the presence of the cocrystal and to elucidate the disagreement between the data reported in refs [4] and [8].

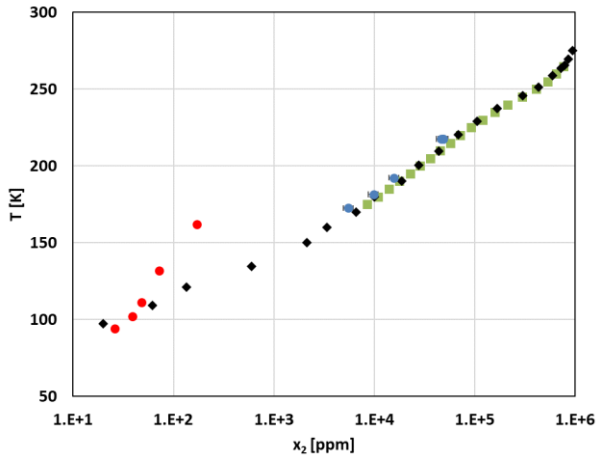

Figure 5.9: solubility limits of solid benzene(2) in liquid ethane(1) at SLE and SLVE as a function of temperature.

♦ ref[8]. ■ ref [9]. ● ref [4]. ● This work

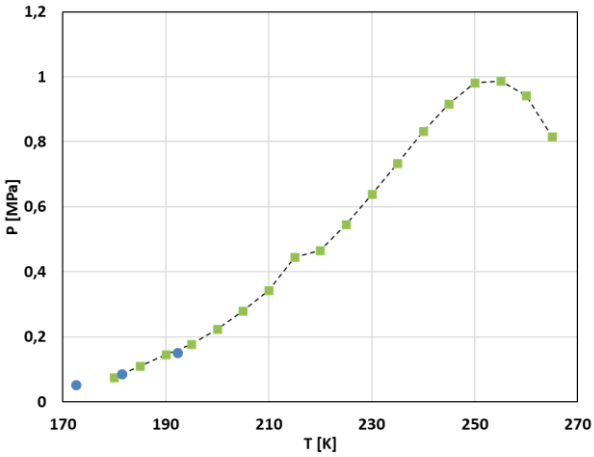

Figure 5.10: SLVE locus of the ethane+benzene system.

■ ref [9]. ● This work,

--- guide for the eyes of the reader

5.5 Conclusion

The new apparatus uses an original sampling system that allows overcoming some of the main limitations of existing static-analytic apparatuses, as the lower pressure limit required for the sampling, which can reach 1 MPa, the vertical temperature gradient between the carrier gas circuit and the equilibrium cell, and the potential dynamic phenomena occurring during sampling.

This apparatus has been tested and validated by investigating the SLE and SLVE conditions of the ethane+benzene system at temperatures down to 170 K, a good agreement between measured and literature values has been observed. However, additional measurements at lower temperatures are required in order to provide more information about the thermodynamic behavior of this system in the temperature range where a cocrystal is stable, and to elucidate the disagreement between two references dealing with SLE data in the low temperature region.

Thanks to the new sampling system, it is now possible at CTP to study phase equilibria in the low-pressure low-temperature region (which is not possible using existing apparatuses). This feature allows extending the use of this apparatus to some studies in planetary science, as the experimental investigation of the phase equilibria occurring in the lakes and seas of Titan (surface pressure around 0.15MPa).

References

[1] R. H. Brown, J. P. Lebreton, J. H. Waite, Titan from Cassini-Huygens. Dordrecht Heidelberg: Springer, 2009.

[2] H. E. Maynard-Casely, R. Hodyss, M. L. Cable, T. H. Vu, M, Rahm, A co-crystal between benzene and ethane: a potential evaporite material for Saturn's moon Titan, IUCrJ, vol, 3, N°3, 192-199, 2016,

[3] T. H. Vu, M. L. Cable, M. Choukroun, R. Hodyss, P. Beauchamp, Formation of a New Benzene–Ethane Co-Crystalline Structure Under Cryogenic Conditions, J. Phys. Chem. A, vol, 118, N° 23, 4087-4094, 2014.

[4] H. Diez-y-Riega. D. Camejo, A. E, Rodriguez, C. E. Manzanares, Unsaturated hydrocarbons in the lakes of Titan: Benzene solubility in liquid ethane and methane at cryogenic temperatures, Planetary and Space Sciencen vol, 99, 28-35, 2014.

[5] W. B. Kay, T. D. Nevens, Liquid-Vapor Equilibrium Relations in Binary Systems: the Ethane-benzene system, Chem. Eng, Prog. Symp, 1952.

[6] K. Ohgaki, F. Sano. T. Katayama, Isothermal vapor-liquid equilibrium data for binary systems containing ethane at high pressures. J. Chem. Eng. Data. vol. 21. N°1, 55-58, 1976

[7] J. T. Reaves, A. T. Griffith, C. B. Roberts, Critical Properties of Dilute Carbon Dioxide + Entrainer and Ethane + Entrainer Mixtures, J. Chem. Eng. Data, vol, 43, N°4, 683-686, 1998.

[8] A. Neumann, R. Mann, W.D. von Szalghary, Löslichkeit von festem Benzol in flüssigen Kohlenwasserstoffen, Kältetechnik, Klimatisierung, vol, 24, 145-149, 1992.

[9] P. H. Liu, K. D. Luks, J. P. Kohn, Three-phase solid-liquid-vapor equilibria of the systems ethane-benzene, ethane-cyclohexane, and ethane-trans-decalin, J. Chem. Eng. Data, vol, 22, 220-221, 1977.

Conclusion and perspectives

A deep bibliographic research has been carried out to collect all the available literature data of phase equilibrium involving molecular solid-phases for natural gas components. This allowed identifying some systems for which the available data were incomplete or inaccurate and several systems for which no data have been found in the literature. The bibliographic research, combined with a rough estimation (based on the temperature and enthalpy of melting) of the most critical components with respect to the risk of crystallization in the natural gas liquefaction process, and the suggestions of the Companies partners of the Joint Industry Project "Evaluation of the crystallization risk in LNG production", allowed identifying the systems for which the low-temperature phase equilibria have been investigated by both experimental and modeling approaches.

The static-analytic method has been used for measuring the solubility limits of the solid benzene, ethylbenzene, p-xylene, o-xylene, m-xylene, and tetrahydrothiophene in methane at temperatures ranging from the triple point temperature of the solid former down to 100 K and at two nominal pressures (3 and 6 MPa). In addition, the effect of the presence of ethane or nitrogen on the solubility limits of benzene and p-xylene has been studied at a nominal pressure of 6 MPa. These data have been obtained in the context of a project funded by industrial partners, thus, they are not reported in this manuscript and will be published at the end of the confidentiality period.

In addition, a deep investigation of the low-temperature phase equilibria of the methane+neopentane system has been carried out using both static-analytic and synthetic-indirect methods. Firstly, the solid-liquid-vapor equilibrium and the solid-liquid equilibrium of this system have been measured; then, vapor-liquid equilibrium data at temperatures down to the near-critical temperature of methane have been measured in order to have more insights into the global thermodynamic behavior of this system. Some additional Solid-Vapor Equilibrium (SVE) and Liquid-Vapor Equilibrium (VLE) at lower temperatures could be useful for having a deep comprehension of the low-temperature behavior of the methane+neopentane system.

For overcoming some of the limitations of our existing static-analytic apparatuses, a new equilibrium cell using an original sampling system has been conceived, designed, and built. This apparatus has been tested and validated by investigating the Solid-Liquid Equilibrium (SLE) and Solid-Liquid-Vapor Equilibrium (SLVE) of the ethane+benzene system at temperatures down to 170 K and a good agreement between measured and literature values has been observed. However, additional measurements at lower temperatures are required in order to provide more information about the thermodynamic behavior of this system. Thanks to this new equilibrium cell, it is now possible at the Center of Thermodynamics of Processes (CTP) to study

phase equilibria in the low-pressure low-temperature region (which was not possible using existing apparatuses).

Concurrently to the experimental work, the possibility of improving the modeling of the low-temperature phase equilibria, especially those involving solid phases, has been explored. The used modeling approach is based on the iso-fugacity condition; the solid phase has been considered as constituted by a pure component and its corresponding fugacity has been calculated using the classical approach initiated by Prausnitz, while the fluid phase fugacity has been calculated using the Peng Robinson equation of state.

Original measurements and literature data have allowed calculating pseudo-experimental activity coefficients that have been used in a new algorithm for the regression of accurate (point by point) binary interaction parameters (k_{ij}) for the representation of the available SLE and SLVE data. This approach has been shown that a constant value of the k_{ij} could be sufficient for the accurate modeling of the phase equilibria involving solid phases.

In a second time, the continuity of the k_{ij} between the Solid-Fluid Equilibrium (SFE) and the Fluid-Fluid Equilibrium (FFE) has been evaluated. For this purpose, a constant k_{ij} has been regressed on SLE and SLVE data of each investigated binary system, the obtained value has been used for predicting the FFE at temperatures close to the triple point temperature of the solid former. The obtained results have been found in a rather good agreement with the literature data and present deviations comparable with those obtained when applying the PPR78 EoS and the PSRK EoS (two widely used models for the calculation of equilibrium between fluid phases).

Based on this finding, the possibility of predicting the SFE using k_{ij} regressed on the FFE has been evaluated. For this purpose, a constant value of the k_{ij} used within the PR EoS with classical mixing rules has been regressed on the low-temperature FFE data of several binary mixtures and then used for predicting the SFE when the PR EoS is coupled with the classical approach. The predicted SFE of the systems investigated in this work showed a good agreement with respect to the literature data. This outcome allows exploiting a highly supplied FFE database for regressing reliable k_{ij} for the modeling of the phase equilibria over a large range of temperatures and particularly suitable for predicting solid-fluid equilibria.

The constancy of the binary interaction parameter at low temperature and its continuity crossing the triple point of the solid former suggest reviewing the mathematical expression of the k_{ij} calculated through the group contribution methods. Indeed, the most suitable expression is the one able to represent the variation of the k_{ij} in the critical region and tends to a constant value at low temperatures. This will allow the accurate modeling of the phase equilibrium over a wide temperature range (from the critical temperature of the heaviest component down to the lowest temperature of the existence of the fluid phases).

The results obtained in this work have been used for providing accurate information about the solubility limits of some components in liquefied natural gas. This allows adopting adequate purification limits before liquefaction, thus avoiding the oversizing of the purification limits and increasing the safety and the profitability of the LNG plants. In addition, the experimental and modeling outcomes of this work are an asset for the investigation of additional systems of interest for the natural gas liquefaction or those of interest for other industrial applications such as the liquefaction of hydrogen or certain scientific fields such as planetary science.

Articles

S. Hoceini, M. Campestrini, P. Stringari, A new experimental apparatus for the study of low-temperature phase equilibria for LNG production, Proceedings of the 16th Cryogenics 2021, pag 137.

P. Stringari, M. Campestrini, S. Hoceini, D. Atig, Gibbs free energy equation of state for solid methane from 21 to 300 K and up to 5000 MPa, J. Chem. Eng. Data 2021, 66, 1157−117.

M. Campestrini, A. Valtz, S. Hoceini, P. Stringari, Methane+neopentane system: VLE measurements and modeling of the global phase diagram, The Journal of Chemical Thermodynamics (Accepted).

P. Stringari, M. Campestrini, S. Hoceini, Gibbs Free Energy Equation of State for Phase I of Solid Benzene from 15 to 488 K and up to 1165 MPa, J. Chem. Eng. Data, (article ASAP).

Most of the experimental data obtained in this work are subject to a confidentiality agreement, thus they will be published by the end of the confidentiality period (July 2023).

Conferences

S. Hoceini, M. Campestrini, P. Stringari, New approach for improving the representation of phase equilibrium in the presence of solid phases: application to LNG production (Poster), ESAT 2021- 31st European Symposium on Applied Thermodynamics (virtual) July 5-9, 2021.

S. Hoceini, M. Campestrini, P. Stringari, A new experimental apparatus for the study of low-temperature phase equilibria for LNG production (oral presentation), The 16th Cryogenics 2021, IIR Conference (virtual) October 5-7, 2021.

Appendix A: summary of the literature data of the binary mixture of interest for the LNG production

Table A.1 gathers the SFE and the SFFE literature data of the system composed of methane and solid former. The references and the number of experimental points are reported in the second and the third column; the range of temperature, pressure, and composition (x refers to the solid former composition the fluid phase) are gathered in the third, fourth, and fifth columns.

The data of the solubility limit of the solid former in ethane, propane, and nitrogen are reported in tables A.2, A.3, and A.4 respectively. Table A.5 reports the literature data of the SFE of a binary mixture of solid formers.

Methane+solid former binary mixture

Table A.1: Summary of the available SFE or SFFE literature data for binary mixture "methane + solid former"

System	Reference	N	Range of T K	Range of P MPa	x range
CH_4+Ethane	[MOR 1959]	8	73 – 90.3		0,311 – 1
CH_4+Propane	[MOR 1959]	8	70.3 – 85.4		0,588 – 1
CH_4+n-Butane	[KUE 1976]	9	106.3 – 127.6	0.12 – 0.14	0.11 – 0.78
	[KUR 1975]	9	90.7 – 134.8		0 – 1
	[BRE 1977]	7	113,3 – 129	0,09 - 0,14	0,283 – 0,8115
CH_4+n-Pentane	[KUE 1976]	27	92.4 – 126	5.1 – 10.4	2×10^{-3} – 0.08
		7	116.5 – 139.8	0.15 – 0.34	0.02 – 0.83
	[KUR 1975]	7	90.7 – 143.5		0 – 1
	[BOY 1987]	6	109.5 – 120.5		8×10^{-3} – 0.05
	[PRE 1971]	3	100.4 – 124.5		1×10^{-3} – 0.02
	[MOR 1963]	2	90.1 – 113.1		2×10^{-3} – 0.01
	[DIC 1973]	7	128.5 – 143.4		0.17 – 0.67
	[BRE 1977]	7	123,4 – 131,3	0,23 - 0,34	0,0509 – 0,4119
CH_4+n-Hexane	[DIC 1973]	22	161.3 – 176.2	1.6 – 1.9	0.06 – 0.9
	[BEC 1956]	12	90.9 – 178.7		0 – 1

	[NEU 1970]	9	103.4 – 150		1.4×10^{-4} – 0.01
	[LUC 1981]	14	138 – 164	0.6 – 1.7	4×10^{-3} – 0.34
	[SHI 1962]	3	164.4 – 164.6	1.9 – 6.6	0.315
		10	162.9 – 177.8	3×10^{-4} – 1.9	0.19 – 1
	[DEM 1975]	7	100 – 160		6×10^{-5} – 0.09
	[KUE 1974]	22	93.8 – 163.7	7 – 13.2	3×10^{-5} – 0.15
	[STR 2012]	22	100.3 – 155.6		7×10^{-5} – 0.019
	[BRE 1977]	8	119,1 – 166,2	0,16 – 1,93	2×10^{-4} – 0,1795
CH_4+n-Heptane	[MOR 1963]	1	113.2		0.0036
	[NEU 1970]	9	103.2 – 150		4×10^{-5} – 3×10^{-3}
	[KUE 1974]	22	94.2 – 166.5	5.6 – 9.6	9×10^{-6} – 0.024
	[TIF 1978]	25	131 – 181	0.4 – 2.2	8×10^{-4} – 0.9
		1	169.35	2.216	0.0236 (L_1)
		1	169.35	2.216	0.32 (L_2)
	[KUR 1975]	1	169.04		0.08 (L_1)
		1	169.04		0.24 (L_2)
	[KOH 1961]	1	169.6	2.337	0.353
		1	191.65	4.785	0.37
CH_4+n-Octane	[PAP 1954]	8	90.9 – 216.3		0 – 1
	[KOH 1976]	9	155 – 190	1.4 – 4.5	2×10^{-4} – 9×10^{-4}
	[KOH 1977]	18	156 – 190	1.4 – 4.5	2×10^{-4} – 8×10^{-4}
		1	191.15	4.65	0.000592
	[TEL 1985]	9	109.9 – 150.1		3×10^{-6} – 3×10^{-5}
	[KOH 1964]	14	165.5 – 216.4	0.5 – 7.1	0.44 – 1
	[BRE 1977]	1	201.15	20.265	0.1
		1	190.69	4.668	
		4	156,3 – 179,7	1,36 – 3,34	4×10^{-4} – $6{,}4\times10^{-3}$
CH_4+n-Nonane	[SHI 1966]	13	177 – 219.3	0.5 – 15.2	0.43 – 1
		1	190.55	4.66	
		1	206.15	27.36	0.095

	[BRE 1977]	5	161,6 – 184,3	1,72 – 4,06	3×10^{-4} – $1,8\times10^{-3}$
CH_4+n-Decane	[BEA 1967]	13	236.8 – 243	0.5 – 7.1	0.59 – 0.97
	[STA 1961]	7	233.4 – 243.4	0.14 – 13	
		1	228.43	27.26	
	[FLO 1995]	1	232	37	0.092
CH_4 + neo-Pentane	[PRE 1971]	03	99.9 – 123.2		0.0101 – 0.0265
	[BAU 1974]	57	199.99 – 257.9	0.36 – 8.19	1.2×10^{-3} – 0.117
CH_4+2,3dymethylbutane	[PRE 1971]	3	100.2 – 123.4		4×10^{-3} – 0.043
CH_4+cyclo-Pentane	[PRE 1971]	2	100.2 – 112.5		2×10^{-3} – 0.013
CH_4+methyl-cyclo-pentane	[OED 1969]	4	132,6 – 140,15	100 – 170	0,118213
CH_4+cyclo-Hexane	[NEU 1970]	9	99.7 – 149		6.5×10^{-5} – 2.4×10^{-3}
	[KOH 1977]	38	154 – 279.8	0.005 – 7.6	3.35×10^{-3} – 1
		1	192.74	4.813	0.0041
	[KOH 1976]	28	155 – 279.8	0.005 – 7.8	3.35×10^{-3} – 1
		1	192.8	4.793	0.00517
CH_4 + Benzene	[LUK 1981]	17	268.1 – 277.7	1.01 – 17.23	0.9815 – 0.7246
		6	165 – 190.5	1.98 – 4.63	1.1×10^{-4} – 1.7×10^{-4}
	[KUE 1974]	37	99.4 – 199.8	5.41 – 13.68	3.9×10^{-7} – 1.4×10^{-3}
	[RIJ a 1992]	73	265.9 – 290.2	10.1 – 78.1	0.2678 – 0.8983
		17	261.8 – 266.7	44.1 – 72.1	0.0804 – 0.2359
		8	119,1 – 166,2	0,16 – 1,93	2×10^{-4} – 0,1795
	[NEU 1972]	12	103.8 – 185.4		6×10^{-6} – 4.83×10^{-3}
	[TEL 1985]	4	148.1 – 178		3.09×10^{-4} – 2.6×10^{-3}
	[HUG 2015]	7	158,7 – 258,4	0,6 – 21,8	2×10^{-4} – 0,001
	[SIA 2020]	7	233,2 – 268,2	2,1 – 8,2	6×10^{-4} – 0,0038
CH_4+Toluene	[KUE 1974]	19	92.1 – 192.6	5.82 – 13.41	3.6×10^{-6} – 2.67×10^{-3}
	[KUR 1975]	1	173.6		0.025 (L_1)

		1	173.6		0.65 (L_2)
	[LUK 1975]	7	133 – 166,4	0,44 – 2,04	$2,7\times10^{-4}$ – $2,7\times10^{-3}$
CH_4+p-xylene	[SIA 2019]	7	277,8 – 285,4	1,5 – 22,5	0,579 – 0,945
CH_4+CO_2	[AGR 1974]	42	137.9 – 198.1	0.2 – 2.8	0.0012 – 0,107
	[BOY 1987]	5	111.5 – 128		3×10^{-4} – 0.0015
	[BRA 1982]	4	194.5 – 213.7		0.205 – 0.865
	[BRE 1958]	9	90.9 – 215.4		0 – 1
	[CHA 1967]	5	166.5 – 195.4		0.019 – 0.2
	[CHE 1968]	9	110.7 – 194.6		3×10^{-4} – 0.126
	[DAV 1962]	42	97.5 – 211.7	0.03 – 4.87	0.0012 – 0.205
	[DON 1954	21	194.5 – 215.7	0.92 – 4.86	
		4	194.5 – 213.7		0.205 – 0.865
	[KUR 1971]	10	165.2 – 210.2	1.9 – 4.85	0.006 – 0.74
	[SHE 2012]	9	112 – 169.9	0.09 – 2.3	2×10^{-4} – 0.029
	[GAO 2012]	9	113.1 – 169.9		2×10^{-4} – 0.029
	[LE 2007]	54	168.6 – 187.7	0.96 – 3	0.01 – 0.03
	[PIK 1959]	103	132.6 – 210.2	0.16 – 4.8	2.6×10^{-4} – 0.59
	[SPA 1983]	11	129.6 – 201.3		0.0016 – 0.21
	[STE 1961]	6	166.5 – 199.8	1.95 – 5.9	0.019 – 0.052
	[STR 1970]	12	110 – 218.3		3.1×10^{-4} – 1
	[VOS 1975]	22	111.6 – 193.3		3.1×10^{-4} – 0.13
	[ZHA 2011]	17	191.1 – 210.3	0.29 – 4.45	0.108 – 0.142
	[PRE 1971]	2	126.4 – 137.5		7×10^{-4} – 2×10^{-3}
	[MRA 1977]	4	183.1 – 210.1	3.36 – 4.83	0.065 – 0.694
CH_4 + H_2S	[CHE 1968]	6	119 – 162.4		0.0012 – 0.017
	[KOH 1958]	21	167 – 185.9	0.05 – 13.66	
CH_4+ tert-butylthiol	[KUE 1980]	14	99.9 – 166.5	6.34 – 7.74	4×10^{-5} – 7.7×10^{-3}
CH_4 + N_2	[FAS 1941]	5	70.8 – 79.1		0.3 – 0.55
	[FED 1925]	14	62.9 - 90		0 – 1
	[OMA 1962	34	62.6 – 90.6		0 – 1

	12	60 – 87.5	0.007 – 0.07	
[TEL 1984]	7	72 – 88.7		0.06 – 0.515

Ethane+solid former binary mixtures

Table A.2: Summary of the available SFE or SFFE literature data for binary mixture "ethane + solid former"

System	Reference	N	Range of T K	Range of P MPa	x range
C_2H_6 + Methane	[MOR 1959]	6	73 – 90,65		0,691 – 1
C_2H_6 + n-Hexane	[MOR 1963]	3	90,1 – 113,2		0,00026 – 0,082
C_2H_6 + n-Octane	[KOH_b 1976]	13	150 - 210	0,007 – 0,17	0,00553 – 0,701
C_2H_6 + n-Decane	[KOH_b 1976]	15	165 - 235	0,086 – 0,36	10^{-3} – 0,6
C_2H_6 + Benzene	[KOH 1976]	19	175 - 265	0,075 – 0,99	0,085 – 0,76
	[NUE 1972]	21	97,2 – 275,2		2×10^{-3} – 0,95
C_2H_6 + p-xylene	[SIA 2019]	5	200,8 – 239,6	0,43 – 5,91	0,0573 – 0,2086
C_2H_6 + cyclo-Hexane	[LIU 1977]	23	145 - 255	0,096 – 0,21	0,0665 – 0,903
	[TIM 1928]	6	168,2 – 245,2		0,221 – 0,85
C_2H_6 + Carbon dioxide	[JEN 1971]	32	99,8 – 214,8	5×10^{-3} – 0,57	0,00013 – 0,9108

Appendix A

Propane+solid former binary mixtures

Table A.3: Summary of the available SFE or SFFE literature data for binary mixture "propane + solid former"

System	Reference	N	Range of T K	Range of P MPa	x range
C_3H_8 + Methane	[MOR 1959]	6	70,15 – 90,65		0,501 – 1
C_3H_8 + Ethane	[MOR 1959]	7	66,85 – 90,3		0,389 – 1
C_3H_8 + Nitrogen	[MOR 1959]	5	64,8 – 101		0,0002 – 0,0048
C_3H_8 + Benzene	[CHE 1981]	22	160 – 265	0,0047 – 0,18	0,00548 – 0,765
	[NUE 1978]	20	95,7 – 273,2		0,000042 – 0,9
C_3H_8 + Toluene	[TEL 1984]	11	110 – 160		0,00519 – 0,272
C_3H_8 + Cyclohexane	[CHE 1981]	19	156 – 245	0,046 – 0,066	0,166 – 0,855
C_3H_8 + Carbon dioxide	[JEN 1971]	33	108,2 – 213,7	0,001 – 0,45	0,00025 – 0,83
	[BRE 1958]	6	105 – 180,2		0,00009 – 0,058
	[VOS 1975]	16	101,7 – 187,3		0,00005 – 0,086
C_3H_8 + n-Decane	[TIF 1979b]	13	180 - 240	0,034 – 0,07	0,00667 – 0,828
	[KOH 1976]	14	179,7 – 230,3		0,0066 – 0,268
C_3H_8 + Hydrogen sulfide	[BRE 1961]	1	171,54		0,217
	[CHE 1968	3	142,5 – 162,5		0,03 – 0,33

Nitrogen+solid former binary micture

Table A.4: Summary of the available SFE or SFFE literature data for binary mixture "nitrogen + solid former"

System	Reference	N	Range of T K	Range of P MPa	x range
N_2 + Methane	[MOR 1959]	11	63,3 – 90,65		0 – 1
	[FAS 1941]	5	70,8 – 79,05		0,452 – 0,698
	[FED 1938]	12	63,1 – 90		0 – 0,89

	[OMA 1962]	26	63,1 – 90,6		0 – 1
	[TEL 1984]	7	72,04 – 88, 71		0,485 – 0,94
N_2 + Ethane	[COX 1950]	3	77,3 – 78,6		0,00776 – 0,00912
	[SZC 1980]	4	69,5 – 85,5		0,0061 – 0,0329
N_2 + Propane	[SZC 1980]	5	64,8 - 101		0,0003 – 0,0048
N_2 + i-Butane	[SZC 1980]	4	80 - 106		0,00015 – 0,00052
N_2 + n-Butane	[SZC 1980]	6	76,8 – 103,4		0,00001 – 0,0001
N_2 + i-Pentane	[SZC 1993]	1	77,4		$0,32*10^{-6}$
N_2 + n-Pentane	[SZC 1993]	1	77,4		$0,03*10^{-6}$
	[PRE 1971]	2	77,4 – 97,2		$(0,6 – 1,3)*10^{-6}$
N_2 + Cyclopentane	[SZC 1993]	1	77,4		$0,018*10^{-6}$
N_2 + n-Hexane	[SZC 1993]	1	77,4		$0,007*10^{-6}$
N_2 + Cyclohexane	[SZC 1993]	1	77,4		$0,005*10^{-6}$
N_2 + Carbon dioxide	[YAK 1975]	9	75 – 115		$1,6*10^{-6}$ – $1,66*10^{-4}$
	[FED 1940]	4	67 – 98		$(2,2 – 7,3)*10^{-6}$
N_2 + neopentane	[BAU 1974]	62	199,6 – 257,86	0,36 – 8,2	0,0076 – 0,11
N_2 + Benzene	[TEL 1985]	11	217,66 - 260		0,000013 – 0,000565

Binary mixture composed by only solid former

Table A.5 : Summary of the available SFE or SFFE literature data for binary mixture "solid former + solid former"

System	Reference	N	Range of T K	Range of P MPa	x range
n-butane + cyclohexane	[CHE 1981]	22	157 - 260	<0,046	0,1864 – 0,963
n-butane + benzene	[CHE 1981	23	160 - 270	<0,061	0,0077 – 0,8637
	[NEU 1972]	20	138,8 – 272,3		0,00263 – 0,901
n-butane + carbon dioxide	[JEN 1971]	19	134,5 – 213,2		0,00028 – 0,855
	[JEN 1971]	12	141,5 – 210,9	< 0,356	
n-butane + n-decane	[CHE 1981	16	165 - 240	<0,046	0,002 – 0,8156
n-pentane + carbon dioxide	[KUR 1974]	23	142,7 – 215,2	0,001 – 0,46	0,004 – 0,9341
i-pentane + carbon dioxide	[KUR 1974]	20	112,5 -215,7	0,0008 – 0,5	0,001 – 0,962
n-hexane + carbon dioxide	[KUR 1974]	20	177,2 – 215,7	0,022 – 0,48	0,0382 – 0,9723
n-heptane+ carbon dioxide	[KUR 1974]	14	182,2 – 215,9	0,041 – 0,48	0,00519 – 0,8
i-pentane + n-pentane	[SAP 1929]	4	116,5 – 134,9		0,272 – 0,795
i-pentane + n-hexane	[TIM 1934]	5	142,2 – 174,4		0,149 – 0,783
n-hexane + cyclohexane	[GAO 1979]	31	170,6 – 279,7	0,1	0 - 1
	[TIM 1928]	9	166,2 – 262,8		0,171 – 0,929
n-hexane + n-octane	[HOE 1951]	4	198,2 – 213,2	0,1	0,3152 – 0,863
n-hexane + benzene	[TIM 1928]	8	181,2 – 273,2		0,069 – 0,913
	[PET 1966]	12	253,8 – 277,1		0,442 – 0,966
	[YOS 1968]	14	237,7 – 275,4		0,3 – 0,95
	[NEU 1972]	12	184,3 – 270,5		0,0315 – 0,854
	[NEU 1978]	20	184,3 – 276,3		0,315 – 0,698
n-heptane + n-octane	[KRA 1949]	13	180,2 – 213,6		0,0995 – 0,9068
n-heptane + Ethylbenzene	[GUI 1980]	11	173,2 – 180,8		0,102 – 0,957
n-heptane + Toluene	[GUI 1980]	10	173,4 – 180,2		0,132 – 0,951

Cyclohexane + n-octane	[OTT 1983]	18	199,5 – 279,7	0 – 1
Cyclohexane + Toluene	[TIM 1928]	7	168,2 – 245,2	0,15 – 0,874
Cyclohexane + p-xylene	[PR 1998]	20	240,4 - 286	0 -1
Benzene + n-heptane	[KEH 1981]	20	181,9 – 275,4	0,0394 – 0,9667
	[LOI 1966]	55	182 – 276,5	0,0353 – 0,9826
Benzene + n-octane	[GOA 1979]	19	213,9 – 278,6	0 – 1
Benzene +cyclohexane	[GOA 1979]	19	232,1 – 279,5	0 – 1
	[TSU 2007]	14	232,1 – 279,6	0 – 1
Benzene + cycloheptane	[GOA 1979]	18	226,4 – 278,6	0 – 1
Benzene +cyclooctane	[GOA 1979]	18	234,2 – 287,7	0 – 1
Benzene + p-xylene	[GOA 1979]	28	252,2 – 286,4	0 – 1
Benzene + o-xylene	[KRA 1949]	15	229,7 – 274,4	0,094 – 0,936
Benzene + m-xylene	[TIM 1959]	9	213 – 264,4	0,2031 – 0,8855
	[KRA 1939]	21	213,6 – 278,7	0 – 1
	[MAG 1926]	11	212,9 – 278,8	0 – 1
Benzene + Ethylbenzene	[KRA 1949]	18	173,2 – 273,2	0,06 – 0,922
	[TIM 1959]	117	170,2 – 278,8	0,0159 – 0,987
Benzene + Toluene	[TIM 1959]	32	170,2 – 276	0,043 – 0,9542
	[PES 1946]	22	170,9 – 277,8	0,0013 – 0,9841
	[KRA 1946]	21	172,6 – 276	0,0042 – 0,94
	[MIT 1926]	13	170,2 – 270,6	0,1284 – 0,962
	[ORM 1921]	14	223,1 – 276,5	0,023 – 0,6252
	[ROB 1919]	15	173,4 – 263,7	0,22 – 0,942
Ethylbenzene + Toluene	[KRA 1949]	13	157,2 – 176,2	0,086 – 0,896
Ethylbenzene + p-xylene	[HYU 2004]	11	177,9 – 286,3	0 - 1
Toluene + m-xylene	[MIT 1926]	11	167,7 – 216,6	0,0585 – 0,8747
	[KRA 1939]	16	169,4 – 220,7	0,04316 – 0,887
	[NAG 1926]	11	167,7 – 216,6	0,0451 – 0,8583
Toluene + o-xylene	[KRA 1949]	11	175,7 – 236,2	0,043 – 0,74

Toluene + p-xylene	[LOH 2001]	18	214,6 – 284,2	0,1 – 0,944
	[KRA 1949]	10	177,2 – 279,2	0,026 – 0,831
m-xylene + o-xylene	[JAK 1995]	33	214,2 – 246	0,038 – 0,943
m-xylene + p-xylene	[JAK 1995]	35	221,6 – 285,5	0,026 – 0,966
	[GEO 1989]	10	272,2 – 286,2	0,7 – 1
o-xylene + p-xylene	[JAK 1995]	41	239,2 – 284,4	0,062 – 0,948

Appendix B: solid-phase fugacity from the Gibbs State Function for a pure component

EqB.1 shows the relation between the solid and the liquid phase fugacity of a pure component at a given pressure (P) and temperature (T).

$$R\ T\ ln\left(\frac{f_0^l(T,P)}{f_0^s(T,P)}\right) = \Delta G^{s\to l}(P,T)\ = \mu_0^l(P,T) - \mu_0^s(P,T) \qquad \text{B.1}$$

Where, R is the gas constant, f_0^s is the fugacity of the pure component in the solid phase and f_0^l is the one in the liquid phase, $\Delta G^{s\to l}$ is the Gibbs free energy variation upon melting, and μ_0^s is the chemical potential of the pure component in the solid phase and μ_0^l is the one in the liquid phase.

Figure B.1 shows a qualitative Pressure-Temperature (P-T) diagram of a pure component, solid black curves show P-T conditions where two phases are at equilibrium (saturation, melting, and sublimation lines); the filled black circle represents the critical point, while the filled triangle represents the triple point. The letters "a" and "b" indicate the solid phase while letters "c" and "d" indicate the liquid phase at the melting point and the triple point, respectively.

Figure B.2 shows the path that can be followed to calculate the total entropy and enthalpy variations occurring while moving from the solid phase ("a") to the liquid phase ("d") at the melting point passing through the solid phase ("b") and the liquid phase ("c") at the triple point.

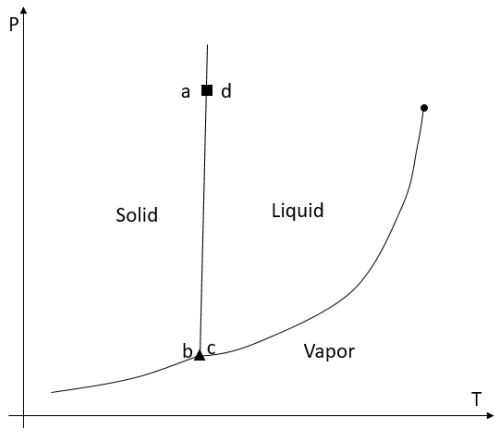

Figure B.1: Qualitative PT phase diagram for a pure component

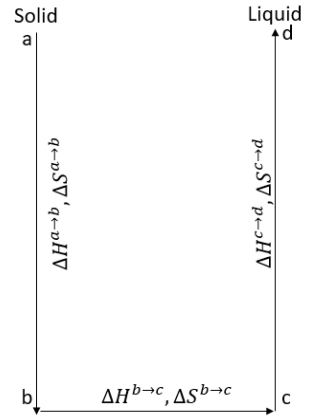

Figure B.2: Alternative path for the quantification of the enthapy and the entropy of melting

Appendix B

The Gibbs energy variation upon melting $(\Delta G^{s\to l})$ can be related to the enthalpy variation $\Delta H^{s\to l}$ and the entropy variation $\Delta S^{s\to l}$, using EqB.2. The enthalpy and the entropy are state functions; they have the particularity of depending only on the initial state and the final state whatever the path used. The path shown in figure B.2 allows the quantification of $\Delta H^{s\to l}$ and $\Delta S^{s\to l}$ from three contributions: as resumed in EqB.3 and EqB.4, the first contribution occurs in the solid phase from point "a" to point "b" $(\Delta H^{a\to b}, \Delta S^{a\to b})$, the second corresponds to the solid-liquid transition at the triple point $(\Delta H^{b\to c}, \Delta S^{b\to c})$, and the last one occurs in the liquid phase from point "c" to point "d" $(\Delta H^{c\to d}, \Delta S^{c\to d})$.

$$\Delta G^{s\to l} = \Delta H^{s\to l} - T\,\Delta S^{s\to l} \qquad \text{B.2}$$

$$\Delta H^{a\to d} = \Delta H^{a\to b} + \Delta H^{b\to c} + \Delta H^{c\to d}$$

$$\Delta H^{a\to d} = \int_T^{T_t} C_p^s\,dT + \int_P^{P_t}\left(V^s - T\left(\frac{\partial V^s}{\partial T}\right)_P\right)dP + \Delta H^{SLE}_{T_tP_t} + \int_{T_t}^{T} C_p^l\,dT + \int_{P_t}^{P}\left(V^l - T\left(\frac{\partial V^l}{\partial T}\right)_P\right)dP \qquad \text{B.3}$$

$$\Delta H^{a\to d} = \Delta H^{s\to l}$$

$$\Delta S^{a\to d} = \Delta S^{a\to b} + \Delta S^{b\to c} + \Delta S^{c\to d}$$

$$\Delta S^{a\to d} = \int_T^{T_t}\frac{C_p^s}{T}\,dT - \int_P^{P_t}\left(\frac{\partial V^s}{\partial T}\right)_P dP + \frac{\Delta H^{SLE}_{T_tP_t}}{T_t} + \int_{T_t}^{T}\frac{C_p^l}{T}\,dT - \int_{P_t}^{P}\left(\frac{\partial V^l}{\partial T}\right)_P dP \qquad \text{B.4}$$

$$\Delta S^{a\to d} = \Delta S^{s\to l}$$

Replacing in EqB.2 $\Delta H^{s\to l}$ and $\Delta S^{s\to l}$ by their expressions from EqB.3 and EqB.4

$$\begin{aligned}\Delta G^{s\to l} = {} & \int_T^{T_t} C_p^s\,dT + \int_P^{P_t}\left(V^s - T\left(\frac{\partial V^s}{\partial T}\right)_P\right)dP + \Delta H^{SLE}_{T_tP_t} + \int_{T_t}^{T} C_p^l\,dT + \int_{P_t}^{P}\left(V^l - T\left(\frac{\partial V^l}{\partial T}\right)_P\right)dP \\ & - T\left[\int_T^{T_t}\frac{C_p^s}{T}\,dT - \int_P^{P_t}\left(\frac{\partial V^s}{\partial T}\right)_P dP + \frac{\Delta H^{SLE}_{T_tP_t}}{T_t} + \int_{T_t}^{T}\frac{C_p^l}{T}\,dT - \int_{P_t}^{P}\left(\frac{\partial V^l}{\partial T}\right)_P dP\right]\end{aligned} \qquad \text{B.5}$$

Making some mathematical simplification, EqB.6 holds

$$\Delta G^{s\to l} = \int_T^{T_t}\Delta C_p^{s\to l}\,dT - T\int_T^{T_t}\frac{\Delta C_p^{s\to l}}{T}\,dT + \int_P^{P_t}\Delta V^{s\to l}\,dP + \Delta H^{s\to l}_{T_tP_t}\left(1 - \frac{T}{T_t}\right) \qquad \text{B.6}$$

Neglecting temperature effects on the heat capacity variation between the solid and the liquid phase $(\Delta C_p^{s\to l})$ and on the volume change at melting $(\Delta V^{s\to l})$, and using triple-point values $(\Delta C^{s\to l}_{P_{T_tP_t}}$ and $\Delta V^{s\to l}_{T_tP_t})$, the Gibbs

free energy variation can be calculated as a function of the P, T, the heat of fusion ($\Delta H_{T_tP_t}^{s\to l}$), the melting heat capacity change ($\Delta C_{P_{T_tP_t}}^{s\to l}$) and the melting volume change at the triple point conditions ($\Delta V_{T_tP_t}^{s\to l}$):

$$\Delta G^{s\to l} = \Delta H_{T_tP_t}^{s\to l}\left(1-\frac{T}{T_t}\right)+\Delta C_{P_{T_tP_t}}^{s\to l}\left(T-T_t-T\ ln\left(\frac{T}{T_t}\right)\right)+\Delta V_{T_tP_t}^{s\to l}(P-P_t) \qquad \text{B.7}$$

Introducing the EqB.7 into EqB.1

$$R\ T\ ln\left(\frac{f_0^l(T,P)}{f_0^s(T,P)}\right)=\Delta H_{T_tP_t}^{s\to l}\left(1-\frac{T}{T_t}\right)+\Delta C_{P_{T_tP_t}}^{s\to l}\left(T-T_t-T\ ln\left(\frac{T}{T_t}\right)\right)+\Delta V_{T_tP_t}^{s\to l}(P-P_t) \qquad \text{B.8}$$

Finally, the expression of the fugacity of the solid phase is given by EqB.9, where the fugacity of the pure liquid phase is calculated using an equation of state.

$$\boldsymbol{f_0^s(T,P)=f_0^l(T,P)\ \exp\left[\frac{\Delta H_{T_tP_t}^{s\to l}}{RT}\left(\frac{T}{T_t}-1\right)+\frac{\Delta C_{P_{T_tP_t}}^{s\to l}}{R}\left(\frac{T_t}{T}-1-ln\left(\frac{T_t}{T}\right)\right)-\frac{\Delta V_{T_tP_t}^{s\to l}}{RT}(P-P_t)\right]} \qquad \text{B.9}$$

Appendix C: The Peng Robinson Equation of State

The Peng Robinson equation is given by the following system of equation

$$P = \frac{RT}{v-b} - \frac{a(T)}{v(v+b)+b(v-b)} \tag{C.1}$$

$$a(T) = 0.457235529\frac{R^2T_c^2}{P_c}\left[1+m\left(1-\sqrt{\frac{T}{T_c}}\right)\right]^2 \tag{C.2}$$

$$b = 0.0777960739\frac{RT_c}{P_c} \tag{C.3}$$

$$m = 0.379642 + 1.487053\omega - 0.26992\omega^2 \tag{C.4}$$

In the case of a multi-component mixture, the van der Waals mixing rules are used

$$a(T) = \sum_{i=1}^{Nc}\sum_{j=1}^{Nc} x_i x_j \sqrt{a_i a_j}\left(1-k_{ij}\right) \tag{C.5}$$

$$b = \sum_{i=1}^{Nc} x_i b_i \tag{C.6}$$

Appendix D

Algorithms for the solid-fluid equilibria calculation

1.1 Solid-liquid equilibrium

FigD.1 shows the algorithm allowing the calculation of the Solid-Liquid Equilibrium (SLE) based on the resolution of the iso-fugacity condition.

At the SLE and for binary mixtures, the degree of freedom is equal to 2; thus, two variables among the Pressure (P), the Temperature (T), and the composition of the liquid phase ($\vec{x}$) are kept constant and only one variable is changed until having the iso-fugacity for the solid phase in the liquid and the solid phase.

Seeing that the solid phases are considered in this work as pure, for the SLE, only the solid former is considered for the resolution of the equilibrium condition. The fugacity of the solid former (subscript 2) in the liquid phase ($\hat{f}_2^L$) is calculated using an equation of state (in this work, the Peng Robinson Equation of State, PR EoS has been used), while the fugacity of the solid former in the solid phase is calculated using the classical approach (CA).

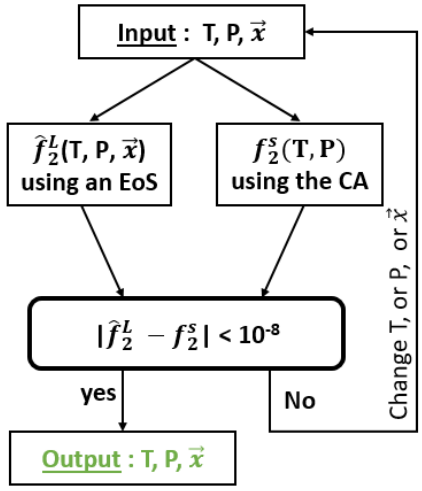

Figure D.1: algorithm allowing the calculation of the SLE based on the iso-fugacity condition

NB: the same algorithm can be used for calculating the Solid-Vapor Equilibrium (SVE). The fugacity of the solid fomer in the liquid phase ($\hat{f}_2^L$) is replaced by its fugacity in the vapor phase ($\hat{f}_2^V$).

Appendix D

1.2 Solid-liquid-vapor equilibrium

FigD.2 shows the algorithm allowing the calculation of the Solid-Liquid-Vapor Equilibrium (SLVE) based on the resolution of the iso-fugacity condition.

For calculating the SLVE for a binary mixture, the pressure, the temperature, and the global composition ($\vec{\mathbf{z}}$) are used as input. A liquid-vapor flash is performed at the given (T, P, $\vec{\mathbf{z}}$) condition. This allows obtaining the composition of the liquid ($\vec{\mathbf{x}}$) and the vapor ($\vec{\mathbf{y}}$) phases and also having the same fugacity for each component in the liquid and the vapor phase. Thus, the only required condition for having a SLVE is the iso-fugacity condition for the solid former in the liquid (or the vapor) phase ($\hat{f}_2^L$) and in the solid phase (f_2^s).

At the SLVE and for binary mixtures, the degree of freedom is equal to 1. Seeing that liquid and the vapor composition are calculated through a flash, only the pressure or the temperature can be changed until having the iso fugacity condition.

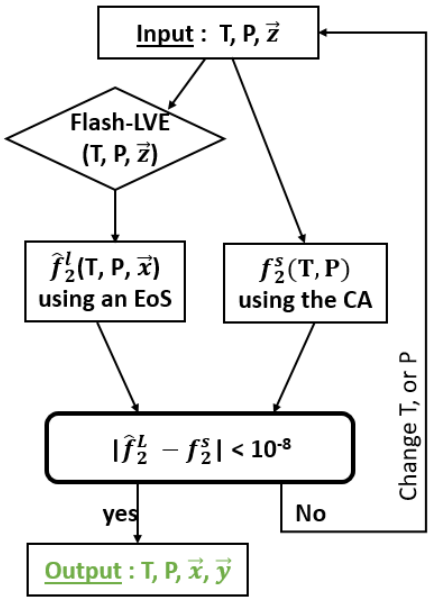

Figure D.2: algorithm allowing the calculation of the SLVE based on the iso-fugacity condition

Appendix D

1.3 Solid-liquid-liquid equilibrium

FigD.3 shows the algorithm allowing the calculation of the Solid-Liquid^{A}-Liquid^{B} Equilibrium (SL^{A}L^{B}E) based on the resolution of the iso-fugacity condition.

For calculating the SL^{A}L^{B}E for a binary mixture, the pressure, the temperature, and the global composition ($\vec{\mathbf{z}}$) are used as input. A liquid-liquid flash is performed at the given (T, P, $\vec{\mathbf{z}}$) condition. This allows obtaining the composition of the liquid^{A} ($\overrightarrow{x^{L_A}}$) and the liquid^{B} ($\overrightarrow{x^{L_B}}$) and also having the same fugacity for each component in the liquid^{A} and the liquid^{B}. Thus, the only required condition for having a SLLE is the iso-fugacity condition for the solid former in the liquid^{A}, $\hat{f}_2^{L_A}$ (or the liquid^{B}) and in the solid phase (f_2^s).

At the SL^{A}L^{B}E and for binary mixtures, the degree of freedom is equal to 1. Seeing that the composition liquid^{A} and the liquid^{B} are calculated through a flash-LL, only the pressure or the temperature can be changed until having the iso fugacity condition.

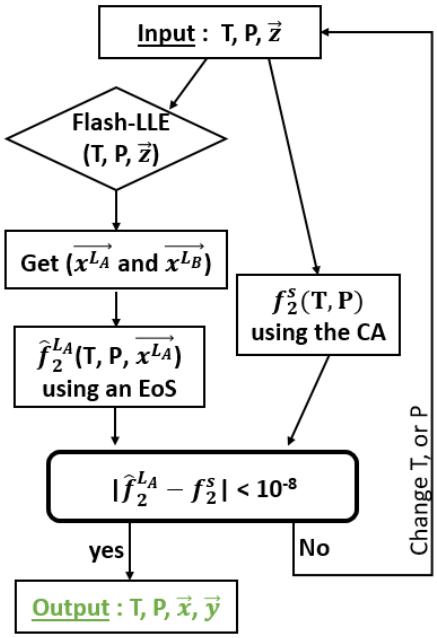

Figure D.3: algorithm allowing the calculation of the SLLE based on the iso-fugacity condition

1.4 Quadruple point

1.4.1 Solid-liquid-liquid-vapor equilibrium

FigD.4 shows the algorithm allowing the calculation of the quadruple point accounting for the Solid-Liquid^{A}-Liquid^{B}-Vapor Equilibrium (SL^{A}L^{B}VE) based on the resolution of the iso-fugacity condition.

For calculating the SL^{A}L^{B}VE for a binary mixture, the pressure, the temperature, and the global composition ($\vec{\mathbf{z}}$) are used as input. A liquid-liquid equilibrium flash and a liquid-vapor flash are performed at the given (T, P, $\vec{\mathbf{z}}$) condition. This allows obtaining the composition of the liquid^{A} ($\overrightarrow{\boldsymbol{x^{L_A}}}$), the liquid^{B} ($\overrightarrow{\boldsymbol{x^{L_B}}}$), and the vapor phase ($\vec{\boldsymbol{y}}$), and also having the same fugacity for each component in the liquid^{A}, the liquid^{B}, and the vapor phase. Thus, the only required condition for having a SL^{A}L^{B}VE is the iso-fugacity condition for the solid former in the liquid^{A}, $\hat{\boldsymbol{f}}_{\boldsymbol{2}}^{\boldsymbol{L_A}}$ (or the liquidB or the vapor phase) and in the solid phase ($\boldsymbol{f}_{\boldsymbol{2}}^{\boldsymbol{s}}$).

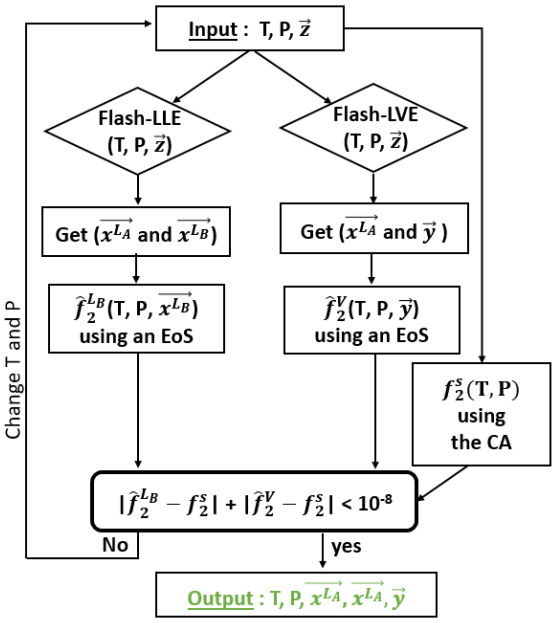

Figure D.4 : algorithm allowing the calculation of the SLLVE based on the iso-fugacity condition

At the SLLVE and for binary mixtures, the degree of freedom is equal to 0. Seeing that the composition liquid^{A}, the liquid^{B}, and the vapor phase are calculated through the flash-LL and the flash-LV; the pressure and the temperature of the system are changed at the same time until having the iso-fugacity condition.

1.4.2 Solid-solid-liquid-vapor equilibrium

FigD.5 shows the algorithm allowing the calculation of the quadruple point accounting for the $Solid_1$-$Solid_2$-Liquid-Vapor Equilibrium (S_1S_2LVE) based on the resolution of the iso-fugacity condition.

For calculating the S_1S_2LVE for a binary mixture, the pressure, the temperature, and the global composition ($\vec{z}$) are used as input. A liquid-vapor flash is performed at the given (T, P, $\vec{z}$) condition. This allows obtaining the composition of the liquid ($\vec{x}$) and the vapor ($\vec{y}$) phases and also having the same fugacity for each component in the liquid and the vapor phase.

Seeing that the $solid_1$ and the $solid_2$ are considered as pure, the iso-fugacity condition is performed separately for the component1 and the component2 at the same pressure and temperature.

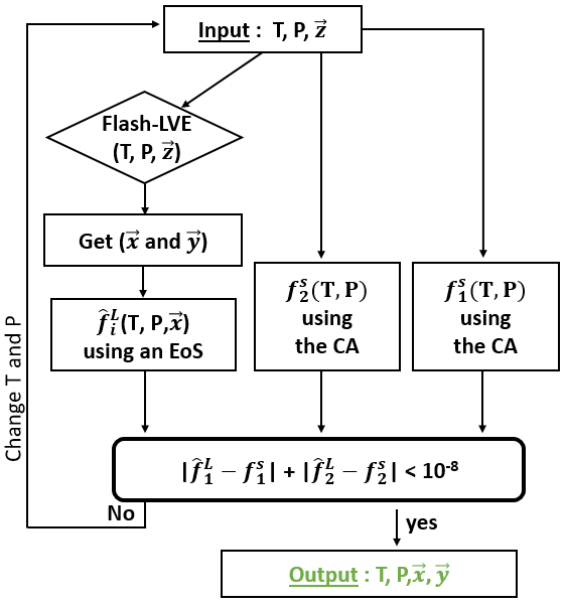

Figure D.5: algorithm allowing the calculation of the S_1S_2LVE based on the iso-fugacity condition

At the S_1S_2LVE and for binary mixtures, the degree of freedom is equal to 0. Seeing that the composition of the liquid, and the vapor phase phases are calculated through the flash-LV; the pressure and the temperature of the system are changed at the same time until having the iso-fugacity condition for the two components.

RÉSUMÉ

Cette thèse vise à étudier les équilibres de phases incluant les solides moléculaires à basses températures (de la température ambiante à environ 100 K) grâce à des mesures originales et le développement de modèles thermodynamiques précis. Les équilibres solide-fluide de plusieurs systèmes d'intérêt scientifique et industriel ont été mesuré sur une large gamme de températures. De plus, une nouvelle cellule permettant d'éliminer certains inconvénients de nos appareillages existants a été développée et validée grâce à des mesures d'équilibre solide-fluide du système éthane+benzène qui ont été en bon accord avec les données de la littérature. Parallèlement aux travaux expérimentaux, les pistes d'amélioration de la représentation et la prédiction des diagrammes de phases incluant les solides moléculaires quand l'équation d'état cubique de Peng Robinson est couplée avec l'approche classique ont été explorées.

Les résultats obtenus dans cette thèse ont permis, d'une part, d'acquérir de nouvelles connaissances sur les diagrammes de phases globaux et les équilibres solide-fluide de plusieurs mélanges, et d'autre part, de fournir des données précises sur les limites de solubilité de certains composants dans le gaz naturel. Cela permet d'adopter des limites de purification optimales du gaz naturel avant sa liquéfaction, ce qui améliore la sécurité et la rentabilité des unités de liquéfaction du gaz naturel.

MOTS CLÉS

Equilibre solide-fluide, mesures expérimentales, modélisation, cryogénie, GNL

ABSTRACT

This thesis aims at investigating the phase equilibrium including molecular solids at low temperatures (from ambient temperature to about 100 K) thanks to original measurements and the development of accurate models. The solid-fluid equilibria of several systems of scientific and industrial interest have been studied over a wide temperature range. In addition, a new equilibrium cell allowing overcoming some drawbacks and limitations of our existing equipment has been designed and built, this new apparatus has been validated by performing solid-fluid equilibrium measurements of the ethane+benzene system, which have shown a good agreement with respect to the available literature data. Concurrently, the possibilities of improving the representation and the prediction of phase diagrams including molecular solids when Peng Robinson cubic equation state is coupled with the classical approach have been explored.

The results obtained in this thesis allowed acquiring new knowledge about the global phase diagrams and the solid-fluid phase equilibria of several mixtures. In addition, this investigation allowed providing accurate values of the solubility limits of certain components in natural gas; this allows adopting optimal purification limits for natural gas before the liquefaction, and thus improving the safety and profitability of the natural gas liquefaction units.

KEYWORDS

Solid-fluid phase equilibrium, experimental measurements, modeling, cryogenics, LNG